

Copyright

by

Andrew William Ritchie

2015

**The Dissertation Committee for Andrew William Ritchie Certifies that this is the
approved version of the following dissertation:**

**QUANTIFYING ELECTROSTATIC FIELDS AT PROTEIN
INTERFACES USING CLASSICAL ELECTROSTATICS
CALCULATIONS**

Committee:

Lauren J. Webb, Supervisor

Ron Elber

Walter Fast

Graeme Henkelman

Pengyu Ren

**QUANTIFYING ELECTROSTATIC FIELDS AT PROTEIN
INTERFACES USING CLASSICAL ELECTROSTATICS
CALCULATIONS**

by

Andrew William Ritchie, B.S. Chem

Dissertation

Presented to the Faculty of the Graduate School of
The University of Texas at Austin
in Partial Fulfillment
of the Requirements
for the Degree of

Doctorate of Philosophy

**The University of Texas at Austin
August 2015**

**QUANTIFYING ELECTROSTATIC FIELDS AT PROTEIN
INTERFACES USING CLASSICAL ELECTROSTATICS
CALCULATIONS**

Andrew William Ritchie, PhD.

The University of Texas at Austin, 2015

Supervisor: Lauren J. Webb

<Abstract: May not exceed 350 words. It should be a continuous description, not disconnected notes or an outline.>

Table of Contents

List of Tables	viii
List of Figures	ix
List of Code and Parameters	xii
Chapter 1 Introduction	1
Chapter 2 Simulation Methods	5
2.1 Labeling and Mutating Proteins <i>in silico</i>	5
2.2 Enhanced Molecular Dynamics in Amber03: N-Dimensional Umbrella Sampling and Weighted Histogram Analysis Method.....	9
2.3 Electrostatic Clustering in Vibrational Chromophore Dihedral Space... <td>19</td>	19
2.4 Side chain orientation: Azimuthal and Polar Angles	24
2.5 Probe Parameterization for AMOEBA	29
2.6 Small Molecule Simulations in AMOEBA	39
Chapter 3 Electrostatic Field Methods.....	40
3.1 Amber03 with Explicit TIP3P Water.....	40
3.1.1 Reaction Field Electrostatics.....	40
3.1.2 Hybrid Solvent Reaction Field Electrostatics and Solute Coulomb Field	40
3.2 Amber03 with Poisson-Boltzmann Continuum Solvent	42
3.2.1 Reaction Field Method.....	43
3.2.2 Grid spacing and size	45
3.2.3 Box Location.....	46
3.3 Amber03 with Poisson-Boltzmann Continuum Solvent and Select Explicit TIP3P Water Molecules	51
3.3.1 5 Å Water Sphere Around the Vibrational Chromophore	51
3.3.2 Single Water Molecule Nearest the Vibrational Chromophore ..	52
3.3.3 Water Molecular Hydrogen Bonding to the Vibrational Chromophore	52
3.4 AMOEBA	54

3.4.1 Poisson-Boltzmann Continuum Solvent	54
3.4.2 Explicit AMOEBA Water	56
3.4.3 Charge Penetration Field Corrections	57
3.5 Vibrational Stark Effect	58
3.6 Virtual Stark Tuning Rate (VSTR) and “Ideal” Dielectrics	58
 Chapter 4 The Role of Electrostatics in Differential Binding of RalGDS to Rap Mutations E30D and K31E Investigated by Vibrational Spectroscopy of Thiocyanate Probes	60
4.1 Introduction	60
4.2 Results	65
4.2.1 Dissociation Constant Measurements	65
4.2.2 Molecular Dynamics Simulations	66
4.2.3 VSE Spectroscopy of the Docked Protein-Protein Complex.....	70
4.3 Discussion	76
 Chapter 5 Optimizing Electrostatic Field Calculations with the Adaptive Poisson-Boltzmann Solver to Predict Electric Fields at Protein-Protein Interfaces I: Sampling and Focusing	95
5.1 Introduction	95
5.2 Results and Discussion	103
5.2.1 Molecular Dynamics Sampling.....	103
5.2.2 Calculation of absolute electrostatic fields	105
Numeric solutions to the LPBE	107
Reaction field method solutions to the LPBE	110
Comparing the numeric solutions of the LPBE to the reaction field method solutions of the LPBE	111
5.2.3 Calculations of relative electrostatic field.....	111
Numeric relative field solutions to the LPBE	112
Reaction field method relative fields	114
Comparing relative fields calculated from the numeric method to the reaction field method	115

Chapter 6 Optimizing Electrostatic Field Calculations with the Adaptive Poisson-Boltzmann Solver to Predict Electric Fields at Protein-Protein Interfaces II: Explicit Near-Probe and Hydrogen Bonding Water Molecules	150
6.1 Introduction	150
6.2 Results and Discussion	153
6.2.1 Calculations of Absolute Fields	153
5 Å Sphere.....	153
Nearest Water.....	157
Hydrogen-bonding Water	158
6.2.2 Calculations of Field Differences:	159
5 Å Sphere.....	160
Nearest Water and Hydrogen-bonding Water.....	161
Chapter 7 Electrostatic Fields at Protein-Protein Interfaces: Increased Sampling Time and Various Electrostatic Methods: A Case for Simulating in Polarizable Force Fields	197
7.1 Introduction	197
7.2 Results.....	197
7.3 Discussion	197
Chapter 8 Electrostatic Fields in Small Thiocyanate Molecules with Ensembles Generated using the AMOEBA Force Field	198
8.1 Introduction	198
8.2 Results.....	198
8.3 Discussion	198
Appendix	199
Glossary	200
References	201

List of Tables

Table 2-1: Sample Parameters for Ryckaert Bellemans dihedral potential function used for validating 2D WHAM code	15
Table 2-2: Umbrella Sampling Parameters, grouped by chapter	16
Table 4-2: Measured vibrational frequencies of SCN-labeled Ral β mutants docked with Rap E30/K31; the observed changes in vibrational frequency upon docking each probe to Ras D30/E31 and each Rap mutant	94
Table 5-1: Percent Volume of Second-Stage APBS Box Filled with Protein Atoms	117
Table 6-1: Average number of Frames Water Molecules Remained within 5 Å of the Thiocyanate N ϵ Atom	163
Table 6-2: Virtual Stark Tuning Rate (VSTR), "ideal" Dielectric Constants (ϵ'), Correlation Coefficients (r), and p-values for APBS Calculations of Electrostatic Fields	164
Table 6-3: Percentage of Total Frames with a Nitrile-Water Hydrogen Bond....	166

List of Figures

Figure 2-1: 2D WHAM Validation	18
Figure 2-2: PB Solvent Reaction Field vs. Solute Analytic Coulomb Field	21
Figure 2-3: Field Values using Clustering Vs. Field Values using All Frames.....	22
Figure 2-4: Correlations and Slopes at Various Cutoff Values	23
Figure 2-5: Representation of azimuthal and polar angles	27
Figure 3-1: Reaction Field Method Schematic	48
Figure 3-2: Representation of Second-Stage Box Positions	49
Figure 3-3: Representative Snapshot Showing 5 Å Water Sphere	53
Figure 4-1: Rap-Ral Interface and Mutation Locations	79
Figure 4-2: Representative Thiocyanate-labeled Protein Spectra.....	80
Figure 4-3: Change in Absorption Energy of Thiocyanate Probes Relative to Rap E30/K31	81
Figure 4-4: Azimuthal and Polar Angles of Simulated CNC Probes.....	82
Figure 4-5: Azimuthal and Polar Angles of Simulated Rap Position 30 and 31 Sidechains	83
Figure 4-6: Convergence Test Based on CNC Dihedral Distributions	85
Figure 4-7: Thiocyanate Probability Distributions	87
Figure 4-8: Rap Position 30 Dihedral Distributions	89
Figure 4-9: Rap Position 31 Dihedral Distributions	91
Figure 5-1: Cyanocysteine Sidechain Dihedral Definitions	118
Figure 5-2: Representative 2D Dihedral Probability Distributions	119
Figure 5-3: 2D Dihedral Probability Distributions	120
Figure 5-4: 1D Umbrella Sampling χ_2 Dihedral Distributions	122

Figure 5-5: 2D Umbrella Sampling χ_2 Dihedral Distribution.....	124
Figure 5-6: Field Convergence Test	125
Figure 5-7: Absolute Field Plots for Various Box Locations - Ral Monomer ...	128
Figure 5-8: Absolute Field Plots for Various Box Locations – Rap E30/K31 ...	130
Figure 5-9: Absolute Field Plots for Various Box Locations – Rap E30D/K31 .	131
Figure 5-10: Absolute Field Plots for Various Box Locations – Rap E30/K31E	132
Figure 5-11: Absolute Field Plots for Various Box Locations – Rap E30D/K31E	133
Figure 5-12: Comparing Absolute and Relative Fields - Rap E30/K31	135
Figure 5-13: Comparing Absolute and Relative Fields - Rap E30D/K31	137
Figure 5-14: Comparing Absolute and Relative Fields - Rap E30/K31E.....	139
Figure 5-15: Comparing Absolute and Relative Fields - Rap E30D/K31E.....	141
Figure 5-16: Comparing Numeric PBE and RFM Relative Fields - Rap E30/K31	143
Figure 5-17: Comparing Numeric PBE and RFM Relative Fields - Rap E30D/K31	145
Figure 5-18: Comparing Numeric PBE and RFM Relative Fields - Rap E30/K31E	147
Figure 5-19: Comparing Numeric PBE and RFM Relative Fields - Rap E30D/K31E	149
Figure 6-1: PB Absolute Field Plots - Monomer	168
Figure 6-2: PB Absolute Field Plots – Rap E30/K31	170
Figure 6-3: PB Absolute Field Plots – Rap E30D/K31	172
Figure 6-4: PB Absolute Field Plots – Rap E30/K31E.....	174
Figure 6-5: PB Absolute Field Plots – Rap E30D/K31E	176
Figure 6-6: Probability of Water Lifetimes - Monomer	178
Figure 6-7: Probability of Water Lifetimes – Rap E30/K31.....	180
Figure 6-8: Probability of Water Lifetimes – Rap E30D/K31	182
Figure 6-9: Probability of Water Lifetimes – Rap E30/K31E	184

Figure 6-10: Probability of Water Lifetimes – Rap E30D/K31E	186
Figure 6-11: Average PB Field as a Function of Sampling Time.....	187
Figure 6-12: Average Field Gradient as a Function of Sampling Time	188
Figure 6-13: PB Relative Field Plots – Rap E30/K31	190
Figure 6-14: PB Relative Field Plots – Rap E30D/K31	192
Figure 6-15: PB Relative Field Plots – Rap E30/K31E	194
Figure 6-16: PB Relative Field Plots – Rap E30D/K31E	196

List of Code and Parameters

Code and Parameters 2-1: Cyanocysteine AMOEBA Parameters	31
Code and Parameters 2-2: Methyl Thiocyanate AMOEBA Parameters.....	33
Code and Parameters 2-3: Ethyl Thiocyanate AMOEBA Parameters.....	34
Code and Parameters 2-4: Hexyl Thiocyanate AMOEBA Parameters	38

Chapter 1 Introduction

Accurate and simple calculation of electrostatic fields in proteins is a subject of longstanding interest in the biophysical community. Continuum Poisson-Boltzmann (PB) models have been used to calculate pK_a values for titratable amino acids.¹⁻⁴ Changes in free energy and pK_a values have been examined using the Protein-Dipoles-Langevin-Dipoles (PDLD) model of Warshel and Levitt, which first introduced solvent polarization by mapping water dipoles to a Langevin grid and including protein dipoles, eliminating the use of a macroscopic dielectric constant in a microscopic system. Comparison to continuum models can be achieved by reintroduction of the concept of solute dielectric through the semi-macroscopic PDLD/S model and PDLD/S-LRA models, which suggest solute dielectrics of at least 2 should be used (higher when solute configurations are not well-considered).⁵⁻⁷ All-atom electrostatics using fixed charge force fields have also seen use in understanding protein electrostatics,⁸⁻¹⁰ specifically in the context of vibrational Stark effect spectroscopy (VSE), allowing for direct measurement of electrostatic fields in complicated systems. Models that include explicit atomic polarization, rather than molecular polarization like PDLD and its variants, have also been used to study protein electrostatics. The fully polarizable force field, atomic multipole optimized energetics for biomolecular applications (AMOEBA) has been used for a variety of electrostatics applications, such as binding free energies^{11, 12} and solvation energies.^{13, 14} Schnieders *et al.*¹⁵ demonstrated that a polarizable multipole Poisson-Boltzmann continuum model, built upon AMOEBA, reproduces protein dipole moments calculated with explicit solvent, suggesting it to be an efficient alternative to expensive solvent sampling for other electrostatics problems such as binding free energies and pK_a prediction. Additionally, mixed QM/MM methods are also being used to investigate protein electrostatics.¹⁶⁻¹⁹

Water also poses a significant challenge in understanding and calculating protein electrostatics. Hydration water²⁰⁻²³ is known to behave differently than bulk water; it is less mobile, has a lower dielectric constant,²⁴ and can play a role in stabilizing protein-protein and protein-ligand interactions.^{25,26} Calculations show that the ordered first and second hydration shells have a significant effect on the electrostatic potential energies of solvated proteins which are inadequately addressed by a purely implicit model, particularly when looking at both positively and negatively charged atoms.²⁷ It has also been shown that these solvation shell effects, and therefore agreement between implicit and explicit solvent models, can be improved by optimizing atomic radii and accounting for charging the solvent in an explicit solvent system.²⁷ Alternatively, a new implicit solvent model, semi-explicit assembly (SEA), has been developed, which differentiates between bulk and structural water and has been shown to approach implicit solvent calculation speeds with the accuracy of explicit solvent models.²⁸

Hydrogen bonding to vibrational chromophores is another difficulty in electrostatics calculations. It has been shown that using *ab initio* absorption frequency calculations on various water clusters and performing a multivariate fit to the calculated electrostatics, can then be used with standard molecular dynamics to yield good agreement with experimentally measured absorption frequencies of small molecules in water clusters.^{19,29,30} Corcelli *et al.*³¹ does this by finding Stark tuning rates for each x, y, z vector components of the calculated electrostatic field and summing these components, while Choi *et al.* uses a weighted sum of electrostatic potentials around the vibrational chromophore.^{29,30} In a QM/MM study of a thiocyanate vibrational chromophore in the enzyme ketosteroid isomerase (KSI), Layfield *et al.* also demonstrates that the explicit consideration of the water molecule nearest to the vibrational probe is important for capturing solvent polarization effects, and therefore calculating vibrational Stark shifts.¹⁶

In the pK_a Cooperative, scientists were challenged to calculate protein pK_a values on a blind protein sample using their computational methods of choice. In the presentation of this challenge, the authors state, “accounting for the heterogeneous response of proteins is generally considered the chief difficulty in modeling pK_a values in proteins.”³² This statement can be generalized for *all* experimentally-measured electrostatic properties in proteins. While many electrostatic field calculations have been shown to work well for solvated small molecules,¹⁰ there is an enormous difference in the number of degrees of freedom between a small (7 atom) methyl thiocyanate in a water cluster and the number of degrees of freedom in a protein, which significantly complicate the protein calculations.^{8,9,33,34} Obtaining a good ensemble of structures is therefore much more computationally intense for a solvated protein system than for a solvated small molecule.

Our data set of vibrational absorption energies measured on systems for which we have extensive MD-based structural information provide a unique opportunity to test the accuracy of various computational outputs. We have two goals of this work. First, we want to understand the strengths and weaknesses of a variety of computational platforms for accurately predicting our data set: a collection of vibrational absorption energies. Under reasonable assumptions, all computational methods yield results which are physically reasonable, yet in a single system, or even a single MD snapshot, the results can vary significantly depending on how they were calculated. We are interested in determining the amount of physical rigor and computational expense required to obtain *in silico* electrostatic fields which are well correlated to the equivalent *in vitro* vibrational absorption frequencies and comparing how the different methods compare to one another. Second, full integration of computational results into our measurements will enhance our

ability to interpret experimental observations and design new experiments in a way that enhances molecular-level understanding of our system.

Our first and most extensive efforts in this area have been solving the Poisson-Boltzmann equation (PBE) to calculate electric fields at the midpoint of the nitrile bond. PB-based computational strategies are common in the biophysical literature because of their speed and ease of implementation, but have been criticized for the nonphysical implementation of an electrostatic continuum in a highly heterogeneous and anisotropic system. However, given their extensive use throughout the community, it is critical to understand the conditions under which PB-based strategies are appropriate and reliable.

***Talk about amoeba

Chapter 2 Simulation Methods

2.1 LABELING AND MUTATING PROTEINS *IN SILICO*

Simulation parameters for cyanocysteine and GDPNP were obtained from previous studies^{8,35}. Simulations were performed using the Amber03 force field in Gomacs.³⁶ Ral starting structures came from the 2RGF³⁷ crystal structure, Ras starting structures came from 1LFD³⁸, and Rap starting structures came from 1GUA³⁹.

Generation of Ral β starting structures has previously been reported.³⁵ In short, all cysteine sidechain atoms except for C β were deleted from 2RGF and the sidechain was renamed to alanine. The C-terminal residues RTFT were taken from the pdb structure 1RAX (deposited in the PDB but unpublished) which ends in KKRTFT, and pasted onto the 2RGF structure, which ends in KKRT, by aligning the backbone atoms of the common KKRT residues and adding the FT coordinates onto the Ral structure file. The first residues in the 2RGF structure are ALA and LEU; these were changed to SER and HIS by renaming the residues in the pdb file, deleting hydrogen atoms, and renaming, using CD1 of LEU as ND1 of HIS. The N-terminal glycine (GLY 4) was modeled using Avogadro, completing the sequence. All missing heavy atoms were added using the tleap utility of Amber Tools.⁴⁰ The end resultant sequence is, starting from the N-terminal, GSH+Ral(2RGF,Cys \rightarrow Ala)+FT.

To make Ras, the GAMGS sequence from chain B of 4K81⁴¹ was used due to previous work which showed it to be the lowest energy conformation of this sequence available in the Protein Data Bank when bound to Ras.⁴² The N-terminal methionine of 1LFD was aligned to the methionine immediately following the GAMGS sequence in

4K81, afterwhich the GAMGS coordinates were added to the Ras structure file. The end resultant sequence is GAMGS+Ras(1LFD).

Rap starting structures and mutations have also already been reported.⁴³ To start, a GSH tag left on the N-terminal methionine after cleavage of the hexa-histidine affinity label during protein purification was modeled onto the N-terminus. This was done by searching the Protein Data Bank for proteins starting with the sequence GSHM (Met is the first Rap residue present in 1GUA). 87 NMR structures and 1 crystal structure were obtained from pdbs 1AQ5 (20 NMR structures)⁴⁴, 1W9R (19 NMR structures)⁴⁵, 2WCY (48 NMR structures)⁴⁶, and 2VKJ (1 crystal structure)⁴⁷. Rap was aligned to the methionine backbone of each GSHM structure using VMD⁴⁸, creating 88 structures containing the GSHM N-terminus. After adding hydrogen atoms using the GROMACS utility pdb2gmx⁴⁹, an energy minimization was performed and the lowest energy structure from this collection was chosen as the Rap model to be used for further calculations. The end resultant sequence is GSHM+Rap(1GUA). It was observed that in some structures, the N-terminal resides of Ralβ protruded between bonded atoms of Rap. To eliminate this nonphysical steric overlap, heavy atom restraints were placed on all but the Ralβ N-terminal GSHM residues and a 500 step gentle minimization was performed in Gromacs⁴⁹.

All side chain mutations were generated in the same manner using Amber Tools.⁴⁰ All side chain atoms except for shared heavy atoms were deleted from the mutation residue. The wild type residue was renamed to the desired residue and the resulting structure was passed to the tleap utility in Amber Tools⁴⁰ to model back in the missing atoms. In this way, starting from 1LFD Ras D30/E31K and 1GUA Rap E30D/K31E the additional Ras constructs D30/E31, D30E/E31, and D30E/E31K, and the additional Rap constructs E30/K31, E30D/K31, and E30/K31E were each constructed.

To generate cyanylated Ral structures N27C_{SCN}, G28C_{SCN}, N29C_{SCN}, Y31C_{SCN}, K32C_{SCN}, and N54C_{SCN}, residues were renamed to MET in the pdb file (because methionine contains the same number of heavy atoms as cyanocysteine), retaining and renaming any atoms common to the native residue and methionine. Missing methionine atoms were added using tleap.⁴⁰ To complete the mutation to cyanocysteine, the MET atoms CG, SD, and CE were renamed SG, CD, and NE and a short energy minimization was performed.

To dock Rap to Ral, the alpha carbons of the GTPase units of 1LFD and 1GUA were first aligned using the Smith-Waterman algorithm⁵⁰ with a gap penalty of -3 (chosen because it gave results most consistent with the STAMP⁵¹ structural alignment in VMD⁴⁸), and the Ral coordinates were merged with the Rap coordinates of 1GUA and saved as a reference structure, Rap(1GUA)+Ral(1LFD). The mutated Rap structure was then aligned to the Rap unit of the Rap(1GUA)+Ral(1LFD) reference structure and the coordinates of the resulting Rap(mutant)+Ral(1LFD) were saved. To dock mutated Ras structures to Ral, the mutated Ras was aligned to the 1LFD Ras and the Ral coordinates were merged with the mutated Ras structure and the coordinates of the resulting Rap(mutant)+Ral(1LFD) were saved. To introduce the probe to the docked system, the cyanylated Ral was aligned to the Ral of each GTPase(mutant)+Ral(1LFD) reference structure, and the GTPase(mutant) coordinates were merged with the cyanylated Ral coordinates to create each GTPase+Probe construct: Ral+N27C_{SCN}, Ral+G28C_{SCN}, Ral+N29C_{SCN}, Ral+Y31C_{SCN}, Ral+K32C_{SCN}, Ral+N54C_{SCN}, Rap E30/K31+N27C_{SCN}, Rap E30/K31+G28C_{SCN}, Rap E30/K31+N29C_{SCN}, Rap E30/K31+Y31C_{SCN}, Rap E30/K31+K32C_{SCN}, Rap E30/K31+N54C_{SCN}, Rap E30/K31E+N27C_{SCN}, Rap E30/K31E+G28C_{SCN}, Rap E30/K31E+N29C_{SCN}, Rap E30/K31E+Y31C_{SCN}, Rap E30/K31E+K32C_{SCN}, Rap E30/K31E+N54C_{SCN}, Rap E30D/K31+N27C_{SCN}, Rap

E30D/K31+G28C_{SCN}, Rap E30D/K31+N29C_{SCN}, Rap E30D/K31+Y31C_{SCN}, Rap
E30D/K31+K32C_{SCN}, Rap E30D/K31+N54C_{SCN}, Rap E30D/K31E+N27C_{SCN}, Rap
E30D/K31E+G28C_{SCN}, Rap E30D/K31E+N29C_{SCN}, Rap E30D/K31E+Y31C_{SCN}, Rap
E30D/K31E+K32C_{SCN}, Rap E30D/K31E+N54C_{SCN}, Ras D30/E31+N27C_{SCN}, Ras
D30/E31+G28C_{SCN}, Ras D30/E31+N29C_{SCN}, Ras D30/E31+Y31C_{SCN}, Ras
D30/E31+K32C_{SCN}, Ras D30/E31+N54C_{SCN}, Ras D30E/E31+N27C_{SCN}, Ras
D30E/E31+G28C_{SCN}, Ras D30E/E31+N29C_{SCN}, Ras D30E/E31+Y31C_{SCN}, Ras
D30E/E31+K32C_{SCN}, Ras D30E/E31+N54C_{SCN}, Ras D30/E31K+N27C_{SCN}, Ras
D30/E31K+G28C_{SCN}, Ras D30/E31K+N29C_{SCN}, Ras D30/E31K+Y31C_{SCN}, Ras
D30/E31K+K32C_{SCN}, Ras D30/E31K+N54C_{SCN}, Ras D30E/E31K+N27C_{SCN}, Ras
D30E/E31K+G28C_{SCN}, Ras D30E/E31K+N29C_{SCN}, Ras D30E/E31K+Y31C_{SCN}, Ras
D30E/E31K+K32C_{SCN}, and Ras D30E/E31K+N54C_{SCN}.

2.2 ENHANCED MOLECULAR DYNAMICS IN AMBER03: N-DIMENSIONAL UMBRELLA SAMPLING AND WEIGHTED HISTOGRAM ANALYSIS METHOD

An umbrella sampling strategy was used to obtain a Boltzmann-weighted statistical ensemble of thiocyanate probe orientations for all MD sampling. Through examining simulated protein structures, it became increasingly apparent that a second degree of freedom, χ_1 , was relevant to our probe conformational distributions. Therefore, two different umbrella sampling strategies were tested: one-dimensional sampling about the thiocyanate χ_2 dihedral angle and two-dimensional umbrella sampling about the thiocyanate χ_1 and χ_2 dihedral angles, shown in Figure 2-1. All molecular dynamics were completed using the GROMACS⁴⁹ software package at 300 K with the AMBER03⁵² force field and periodic boundary conditions.

Six probe locations on RalGDS were examined: N27C_{SCN}, G28C_{SCN}, N29C_{SCN}, Y31C_{SCN}, K32C_{SCN}, and N54C_{SCN}, in the monomeric state and docked to each GTPase system examined. We have therefore examined all probe locations and mutated constructs for which experimental data are available. Six structures for each system modeled were generated by fixing the thiocyanate χ_2 dihedral angle from 0° to 300° in 60° increments. Each structure was sampled with a dihedral potential that was flat within ± 30° of the fixed-dihedral position and quadratic with a force constant of 1000 kJ mol⁻¹ rad⁻² otherwise. These restraining potentials were carried through for the duration of the system set-up and simulation. Each structure was energy minimized with cut-off electrostatics, solvated with tip3p water⁴⁴ in a dodecahedron box, charge balanced by randomly replacing the appropriate number of water molecules with sodium or chloride ions using the genion GROMACS utility, and solvent relaxed by sampling for 20 ps with position restraints on all non-solvent heavy atoms with a force constant of 1000 kJ mol⁻¹

nm⁻² using PME^{53,54} electrostatics with a real-space cut-off of 0.9 nm, spacing of 0.12 nm, and interpolation order 4. Each rotamer of each system was then sampled using the GROMACS stochastic dynamics integrator, constraints on hydrogen-bonds using the LINCS algorithm⁵⁵, and PME electrostatics for 3 ns, recording snapshots every 5 ps, for a total of 18 ns of simulation and 3606 frames for each system. To test for structural rearrangements at positions 30 and 31 of Rap that would significantly influence the measured electrostatic field, the χ_1 dihedral angle on Rap residues 30 and 31 were each individually biased to create a Boltzmann-weighted ensemble of χ_1 rotomers. Rotomer libraries of Rap E30/K31, Rap E30D/K31, Rap E30/K31E, and the double mutant Rap E30D/K31E were created using the strategy described above. Once again, structures containing dihedral angles from 0° to 300° in 60° degree increments were generated for each mutant; these were energy minimized, solvated in tip3p water, relaxed, and then sampled for 3 ns each, generating 18 ns of simulation for each biased torsional angle. To summarize, for 24 mutant-containing rotomer structures, MD sampling included 18 ns of simulation biasing the nitrile probe, 18 ns of simulation biasing of Rap position 30, and 18 ns of simulation biasing of Rap position 31, for a total of 1296 ns of MD simulation of this system

Each frame was assigned to one of 72 5° bins from -180° to 175° based on the χ_2 dihedral angle. The weighted histogram analysis method (WHAM)^{56,57} was then used to calculate a torsional potential of mean force (PMF) for each of N bins i , which is related to the torsional probability distribution for each bin i (P_i) described by equation (2-1):

$$P_i = \frac{e^{-\beta \cdot PMF_i}}{\sum_{j=0}^N e^{-\beta \cdot PMF_j}}, \quad \beta = \frac{1}{k_b T} \quad (2-1)$$

which is the typical Boltzmann distribution function for a state i divided by the partition function, where T is the temperature in Kelvin, k_b is the Boltzmann constant, and PMF_j is the PMF for some state j . In this way, a Boltzmann-weighted distribution of structures was assembled in order to determine the average orientation of both the thiocyanate residues and the side chains at Rap positions 30 and 31 for comparing to experimental data.

The two-dimensional umbrella sampling was done in much the same way as the one-dimensional sampling, with few minor changes. The χ_1 angle was fixed from 0° to 300° in 30° increments, resulting in 12 structures. Each of these structures then had the χ_2 angle fixed from 0° to 300° in 30° increments, resulting in 144 total structures. To avoid steric clashes in the starting structures, for each χ_2 rotation, the distance between the center of mass coordinate of each rotated atom and every non-rotated atom was calculated. If a distance was found to be less than 1.5 \AA , the χ_2 angle was rotated $\pm 1.5^\circ$ from the dihedral center and the distances were recalculated. This was done until all non-bonded atoms were at least 1.5 \AA from each rotated atom. Next, two harmonic dihedral restraining potentials were generated for each structure, one for the χ_1 dihedral angle and one for the χ_2 dihedral angle. Following the same set-up strategy used in the one-dimensional sampling, the system was then energy minimized with cut-off electrostatics and dihedral force constants of $1000 \text{ kJ mol}^{-1} \text{ rad}^{-2}$, solvated in tip3p water in a dodecahedron box, and charge balanced as described above. The system underwent solvent relaxation using PME electrostatics for 20 ps with a force constant of $1000 \text{ kJ mol}^{-1} \text{ nm}^{-2}$ on heavy backbone atoms, dihedral force constants of $150 \text{ kJ mol}^{-1} \text{ rad}^{-2}$, and unrestrained side-chain atoms. Each of the 144 χ_1 - χ_2 rotamers were then sampled for 400 ps using the GROMACS stochastic dynamics integrator with PME electrostatics (again, with a real-space cut-off of 0.9 nm, spacing of 0.12 nm, and interpolation order 4) and

dihedral restraining potentials of $70 \text{ kJ mol}^{-1} \text{ rad}^{-2}$, for a total of 57.6 ns of simulation and 11664 frames for each system. It is worth reiterating that each step used a progressively smaller dihedral restraining potential. This was done to ensure that the dihedral angles of the final structure before sampling were as close as possible to the umbrella-sampling window while still allowing nearby residues to relax to orientations that accommodate the inclusion of our probe. Starting with a large restraining potential fixes the probe to a specific location orientation and forcibly moves nearby residues to accommodate the probe to minimize interaction energies. Subsequent weakening of the restraining potential allows the probe to respond to its surroundings in a manner more typical of MD, allowing both the probe as well as the residues near the probe to relax to energy minimized orientations. Without this subsequent weakening, many simulations resulted in dihedral forces becoming larger than the integrator can or is expected to handle, which were usually caused by steric clashes between the probe and side-chain atoms.

A Boltzmann-weighted statistical ensemble of structures obtained from two-dimensional sampling was then assembled using WHAM. Each frame was assigned to one of $5184 5^\circ$ by 5° bins. The bins were assigned based on equation (2-2), where b_1 is the one-dimensional χ_1 bin number, b_2 is the one-dimensional χ_2 bin number, B_i is the total number of bins in degree of freedom i (72 for all two-dimensional sampling done), and i_{index} refers to the subscript on b . Conditional probability was assumed.

$$\text{Bin}(b_1, b_2) = \sum_{i=b_1, b_2} B_i^{2-i_{\text{index}}} \cdot i \quad (2-2)$$

To validate our 2D WHAM code, we examined a Ryckaert-Bellemans dihedral potential, shown in equation (2-3), where ϕ is some angle and n and C_n are some example parameters obtained from the GROMACS manual, shown in Table 2-1. This is a very simple potential function with no contributions from any other source, unlike the

potential energy calculation in a protein, which will be influenced by various force field parameters such as bond force constants. However in WHAM, the sources of the potentials are not distinguished, and we are able to use the simple Ryckaert-Bellemans model to validate the code. We constructed the PMF from the sum of the potentials for a given pair of coordinates and the unbiased probability distribution, $p^*(\chi_1, \chi_2)$, using the ratio of the Boltzmann distribution function to the partition function, shown in equation (2-4), over an array of 2D dihedral angles ranging from -180° to 180° .

$$V_{rb} = \sum_{n=0}^5 C_n (\cos(\phi - \pi))^n \quad (2-3)$$

Next, we constructed the PMF and probability distribution landscapes, shown in Figure 2-1a. We then applied biasing potential windows to each dimension in a manner that mimics the methods used in GROMACS. The biased probability, $p(\chi_1, \chi_2)$, is given by equation (2-5). We then performed a Monte Carlo simulation centered on each of 144 biased windows, each with dimensions of $30^\circ \times 30^\circ$, with a probability $p(\chi_1, \chi_2)$ of sampling a given pair of dihedral angles, which was then analyzed using our 2D WHAM code to return the unbiased PMF and $p^*(\chi_1, \chi_2)$.

$$p^*(\chi_1, \chi_2) = \frac{e^{-\beta(V_{rb}(\chi_1) + V_{rb}(\chi_2))}}{\int \int e^{-\beta(V_{rb}(\chi_1) + V_{rb}(\chi_2))} d\chi_1 d\chi_2} \quad (2-4)$$

$$p(\chi_1, \chi_2) = \frac{e^{-\beta(V_{rb}(\chi_1) + V_1 + V_{rb}(\chi_2) + V_2)}}{\int \int e^{-\beta(V_{rb}(\chi_1) + V_1 + V_{rb}(\chi_2) + V_2)} d\chi_1 d\chi_2} \quad (2-5)$$

Figure 2-1 shows the analytical PMF and probability distributions (a), WHAM PMF and probability distributions on 144 windows each containing 40 frames (b), WHAM PMF and probability distributions on 144 windows each containing 80 frames (c), WHAM PMF and probability distributions on 144 windows each containing 160 frames (d), and WHAM PMF and probability distributions on 144 windows each containing 1000 frames (e). The major features of the probability distribution become

clear after only 40 frames; after 80 frames the probability distributions look very similar to the analytical distribution, and after 160 frames very little improvement is seen. We can also see that the high probability regions, representing the staggered orientations, have PMF landscapes that look like the analytical PMF, although the gauche regions appear to be ill characterized still. After 1000 frames the probability distribution is nearly identical to the analytical distribution and the moderate ranges of the PMF (light blue, $> 17.92 \text{ kJ mol}^{-1}$) now quantitatively approach the predictions of the analytical expression. Exact analytical PMF matching of low probability regions is very slow, requiring ≥ 10000 frames. From these results we conclude that the PMF converges to the analytical expression slowly for regions of low probability and quickly for regions of high probability. Table 2-2 summarizes the umbrella sampling setups for each project, listed by chapter.

The code for performing WHAM analysis can be accessed at:
<https://github.com/webbgroup-physical-chemistry/wham>

Table 2-1: Sample Parameters for Ryckaert Bellemans dihedral potential function used for validating 2D WHAM code

	Constraint (kJ mol⁻¹)		Constraint (kJ mol⁻¹)
C₀	9.28	C₃	-3.06
C₁	12.16	C₄	-26.24
C₂	-13.12	C₅	-31.5

Table 2-2: Umbrella Sampling Parameters, grouped by chapter

Chapters	Biasing Coordinate	Umbrella Window Size	Biasing Potential Shape	Windows per Experiment	Simulation Time per Experiment	Total Simulation Time
4, 5	CNC χ_2	60°	Quadratic-Flat-Quadratic	6	3.0 ns	18.0 ns
4	Position 30 χ_1	60°	Quadratic-Flat-Quadratic	6	3.0 ns	18.0 ns
4	Position 31 χ_1	60°	Quadratic-Flat-Quadratic	6	3.0 ns	18.0 ns
5, 6	CNC χ_1 , χ_2	30°	Quadratic	144	0.4 ns	57.6 ns
7	CNC χ_1 , χ_2	30 °	Quadratic	144	2.0 ns	288.0 ns
8	N/A	N/A	N/A	N/A	4-7 ns	4-7 ns

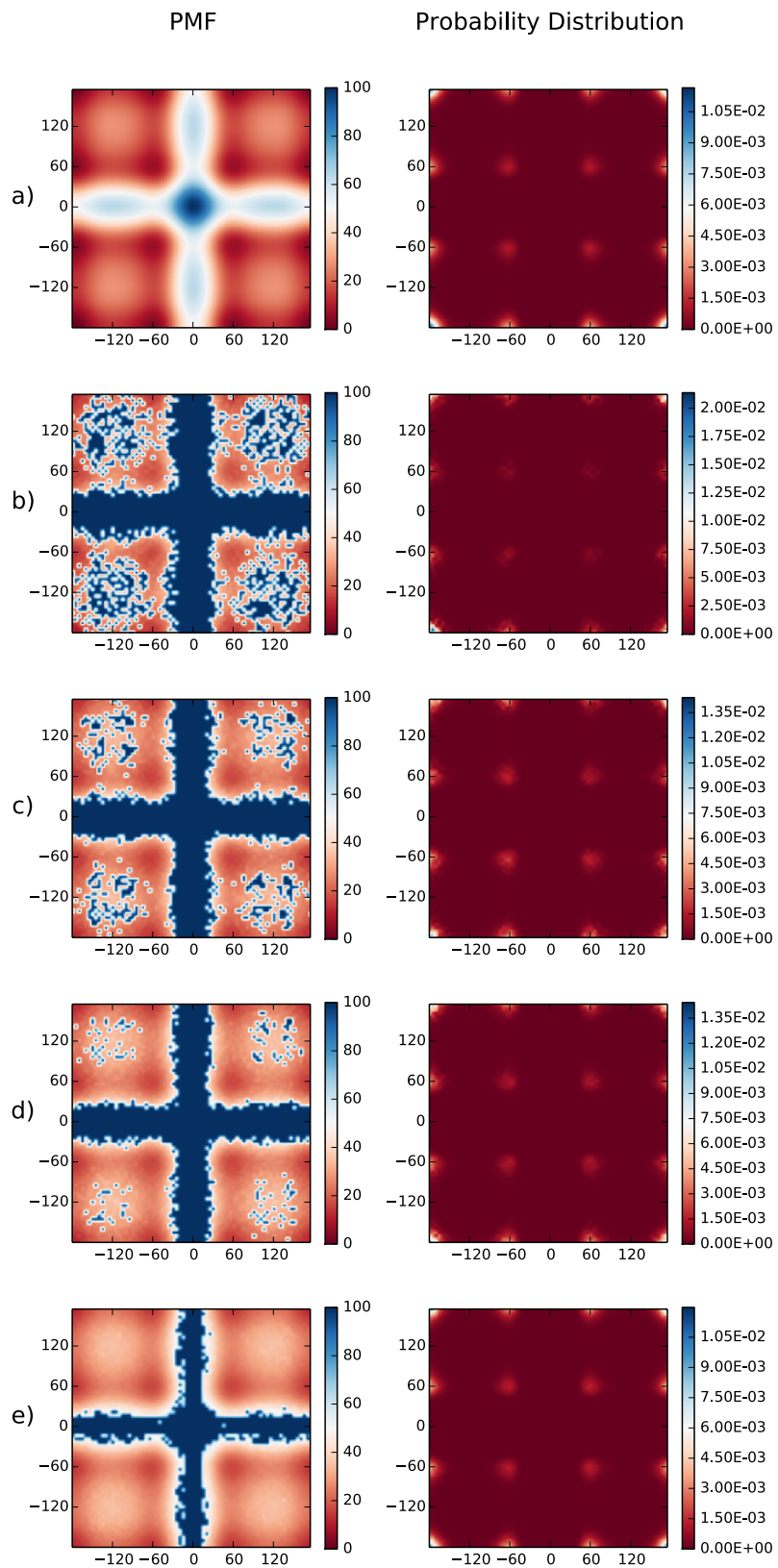


Figure 2-1: 2D WHAM Validation

Comparison between the (left) potential of mean force (PMF) and the (right) dprobability distributions of a) an analytic Ryckaert-Bellemans dihedral potential and Monte Carlo 2D umbrella sampling for b) 40 frames/biasing window; c) 80 frames/biasing window; d) 160 frames/biasing window; e) 1000 frames/biasing window. Units on the PMF are kJ mol⁻¹.

2.3 ELECTROSTATIC CLUSTERING IN VIBRATIONAL CHROMOPHORE DIHEDRAL SPACE

The largest bottleneck for these sorts of calculations we do are the electrostatics. A single node on Stampede can generate >10 ns of simulation per day. That number can be increased (logarithmically) by using additional nodes. However, the continuum solvent electrostatics calculations take anywhere from 45-60 seconds (APBS) to \$\approx\$ 20 minutes (AMOEBA) per frame. If we keep every 4 ps and collect 250 frames per nanosecond, then the electrostatics require 5-8 ns/day for APBS calculations and approximately 0.3 ns/day for AMOEBA calculations. This can be decreased further by running the serial calculations in parallel. Regardless, it would be convenient to find some method of pruning the total number of frames for continuum electrostatics calculations while ensuring that the average field does not differ significantly from the average using every frame.

For convenience, the vacuum electrostatic field at the nitrile due to solute only was chosen as an indicator of total electrostatic field. In the absence of solvent, this is trivial to calculate for both point charge force fields (Amber03) as well as multipole force fields (AMOEBA). This was chosen because it was 1) intuitive and 2) there is consistently a good correlation between the solute Coulomb field and the PB solvent reaction field, as seen in Figure 2-2, suggesting that frames which well represent the Coulomb field also well represent the reaction field.

We then took advantage of the weighted averaging over binned data. The Boltzmann weighted average is calculated as in equation (2-6),

$$\langle x \rangle = \sum_{i=1}^{\text{nbins}} \rho_i \sum_{j=1}^{c_i} \frac{x_{ij}}{c_i} \quad (2-6)$$

where the probability of being in each bin i is ρ_i , the number of times bin i is visited is c_i , and each value in bin i is x_{ij} for $j = 1$ to $j = c_i$. There exists some subarray of values in bin i that has k_i values, where $k_i \geq c_i$ entries and $\left| \sum_{j=1}^{k_i} \frac{x_{ij}}{k_i} - \sum_{j=1}^{c_i} \frac{x_{ij}}{c_i} \right| \leq \chi$, where χ is some threshold. As χ approaches 0, k_i approaches c_i , and the subarray is the full array and the averages are identical. Using the a set of test data where umbrella windows were centered every 120 degrees (at 60°, 180°, and 300°, the expected alkane maximum probability torsions) with a flat biasing potential $\pm 60^\circ$ of the window center and a force constant of **XXX, the clustered average field for each Ral probe in the monomeric state, docked to each of the four Rap1a mutants and each of the four Ras mutants is plotted against their average field for various values of χ , indicated in the upper-left corner of each subplot, from the full data sets in Figure 2-3. From this, it's clear that the clustered averages are linearly correlated to the full averages. The correlation coefficients and best-fit slopes have also been plotted as a function of the cutoff, χ , in Figure 2-4. Even for a relatively large $\chi = 1$, the clustered correlation coefficient and slope is *very* close to 1.0. In general, as χ approaches zero, the correlation coefficient and slope also approach zero. Moreover, at a $\chi = 0.01$, only approximately 20% of all frames are used, which is a significant decrease in computation requirement. This method also has the advantage of guaranteeing that the property the cluster is based on always has a clustered average nearly identical to the full average, which is a useful sanity check.

The code for electrostatic clustering, cluster_framelist.py, can be accessed at:
https://github.com/awritchie/python_scripts

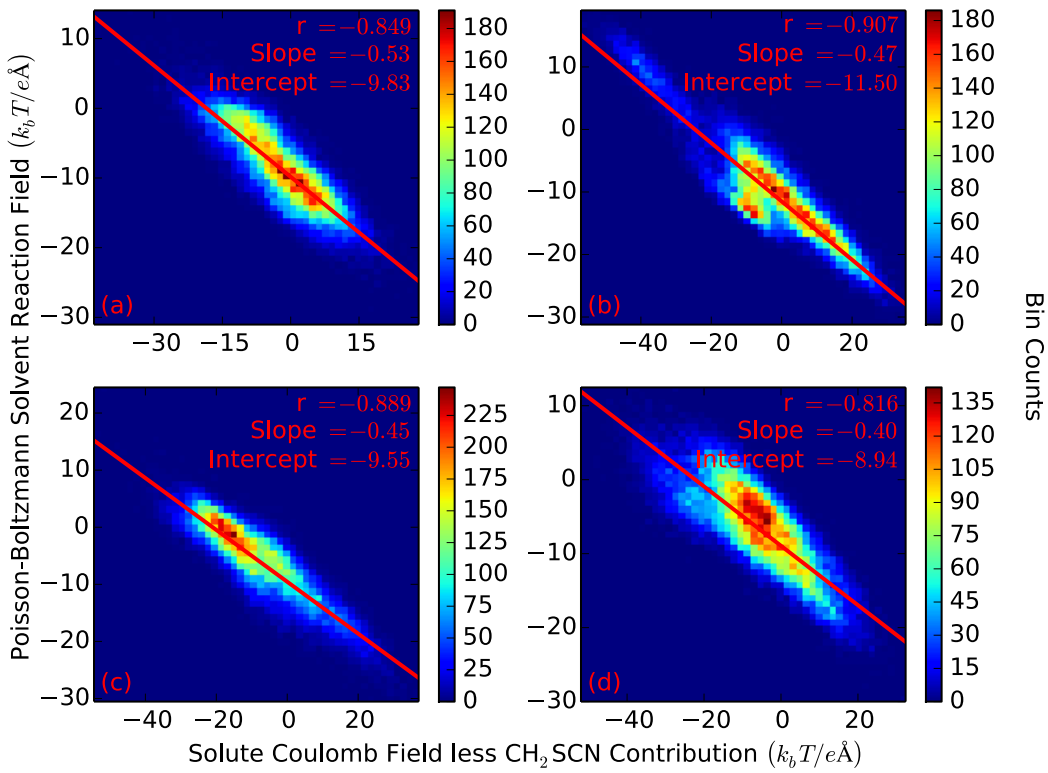


Figure 2-2: PB Solvent Reaction Field vs. Solute Analytic Coulomb Field

Comparison between the analytic Coulomb field at the nitrile bond midpoint due to solute (less the contributions due to the probe itself) (x-axis) and the solvent reaction field at the nitrile bond midpoint (y-axis) using Amber03 point charges for a) Ral G28C_{SCN} monomer; b) Ral N54C_{SCN} monomer; c) Ral G28C_{SCN} docked to wild type Rap; d) Ral N54C_{SCN} docked to wild type Rap. Correlation coefficients (r), slopes (m), and y-intercepts (int), are indicated in the upper-right corner of each figure.

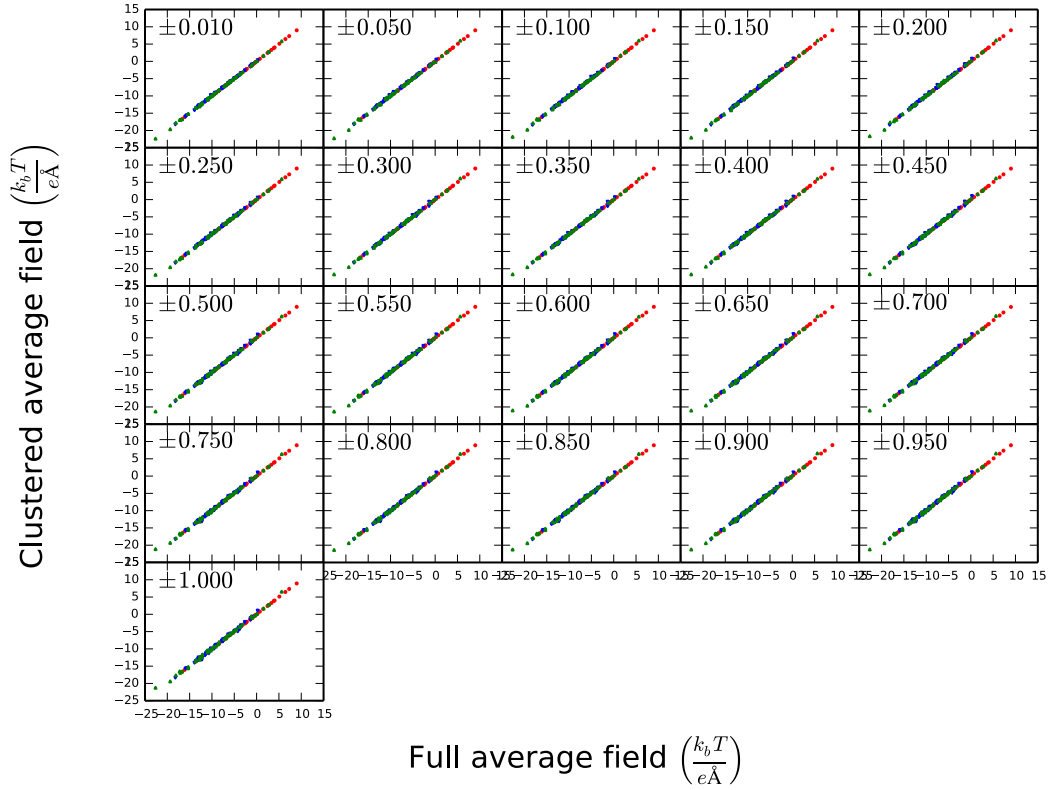


Figure 2-3: Field Values using Clustering Vs. Field Values using All Frames

Average Coulomb electrostatic field (red), solvent reaction field (blue), and the electrostatic field calculated using the AMOEBA force field (green) from clustered frames versus the respective full averages for various cutoff values, χ , indicated in the top left corner of each box.

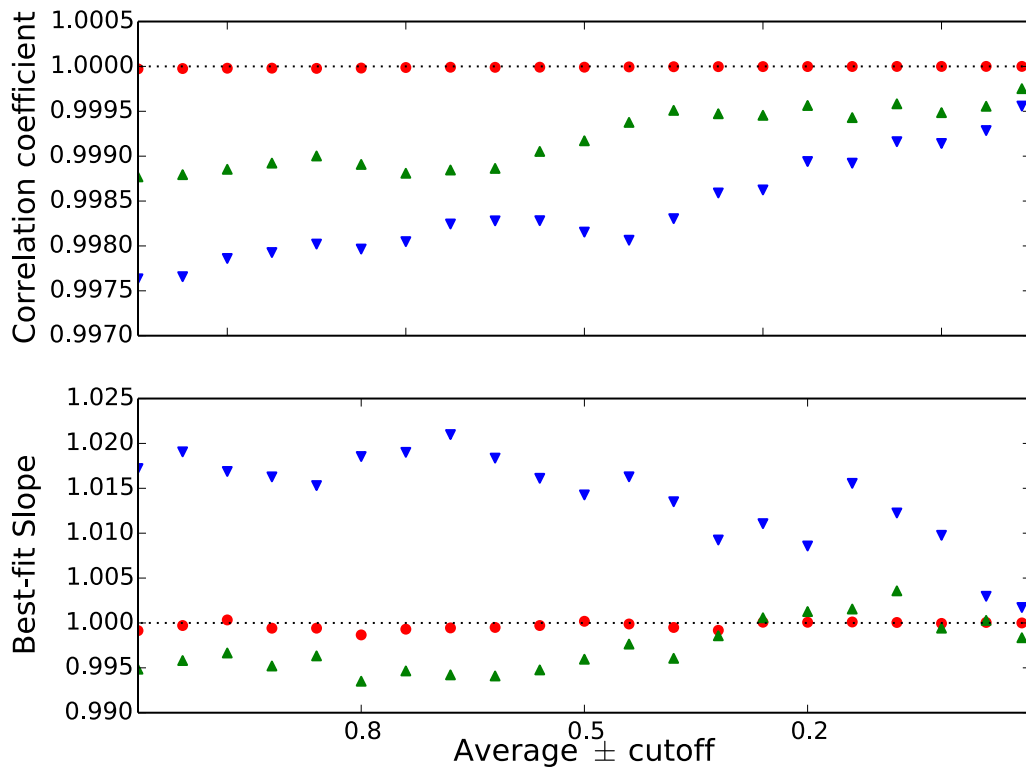


Figure 2-4: Correlations and Slopes at Various Cutoff Values

Correlation coefficients of the Coulomb electrostatic field (red), solvent reaction field (blue), and the electrostatic field calculated using the AMOEBA force field (green) as a function of the cutoff, χ . (Bottom) Best-fit slopes of the Coulomb electrostatic field (red), solvent reaction field (blue), and the electrostatic field calculated using the AMOEBA force field (green) as a function of the cutoff, χ .

2.4 SIDE CHAIN ORIENTATION: AZIMUTHAL AND POLAR ANGLES

To analyze our molecular dynamics simulations of the torsional distribution of the thiocyanate residue on each Ral β mutant and on the side chains at Rap positions 30 and 31, we defined two angles for each side chain with respect to the Rap-Ral β surface, which we term azimuthal and polar angles. The azimuthal angle (θ) was defined by measuring the angle between the side chain of interest and the average plane between the Rap and Ral β protein surfaces. This plane was generated in the same manner as Ensign *et al.*⁴² The positions of the C α atoms of the Rap surface residues Q25, D33, P34, T35, I37, E37, D38, Y40, R41, and K42 from the Rap-Ral β starting structure were fit with a least squares regression to obtain the Rap surface plane. Similarly, the Ral β surface plane was obtained by a least squares fit of the C α atoms of the Ral β surface residues I18, R20, N27, G28, N29, M30, Y31, K32, S33, K52, and N54 in the same structure. These two planes were averaged to define the surface plane of the Rap-Ral β interface and a normalized vector, \vec{N} , orthogonal to this plane. The vector, \vec{v} , defining the orientation of the side chain was the C δ -N ϵ bond vector for cyanocysteine, the C α -C γ vector for aspartate, the C α -C δ vector for glutamate, and the C α -N ζ vector for lysine. For each MD snapshot, the heavy atoms of each frame were aligned to the starting structure, and the azimuthal angle was calculated from Equation (2-7):

$$\theta = 90^\circ - \cos^{-1}(\vec{N} \cdot \vec{v}) \quad (2-7)$$

To generate the polar angle (ϕ), a reference axis called the polar axis was first constructed from the intersection of the surface plane defined above with a second plane defined by the least squares fit of all alpha carbons in starting structure (note: this plane is not necessarily orthogonal to the surface plane). The vector orthogonal to both the surface plane as well as this vertical plane was calculated from the cross product. This

vector, \vec{X} , is the polar axis. The angle between the polar axis and the vector in plane along the x-axis was calculated from the inverse cosine of the dot product, where the sign of the angle was determined by the sign of the y coordinate (since inverse cosine only returns the absolute value of the angle from 0° to 180°). The angle between the nitrile C δ -N ϵ vector and the vector along the x-axis was calculated in the same manner, including sign determination. The polar angle (ϕ) was then determined by equation (2-8),

$$\phi = \cos^{-1}(\vec{x} \cdot \vec{B}_p) - \cos^{-1}(\vec{X} \cdot \vec{x}) - 90^\circ \quad (2-8)$$

where \vec{B}_p is the projection of the normalized bond vector onto the surface plane, and \vec{x} is a reference vector on the average surface plane along the $x = 0$ axis. In this way, a complete 360° perspective of polar angles were determined. Figure 2-5 is a visual representation of these two angles superimposed on the structure of the Rap-Ral β interface. Figure 2-5A defines a surface plane at the interface of Rap (above the plane) and Ral (below the plane); azimuthal angles are reported relative to this plane. When the cross hairs on Figure 2-5B are translated to the C α atom of each simulated residue on Rap or Ral β (represented as spheres), they become the origin of the polar angles shown in Figure 4-4 and Figure 4-5.

To obtain Boltzmann weighted angle averages, the cyclic boundaries had to be considered to avoid obtaining averages that would be affected by an arbitrary decision for the position of our torsional angle at 0° . We calculated a cyclic average angle for n equally weighted values of θ from equation (2-9). Each frame was assigned to a bin j , with each bin j having a probability of p_j , resulting in 72 bins, each having m_j equally probable members.

$$\langle \theta \rangle = \text{atan2}\left(\frac{1}{n} \sum_{j=1}^n \sin\theta_j, \frac{1}{n} \sum_{j=1}^n \cos\theta_j\right) \quad (2-9)$$

When all probabilities p_j are equal, then dividing the sum of values of $\sin \theta$ expressed in Equation (2-9) by the quantity in each bin (m_j) is equivalent to the special case of summing the products of each value times the probability of that value, shown in equation (2-10):

$$\langle \theta \rangle = \text{atan}2 \left[\sum_{j=1}^{72} \left(p_j \cdot \frac{1}{m_j} \sum_{i=1}^{m_j} \sin \theta_i \right), \sum_{j=1}^{72} \left(p_j \cdot \frac{1}{m_j} \sum_{i=1}^{m_j} \cos \theta_i \right) \right] \quad (2-10)$$

Mardia, *et al.*⁵⁸ have previously demonstrated that the variance for a cyclic average can be described by equation (2-11):

$$\langle \theta^2 \rangle - \langle \theta \rangle^2 = 1 - \frac{1}{n} \sqrt{\left(\sum_{j=1}^n \cos \theta_j \right)^2 + \left(\sum_{j=1}^n \sin \theta_j \right)^2} \quad (2-11)$$

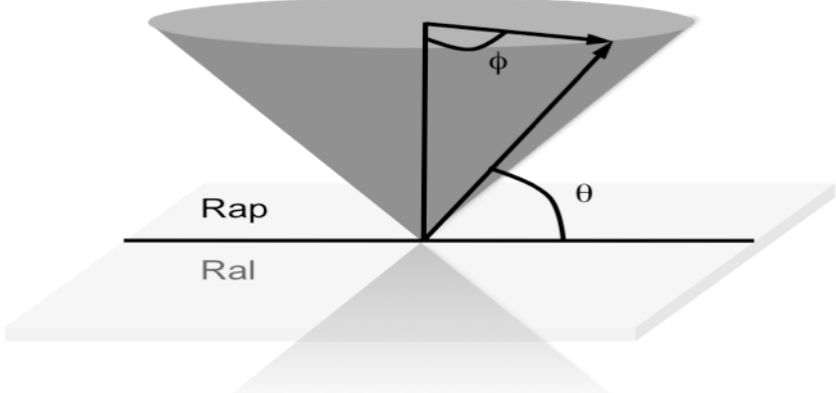
which was then rearranged to accommodate weighting, yielding equation (2-12):

$$\langle \theta^2 \rangle - \langle \theta \rangle^2 = 1 - \sqrt{\left[\sum_{j=1}^{72} \left(p_j \cdot \frac{1}{m} \sum_{i=1}^{m_j} \sin \theta_j \right) \right]^2 + \left[\sum_{j=1}^{72} \left(p_j \cdot \frac{1}{m} \sum_{i=1}^{m_j} \cos \theta_j \right) \right]^2} \quad (2-12)$$

The code for calculating azimuthal and polar angles, azimop.py, and the code for performing Boltzmann-weighting over a periodic coordinate, circular_boltzmann_Weight.py, can both be accessed at:

https://github.com/awritchie/python_scripts

A



B

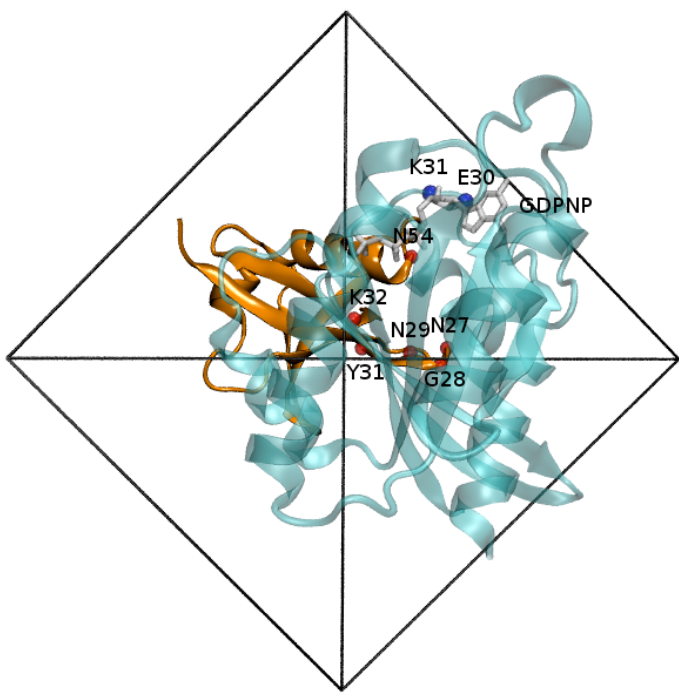


Figure 2-5: Representation of azimuthal and polar angles

Representation of the azimuthal (θ) and polar (ϕ) angles. (A) The surface plane was defined by the average of the plane fit with all $C\alpha$ atoms. Azimuthal angles are shown

relative to this plane, where Rap is above the plane and Ral is below the plane. (B) Representation of the polar angle. Translating the black cross hairs to the $C\alpha$ of each residue (represented by spheres) determines the origin of the polar angles presented in Figure 4-4 and Figure 4-5. Rap is shown in blue and Ral in orange.

2.5 PROBE PARAMETERIZATION FOR AMOEBA

<Body text to begin here.>

1.	atom	259	55	CB	"CNC CB"	6	12.011	4
2.	atom	260	56	SG	"CNC SG"	16	32.066	2
3.	atom	261	57	CD	"CNC CD"	6	12.011	2
4.	atom	262	58	NE	"CNC NE"	7	14.007	1
5.	atom	263	59	HB	"CNC HB"	1	1.008	1
6.								
7.	multipole	259	8	260		-0.15228		
8.						0.07407	0.00000	0.31740
9.						-0.15117		
10.						0.00000	-0.21945	
11.						-0.19282	0.00000	0.37062
12.	multipole	260	259	261		0.33074		
13.						0.44389	0.00000	0.28736
14.						1.22369		
15.						0.00000	-2.16613	
16.						-0.31636	0.00000	0.94244
17.	multipole	261	260	262		0.24556		
18.						0.06457	0.00000	-0.41800
19.						0.15740		
20.						0.00000	0.22633	
21.						0.26601	0.00000	-0.38373
22.	multipole	12	8	259		0.12898		
23.						0.02551	0.00000	0.07014
24.						0.19051		
25.						0.00000	0.17012	
26.						-0.01582	0.00000	-0.36063
27.	multipole	263	259	8		0.09179		
28.						-0.07114	0.00000	-0.02080
29.						-0.16061		
30.						0.00000	-0.02258	
31.						-0.03267	0.00000	0.18319
32.	multipole	262	261	260		-0.58843		
33.						-0.00512	0.00000	-0.24238
34.						0.32332		
35.						0.00000	0.16836	
36.						-0.08202	0.00000	-0.49168
37.								
38.	polarize	259			1.3340	0.3900	263	
39.	polarize	260			3.3000	0.3900	261	
40.	polarize	261			1.3340	0.3900	260	262
41.	polarize	262			1.0730	0.3900	261	
42.	polarize	263			0.4960	0.3900	259	
43.								
44.	vdw	58			3.7100	0.1050		
45.	vdw	55			3.7800	0.1060		
46.	vdw	56			4.0050	0.3550		
47.	vdw	57			3.7800	0.1060		
48.	vdw	59			2.8700	0.0330	0.900	
49.	bond	55	7		323.0000	1.5317		
50.	bond	55	56		235.8000	1.8353		
51.	bond	55	59		341.0000	1.0817		
52.	bond	56	57		235.8000	1.7060		
53.	bond	57	58		450.0000	1.1374		
54.	angle	7	55	56	53.2000	109.6948		

55. angle	7	55	59	42.4400	110.8048													
56. angle	56	55	59	60.2400	108.4887													
57. angle	59	55	59	39.5700	108.8231													
58. angle	55	7	3	60.0000	108.7411													
59. angle	55	7	1	80.0000	112.9036													
60. angle	55	7	6	38.0000	109.5706													
61. angle	55	56	57	60.4300	98.5327													
62. angle	56	57	58	60.0000	178.6763													
63. strbnd	7	55	56	18.7000	18.7000													
64. strbnd	7	55	59	11.5000	11.5000													
65. strbnd	56	55	59	11.5000	11.5000													
66. strbnd	55	7	3	18.7000	18.7000													
67. strbnd	55	7	1	18.7000	18.7000													
68. strbnd	55	7	6	11.5000	18.7000													
69. strbnd	55	56	57	-5.7500	-5.7500													
70. torsion	56	55	7	3	-													
	1.010	0.0	1	1.230	180.0	2	1.000	0.0	3	# CYS	3	7	8	12				
71. torsion	56	55	7	1	-0.160	0.0	1	1.080	180.0	2	-							
	1.520	0.0	3	# CYS	1	7	8	12										
72. torsion	56	55	7	6	0.000	0.0	1	0.000	180.0	2	0.475	0.0	3	# CYS	6	7	8	12
73. torsion	59	55	7	3	0.000	0.0	1	0.000	180.0	2	0.180	0.0	3	# CYS	3	7	8	9
74. torsion	59	55	7	1	0.000	0.0	1	0.000	180.0	2	0.500	0.0	3	# CYS	1	7	8	9
75. torsion	59	55	7	6	0.000	0.0	1	0.000	180.0	2	0.299	0.0	3	# CYS	6	7	8	9
76. torsion	7	55	56	57	-0.4400	0.0	1	-										
	0.2600	180.0	2	0.6000	0.0	3	# EtSCN	C1	C2	S	C							
77. torsion	59	55	56	57	0.0000	0.0	1	0.0000	180.0	2	0.6600	0.0	3	# EtSCN	H2	C2	S	C
78. torsion	55	7	3	1	0.929	0.0	1	0.328	180.0	2	0.000	0.0	3	# CYS	1	3	7	8
79. torsion	55	7	3	5	0.000	0.0	1	0.000	180.0	2	0.000	0.0	3	# CYS	5	3	7	8
80. torsion	55	7	1	3	2.576	0.0	1	1.011	180.0	2	0.825	0.0	3	# CYS	3	1	7	8
81. torsion	55	7	1	4	0.000	0.0	1	0.000	180.0	2	0.000	0.0	3	# CYS	4	1	7	8
82. torsion	55	56	57	58	0.0000	0.0	1	0.0000	180.0	2	0.5000	0.0	3	# EtSCN	C2	S	C	N

Code and Parameters 2-1: Cyanocysteine AMOEBA Parameters

1.	atom	271	67	H1	"MeSCN H1"		1	1.008	1
2.	atom	272	68	C1	"MeSCN C1"		6	12.011	4
3.	atom	273	69	S	"MeSCN S"		16	32.066	2
4.	atom	274	70	C	"MeSCN C"		6	12.011	2
5.	atom	275	71	N	"MeSCN N"		7	14.007	1
6.									
7.	multipole	272	273	271		-0.22754			
8.						0.00000	0.00000	-0.02449	
9.						0.72145			
10.						0.00000	0.72145		
11.						0.00000	0.00000	-1.44290	
12.	multipole	273	272	274		0.33074			
13.						0.44389	0.00000	0.28736	
14.						1.22369			
15.						0.00000	-2.16613		
16.						-0.31636	0.00000	0.94244	
17.	multipole	274	273	275		0.24556			
18.						0.06457	0.00000	-0.41800	
19.						0.15740			
20.						0.00000	0.22633		
21.						0.26601	0.00000	-0.38373	
22.	multipole	271	272	273		0.07989			
23.						0.02678	0.00000	-0.31473	
24.						0.66454			
25.						0.00000	-0.00998		
26.						0.17231	0.00000	-0.65456	
27.	multipole	275	274	273		-0.58843			
28.						-0.00512	0.00000	-0.24238	
29.						0.32332			
30.						0.00000	0.16836		
31.						-0.08202	0.00000	-0.49168	
32.									
33.	polarize	271			0.4960	0.3900	272		
34.	polarize	272			1.3340	0.3900	271	273	
35.	polarize	273			3.3000	0.3900	272	274	
36.	polarize	274			1.3340	0.3900	273	275	
37.	polarize	275			1.0730	0.3900	274		
38.									
39.	vdw	68			3.7800	0.1060			
40.	vdw	69			4.0050	0.3550			
41.	vdw	70			3.7800	0.1060			
42.	vdw	67			2.8700	0.0330	0.900		
43.	vdw	71			3.7100	0.1050			
44.	bond	68	69		235.8000	1.8209			
45.	bond	68	67		341.0000	1.0794			
46.	bond	69	70		235.8000	1.7068			
47.	bond	70	71		450.0000	1.1373			
48.	angle	69	68	67	60.2400	110.5747			
49.	angle	67	68	67	39.5700	110.6263			
50.	angle	68	69	70	60.4300	99.4461			
51.	angle	69	70	71	60.0000	178.9042			
52.	strbnd	69	68	67	11.5000	11.5000			
53.	strbnd	68	69	70	-5.7500	-5.7500			
54.	torsion	67	68	69	70	0.0000 0.0 1	0.0000 180.0 2	0.6600 0.0 3	

```
| 55. torsion      68   69   70   71      0.0000 0.0 1  0.0000 180.0 2  0.5000 0.0 3
```

Code and Parameters 2-2: Methyl Thiocyanate AMOEBA Parameters

1.	atom	264	60	C1	"EtSCN C1"	6	12.011	4
2.	atom	265	61	H1	"EtSCN H1"	1	1.008	1
3.	atom	266	62	C2	"EtSCN C2"	6	12.011	4
4.	atom	267	63	H2	"EtSCN H2"	1	1.008	1
5.	atom	268	64	S	"EtSCN S"	16	32.066	2
6.	atom	269	65	C	"EtSCN C"	6	12.011	2
7.	atom	270	66	N	"EtSCN N"	7	14.007	1
8.								
9.	multipole	264	266	265	-0.18333			
10.					0.00000	0.00000	0.32541	
11.					-0.25019			
12.					0.00000	-0.25019		
13.					0.00000	0.00000	0.50038	
14.	multipole	266	264	268	-0.23503			
15.					0.06819	0.00000	0.15097	
16.					-0.26732			
17.					0.00000	-0.08487		
18.					-0.08743	0.00000	0.35219	
19.	multipole	267	266	264	0.09244			
20.					-0.00077	0.00000	-0.03413	
21.					0.02305			
22.					0.00000	0.01348		
23.					-0.00070	0.00000	-0.03653	
24.	multipole	265	264	266	0.08187			
25.					0.01969	0.00000	-0.08459	
26.					0.06966			
27.					0.00000	0.02253		
28.					-0.00032	0.00000	-0.09219	
29.	multipole	268	266	269	0.33074			
30.					0.44389	0.00000	0.28736	
31.					1.22369			
32.					0.00000	-2.16613		
33.					-0.31636	0.00000	0.94244	
34.	multipole	269	268	270	0.24556			
35.					0.06457	0.00000	-0.41800	
36.					0.15740			
37.					0.00000	0.22633		
38.					0.26601	0.00000	-0.38373	
39.	multipole	270	269	268	-0.58843			
40.					-0.00512	0.00000	-0.24238	
41.					0.32332			
42.					0.00000	0.16836		
43.					-0.08202	0.00000	-0.49168	
44.								
45.	polarize	264			1.3340	0.3900	265 266	
46.	polarize	265			0.4960	0.3900	264	
47.	polarize	266			1.3340	0.3900	264 267	
48.	polarize	267			0.4960	0.3900	266	
49.	polarize	268			3.3000	0.3900	269	

50. polarize	269		1.3340	0.3900	268	270
51. polarize	270		1.0730	0.3900	269	
52.						
53. vdw	60		3.8200	0.1040		
54. vdw	62		3.7800	0.1060		
55. vdw	64		4.0050	0.3550		
56. vdw	65		3.7800	0.1060		
57. vdw	63		2.8700	0.0330	0.900	
58. vdw	61		2.9800	0.0240	0.920	
59. vdw	66		3.7100	0.1050		
60. bond	60	62	345.3000	1.5227		
61. bond	60	61	341.0000	1.0855		
62. bond	62	64	323.0000	1.8329		
63. bond	62	63	341.0000	1.0809		
64. bond	64	65	235.8000	1.7068		
65. bond	65	66	450.0000	1.1376		
66. angle	62	60	61	42.4400	111.1890	
67. angle	61	60	61	39.5700	108.4478	
68. angle	60	62	64	53.2000	114.3035	
69. angle	60	62	63	42.4400	111.8003	
70. angle	64	62	63	60.2400	108.0491	
71. angle	63	62	63	45.5700	107.8321	
72. angle	62	64	65	60.4300	99.8280	
73. angle	64	65	66	60.0000	179.1383	
74. strbnd	62	60	61	11.5000	11.5000	
75. strbnd	60	62	64	18.7000	18.7000	
76. strbnd	60	62	63	11.5000	11.5000	
77. strbnd	64	62	63	11.5000	11.5000	
78. strbnd	62	64	65	-5.7500	-5.7500	
79. torsion	61	60	62	64	0.0000 0.0 1 0.0000 180.0 2 0.4750 0.0 3	
80. torsion	61	60	62	63	0.0000 0.0 1 0.0000 180.0 2 0.2990 0.0 3	
81. torsion	60	62	64	65	-0.4400 0.0 1 -0.2600 180.0 2 0.6000 0.0 3	
82. torsion	63	62	64	65	0.0000 0.0 1 0.0000 180.0 2 0.6600 0.0 3	
83. torsion	62	64	65	66	0.0000 0.0 1 0.0000 180.0 2 0.5000 0.0 3	

Code and Parameters 2-3: Ethyl Thiocyanate AMOEBA Parameters

1. atom	276	72	C1	"HxSCN C1"	6	12.011	4
2. atom	277	73	C2	"HxSCN C2"	6	12.011	4
3. atom	278	74	H1	"HxSCN H1"	1	1.008	1
4. atom	279	75	C3	"HxSCN C3"	6	12.011	4
5. atom	280	76	H2	"HxSCN H2"	1	1.008	1
6. atom	281	77	H3	"HxSCN H3"	1	1.008	1
7. atom	282	78	C4	"HxSCN C4"	6	12.011	4
8. atom	283	79	C5	"HxSCN C5"	6	12.011	4
9. atom	284	80	H4	"HxSCN H4"	1	1.008	1
10. atom	285	81	H5	"HxSCN H5"	1	1.008	1
11. atom	286	82	C6	"HxSCN C6"	6	12.011	4
12. atom	287	83	H6	"HxSCN H6"	1	1.008	1
13. atom	288	84	S	"HxSCN S"	16	32.066	2
14. atom	289	85	C	"HxSCN C"	6	12.011	2
15. atom	290	86	N	"HxSCN N"	7	14.007	1
16.							

17.	multipole	279	282	277	-0.12665		
18.					0.16365	0.00000	0.14302
19.					0.06092		
20.					0.00000	-0.43628	
21.					-0.27661	0.00000	0.37536
22.	multipole	276	277	278	-0.15938		
23.					0.00000	0.00000	0.26734
24.					-0.20136		
25.					0.00000	-0.20136	
26.					0.00000	0.00000	0.40272
27.	multipole	283	282	286	-0.11656		
28.					0.24230	0.00000	0.09285
29.					0.15205		
30.					0.00000	-0.43470	
31.					-0.43635	0.00000	0.28265
32.	multipole	282	279	283	-0.11327		
33.					0.22022	0.00000	0.08479
34.					0.15602		
35.					0.00000	-0.44910	
36.					-0.36114	0.00000	0.29308
37.	multipole	277	279	276	-0.12195		
38.					0.19367	0.00000	0.15795
39.					-0.01138		
40.					0.00000	-0.31282	
41.					-0.22362	0.00000	0.32420
42.	multipole	286	283	288	-0.18161		
43.					0.04843	0.00000	0.18545
44.					-0.01034		
45.					0.00000	-0.10804	
46.					-0.18618	0.00000	0.11838
47.	multipole	280	277	279	0.05998		
48.					0.00441	0.00000	-0.07636
49.					0.04595		
50.					0.00000	0.03338	
51.					-0.00973	0.00000	-0.07933
52.	multipole	284	282	279	0.06214		
53.					0.02649	0.00000	-0.05387
54.					0.01977		
55.					0.00000	0.03305	
56.					-0.00324	0.00000	-0.05282
57.	multipole	281	279	282	0.05805		
58.					0.00916	0.00000	-0.05550
59.					0.03877		
60.					0.00000	0.02937	
61.					-0.06123	0.00000	-0.06814
62.	multipole	285	283	282	0.07555		
63.					0.01936	0.00000	-0.04776
64.					0.05942		
65.					0.00000	0.03376	
66.					-0.01589	0.00000	-0.09318
67.	multipole	278	276	277	0.05847		
68.					0.01125	0.00000	-0.10159
69.					0.06569		
70.					0.00000	0.03435	
71.					-0.03952	0.00000	-0.10004
72.	multipole	287	286	283	0.07235		
73.					0.02117	0.00000	-0.04358

74.					0.04575
75.				0.00000	0.03869
76.				-0.01006	0.00000
77.	multipole	288	286	289	0.33074
78.				0.44389	0.00000
79.				1.22369	
80.				0.00000	-2.16613
81.				-0.31636	0.00000
82.	multipole	289	288	290	0.24556
83.				0.06457	0.00000
84.				0.15740	
85.				0.00000	0.22633
86.				0.26601	0.00000
87.	multipole	290	289	288	-0.58843
88.				-0.00512	0.00000
89.				0.32332	
90.				0.00000	0.16836
91.				-0.08202	0.00000
92.					-0.49168
93.	polarize	276		1.3340	0.3900
94.	polarize	277		1.3340	0.3900
95.	polarize	278		0.4960	0.3900
96.	polarize	279		1.3340	0.3900
97.	polarize	280		0.4960	0.3900
98.	polarize	281		0.4960	0.3900
99.	polarize	282		1.3340	0.3900
100.	polarize	283		1.3340	0.3900
101.	polarize	284		0.4960	0.3900
102.	polarize	285		0.4960	0.3900
103.	polarize	286		1.3340	0.3900
104.	polarize	287		0.4960	0.3900
105.	polarize	288		3.3000	0.3900
106.	polarize	289		1.3340	0.3900
107.	polarize	290		1.0730	0.3900
108.					289
109.	vdw	75		3.8200	0.1010
110.	vdw	72		3.8200	0.1010
111.	vdw	79		3.8200	0.1010
112.	vdw	78		3.8200	0.1010
113.	vdw	73		3.8200	0.1010
114.	vdw	82		3.7800	0.1060
115.	vdw	84		4.0050	0.3550
116.	vdw	85		3.7800	0.1060
117.	vdw	76		2.9800	0.0240
118.	vdw	80		2.9800	0.0240
119.	vdw	77		2.9800	0.0240
120.	vdw	81		2.9800	0.0240
121.	vdw	74		2.9600	0.0240
122.	vdw	83		2.8700	0.0330
123.	vdw	86		3.7100	0.1050
124.	bond	75	78	453.0000	1.5299
125.	bond	75	73	453.0000	1.5298
126.	bond	75	77	341.0000	1.0885
127.	bond	72	73	323.0000	1.5282
128.	bond	72	74	341.0000	1.0863
129.	bond	79	78	453.0000	1.5312
130.	bond	79	82	345.3000	1.5276

131.	bond	79	81	341.0000	1.0866
132.	bond	78	80	341.0000	1.0879
133.	bond	73	76	341.0000	1.0878
134.	bond	82	84	235.8000	1.8351
135.	bond	82	83	341.0000	1.0810
136.	bond	84	85	235.8000	1.7063
137.	bond	85	86	450.0000	1.1375
138.	angle	78	75	48.2000	113.1072
139.	angle	78	75	38.0000	109.3223
140.	angle	73	75	38.0000	109.2787
141.	angle	77	75	39.5700	106.3036
142.	angle	73	72	42.4400	111.1869
143.	angle	74	72	39.5700	107.7267
144.	angle	78	79	48.2000	111.5264
145.	angle	78	79	38.0000	109.6162
146.	angle	82	79	38.0000	109.5120
147.	angle	81	79	39.5700	106.9493
148.	angle	75	78	48.2000	112.7564
149.	angle	75	78	38.0000	109.3923
150.	angle	79	78	38.0000	109.3217
151.	angle	80	78	39.5700	106.4572
152.	angle	75	73	48.2000	112.9179
153.	angle	75	73	38.0000	109.3170
154.	angle	72	73	38.0000	109.3845
155.	angle	76	73	45.5700	106.3035
156.	angle	79	82	53.2000	109.0812
157.	angle	79	82	42.4400	111.1744
158.	angle	84	82	60.2400	108.2095
159.	angle	83	82	39.5700	108.8985
160.	angle	82	84	60.4300	99.5693
161.	angle	84	85	60.0000	179.0730
162.	strbnd	78	75	18.7000	18.7000
163.	strbnd	78	75	11.5000	18.7000
164.	strbnd	73	75	11.5000	18.7000
165.	strbnd	73	72	11.5000	11.5000
166.	strbnd	78	79	18.7000	18.7000
167.	strbnd	78	79	11.5000	18.7000
168.	strbnd	82	79	11.5000	18.7000
169.	strbnd	75	78	18.7000	18.7000
170.	strbnd	75	78	11.5000	18.7000
171.	strbnd	79	78	11.5000	18.7000
172.	strbnd	75	73	18.7000	18.7000
173.	strbnd	75	73	11.5000	18.7000
174.	strbnd	72	73	11.5000	18.7000
175.	strbnd	79	82	18.7000	18.7000
176.	strbnd	79	82	11.5000	11.5000
177.	strbnd	84	82	11.5000	11.5000
178.	strbnd	82	84	85	-5.7500
179.	torsion	73	75	78	0.576 0.0 1 -
0.017	180.0 2	2.031	0.0 3		
180.	torsion	73	75	78	0.000 0.0 1 0.000 180.0 2 0.000
0.0 3					
181.	torsion	77	75	78	0.000 0.0 1 0.000 180.0 2 0.000
0.0 3					
182.	torsion	77	75	78	0.000 0.0 1 0.000 180.0 2 0.000
0.0 3					

183.	torsion	78	75	73	72	0.484	0.0	1	0.014	180.0	2	2.221
0.0	3											
184.	torsion	78	75	73	76	0.000	0.0	1	0.000	180.0	2	0.000
0.0	3											
185.	torsion	77	75	73	72	0.000	0.0	1	0.000	180.0	2	0.000
0.0	3											
186.	torsion	77	75	73	76	0.000	0.0	1	0.000	180.0	2	0.000
0.0	3											
187.	torsion	74	72	73	75	0.0000	0.0	1	0.0000	180.0	2	0.3410
0.0	3											
188.	torsion	74	72	73	76	0.0000	0.0	1	0.0000	180.0	2	0.2990
0.0	3											
189.	torsion	82	79	78	75	0.364	0.0	1	-			
0.024	180.0	2	1.958	0.0	3							
190.	torsion	82	79	78	80	0.000	0.0	1	0.000	180.0	2	0.000
0.0	3											
191.	torsion	81	79	78	75	0.000	0.0	1	0.000	180.0	2	0.000
0.0	3											
192.	torsion	81	79	78	80	0.000	0.0	1	0.000	180.0	2	0.000
0.0	3											
193.	torsion	78	79	82	84	-						
0.688	0.0	1	0.489	180.0	2	1.957	0.0	3				
194.	torsion	78	79	82	83	0.000	0.0	1	0.000	180.0	2	0.000
0.0	3											
195.	torsion	81	79	82	84	0.000	0.0	1	0.000	180.0	2	0.000
0.0	3											
196.	torsion	81	79	82	83	0.000	0.0	1	0.000	180.0	2	0.000
0.0	3											
197.	torsion	79	82	84	85	-						
2.643	0.0	1	0.709	180.0	2	1.072	0.0	3				
198.	torsion	83	82	84	85	0.000	0.0	1	0.000	180.0	2	0.000
0.0	3											
199.	torsion	82	84	85	86	0.0000	0.0	1	0.0000	180.0	2	0.5000
0.0	3											

Code and Parameters 2-4: Hexyl Thiocyanate AMOEBA Parameters

2.6 SMALL MOLECULE SIMULATIONS IN AMOEBA

<Body text to begin here.>

Chapter 3 Electrostatic Field Methods

3.1 AMBER03 WITH EXPLICIT TIP3P WATER

3.1.1 GROMACS Reaction Field Electrostatics

The explicit TIP3P⁴⁴ solvent method we used to calculate electrostatic fields uses keyword “coulombtype = reaction-field” in GROMACS,^{49,59-61} allowing the system to be treated with periodic boundary conditions. Forces are calculated using equation (3-1), where q is the charge on an atom, ϵ_{solute} is the dielectric of the short-range interactions and was set to 1, $\epsilon_{\text{solvent}}$ is the dielectric of the long-range interactions and was set to 78, \vec{r}_c is the scaling distance where the potential decays to zero and was set to 1.0 nm, and \vec{r}_{ij} is the distance between two charges. The reaction field interaction is a modification of Coulomb’s law which switches from one dielectric value at short-ranged to a second (typically larger) dielectric value at long ranges.

$$\vec{\text{Force}}_{\text{RF},i}(\vec{r}_{ij}) = \frac{1}{4\pi\epsilon_0} \frac{q_i q_j}{\epsilon_{\text{solute}}} \left[\frac{1}{r_{ij}^2} - \frac{2r_{ij}}{r_c^3} \frac{(\epsilon_{\text{solvent}} - \epsilon_{\text{solute}})}{(2\epsilon_{\text{solvent}} + \epsilon_{\text{solute}})} \right] \frac{\vec{r}_{ij}}{r_{ij}} \quad (3-1)$$

To calculate the field at the nitrile, we first placed a test charge ($q = +1$) at the nitrile midpoint for every frame in our MD trajectories. We then used the “rerun” option of the GROMACS molecular dynamics engine, mdrun, to calculate the forces on every atom, including the test charge. Dividing the force on the test charge by its charge (+1) gives the field at the test charge, which was then projected along the nitrile CN bond vector.

3.1.2 Hybrid Solvent Reaction Field Electrostatics and Solute Coulomb Field

Because the reaction field coulomb interaction is additive, we are able to break the electrostatic field down into contributions from specific atoms or species.⁴² By

setting the charge on all solute atoms to zero, we are able to solve for the solvent reaction field of the system. We then calculated the analytical Coulomb field (equation (3-2)) as the bond mid-point, looking only at solute atoms, and summed it with the reaction field electrostatics solvent reaction field to obtain a total field. In this way, water near the probe is treated as structural water with an un-screened dielectric of 1, while water significantly further away from the probe is treated as bulk water with a damped dielectric of 78. Contrarily, all solute atoms are treated with an un-screened dielectric of 1, rather than atoms sufficiently far from the probe being screened by more than simple distance.

$$\vec{F}_{\text{Coulomb}}(\vec{r}) = \frac{1}{4\pi\epsilon_0} \frac{1}{\epsilon_{\text{solute}}} \sum_i \frac{q_i \vec{r}}{\vec{r}^3} \quad (3-2)$$

The code for inserting the test charge, gmx_insert_dummy_atom into a GROMACS trajectory file can be accessed at: https://github.com/awritchie/my_gmx

The code for calculating the solute electrostatic field at a point, gmx2pqr, can be accessed at: https://github.com/awritchie/my_gmx

3.2 AMBER03 WITH POISSON-BOLTZMANN CONTINUUM SOLVENT

The non-linear Poisson-Boltzmann equation (NLPBE) is given in equation (3-3), where $\phi(\bar{r})$ is the potential as a function of the position vector \bar{r} , $\varepsilon(\bar{r})$ is the spatially dependent protein interior dielectric, $\bar{\kappa}^2$ is the ion accessibility coefficient, and $\rho(\bar{r})$ is the charge distribution density.⁶²

$$\nabla \cdot \varepsilon(\bar{r}) \nabla \phi(\bar{r}) = \varepsilon(\bar{r}) \bar{\kappa}^2 \sinh \phi(\bar{r}) - 4\pi \rho(\bar{r}) \quad (3-3)$$

Assuming a small potential, $\phi \ll k_b T/q$, the approximation $\sinh(\phi) \approx \phi$ can be used to formulate the linear Poisson-Boltzmann equation (LPBE), equation (3-4), although it has previously been reported that the solutions to the LPBE and the NLPBE differ only by a few $k_b T/q$ even when the linearity condition does not hold:^{63, 64}

$$\nabla \cdot \varepsilon(\bar{r}) \nabla \phi(\bar{r}) = \varepsilon(\bar{r}) \bar{\kappa}^2 \phi(\bar{r}) - 4\pi \rho(\bar{r}) \quad (3-4)$$

Solutions to the LPBE were calculated using APBS's multigrid solver^{65, 66}. For both one-dimensional and two-dimensional umbrella-sampling strategies, each frame was examined using APBS, and a Boltzmann-weighted average field for each system was calculated based on the dihedral probability distributions previously described. A two-stage manual focusing strategy (APBS keyword “mg-manual”) was used, in which the system was centered in a 240 Å x 240 Å x 240 Å box with 97 grid points in each dimension and a single Debye-Huckle boundary condition at 300 K. A cubic B-spline was used to map the discretized atomic point charges to the grid. Ion concentrations of 0.150 M +1 charge ions of radius 2.0 Å and 0.150 M -1 charge ions of radius 2.0 Å were included to account for buffer in solution. We used the molecular surface model (“srfm mol”) with a surface sphere density of 10.0 (“sdens 10.0”). The solvent dielectric was 78.0, appropriate for bulk water. The choice of protein dielectric is significantly more ambiguous, with values typically ranging from 2 to 40.⁶⁷ When all interactions are treated

explicitly (permanent dipole moments, induced dipole moments (polarizability), and explicit solvent), a protein dielectric of one is most appropriate.^{68,69} Since we have directly modeled structural fluctuations but not polarizability, we chose an interior dielectric of 2.0. Because the calculated field scales linearly with the interior dielectric chosen, and thus the choice of interior dielectric to be used is by no means well defined,⁷⁰ we are less concerned with the value of the protein dielectric, since an “ideal” dielectric value can be extrapolated from the slope of the fit to experimental data (*vida infra*).

The field along the nitrile bond length was calculated by examining the potential gradient along the bond vector. This was done by inserting 11 dummy atoms with charge, mass, and radius of zero, evenly spaced along the nitrile bond length. The potential at each of these dummy atoms was interpolated from the nearest grid points using a linear spline with the “write atompot flat” keyword in APBS. It was observed that the potential changed linearly within ~0.3 Å of the bond midpoint, so the central five dummy atoms were used to determine a first order polynomial of potential *versus* position, and the electrostatic field at the bond midpoint was taken as the negative of the slope.

3.2.1 Reaction Field Method

To minimize errors due to using numerical solutions to the LPBE, we have independently solved for both the numeric solvent reaction field potential (SRF), described in equation (3-5) where each $\phi(\vec{r})$ is a solution to the LPBE (equation (3-4)) at different solvent dielectric, as well as the analytic coulomb field of the solute, then summing the resulting fields to obtain the total electrostatic field of the system, which we refer to as the reaction field method (RFM), shown in equation (3-7) the first term is the negative gradient of the solvent reaction field potential at a point in space \vec{r} and is given

in equation (3-6) and the second term is simply the analytical expression for the Coulomb field at the same point in space, shown in equation (3-2).^{26,33}

$$SRF = \phi(\vec{r})_{(\epsilon_{\text{solute}} \neq \epsilon_{\text{solvent}})} - \phi(\vec{r})_{(\epsilon_{\text{solute}} = \epsilon_{\text{solvent}})} \quad (3-5)$$

$$\vec{F}_{\text{SRF}}(\vec{r}) = -\nabla \left(\phi(\vec{r})_{(\epsilon_{\text{solute}} \neq \epsilon_{\text{solvent}})} - \phi(\vec{r})_{(\epsilon_{\text{solute}} = \epsilon_{\text{solvent}})} \right) \quad (3-6)$$

$$\text{Reaction Field Method (RFM)} : \vec{F}_{\text{RFM}}(\vec{r}) = \vec{F}_{\text{SRF}}(\vec{r}) + \vec{F}_{\text{Coulomb}}(\vec{r}) \quad (3-7)$$

This requires two numeric PBE solutions and one analytic Coulomb solution for each system and is described schematically in Figure 3-1. The SRF is calculated numerically from the difference between the PBE solution for the solvated potential and the PBE solution for the reference potential, illustrated in Figure 3-1A. The solvated potential, $\phi(r)_{\epsilon_{\text{solute}} \neq \epsilon_{\text{solvent}}}$, represented by the leftmost image in Figure 3-1A, is solved for a solute with dielectric ϵ_{solute} solvated in a continuum of dielectric $\epsilon_{\text{solvent}}$ and the reference electrostatic potential, $\phi(r)_{\epsilon_{\text{solute}} = \epsilon_{\text{solvent}}}$, represented by the middle image in Figure 3-1A, is obtained for a solute with dielectric ϵ_{solute} solvated in a continuum also having a dielectric ϵ_{solute} . Removing the reference potential from the solvated potential results in only the potential generated by the solvent polarizing about the solute, represented by the rightmost image in Figure 3-1A. Since our initial work, APBS now has the “lrbpe” keyword, which solves for the SRF directly without requiring a reference calculation. Figure 3-1B shows the SRF (leftmost image) result being added to the analytical solution to the Coulomb field for all protein atoms in a dielectric ϵ_{solute} , (middle image), resulting in a total field which uses a numeric solution for the contribution of the implicit solvent and an analytic solution for the contribution of the explicit solute. In this way, numerical errors in the final result are reduced by only solving for part of the system (the solvent) numerically. This also decreases the calculation sensitivity to input parameters such as box size, grid spacing, box location, charge mapping method, etc.

3.2.2 Grid spacing and size

Six sets of box size and grid dimensions were used. The 30 Å box and 60 Å box were centered on system center of mass. The other four boxes were each centered on NC δ , system center of mass, and RalGDS center of mass, with four different sets of grid spacings (GS), for a total of 14 calculations per frame (excluding the first-stage box calculations): two 19^3 Å³ boxes with 161 and 193 grid points in each dimension with a GS of 0.119 Å/grid point and 0.099 Å/grid point respectively; two 10^3 Å³ boxes with 161 and 193 grid points in each dimension with a GS of 0.062 Å/grid point and 0.052 Å/grid point respectively; a 30 Å x 45 Å x 40 Å box with 129 x 193 x 161 grid points in each dimension with a GS of (0.234, 0.234, 0.250) Å/grid point; and a 60 Å x 45 Å x 40 Å box with 257 x 193 x 161 grid points in each dimension with a GS of (0.234, 0.234, 0.250) Å/grid point. Box sizes will be referred to as the 10 Å box, 19 Å box, 30 Å box, and 60 Å box, respectively, while grid dimensions will be referred to as 161 grid points, 193 grid points, 129 grid points, and 257 grid points, respectively.

The reaction field method was used for the 10 Å box and 19 Å box using 193 grid points for each as well as for the 60 Å box. The system parameters are identical to those previously described for the first term in equation (3-5). For the second term in equation (3-5), the solvent and interior dielectric were both set to 2.0. The analytic Coulomb protein field was taken using the typical Coulomb field expression with a dielectric value of 2.0 and projecting the electrostatic field vector along the nitrile bond vector. This was done for the NC δ box location, system center of mass box location, and RalGDS box location. In total, 7 additional calculations were carried out per frame (excluding the first-stage box calculations).

3.2.3 Box Location

The first-stage box provided the boundary conditions for the second-stage box, and various strategies for constructing second-stage boxes were examined. Different combinations of box center locations, box dimensions, and the number of grid points were examined, as described in the Introduction. By translating the box away from the solvent and towards the protein, we hoped to reduce how often the discontinuity in dielectric environment occurs in the second-stage calculation. The remaining parameters used were identical to those of the first-stage box.

Three different box centers were used: the C δ atom of the cyanocysteine side chain (i.e nitrile carbon), the center of mass of the entire system (excluding water), and the center of mass of the RalGDS protein containing the thiocyanate probe (excluding water). These boxes will be referred to as NC δ , system center of mass, and RalGDS center of mass, respectively. Unless otherwise specified, the NC δ box was used. Representative snapshots of each box are shown in Figure 3-2 for the nitrile probe positioned at RalGDS N27C_{SCN} (black: 60 Å system center of mass; red: 10 Å NC δ ; green: 10 Å system center of mass; and blue: 10 Å RalGDS center of mass). The position of the nitrile C δ was selected as the center of the NC δ box. The center of the system center of mass box was selected as a point along the vector between the furthest of the nitrile C δ and N ϵ and the center of mass of the Rap/RalGDS system. If the distance to the center of mass of the system and the furthest of the nitrile atoms was less than 45% of the smallest box dimension (90% of half the smallest dimension), then system center of mass was the center of mass of Rap/RalGDS system. Otherwise, the box center was translated 45% of the smallest box dimension toward the center of mass of the Rap/RalGDS system. This treatment ensures that the entirety of the C δ -N ϵ bond vector is always within the box. RalGDS center of mass was treated in the same manner, except

it used only the center of mass of the RalGDS part of the protein. In the case of calculations conducted on SCN-containing RalGDS monomer structures, RalGDS center of mass and system center of mass were identical.

The code for calculating generating .pqr files for APBS, gmx2pqr, can be accessed at: https://github.com/awritchie/my_gmx

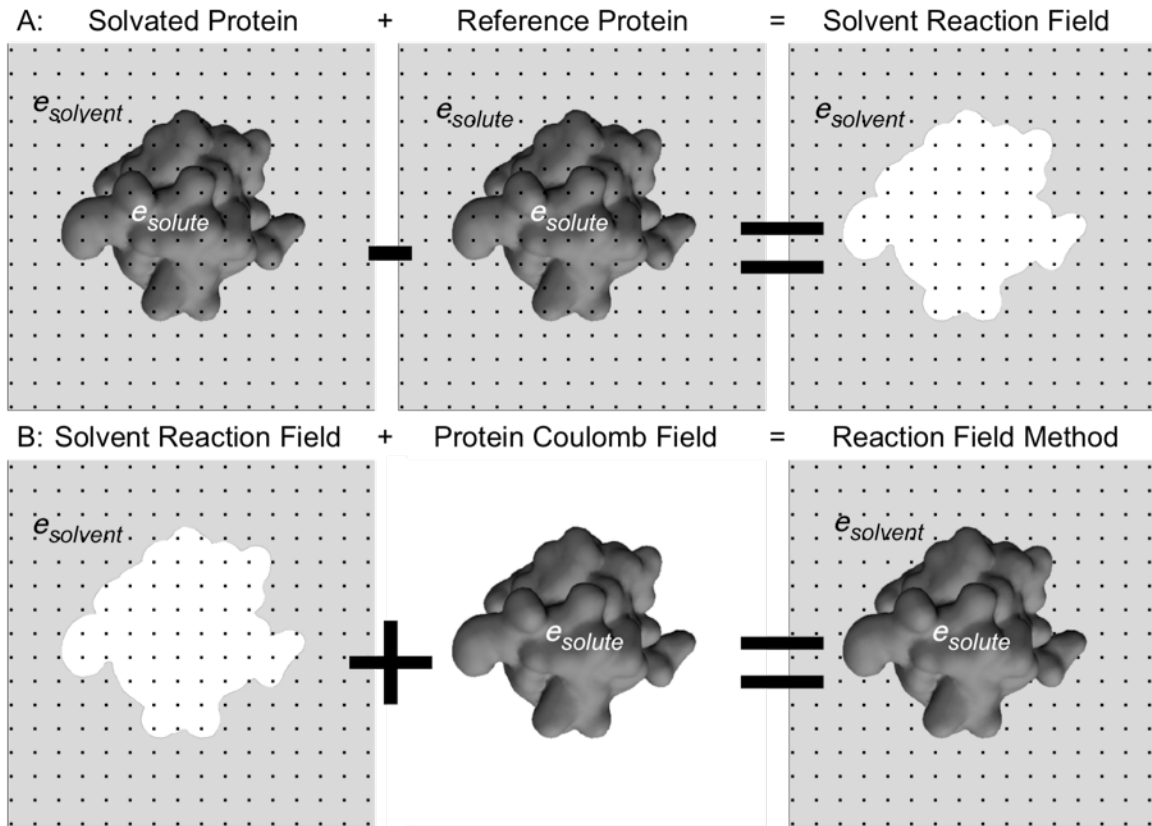


Figure 3-1: Reaction Field Method Schematic

A schematic diagram of the reaction field method (RFM). A) Method for solving the solvent reaction field potential numerically using the Poisson-Boltzmann equation. Top left: The solvated electrostatic potential. Top middle: The reference electrostatic potential. Top right: The reference electrostatic potential is removed from the solvated electrostatic potential, leaving only the electrostatic potential due to solvent—the solvent reaction field potential. B) Method for combining the numerical solution to the solvent reaction field potential to the analytic coulomb field. Bottom left: The numeric solvent reaction field potential. Bottom middle: The analytic field obtained from Coulomb's Law. Bottom right: The total electrostatic field is the sum of the numeric solvent reaction field and the analytic coulomb field.

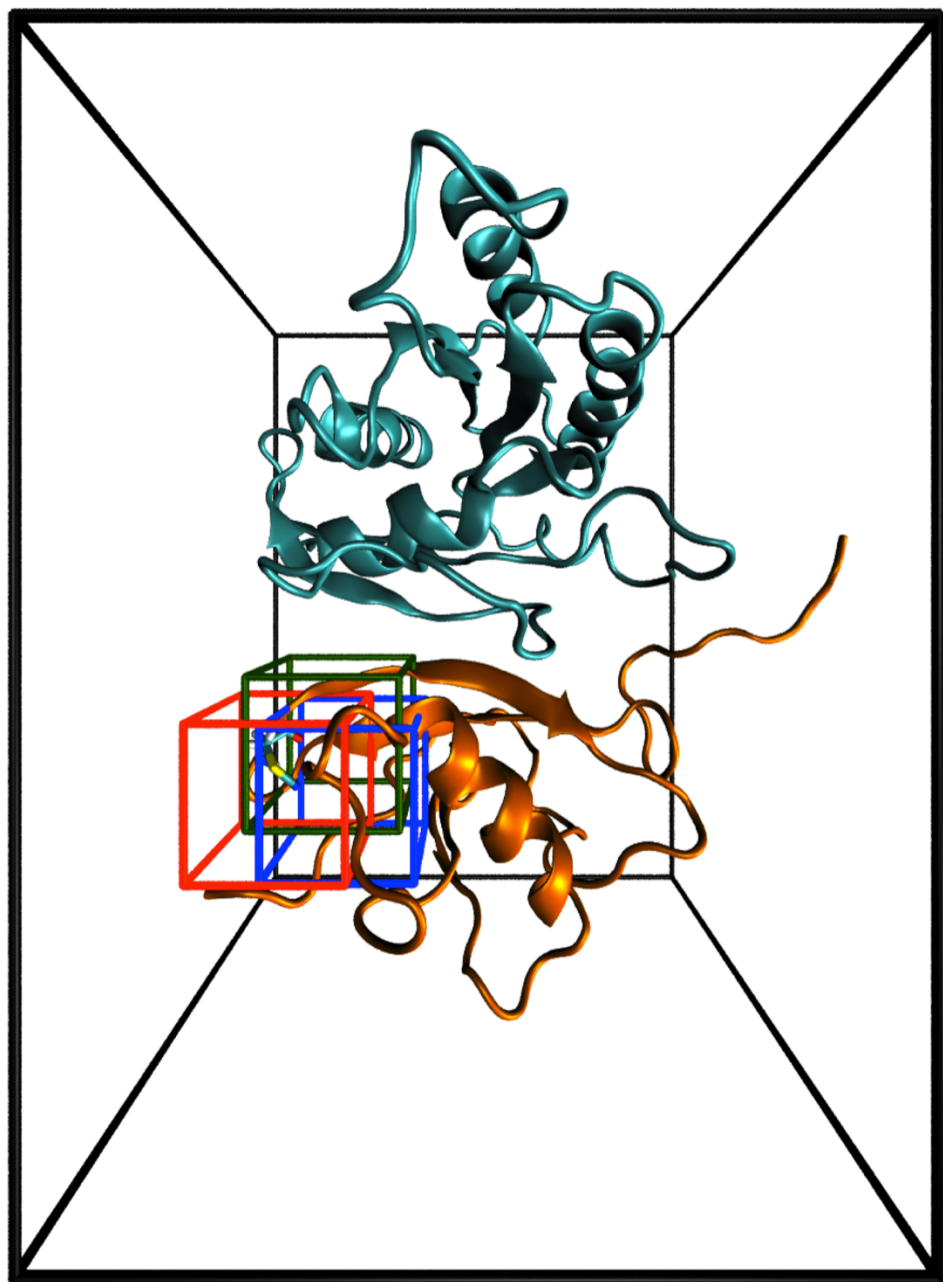


Figure 3-2: Representation of Second-Stage Box Positions

A representative snapshot of the WT Rap-RalGDS N27C_{SCN} protein complex demonstrating the position and sizes of the boxes used to calculate electrostatic fields in APBS. Black: 60 Å system center of mass; red: 10 Å NC δ ; green: 10 Å system center of mass; blue: 10 Å RalGDS center of mass.

3.3 AMBER03 WITH POISSON-BOLTZMANN CONTINUUM SOLVENT AND SELECT EXPLICIT TIP3P WATER MOLECULES

For the following, all electrostatics were done using the reaction field method and the numeric solution to the LPBE. In all cases, water molecules selected are explicitly treated as part of the solute calculation. Here we are merely addressing the water selection criteria.

We examined three different methods for selecting individual water molecules to be included in the explicit portion of the calculation: 1) all water within 5 Å of the nitrile N ϵ atom, 2) the water molecule closest to the nitrile N ϵ atom, and 3) any water molecules hydrogen-bonding to the nitrile N ϵ atom. Frames were prepared using the GROMACS g_select utility in conjunction with trjconv to remove all solvent that was more than 15 Å away from the nitrile N ϵ . Each frame was further processed using Python scripts to generate a .pqr file containing explicit water molecules selected through each of the three methods.

3.3.1 5 Å Water Sphere Around the Vibrational Chromophore

Figure 3-3 demonstrates a 5 Å solvent sphere for a snapshot of RalG28C_{SCN} docked to WT Rap. We chose a 5 Å radius sphere because it is large enough that it will include any waters significantly interacting with the nitrile. The sphere was centered on the N ϵ rather than the C δ because the nitrogen can act as a hydrogen-bond acceptor and, should this be occurring in the simulation, we want to be sure to capture those water molecules. Each 5 Å sphere frame could contain zero (~1.4% of frames), one (~2.7% of frames), or more (~95.9% of frames) water molecules in the frame.

3.3.2 Single Water Molecule Nearest the Vibrational Chromophore

The water molecule with the closest atom (oxygen or either hydrogen) was considered the nearest water molecule, where or not that water molecule met hydrogen bonding criteria. Each nearest water frame was guaranteed to have exactly one water molecule.

3.3.3 Water Molecular Hydrogen Bonding to the Vibrational Chromophore

We considered a water molecule to be hydrogen-bonded to the nitrile if the $N\epsilon$ --H separation was $\leq 2.25 \text{ \AA}$ and the $N\epsilon$ --H-O smallest angle was $\geq 138^\circ$, which were chosen to reach the extremes of the nitrile-water parameters reported by Le Questel *et al.*⁷¹ For both the 5 Å sphere and hydrogen-bonding methods, if a frame did not have a water molecule fitting the respective criteria, no explicit water molecules were included and the LPBE solutions from the original, entirely implicit calculations, were used for that frame. Each hydrogen-bonding water frame could have exactly zero (~89.3% of frames) or exactly one (~10.7% of frames) water molecule in each frame.

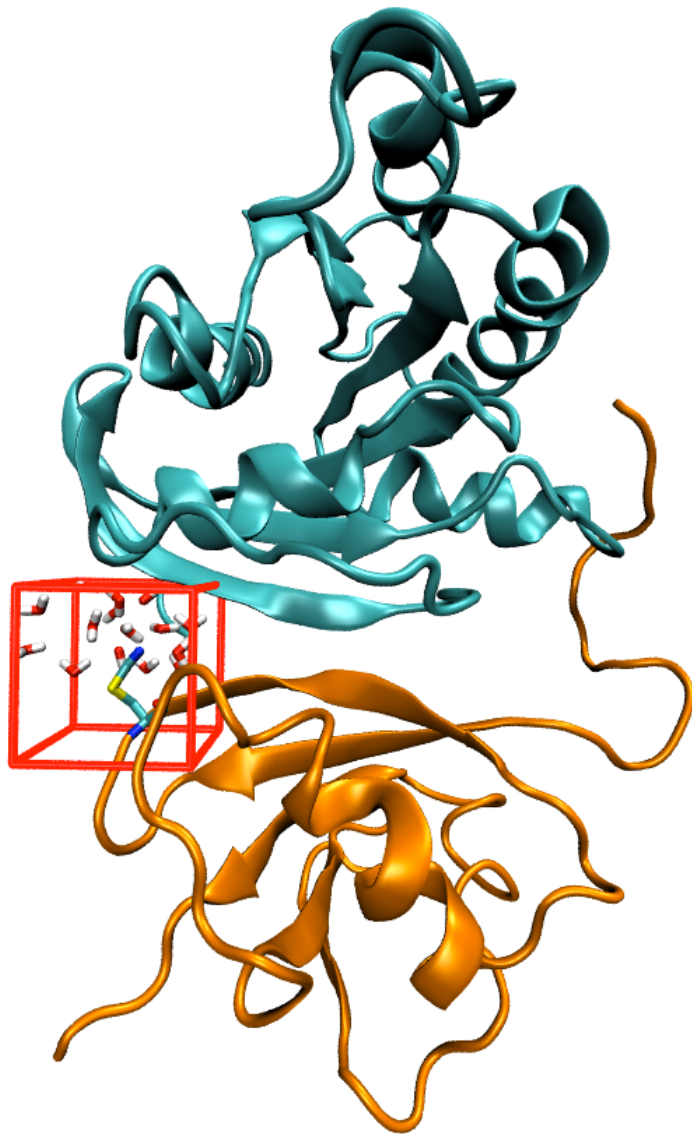


Figure 3-3: Representative Snapshot Showing 5 Å Water Sphere

A representative snapshot of RalGDS G28C_{SCN} (orange) docked to Rap E30/K31 (cyan) demonstrating the size of the 10³Å³ second-stage box (red) used to calculate the electrostatic field in APBS and showing water molecules within 5 Å of the nitrile Nε.

3.4 AMOEBA

3.4.1 Calculating Electrostatic Fields in AMOEBA

We have calculated the electrostatic field experienced by the vibrational chromophore using two methods. The first method is to consider the field at the bond midpoint as the average of the fields at the nitrile carbon and the nitrile nitrogen. This method is relatively simple to implement and requires little-to-zero code modifications in Tinker. The induced dipole of an atom or molecule, $\vec{\mu}_{\text{induced}}$, is given by equation (3-8), where α is the isotropic polarizability and \vec{F} is the local electrostatic field. This can be trivially rearranged to solve for the electrostatic field. The Tinker “analyze” program was modified to report the induced dipole moment of every atom (or in the case of performing the molecular dynamics in Tinker with the AMOEBA force field, the “save-induced” keyword was used), and the field was calculated using equation (3-9). Field calculated in this way will hereafter be referred to as the induced method (IM).

$$\vec{\mu}_{\text{induced}} = \alpha \vec{F} \quad (3-8)$$

$$\vec{F} = \frac{1}{2} \left(\frac{\mu_{C, \text{induced}}}{\alpha_C} + \frac{\mu_{N, \text{induced}}}{\alpha_N} \right) \quad (3-9)$$

The other method is to calculate the electrostatic field exactly at the bond midpoint. While this requires some code modifications, it has the advantage of being trivial to examine or remove the electrostatic field contributions of specific atom or atom fragments in the system without removing information about the system’s response (via induced dipole moments) to the removed parts. This is useful, for example, for removing the contributions of the SCN atoms to the electrostatic field since they should, on average, always have the same geometry relative to each other and therefore always have the same monopole, permanent dipole, and quadrupole field values. In other words, we

don't care about the field created by the SCN atoms, but rather the field external to the SCN, which is created by the atoms surrounding the SCN. Likewise, we don't want to simply zero the multipoles on the SCN atoms because the solvent and non-probe solute atoms *do* respond to the presence of the SCN, and that is something that should be detectable via VSE.

$$\begin{aligned}
 \vec{f}_{i,\text{monopole}}(\vec{r}_i) &= \frac{q_i}{r_i^3} \vec{r}_i \\
 \vec{f}_{i,\text{dipole}}(\vec{r}_i) &= \frac{3(\vec{p} \cdot \vec{r}_i)}{r_i^5} \vec{r}_i - \frac{\vec{p}}{r_i^3} \\
 \vec{f}_{i,\text{quadrupole}}(\vec{r}_i) &= \frac{15}{2r_i^7} \left[\sum_{j=(x,y,z)} \sum_{k=(x,y,z)} \vec{r}_{ij} \vec{r}_{ik} Q_{ijk} \right] \vec{r}_i - \frac{6}{r_i^5} \sum_{j=(x,y,z)} Q_{ijj} \vec{r}_{ij} \\
 \vec{F}(\vec{r}_i) &= \frac{1}{4\pi\epsilon_0} \sum_i^{N\text{ atoms}} \vec{f}_{i,\text{monopole}}(\vec{r}_i) + \vec{f}_{i,\text{dipole}}(\vec{r}_i) + \vec{f}_{i,\text{quadrupole}}(\vec{r}_i)
 \end{aligned} \tag{3-10}$$

Equation (3-10) is the multipole expansion for an electrostatic field, where \vec{r} is some position vector, ϵ_0 is the permittivity of free space, q is the monopole charge of an atom, \vec{p} is the total dipole vector of an atom and is the sum of $\vec{\mu}_{\text{permanent}}$ and $\vec{\mu}_{\text{induced}}$, and Q_{jk} is the traceless tensor describing the quadrupole of an atom. For every frame, $\vec{F}(\vec{r})$ was solved at \vec{r} equals the nitrile bond midpoint. This is solved *after* the induced dipoles are solved to self consistency, meaning the contributions of all atom in the structure file are allowed to mutually polarize each other and the removal of any single atom does not induce a many-body effect on the resultant field calculation. This method will hereafter be referred to as the midpoint method (MPM).

3.4.2 Poisson-Boltzmann Continuum Solvent

All non-solvent atoms were kept and a Tinker .xyz file was generated for each frame using custom code written in C++ and linked against the GROMACS 4.6.x libraries. The “PB-HPMF” keyword was used, which uses APBS to iteratively solve for

the induced dipole to self consistency{Schnieders, 2007 #466}. Induced dipoles were solved to self-consistency of 0.01 D, which typically required 4 iterations of the SRF (or 8 PB solutions) for the protein systems. As before, we used ion concentrations of 0.150 M +1 charge ions of radius 2.0 Å and 0.150 M -1 charge ions of radius 2.0, the molecular surface model (“srfm mol”) with a surface sphere density of 10.0 (“sdens 10.0”) and a solvent dielectric of 78.0. A solute dielectric of 1.0 was used since polarizability is directly modeled in the force field. Once the induced dipoles were solved to self-consistency, equation (3-10) was used to find the field at the nitrile bond midpoint. Because focusing was not implemented in APBS-linked Tinker, a multiple Debye-Hückel boundary condition was used and the box size and grid dimensions were those automatically chosen by Tinker (guaranteed to fully encompass the solute with a grid spacing of 0.5 Å between grid points).

3.4.3 Explicit AMOEBA Water

All atoms were kept and a Tinker .xyz file was generated for each frame using custom code written in C++ and linked against the GROMACS 4.6.x libraries. Aside from TIP3P water (having AMOEBA water parameters) and therefore excluding “PB-HPMF” and its associated keywords, these calculations were performed identically to the AMOEBA with PB calculations with one special consideration. Because a dodecahedron box was used for the simulations in Amber03 and Tinker does not (currently) support a dodecahedron periodic box, periodicity was included in neither the IM nor the MPM field calculations. In simulations performed in Tinker with AMOEBA, a truncated octahedron box was used and periodicity is included for the self-consistent field calculations as well as the IM, although for the final calculation of $\vec{F}(\vec{r})$ using the MPM, only the minimum-distance images were used. In either case, because electrostatic fields go to zero quickly

as a function of distance and the box sizes were sufficiently large, the differences were negligible.

3.4.4 Charge Penetration Field Corrections

<Body text to begin here.>

$$E_{\text{cp}}(r_{ij}) = \begin{bmatrix} Z_i Z_j \\ -Z_i(Z_j - q_j)(1 - \exp(-\alpha_j r_{ij})) \\ -Z_j(Z_i - q_i)(1 - \exp(-\alpha_i r_{ij})) \\ +(Z_i - q_i)(Z_j - q_j)(1 - \exp(-\beta_i r_{ij}))(1 - \exp(-\beta_j r_{ij})) \end{bmatrix} \quad (3-11)$$

$$V_{\text{cp}}(\vec{r}) = \sum_i^{N_{\text{atoms}}} \left[z_i - (z_i - q_i) \cdot (1 - e^{-\alpha_i r_i}) \right] / r_i \quad (3-12)$$

$$\vec{F}_{\text{cp}}(\vec{r}) = \sum_i^{N_{\text{atoms}}} \left(\frac{q_i}{r_i^2} - \frac{q_i e^{-\alpha_i r_i}}{r_i^2} - \frac{\alpha_i q_i e^{-\alpha_i r_i}}{r_i} + \frac{z_i e^{-\alpha_i r_i}}{r_i^2} + \frac{\alpha_i z_i e^{-\alpha_i r_i}}{r_i} \right) \frac{\vec{r}_i}{r_i} \quad (3-13)$$

The code to convert a GROMACS trajectory into a series of Tinker .xyz files, gmx2xyz, can be accessed at: https://github.com/awritchie/my_gmx

The code to calculate the electrostatic field at a point in Tinker, calc_field.f, can be accessed at: https://github.com/awritchie/tinker_tools

The code to calculate the charge penetration corrects, gmx_gmx2amoeba_cp, can be accessed at: https://github.com/awritchie/my_gmx

3.5 VIBRATIONAL STARK EFFECT

The vibrational Stark effect (VSE) relates the change in vibrational absorption frequency of a probe harmonic oscillator to a change in electric field, as shown in equation (3-14), where $\Delta\bar{\mu}$, the Stark tuning rate, is the difference in dipole moments from the ground state to the first vibrationally excited state of the probe, $\Delta\bar{v}$ is the change in vibrational absorption energy, and $\Delta\bar{F}$ is the change in external electric field caused by a known perturbation to the system:^{35, 72-78}

$$\Delta E = hc\Delta\bar{v} = -\Delta\bar{\mu} \cdot \Delta\bar{F} \quad (3-14)$$

Additional higher order terms, such as difference polarizability, are also present in the Stark effect; however, in VSE spectroscopy, their contribution is small relative to the difference dipole and thus are not considered in our analysis.^{76, 77}

3.6 VIRTUAL STARK TUNING RATE (VSTR) AND “IDEAL” DIELECTRICS

Fitting the calculated electric fields to the experimental vibrational absorption frequencies yields a linear equation in which the fitted slope is related to the negative inverse of the Stark tuning rate (3-15), where we subbed in the vibrational Stark effect for $\Delta\tilde{v}$. In this way we can calculate an observed or virtual Stark tuning rate (VSTR) from our calculations, which can then be compared to the known, experimental Stark tuning rate for a thiocyanate probe of $0.77 \text{ cm}^{-1}/(\text{MV cm}^{-1}) = 1.99 \text{ cm}^{-1}/(k_b T/e\text{\AA})$.

$$\begin{aligned} \Delta\bar{F} &= m(\Delta\tilde{v}) = m(-\Delta\bar{\mu}' \Delta\bar{F}) \\ \Delta\bar{\mu}' &= -\frac{1}{m} = VSTR \end{aligned} \quad (3-15)$$

We can also calculate an “ideal” dielectric, $\varepsilon'(\bar{r})$, required to force the VSTR to be equal to the known Stark tuning rate. The “ideal” dielectric can be calculated using the

VSTR, $\Delta\bar{\mu}'$, the experimental Stark tuning rate, $\Delta\bar{\mu}$, and solute dielectric, $\varepsilon(\bar{r})$, using equation (3-16).^{70,79}

$$\begin{aligned}\Delta\bar{F}(\bar{r})\varepsilon(\bar{r}) &= \Delta\bar{F}'(\bar{r})\varepsilon'(\bar{r}) \\ \frac{\varepsilon(\bar{r})}{\Delta\bar{\mu}} &= \frac{\varepsilon'(\bar{r})}{\Delta\bar{\mu}'}\end{aligned}\tag{3-16}$$

Chapter 4 The Role of Electrostatics in Differential Binding of RalGDS to Rap Mutations E30D and K31E Investigated by Vibrational Spectroscopy of Thiocyanate Probes

4.1 INTRODUCTION

The human proteins p21^{Ras} (hereafter Ras) and Rap1A (hereafter Rap) are members of the Ras family of guanosine triphosphate (GTP)-hydrolyzing proteins that switch between an ON state when bound to GTP and an OFF state when bound to guanosine diphosphate (GDP) in the regulation of signal transduction pathways⁸⁰. When in the GTP-bound ON state, both proteins dock to the Ras binding domain (RBD) of downstream effector proteins to propagate a signal transduction cascade. As members of the Ras superfamily of GTPases, Ras and Rap are similar in both sequence and structure; they share 50% amino acid identity³⁹, 80% amino acid homology, and have nearly identical structure and effector binding surfaces (rmsd of 0.7 Å for homologous residues).

Despite these similarities, Ras and Rap have very different functions within the cell. Ras is involved in the propagation of chemical signals that regulate cell division, cell survival and apoptosis, and has been a focus of research in molecular oncology for many years⁸¹⁻⁸³. The biological function of Rap is less well understood, but it has recently been shown to play a role in cellular adhesion⁸⁴ and has been implicated in cancer metastasis^{85, 86}. The origin of the functional specificity of these two similar proteins lies in the ability of Ras and Rap to bind to different downstream effectors while in the GTP-bound ON state, thus initiating different signaling cascades. One of the best studied downstream effector proteins of Ras is the human protein c-Raf-1 (hereafter Raf), while Rap is thought to interact most strongly with the Ras binding domain (RBD) of the downstream effector Ral guanosine dissociation stimulator (RalGDS, hereafter Ral).

While the structures of the RBD of the downstream effector proteins are very similar^{38,39}, measurements of thermodynamic ^{35,87-89} parameters of the protein-protein binding events (DG_{dock} and K_d) indicate high specificity between the two GTPases and their appropriate downstream effector. Given the structural similarities of these protein-protein interfaces, a possible mechanism for the binding specificity that each GTPase shows for its appropriate downstream effector could be based on differences in electrostatic complementarity at the protein-protein interface. To investigate this hypothesis, the binding of these two GTPases to a variant of Ral have previously been investigated by our laboratory through both experimental and computational methods^{8,35} in order to explore the contribution of electrostatic fields to interface formation in a system in which structural factors are controlled as much as possible.

In 1995, Herrmann and coworkers^{89,90} demonstrated the importance of the amino acids at positions 30 and 31 on Ras and Rap in discriminating downstream effector partners. These amino acids, Ras Asp 30 and Glu 31 and Rap Glu 30 and Lys 31, are positioned at the protein-protein binding interface, and studies involving reversion mutations of Rap to Ras have shown that these residues are involved with the interactions with downstream binding partners. Those studies found that the charge reversion mutation Rap K31E and the double mutation Rap E30D/K31E cause the dissociation constant with the downstream effector Raf to resemble Ras D30/E31 more closely than Rap E30/K31⁹⁰. Furthermore, the double mutant Rap E30D/K31E co-crystallized with the downstream effector Raf, which usually binds more strongly to Ras. Similarly, the mutation Ras E31K was used to co-crystallize Ras with Ral, normally Rap's immediate downstream effector³⁸, and the double reversion mutant Ras D30E/E31K has significantly reduced binding affinity with Raf⁹¹. The role of these mutations in creating strong binding

affinity for an alternative downstream effector suggested an electrostatic mechanism caused by altering the charge of the residue at position 31 on either GTPase.

The arrangement of amino acid charges from secondary and tertiary protein structure can generate large and heterogeneous electrostatic fields that affect all protein function, including protein-protein interactions.^{2, 3, 7, 92-94} Vibrational Stark effect (VSE) spectroscopy is a recently developed experimental technique capable of measuring electrostatic fields in proteins^{42, 58, 72-77}. In VSE spectroscopy, the intrinsic response of a probe vibrational oscillator to its local electrostatic environment is measured spectrally and is used to quantitate the magnitude and direction of the local electric field to which the probe is exposed. After calibration, the probe is inserted into a known position of a protein where it becomes a highly local, sensitive, and directional reporter of fluctuations of the protein's electrostatic field caused by structural or chemical perturbations to the protein. For example, the formation of a protein-protein interface through a docking interaction may induce changes in the absorption energy of a probe located on each protein surface as that probe is exchanged from an electrostatic field generated by the protein-water interface to one generated by the protein-protein interface.

The nitrile stretching vibration is one of several useful VSE probes that have been identified⁷⁷. Several characteristics of the nitrile oscillator make it particularly attractive; its absorption energy of ~2100-2250 cm⁻¹ is in a region of the spectrum that is outside the vibrational background of a complex biomolecule, it is reasonably sensitive to fields of the magnitude thought to be present in proteins, and it can be incorporated into proteins with relative ease⁹⁵. There are a growing number of reports describing VSE spectroscopy of nitrile probes to study the function of electrostatic fields in enzyme active sites^{42, 58, 72-74}. Recently in our laboratory, VSE spectroscopy has been used to study the change in absorption energy of the nitrile probe incorporated at eleven locations on

the surface of Ral that become buried in the protein-protein interface upon binding to either Ras D30/E31 or Rap E30/K31³⁵. This study determined that at some probe locations the change in absorption upon binding to Ras D30/E31 and Rap E30/K31 was the same, while at other locations the change was different, suggesting that these latter amino acids may participate in an electrostatic mechanism that enables Ral to distinguish Ras from Rap. Furthermore, measurement of the dissociation constant of the docking of the GTPases with nitrile-containing Ral mutants showed no deleterious effect of the spectroscopic probe on the formation of the docked complex. These measurements were later confirmed through extensive molecular dynamics sampling of the protein-protein complex⁸. We hypothesized that several of these Ral-based nitrile probes would be ideal for investigating our hypothesis of an electrostatic mechanism for binding discrimination mediated by the charge on position 31 of these two GTPases.

In this report, we describe the systematic investigation of the effect of the E30D and K31E mutations to Rap on the local electrostatic fields formed by docking to the downstream effector and measured by the nitrile probe at six locations on the surface of the RBD of Ral using VSE, molecular dynamics (MD) simulations, and dissociation constant (K_d) measurements. We selected 6 amino acids on Ral that are positioned in the protein-protein interface near positions 30 and 31 of Ras and Rap when the docked complex is formed: N27, G28, N29, Y31, K32, and N54. The locations of these amino acids within the Rap-Ral interface, as well as Rap positions 30 and 31, are shown in Figure 4-1. Positions N27 and Y31 were selected because at these probe locations, we previously measured a significant difference between docking of Ras D30/E31 versus Rap E30/K31³⁵, and wanted to investigate whether these observations were due to the different amino acid identity at positions 30 and 31. Position N29 was chosen because, along with position N27, molecular dynamics (MD) structural sampling of the

thiocyanate side chain within the docked complex showed that the nitrile group has the largest angle with respect to the Ras-Ral interfacial plane of the collection of Ral-based probes we have investigated, approximately 45° from the plane of the Ras-Ral interface⁸. Because the effect of the change in electrostatic field is on the projection of the field vector onto the nitrile probe bond axis, these positions seemed the most likely to feel the effect of the field vector at positions 30 and 31 of Rap, which appear from the crystal structures 1LFD³⁸ and 1GUA³⁹ to be approximately perpendicular to the interface. Gly28 was chosen as intermediate between these two residues. Finally, positions K32 and N54 were selected based on their physical proximity to the side chains of positions 30 and 31 on the GTPase once the docked complex formed.

Each of the six Ral amino acids were mutated to cysteine, then chemically modified to introduce the nitrile VSE probe in the form of the thiocyanate. These mutants were then bound to Rap E30/K31, Rap E30D, Rap K31E, and the double mutant Rap E30D/K31E. The difference in vibrational absorption energy, Dn_{obs} , between the Ral monomer and the docked complex was measured by Fourier transform infrared spectroscopy (FTIR). The dissociation constant of the docked complex, K_d , was determined through a fluorescence assay. Finally, extensive MD simulations on docked complexes of all Rap and Ral variants were conducted to determine Boltzmann-weighted orientational data for the Ral-based nitrile probes and for the side chains at Rap positions 30 and 31. These simulations demonstrate that the mutation K31E is almost exclusively responsible for changes in side chain orientations at Rap positions 30 and 31 that cause the observed change in K_d . VSE spectroscopy demonstrates that only two of the probe locations examined, at N27C and N29C displayed a change in the absorption energy upon binding the Ras-like Rap double mutants that strongly resembled the change for Ras D30/E31. However, several of these probes did respond in an additive manner to the

individual single mutations. In some cases, these effects are replicated in subtle structural changes at positions 30 and 31 observed in molecular dynamics sampling. These studies support both a structural and electrostatic mechanism to explain observed differences in GTPase-effector binding.

4.2 RESULTS

4.2.1 Dissociation Constant Measurements

Measured dissociation constants of both WT and SCN-labeled Ral β mutants docking with all GTPases studied here are reported in Table 4-1. Binding of WT Ral to Rap E30/K31 was approximately 10-fold faster than binding to Ras D30/E31, as has been reported before^{35, 89, 90}. Any effect of the thiocyanate probe on the formation of the interface can be investigated by comparing K_d values obtained for wild type (WT) Ral versus the SCN-labeled Ral β mutants docking to Ras D30/E31 and Rap E30/K31 in Table 4-1. Although there are some variations in the absolute value of these numbers, they are for the most part small. The two largest deviations, caused by Ral β G28C_{SCN} (reduced K_d by an order of magnitude) and Ral β Y31C_{SCN} (increased K_d by an order of magnitude), still showed an order of magnitude increase in K_d when binding to Ras D30/E31 as opposed to Rap E30/K31, as is expected from our previous work. The dissociation constants presented in Table 4-1 demonstrate that the presence of the SCN probe on Ral β mutants did not substantially affect binding to either Ras D30/E31 or Rap E30/K31, as has been observed before³⁵. Along with results from molecular dynamics sampling of this system, described below, this is strong circumstantial evidence that the nitrile VSE probe does not significantly alter the interface formed between Rap and the SCN-labeled Ral β mutants compared to the WT interaction. Our experimental

mutagenesis and chemical labeling strategy therefore does not destroy the protein-protein interaction that we are attempting to measure.

The results in Table 4-1 confirm previous reports that the reversion mutation at Rap position 31 alters the binding interaction between Rap and Ral to resemble that of Ras and Ral. All SCN-labeled Ral β mutants interacted with Rap E30/K31E with a K_d 10-fold higher than with Rap E30/K31, and this effect was preserved in the double mutant Rap E30D/K31E. The single mutation Rap E30D/K31 had no effect on binding, and all K_d values measured with that construct were essentially identical to Rap E30/K31. It is therefore clear that the amino acid located at position 31 of the GTPase is critical in the mechanism that enables Ral to distinguish structurally similar but functionally distinct GTPases for appropriate binding. Exploring the structural and electrostatic components of that mechanism is the subject of the MD sampling and VSE spectroscopy discussed here.

4.2.2 Molecular Dynamics Simulations

Structural details of the interface formed between Rap and Ral have been investigated with two high-quality crystal structures, 1GUA and 1LFD^{38,39}. These are crucial starting points for any comprehensive biochemical understanding of the Rap-Ral interactions, but the static structures of these proteins might not represent the full range of side chain conformations of either our SCN probe or positions 30 and 31 of the GTPase, and so are not sufficient for our purposes. Furthermore, our experiments are on an unnatural variant of the system, the SCN-labeled Ral β mutant. Although our K_d measurements indicate that the presence of the thiocyanate probe does not significantly disrupt interface formation, knowledge of the structure and orientation of the probe within the interface is necessary to interpret vibrational absorption data. To address these

issues, we performed extensive molecular dynamics sampling of each SCN-labeled Ral β mutant docked with Rap E30/K31 and the Rap mutants E30D/K31, E30/K31E, and E30D/K31E to accumulate a Boltzmann-weighted ensemble of the orientations of the thiocyanate group and the side chains at Rap positions 30 and 31. The WHAM-derived χ_2 torsional probability distribution for all thiocyanate groups and χ_1 torsional probability distribution side chains at Rap positions 30 and 31 are shown in Figure 4-7, Figure 4-8, and Figure 4-9. Similar to what we have seen previously⁸, the torsional distribution for all studied side chains was characteristic of an unhindered alkyl group, with three probability maxima separated by $\sim 120^\circ$ and essentially no significant difference depending on the chemical identity of either the SCN-labeled Ral β mutant in the docked complex (Figure 4-7) or the Rap variant (Figure 4-8 and Figure 4-9). Our MD sampling strategy therefore provides us with a comprehensive ensemble of structures of each docked Rap-Ral β variant studied with VSE spectroscopy to aid in interpreting our spectroscopic results.

To analyze our molecular dynamics simulations of the torsional distribution of the thiocyanate residue on each Ral β mutant and on the side chains at Rap positions 30 and 31, we defined two angles for each side chain with respect to the Rap-Ral β surface, which we term azimuthal and polar angles. These two angles are shown schematically in Figure 2-5. When the cross hairs on Figure 2-5 are translated to the C α atom of each simulated residue on Rap or Ral β (represented as spheres), they become the origin of the polar angles shown in Figure 4-4 and Figure 4-5. These simulations were compared with previous simulations of the Ras-Ral β binding interface⁸, and in all cases, the orientation of the nitrile at the docked interface for Ras D30/E31 and Rap E30/K31 are identical, within the error distribution of the Boltzmann-weighted ensemble. This indicates that the structure of the probe at the interface of these two GTPases is very similar, as expected by the structural similarities of the crystal structures, the amino acid homology of the

GTPases, and the fact that the measured K_d values of the SCN-labeled Ral β mutants dock with Ras D30/E31 and Rap with the same dissociation constant as WT Ral. Furthermore, as seen in Figure 4-7, mutations to positions 30 and 31 of Rap did not substantially alter the orientation of the nitrile probe at the interface, with all 6 nitrile positions remaining approximately constant with the same dihedral distribution for Rap E30/K31, or the E30D, K31E, E30D/K31E mutations. The consistency of the probe orientation in these Boltzmann-weighted ensembles is further indication of the structural robustness of these interacting proteins, making them suitable for systematic measurements of electrostatic fields at the protein-protein interface without compromising structural integrity of the interface. This observation is important to justify using VSE spectroscopy to explore the biochemistry of Rap-Ral binding with a spectroscopic technique that doesn't compromise the very interaction we are interesting in studying.

The azimuthal and polar angles of the side chains at Rap positions 30 and 31 for each mutant studied here are shown in Figure 4-5. When looking at position 30 (Figure 4-5A), the azimuthal angles showed essentially no difference depending on either the Rap mutant or the SCN-labeled Ral β mutant to which it was docked. In most cases, the aspartate (for E30D and E30D/K31E) or glutamate vector (for WT and Rap K31E) pointed approximately parallel and slightly below the Rap-Ral surface plane. The single exception to this was when Rap E30D was docked with Ral β K32C_{SCN}, where it was observed that the residue oriented itself 5° above the Rap-Ral β K32C_{SCN} surface plane. The polar angles of the side chain at position 30 (Figure 4-5B) showed significantly more fluctuations, but these fluctuations were essentially random and all demonstrated very large WHAM-derived standard deviations. This suggests that both aspartate and glutamate side chains at this position undergo large polar motions that are not influenced by the chemical identity of position 31 or the location of the thiocyanate probe.

The side chains at Rap position 31 behaved very differently. The azimuthal angles of the side chain at Rap position 31 (Figure 4-5C) were pointed significantly further below the Rap-Ral β mutant plane than at position 30 (55-60° below the surface plane for position 31 versus < 25° below the surface plane for position 30), but with the exception of docked to Ral β Y31C_{SCN}, all Rap mutants behaved identically. The distribution of polar angles of mutants of Rap position 31, however, displayed a significant dependence on the identity of the residue at position 31 (Figure 4-5D). Although again the distribution of observed angles for each Rap mutant was large, an obvious trend appeared in the data. With the sole exception Rap mutants docked to Ral β N54C_{SCN}, Rap E30/K31 and the Rap E30D behaved identically, while the Rap mutants K31E and E30D/K31E also behaved identically. This strongly supports the evidence that mutations at Rap K31 are most important for determining binding to the downstream effector Ral, and that mutations to Rap E30 do not significantly affect the behavior of either Rap E30/K31 or Rap K31E. Both of these observations are consistent with our observations of differences in dissociation constants between WT and mutated Rap binding to the downstream effector Ral.

We investigated the causes of the difference in orientation between the lysine and glutamate side chains at Rap position 31 through inspection of representative MD snapshots. This clearly revealed that when a lysine is at position 31, it pointed towards a hydrogen bonding acceptor pocket formed by Ral β D51, N54, and E58. When this side chain was mutated to Rap K31E in either the single or double mutant, the negatively charged Glu reoriented to avoid electrostatic repulsion with the Ral β surface caused by the hydrogen bond accepting pocket created by these three residues. This appears to be the central cause for both the dissociation constant and electrostatic differences between Rap-Ral β binding and Ras-Ral β binding described here. As discussed above, this

behavior was not observed when the Rap constructs were docked with Ral β N54C_{SCN}; investigation of MD structures showed that this probe location disrupted the hydrogen bonding pocket sufficiently to cause this portion of the Ral β surface retracted slightly from the Rap-Ral β interface, leaving K31 without the hydrogen bonding pocket. Although the importance of this hydrogen bonding pocket can be hypothesized from the 1LFD crystal structure (of Ras variant E31K docked with RalGDS), our MD sampling has provided the first confirmation of the observed biochemical behavior of Ras and Rap with direct structural evidence.

4.2.3VSE Spectroscopy of the Docked Protein-Protein Complex

A principle goal of the work described here is to deconvolute the effects of structural and electrostatic influences on protein-protein interface formation. Our systematic molecular dynamics simulations allowed us to highlight differences between WT and mutant Rap that appeared to be due entirely to subtle changes in structure. With that information, a systematic exploration of electrostatic factors was conducted by measuring changes in electrostatic interactions between the GTPase and the downstream effector Ral by VSE spectroscopy of vibrational probes placed at the GTPase-effector interface. In this section we systematically review the spectroscopic results from each VSE probe, then draw general conclusions in the Discussion section.

Ral β N27C_{SCN} and N29C_{SCN}: Selection of each of the 6 SCN-labeled Ral β probes was based on consideration of each probes' orientation compared to the Rap-Ral β interface, proximity to the Rap positions 30 and 31, and large differences in vibrational absorption energy upon binding to Ras D30/E31 and Rap E30/K31 measured in a previous study³⁵. N27C_{SCN} and N29C_{SCN} were selected for probe placement because our Boltzmann-weighted molecular dynamics simulations of the orientations of the 6

thiocyanate probes when docked with each of the Rap constructs determined that thiocyanate group on these two Ral β mutants had some of the largest angles with respect to the plane of the Ras-Ral β interface of any of our probes, approximately 20-30° above the surface plane (Figure 4-4A)⁸. Because VSE spectroscopy is only sensitive to changes in the electrostatic field vector projected onto the nitrile bond axis, and because, as shown in Figure 4-5C, mutations to Rap K31 were themselves close to perpendicular to the Rap-Ral β surface plane, probes perpendicular to the Rap-Ral β plane would be most sensitive to mutations to Rap K31. A Ral β -based SCN probe that was itself as close to perpendicular to the Rap-Ral β surface plane would therefore be in an appropriate position to observe changes caused by the charge reversion mutation at position 31.

An example of the VSE data collected here is shown in Figure 4-2. The Ral β N29C_{SCN} mutant was incubated with each Rap mutant, concentrated, and the absorption energy of the nitrile probe was recorded and compared with the measured absorption energy when bound to Rap E30/K31 from a previous study³⁵. When docked with Rap E30D, the thiocyanate absorption energy was 2160.8 cm⁻¹, identical to the observed absorption energy when Ral β N29C_{SCN} was bound to Rap E30/K31. When Ral β N29C_{SCN} was incubated with Rap K31E, the absorption energy was 0.6 cm⁻¹ higher in energy than when docked with Rap E30/K31, 2161.4 cm⁻¹. However, when docked with the double mutant, Rap E30D/K31E, the absorption energy of the thiocyanate shifted 0.8 cm⁻¹ higher in energy (2161.6 cm⁻¹). Both Rap mutants containing K31E were therefore more similar to the observed absorption energy when Ral β N29C_{SCN} is docked with Ras D30/E31 (2161.1 cm⁻¹) than with Rap E30/K31. This means that the probe is experiencing an electrostatic environment in the double mutant E30D/K31E that is more like that of Ras D30/E31 than to Rap E30/K31, although the effect is small.

Changes in the absorption energy ($\Delta\nu_{\text{obs}}$) of the thiocyanate on each SCN-labeled Ral β mutant due to binding for each SCN-labeled Ral β mutant studied here are summarized in Table 4-2 and Figure 4-3. In these figures, all absorption energies are referenced to the absorption energy of the nitrile probe when docked with Rap E30/K31 (i.e. $\Delta\nu_{\text{obs}} = 0$ represents no change from the thiocyanate absorption energy when docked with Rap E30/K31 reported previously)³⁵. These shifts are related to the change in electrostatic field through the known value of the Stark tuning rate of the cyanocysteine probe, of $0.7 \text{ cm}^{-1}/(\text{MV/cm})$; the values of ΔF determined from equation (3-14) are reported in Table 4-2.

When the probe is located at Ral β N27C_{SCN} and N29C_{SCN}, the data in Figure 4-3 clearly show that both the single and double reversion mutants Rap K31E and E30D/K31E have VSE absorption energies that are similar to Ras D30/E31, not Rap E30/K31. In both cases, the single mutation Rap E30D appears to have a negligible effect on the electrostatic environment of the probe. At these particular probe locations, therefore, the double reversion mutation does indeed revert the electrostatic field of Rap back to that found in Ras, supporting our hypothesis. Although these energy shifts are small, the trend towards higher absorption energies when bound to Ras D30/E31 and the double mutant Rap E30D/K31E than when bound to Rap E30/K31 are clear. The relatively small effect of mutations on the magnitude of the absorption energy of Ral β N29C_{SCN} in particular may be due to the fact that calculations have indicated that the nitrile at this location is actually most sensitive to changes in electrostatic field caused by amino acid mutations at the Ral surface, thus screening the effect of mutations made to the Ras surface⁸. This effect is currently being investigated in our laboratory and will be described in a future report.

K32C_{SCN} and N54C_{SCN}: The closest Ralβ amino acid to positions 30 and 31 is N54, (a distance from backbone atoms of approximately 11-16 Å in our Boltzmann-weighted ensemble of structures). Because MD simulations indicated that this also was oriented above the Rap-Ralβ surface plane, this probe location was also selected for this study. As shown in Figure 4-3, the two single mutations E30D and K31E have small but opposite effects on the absorption energy of N54C_{SCN} when compared to Rap E30/K31; Rap E30D is 0.4 cm⁻¹ higher in absorption energy, while Rap K31E is 0.1 cm⁻¹ lower in absorption energy. The combined effect of the double mutant Rap E30D/K31E, however, gave a VSE shift 0.2 cm⁻¹ higher in energy than Rap E30/K31, resulting in an absorption energy that was approximately the sum of the behavior of the two single mutations. As discussed above, because N54C_{SCN} visibly disrupted the hydrogen-bonding interaction with Rap K31 in the docked complex, it is likely that the structural disruption of this interface means that this position is not appropriate for deconvoluting structural and electrostatic effects. This observation demonstrates the importance of investigation both structural and electrostatic contributions to the biochemical question of interest.

The nitrile vibrational probe was also placed at Ralβ K32C_{SCN} because of its proximity to positions 30 and 31 on the GTPase in the docked complex. As can be seen in Table 4-2 and Figure 4-3, although the measured error in $\Delta\nu_{obs}$ was larger than other positions, there was a dramatic effect of the mutation Rap K31E on the absorption energy of the thiocyanate compared to Rap E30/K31 (-1.0 cm⁻¹), while Rap E30D caused only a small perturbation (-0.2 cm⁻¹). The behavior of the double mutant Rap E30D/K31E was the sum of these two shifts, -1.2 cm⁻¹. This was very different from the response on binding to Ras D30/E31, which showed a shift in absorption energy of +0.7 cm⁻¹ compared to Rap E30/K31. Thus, again, the differences in the electrostatic fields

between Ras D30/E31 and Rap E30/K31 experienced by the probe at Ral β K32C_{SCN} did not appear to be caused by the reversion mutations at positions 30 and 31 of Rap.

These two probe locations responded to the double mutant Rap E30D/K31E essentially as the addition of each single E30D and K31E mutation. When the probe was at N54C_{SCN}, the mutation E30D caused an increase in absorption energy relative to Rap E30/K31, while K31E caused a decrease in absorption energy. The double mutant E30D/K31E shifted approximately halfway between these two extremes. In the case of the probe at location Ral β K32C_{SCN}, both single mutations caused a reduction in the absorption energy of the nitrile probe, while the double mutation caused a shift that was the sum of the two. In these two cases, it appears that we are measuring additive electrostatic effects as would be predicted by a simple model of adding electrostatic fields together. However, in neither case did the double reversion mutation to Rap produce an electrostatic environment measured by the probe that was similar to Ras.

G28C_{SCN} and Y31C_{SCN}: We chose Ral β G28C_{SCN} as a probe location because it was between positions N27 and N29, even though it did not meet other desirable criteria. Previous studies had shown very little sensitivity to differences in binding to Ras D30/E31 versus Rap E30/K31,³⁵ and a position in the docked complex that was more consistently parallel to the surface than either N27C_{SCN} or N29C_{SCN}.⁸ Even still, this probe did respond strongly to mutants Rap E30D and K31E (+1.0 cm⁻¹ and +0.5 cm⁻¹ versus Rap E30/K31, respectively), compared to a shift of -0.8 cm⁻¹ when bound to Ras D30/E31. The double mutant, Rap E30D/K31E, however, only demonstrated a shift of +0.2 cm⁻¹ compared to Rap E30/K31. The probe at this location thus reacted in a manner in which the two single mutations appear to cancel each other out.

Position Ral β Y31C_{SCN} was selected for study because the change in electrostatic field upon docking to Rap E30/K31 differed from Ras D30/E31 by a large amount, 0.8

cm^{-1} , and resulted in changes in field in the opposite direction. As shown in Table 4-2, both single mutants Rap E30D and Rap K31E shifted the absorption energy of the nitrile probe on Ral β Y31C_{SCN} to lower energy, by -2.0 cm^{-1} and -1.0 cm^{-1} respectively. However, the combined effect of the double mutant was to shift the absorption energy lower by only -0.2 cm^{-1} compared to Rap E30/K31, substantially less than either single mutant. As shown in our molecular dynamics simulations, there is a significant reorientation of the side chain at position Rap 31 above (azimuthal angle) and away from (polar angle) Ral β Y31C_{SCN} in the mutants Rap K31 and E30D/K31E which are likely causing this probe to become significantly less sensitive to change in electrostatic field in the binding region in which we are interested.

At both of these locations on the protein surface, Ral β G28C_{SCN} and Ral β Y31C_{SCN}, although each single Rap mutant caused a large change in absorption energy (higher in energy at Ral β G28C_{SCN}, and lower in energy at Ral β Y31C_{SCN}), the double mutant effectively canceled out those changes in both cases. While MD sampling of position Ral β Y31C_{SCN} makes it clear that this is likely due to a large structural reorientation of the Rap sidechain position 31, the influences of the probe at position Ral β G28C_{SCN} are much less clear. After extensive inspection of our MD simulations, we have found no significant structural differences near G28C_{SCN} to explain this observation. It could be that the distance between G28 and the region of the binding surface we are investigating by mutations at Rap E30 and K31 make Ral β G28C_{SCN} an ineffective probe for this study. This result is noteworthy, however, because the distance over which linear VSE effects can be accurately measured has still not been experimentally established.

4.3 DISCUSSION

This study was motivated by functional observations that positions 30 and 31 of Ras and Rap, which are among the few chemical differences between the Ras and Rap interfaces, could help discriminate appropriate downstream effectors for each GTPase. Because of the structural similarities of these two protein surfaces, it is possible that downstream effector binding selectivity could be caused by changes in the electrostatic fields at the GTPase-effector interface caused by mutations at position 30 and 31, and in particular by the reversal of charge caused by the K31E mutation. Measuring this effect from the perspective of the downstream effector Ral, which can bind to both GTPases, proved useful to explore this aspect of GTPase function. Previous experimental work and extensive MD sampling provided us with criteria to guide the selection of useful places to position the nitrile probe on the Ral β surface. Three criteria that were used were 1) angle of the nitrile with respect to the GTPase-effector interface, with probes perpendicular to the plane of the interface preferred ($N27C_{SCN}$ and $N29C_{SCN}$); 2) proximity to positions 30 and 31 when the docked complex is formed ($K32C_{SCN}$ and $N54C_{SCN}$), and 3) previously measured discrimination in absorption energy when docking to Ras as opposed to Rap, indicating those probes end up in significantly different electrostatic environments after the docked complex is formed ($N27C_{SCN}$, $N29C_{SCN}$, and $Y31C_{SCN}$). The location $G28C_{SCN}$ was chosen because of its position between $N27C_{SCN}$ and $N29C_{SCN}$, not because of any favorable selection criteria, and could be considered as a control location on the Ral β surface. No probe displayed ideal behavior in all three selection criteria, and some probes were favorable from one aspect but unfavorable from another. For example, $N27C_{SCN}$ and $N29C_{SCN}$ were the most perpendicular of all of the Ral β mutant, but were far removed from Rap positions 30 and 31 in the docked complex. Thus even with detailed structural and electrostatic studies we have carried out on these GTPases, working within

the limitations of the biological system does not allow us to design a perfect experiment. All probes will experience a convolution of favorable and unfavorable interactions, and all probes will be unique. Electrostatic fields must therefore be explored from the perspectives of multiple probes, and information taken from the aggregation of the data.

We observed three general trends from the six probe locations studied here. The first was seen with N27C_{SCN} and N29C_{SCN}, which displayed the Rap-to-Ras reversion behavior caused by the double mutation Rap E30D/K31E. The absorption energy of this double mutant essentially matched that of Ras D30/E31, and in both cases was caused almost exclusively by the mutation K31E, not E30D. This is direct confirmation of hypotheses proposed from previous crystallographic and docking studies that the difference between Ras and Rap at these two positions leads to the functional discrimination these two GTPases have for different downstream effectors. The second observed trend was that of the double mutant displaying a difference in absorption energy that was simply the sum of the effect caused by the two single mutations. This was seen at positions K32C_{SCN} and N54C_{SCN}. This is strong experimental evidence that these mutations cause very little disruption in the docked complex, and experience additive changes in electrostatic field that can be measured by VSE spectroscopy of appropriately placed probes. However, it is important to study these effects from as many different probe locations as possible, because the third trend was less easily interpreted. For two probe locations, G28C_{SCN} and Y31C_{SCN}, while each single Rap mutation caused a large shift in vibrational absorption energy, the double mutant Rap E30D/K31E behaved essentially identically to Rap E30/K31. We have found no structural cause for this behavior. These residues may simply be unimportant for the formation of the Rap-Ral interface, and changes in electrostatic field measured by probes at these locations may not be correlated with changes in Rap-Ral interface formation.

In summary, this study demonstrates that while VSE spectroscopy is a useful tool for examining molecular-level mechanism of electrostatic events in complex biological systems, the convolution of distance, orientation, and change in determining the change in local electrostatic field actually experienced by the nitrile probe needs to be carefully interpreted. Observation of reversion behavior in the double mutant Rap E30D/K31E with the probes Ral β N27C_{SCN} and N29C_{SCN} strongly supports the role these two positions play in supporting an electrostatic mechanism of functional discrimination in GTPase-effector binding. Although these probe locations displayed the reversion mutation behavior that we were predicting when designing these experiments, the convolution of structure and sensitivity to mutations on the surface of Rap demonstrate that unambiguous measurement of electrostatic effects at the Rap-Ral interface will be difficult to achieve. Molecular dynamics sampling appears to be particularly useful in selection of appropriately placed VSE probes. Further experiments on WT and mutant Rap will be guided by extensive MD and continuum electrostatic calculations.

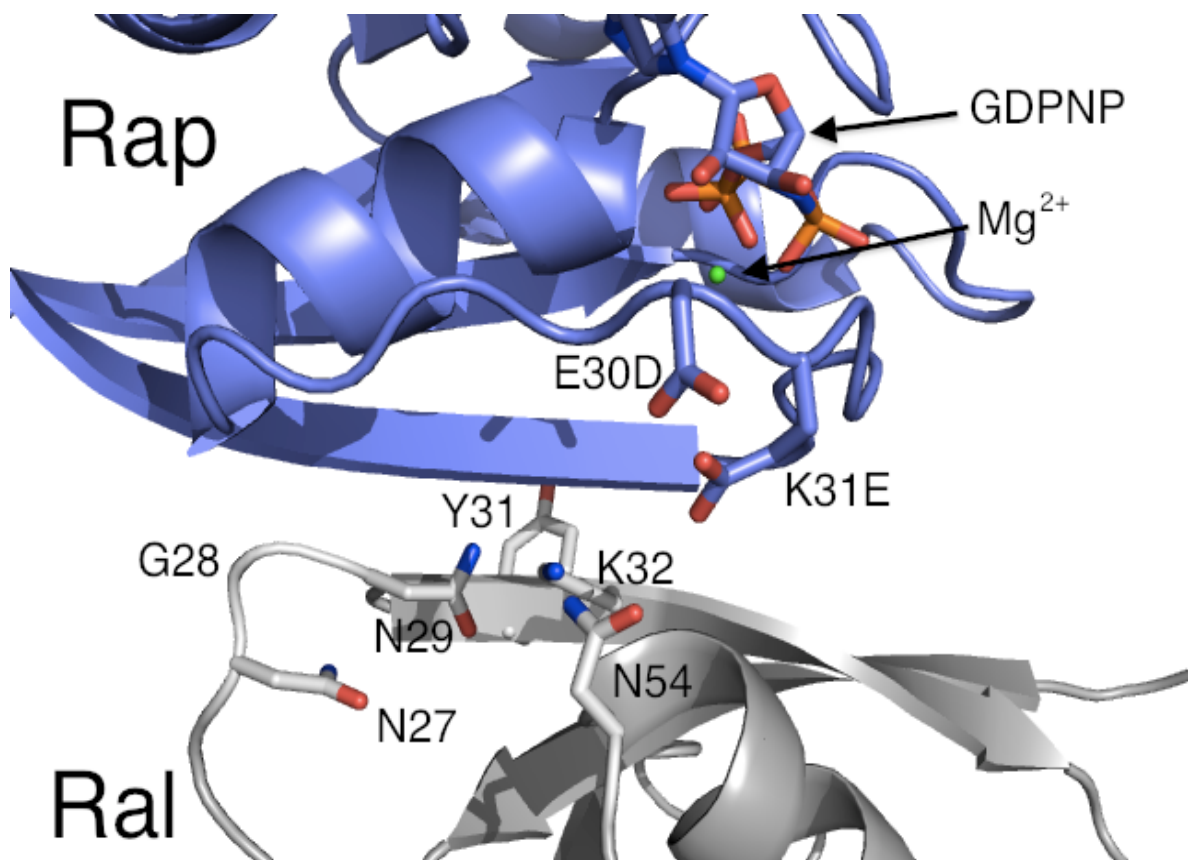


Figure 4-1: Rap-Ral Interface and Mutation Locations

The Rap (blue)-Ral (gray) interface, highlighting Rap E30D and K31E and six amino acids on Ral that were selected for positioning the thiocyanate VSE probe in this study. The figure was prepared by aligning Rap from 1GUA³⁹ (containing the mutations E30D/K31E) to Ras docked with Ral from 1LFD³⁷.

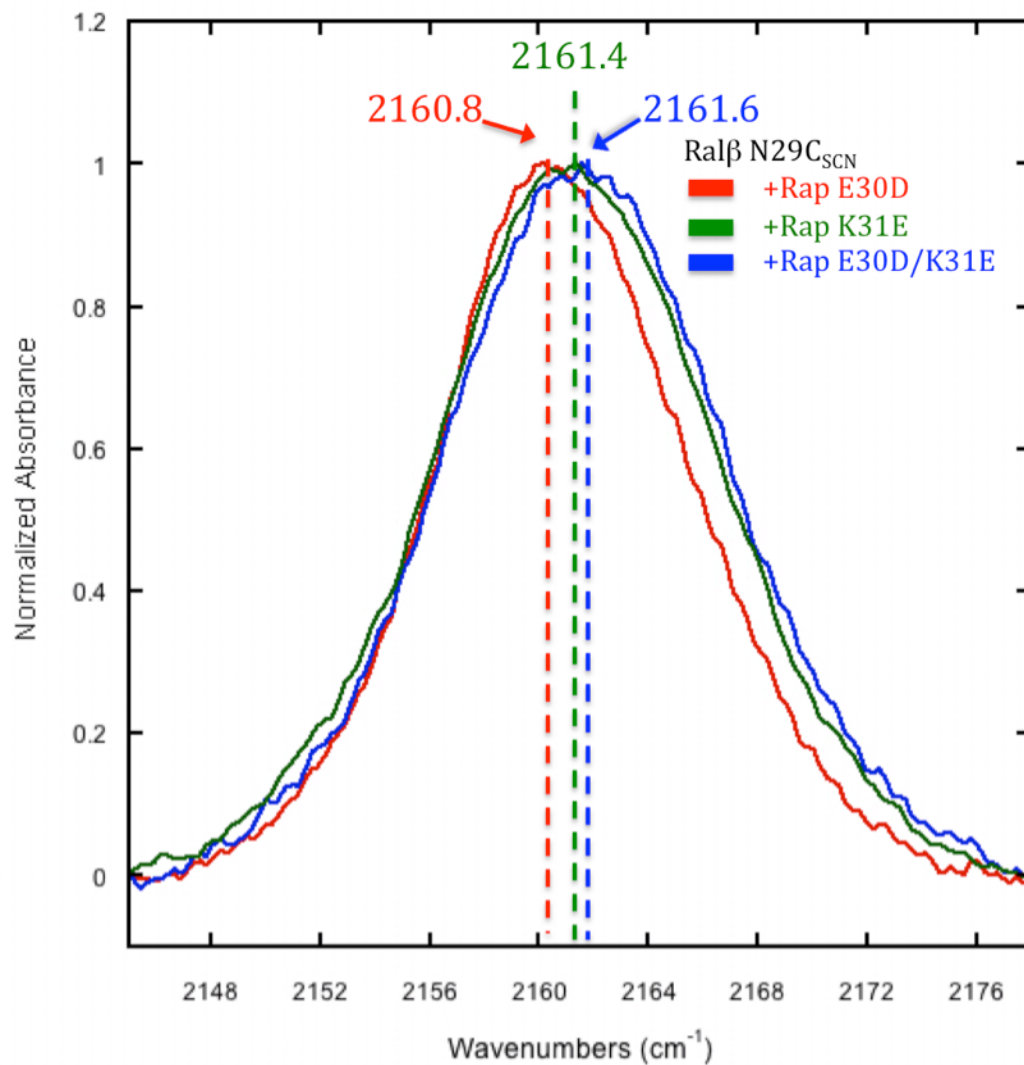


Figure 4-2: Representative Thiocyanate-labeled Protein Spectra

Normalized absorbance of thiocyanate on Ral β N29C_{SCN} measured when docked with Rap E30D (red, 2160.8 cm⁻¹), Rap K31E (green, 2161.4 cm⁻¹), and Rap E30D/K31E (blue, 2161.6 cm⁻¹).

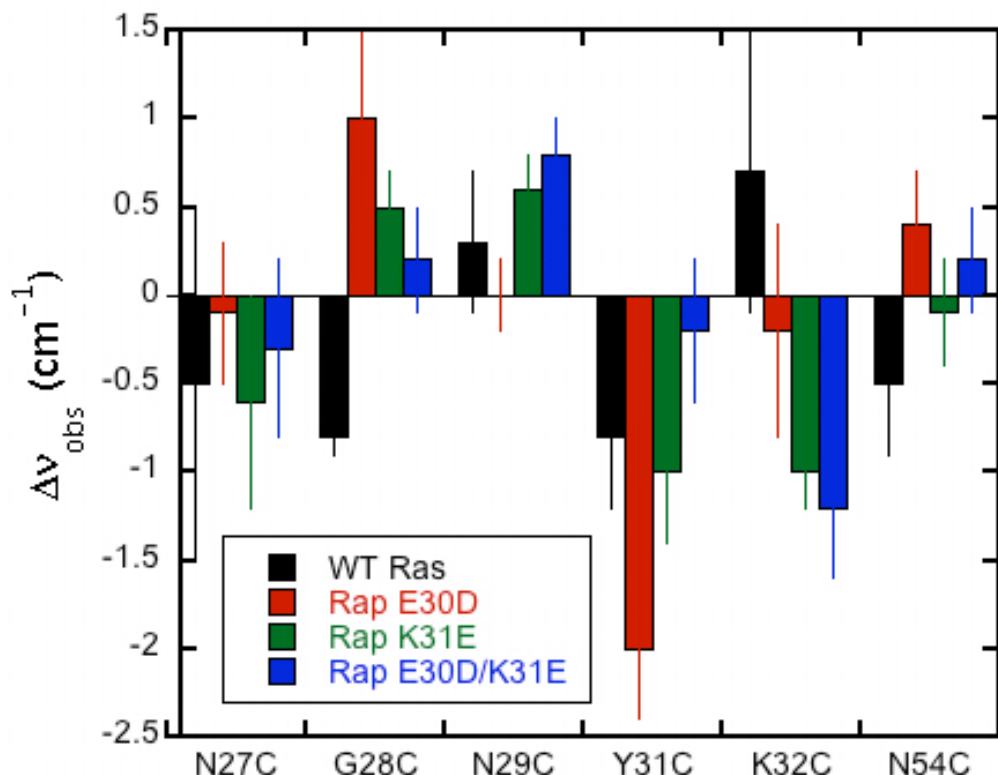


Figure 4-3: Change in Absorption Energy of Thiocyanate Probes Relative to Rap E30/K31

Change in absorption energy compared to WT Rap, Δv_{obs} , of a nitrile probe on SCN-labeled Ral β mutants when bound to WT Ras (blue), Rap E30D (red), Rap K31E (green), and Rap E30D/K31E (blue) where $\Delta v_{obs} = 0$ represents no change from the thiocyanate absorption energy when bound to WT Rap reported in Table 4-2. Error bars represent propagation of error of v_{obs} .

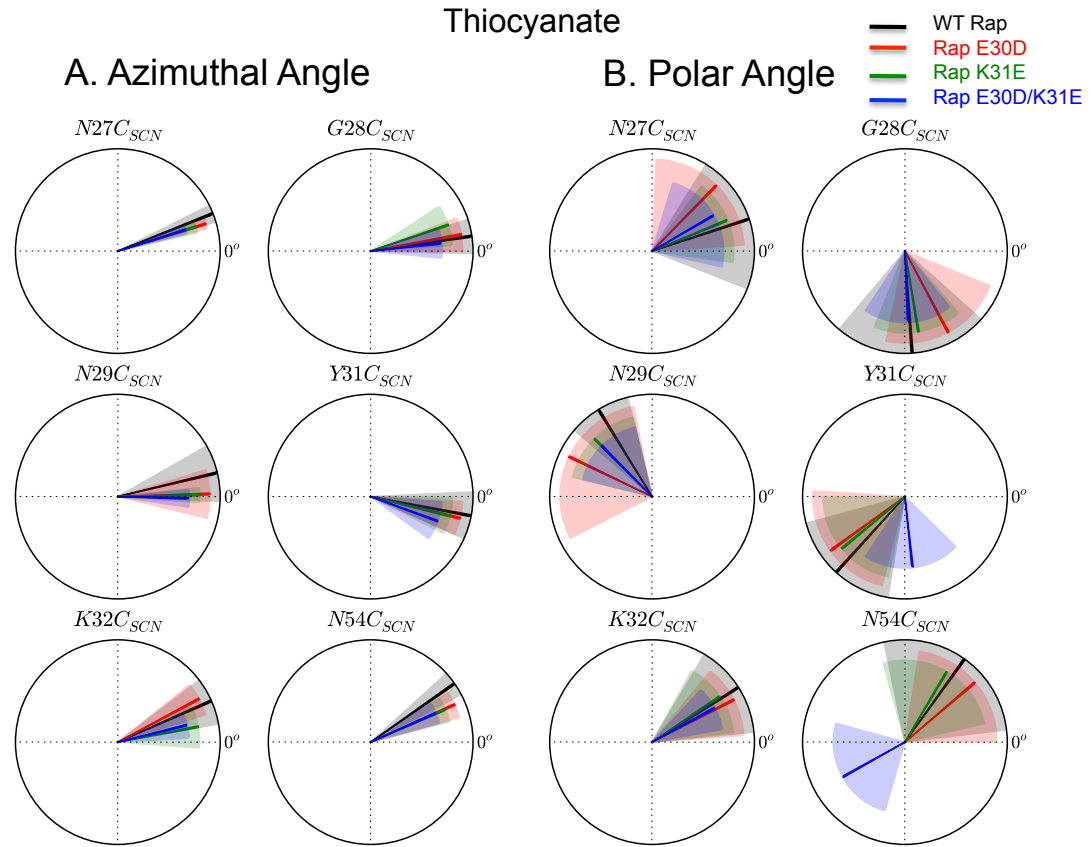


Figure 4-4: Azimuthal and Polar Angles of Simulated CNC Probes

(A) Azimuthal and (B) Polar angles of the thiocyanate on SCN-labeled Ral β mutants calculated from each mutant docked with Rap E30/K31 (black), Rap E30D/K31 (red), Rap E30/K31E (green), and Rap E30D/K31E (blue). Azimuthal angles are shown relative to the Rap-Ral β surface plane. Polar angles are shown relative to the coordinate system described in Figure 2-5B. The shaded area represents one standard deviation on the calculated angle from the Boltzmann-weighted ensemble of structures derived from Equation (2-12)***S6.

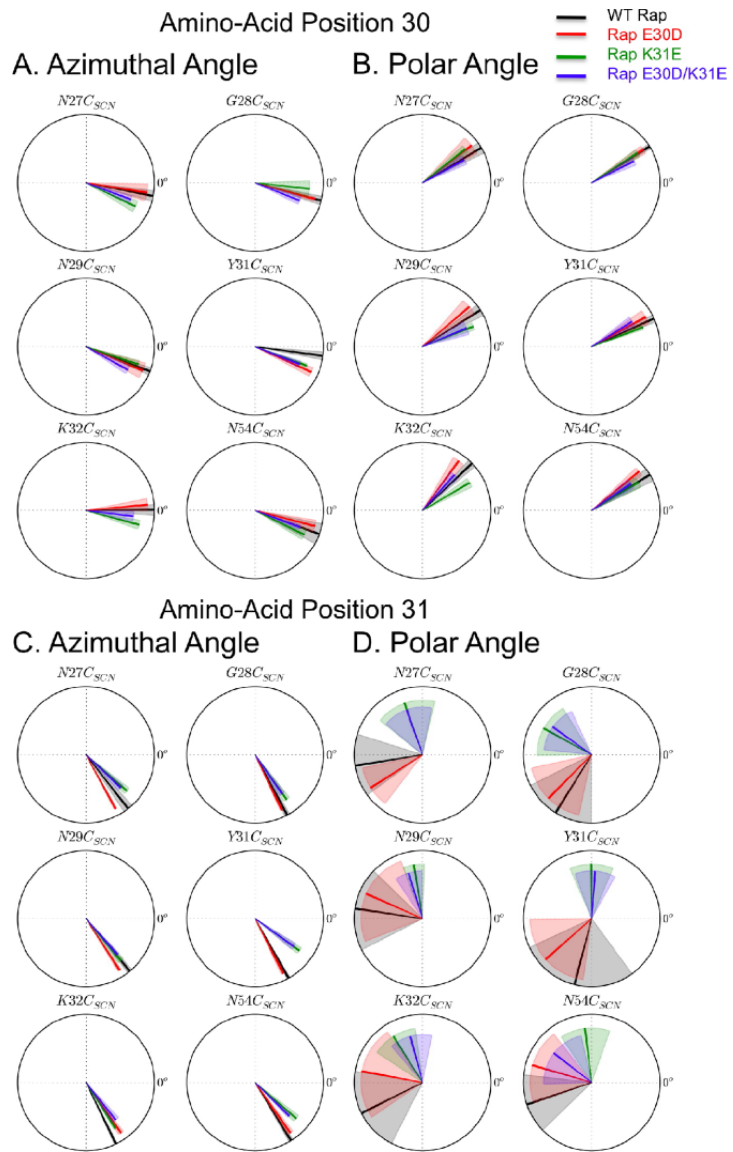


Figure 4-5: Azimuthal and Polar Angles of Simulated Rap Position 30 and 31 Sidechains

Azimuthal and polar angles of the side chain at Rap positions 30 and 31 in Rap E30/K31 (black), Rap E30D/K31 (red), Rap E30/K31E (green), and Rap E30D/K31E (blue). (A) Azimuthal angle at Rap position 30; (B) polar angle at Rap position 30; (C) azimuthal angle at Rap position 31; (D) polar angle at Rap position 31. Azimuthal angles are shown relative the Rap-Ral surface plane. Polar angles are shown relative to the

coordinate system shown in Figure 2-5. Dashed lines represent one standard deviation on the calculated angle from the Boltzmann-weighted ensemble of structures. ***Find better quality image

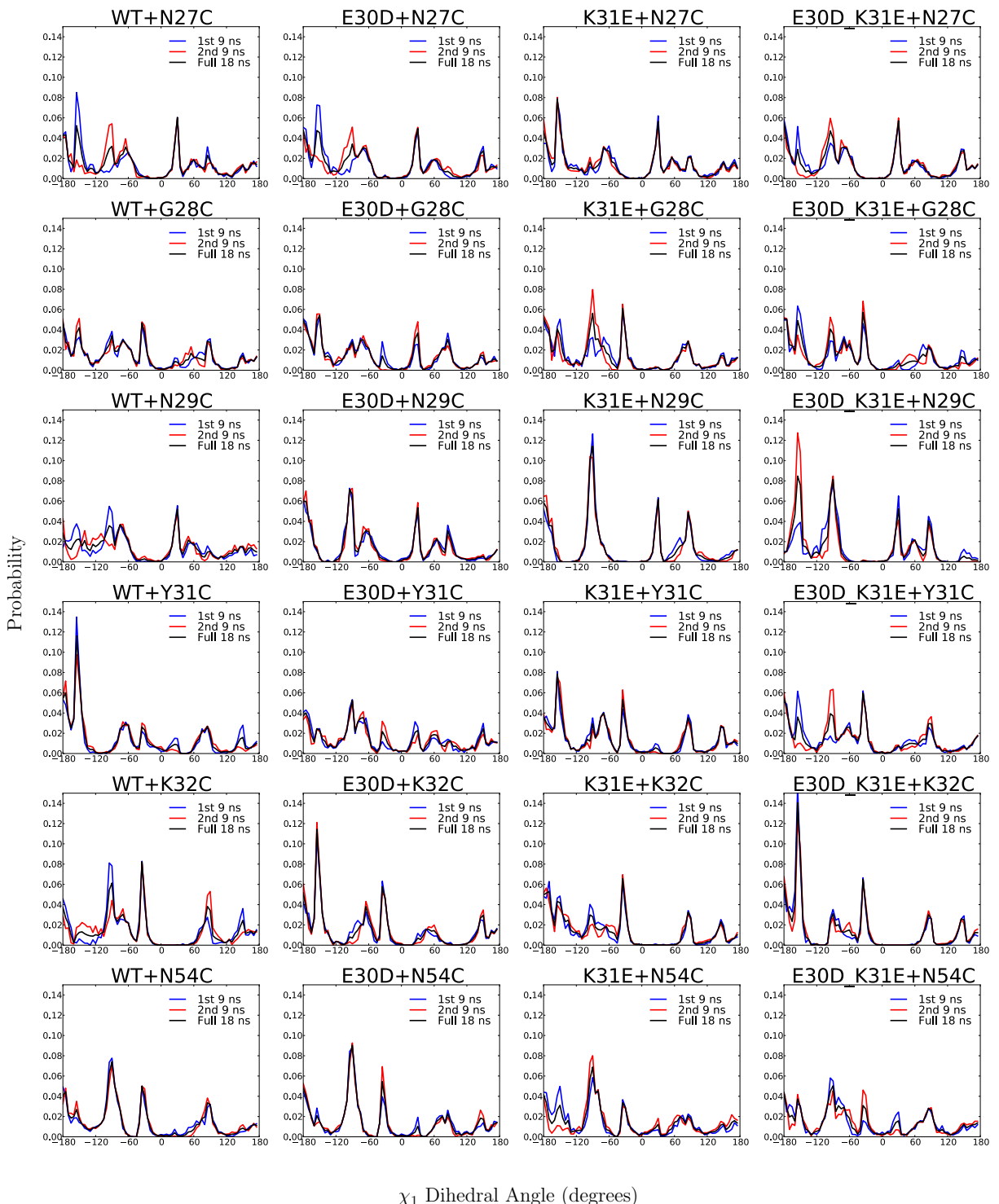


Figure 4-6: Convergence Test Based on CNC Dihedral Distributions

Probability distributions of the cyanocysteine χ_2 dihedral angle derived from WHAM of the first half (blue), second half (red), and total simulation time (black) for each Ral β mutant docked to WT Rap and each of its mutants.

Thiocyanate Dihedral Angles

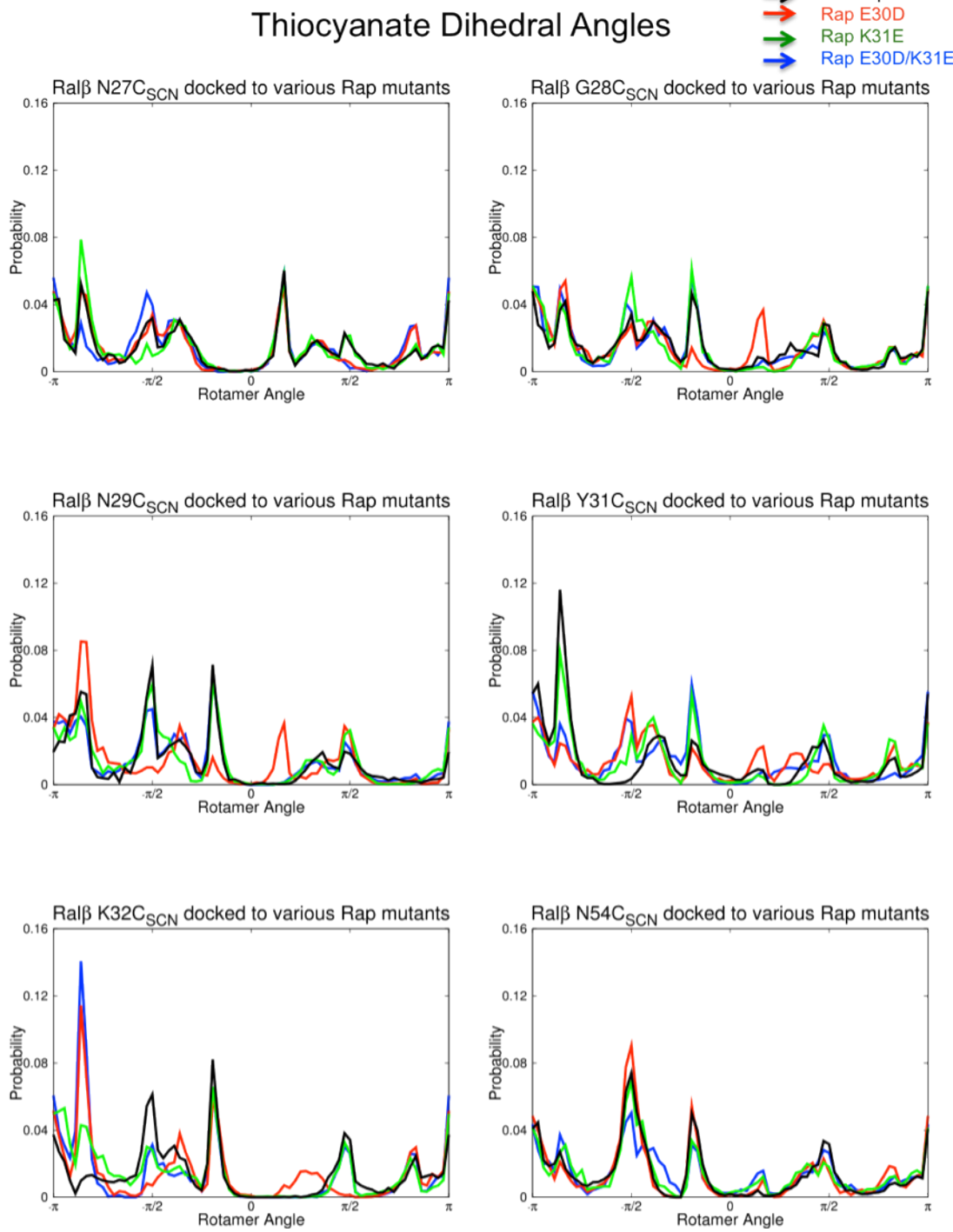


Figure 4-7: Thiocyanate Probability Distributions

Probability distributions, derived from WHAM, of the thiocyanate probe χ_2 dihedral torsion for SCN-labeled Ral β mutants docked with WT Rap (black), Rap E30D (red), Rap K31E (green), and Rap E30D/K31E (blue).

Residue 30 Dihedral Angles


 WT Rap
 Rap E30D
 Rap K31E
 Rap E30D/K31E

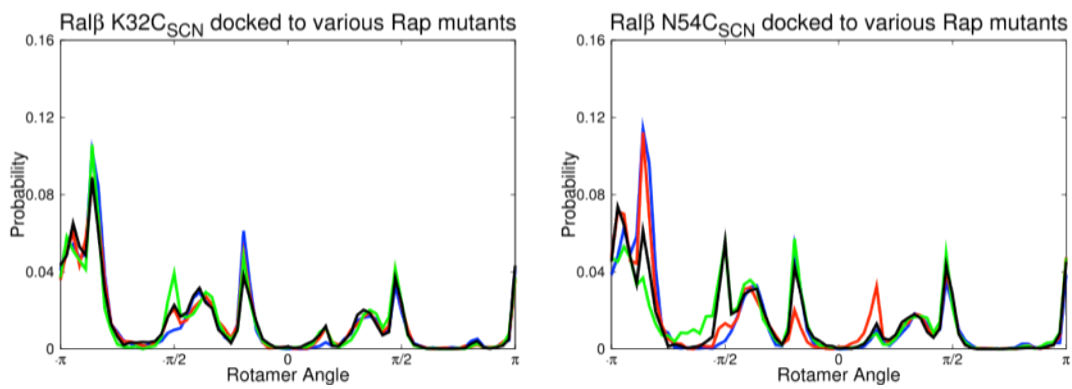
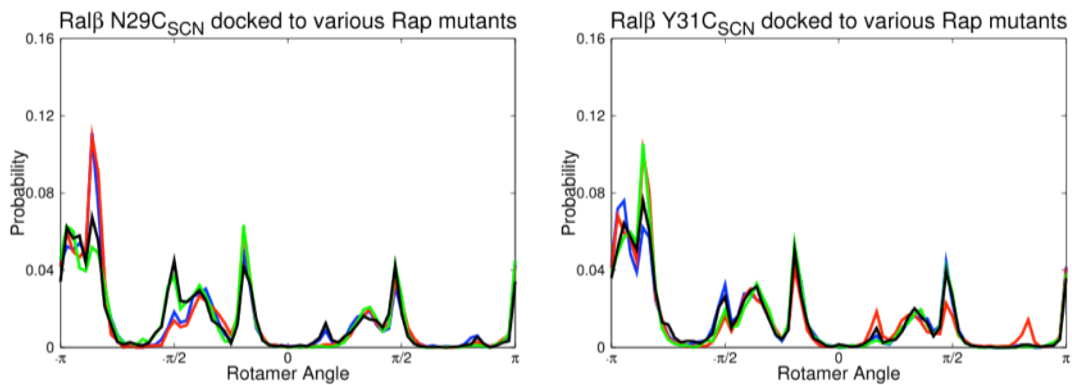
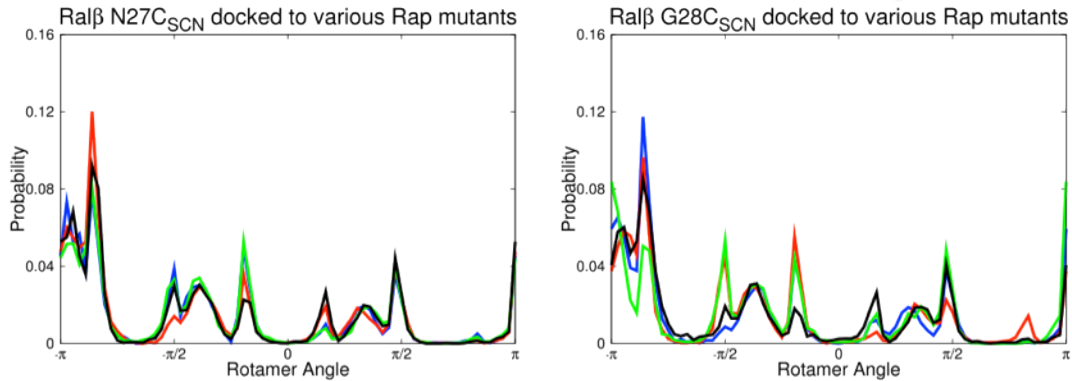


Figure 4-8: Rap Position 30 Dihedral Distributions

Probability distributions, derived from WHAM, of the side chain χ_1 dihedral torsion for Rap position 30 on SCN-labeled Ral β mutants docked with WT Rap (black), Rap E30D (red), Rap K31E (green), and Rap E30D/K31E (blue).

Residue 31 Dihedral Angles

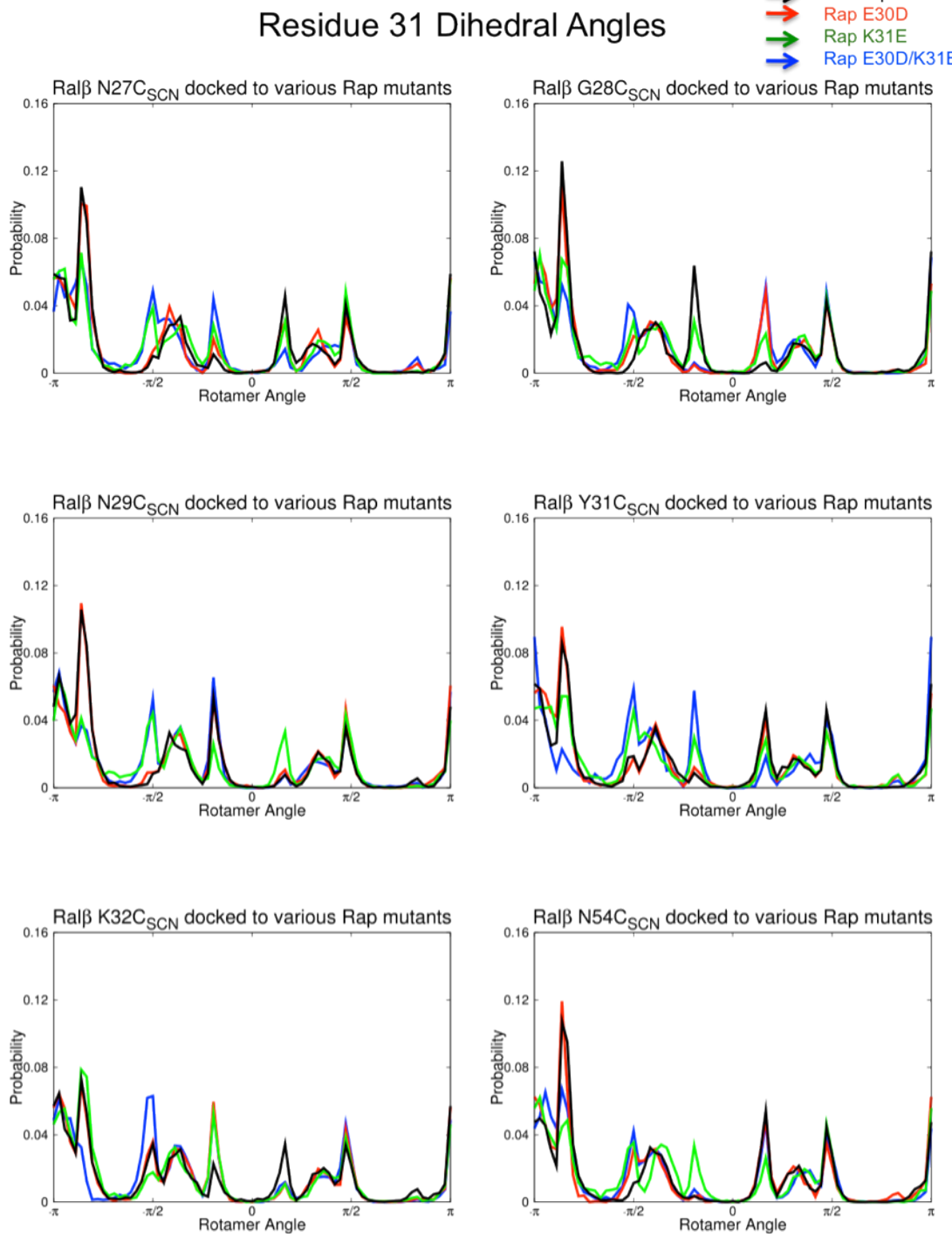


Figure 4-9: Rap Position 31 Dihedral Distributions

Probability distributions, derived from WHAM, of the side chain χ_1 dihedral torsion for Rap position 31 on SCN-labeled Ral β mutants docked with WT Rap (black), Rap E30D (red), Rap K31E (green), and Rap E30D/K31E (blue).

Table 4-1: Dissociation constant of the formation of docked complexes of SCN-labeled Ral β mutants with GTPases

GTPase	Ral β Mutation K _d (μ M)						
	WT	N27C _{SCN}	G28C _{SCN}	N29C _{SCN}	Y31C _{SCN}	K32C _{SCN}	N54C _{SCN}
Rap E30/K31	0.26 \pm 0.09	0.30 \pm 0.05	0.04 \pm 0.004	0.15 \pm 0.08	1.0 \pm 0.1	0.69 \pm 0.18	0.91 \pm 0.20
Ras D30/E31	1.4 \pm 0.2	7.3 \pm 2.2	4.8 \pm 1.1	3.1 \pm 0.6	12.9 \pm 4.8	6.0 \pm 2.3	4.7 \pm 0.4
Rap E30D	0.24 \pm 0.06	0.12 \pm 0.01	0.03 \pm 0.015	0.10 \pm 0.02	0.89 \pm 0.35	0.34 \pm 0.09	0.79 \pm 0.10
Rap K31E	1.8 \pm 0.7	2.9 \pm 0.7	8.1 \pm 1.5	6.0 \pm 1.1	6.2 \pm 2.0	1.9 \pm 0.8	2.2 \pm 1.5
Rap E30D/K31E	1.0 \pm 0.1	5.4 \pm 1.0	2.5 \pm 0.3	5.0 \pm 1.7	2.0 \pm 0.2	1.8 \pm 0.5	1.1 \pm 0.3

Table 4-2: Measured vibrational frequencies of SCN-labeled Ral β mutants docked with Rap E30/K31; the observed changes in vibrational frequency upon docking each probe to Ras D30/E31 and each Rap mutant

GTPase	$\tilde{\nu}$ (cm $^{-1}$)	Ral β Mutant					
		N27C	G28C	N29C	Y31C	K32C	N54C
Difference Compared to Rap E30/K31							
Ras D30/E31	$\Delta\tilde{\nu}$ (cm $^{-1}$)	-0.5 (1.0)	-0.8 (0.1)	0.3 (0.4)	-0.8 (0.4)	0.7 (0.8)	-0.5 (0.4)
	ΔF (MV/cm)	0.7 (1.4)	1.1 (0.1)	-0.4 (0.6)	1.1 (0.6)	-1.0 (1.1)	0.7 (0.6)
Rap E30D	$\Delta\tilde{\nu}$ (cm $^{-1}$)	-0.1 (0.4)	1.0 (0.5)	0.0 (0.2)	-2.0 (0.4)	-0.2 (0.6)	0.4 (0.3)
	ΔF (MV/cm)	0.1 (0.6)	-1.4 (0.7)	0.0 (0.3)	2.9 (0.6)	0.3 (0.8)	-0.6 (0.4)
Rap K31E	$\Delta\tilde{\nu}$ (cm $^{-1}$)	-0.6 (0.6)	0.5 (0.2)	0.6 (0.2)	-1.0 (0.4)	-1.0 (0.2)	-0.1 (0.3)
	ΔF (MV/cm)	0.9 (0.9)	-0.7 (0.3)	-0.9 (0.3)	1.4 (0.6)	1.4 (0.3)	0.1 (0.4)
Rap E30D/K31E	(cm $^{-1}$)	-0.3 (0.5)	0.2 (0.3)	0.8 (0.2)	-0.2 (0.4)	-1.2 (0.4)	0.2 (0.3)
	ΔF (MV/cm)	0.4 (0.7)	-0.3 (0.4)	-1.1 (0.3)	0.3 (0.6)	1.7 (0.6)	-0.3 (0.4)

Chapter 5 Optimizing Electrostatic Field Calculations with the Adaptive Poisson-Boltzmann Solver to Predict Electric Fields at Protein-Protein Interfaces I: Sampling and Focusing

5.1 INTRODUCTION

Electrostatic interactions are an important force in all biological macromolecules, influencing fundamental processes such as protein folding, ligand binding, signal transduction, macromolecular interactions, and more.⁹⁶⁻¹⁰⁸ Experimental measurement of electrostatic forces in biomolecules is a difficult and long-standing problem in biophysics, and so electrostatic effects on numerous biological structures and processes are usually investigated *in silico* through a variety of computational strategies. Many computational techniques exist for quantitatively predicting the strength and direction of biomolecular electrostatic fields, such as combined quantum mechanical / molecular mechanics (QM/MM) calculations,^{17, 18, 29, 109-111} the protein dipole-Langevin dipoles (PDLD) method of Warshel and Levitt,⁶ the continuum Poisson-Boltzmann (PB) model,^{46, 62, 65, 66, 68, 112-116} and Coulomb potentials using both fixed-charge⁴² and polarizable force fields.^{13, 68, 97, 117-121} All of these methods vary tremendously in their physical basis, scope, computational expense, and application.

Within this diverse set of computational strategies, PB approaches have become common for addressing electrostatic questions of importance across many areas of biophysics and biochemistry because they are quick, easy to implement, and have a low barrier to application both in technical difficulty and in infrastructure requirements.⁶³

Solutions to the LPBE are now used extensively throughout biophysical and biochemical studies to evaluate important protein properties such as free energy of ligand binding¹²²⁻¹²⁴ or protein-protein docking.¹²⁵⁻¹²⁷ However, it has been difficult to bridge

theoretical electrostatic calculations with experimental considerations by validating the results of the LPBE with direct experimental measurements of electrostatic fields in biomolecules. Attempts to do this have often relied on experimental observables that are indirectly related to the electrostatic environment, such as ^{19}F resonance studies, pK_a titrations,^{69, 128-133} or isothermal titration calorimetry,¹³⁴⁻¹³⁷ making quantitative interpretation of purely electrostatic effects difficult.⁸⁶ Because of this, there is an important need for new data sets that measure electrostatic fields directly and against which the results of different electrostatics calculation strategies can be compared and contrasted.

Our laboratory has approached this difficulty by using vibrational Stark effect spectroscopy (VSE)^{73, 75-77} to measure electrostatic fields in proteins directly. We have applied VSE spectroscopy to nitrile vibrational probes placed throughout the protein-protein interface of Ras-like guanosine triphosphatases (GTPases) docked with downstream effector protein domains. The Ras superfamily of GTPases, which have over 150 variants in human cells,¹³⁸ plays a significant role in a number of different signal transduction cascades in healthy cells.⁸⁰ The human oncoprotein p21^{Ras} (hereafter “Ras”) and a related GTPase, Rap, share 50% amino acid identity,³⁹ 80% amino acid homology, and have a RMSD of 0.7 Å, and yet show significant differences in their binding specificity to their respective downstream effector proteins *in vitro*.^{35, 87-89} It has been postulated by our laboratory that due to their large structural similarities, these functional differences are due to electrostatic interactions at the docked protein-protein interface. Our laboratory has investigated this hypothesis with VSE spectroscopy, and several publications have provided an extensive set of experimental data against which to compare the results of electrostatic calculations.^{35, 43}

In the experimental work previously done in our laboratory, a thiocyanate probe has been introduced to the Rap downstream effector RalGDS through site-directed mutagenesis of the labile cysteine side chain and subsequent chemical labeling to the nitrile-containing cyanocysteine side chain,⁷² and VSE spectroscopy has been used to measure electrostatic fields in the docked Rap-RalGDS construct.^{35,43} We have focused on the thiocyanate probe for these experiments because it has a large difference dipole moment or Stark tuning rate, $\Delta\bar{\mu}$, ($0.77 \text{ cm}^{-1}/(\text{MV cm}^{-1}) = 1.99 \text{ cm}^{-1}/(\text{k}_b\text{T/e}\text{\AA})$), absorbs in an unpopulated region of the infrared spectrum (typically $2100\text{-}2300 \text{ cm}^{-1}$), and is small, minimizing perturbations to the probed system.⁷³ The difference in vibrational absorption energies of the nitrile probe on the surface of RalGDS in the docked complexes was compared to that on the monomeric protein to obtain an experimental value of $\Delta\tilde{v}$ in equation (3-14). Because $\Delta\bar{\mu}$ is parallel to the nitrile bond axis, the dot product is equal to the scalar product and equation (3-14) is simplified to equation (5-1):

$$\Delta E = hc\Delta\tilde{v} = -\Delta\bar{\mu}\Delta\vec{F} \quad (5-1)$$

These experimental data provide a unique opportunity to test the predictions from electrostatic computational strategies, including LPBE methods, by attempting to reproduce the observed vibrational energy shifts due to the binding of RalGDS to the GTPase Rap and rationalizing the successes and failures of these attempts based on the physics of the system and the capabilities of the calculation. This system therefore serves as a tool for comparing our computational methods to experimental results.

Previous computational work examining the electrostatic interactions of Ras docked to RalGDS has been done in our laboratory using two electrostatic methods: Coulomb interactions with explicit waters⁴² and the implicit solvent, continuum-model LPBE.⁷⁰ To solve the LPBE, we chose to use the Adaptive Poisson-Boltzmann Solver (APBS) software package.¹⁰² APBS is a Poisson-Boltzmann equation solver which can

use both multigrid^{65, 66} and finite-element methods^{139, 140} to solve the PB equation, and has been widely used for solvation free energy calculations.^{6, 115} It is highly tunable, well documented, easy to use, free, and has the active and continuing support of a development community to ensure reliability and reproducibility of results.¹⁴¹ Furthermore, APBS has already been successfully integrated with the AMOEBA polarizable force field for solvation free energy calculations, and is being used in our laboratory to test the benefits of polarizable *versus* point-charge force fields.⁶⁸

Work in our group has previously used APBS to test the reliability of LPBE solutions for predicting experimental vibrational spectroscopy data on Ras docked to nitrile-labeled RalGDS mutants.^{35, 42} These studies employed a two-stage focusing strategy where an initial calculation on a large box filled with a coarse grid (“first stage”) provides the boundary conditions for a second calculation within a smaller box filled with a significantly finer grid (“second stage”).¹⁰⁶ We have shown that decreasing the second stage calculation box sizes and increasing grid density led APBS calculations to converge to a particular numerical value for an individual structure.⁷⁰ This work raised two outstanding questions that are the subject of the current investigation: 1) what is the most productive focusing strategy available for balancing accuracy of the results with time and resources used; and 2) what computational strategy provides the most accurate results for both absolute vibrational absorption energies measured on both the monomeric RalGDS surface and the docked Rap-RalGDS construct. To address these questions, in the current report we are using a recently published data set in which nitrile-labeled RalGDS constructs were bonded both with WT Rap and three Rap mutants, E30D, K31E, and E30D/K31E, that had been generated to revert the function of Rap to that of the structurally similar but functionally distinct GTPase Ras.⁴³ Apart from addressing the questions stated above, this also presents an opportunity to test APBS against an entirely

new data set based on VSE experiments, to determine the generality of our observations and conclusions.

To address our first question, in the work reported here we have focused primarily on the two smallest boxes and the two highest grid densities previously tested: a 19^3 \AA^3 box with either 193 and 161 grid points in each dimension, and a 10^3 \AA^3 box with either 193 and 161 grid points in each dimension. We have also looked at larger boxes with lower grid density to determine whether a high-resolution field at the bond vector was more or less important than explicitly considering a larger number of protein atoms in the second stage calculation. This was done with a $30 \text{ \AA} \times 45 \text{ \AA} \times 40 \text{ \AA}$ box and a $60 \text{ \AA} \times 45 \text{ \AA} \times 40 \text{ \AA}$ box, each with approximately 0.25 \AA between grid points in each dimension. Increasing the grid density of the larger boxes to match the finest grid spacing of the smaller boxes requires more than a 100-fold increase in memory and almost 100-fold increase in the number of processors, as estimated by the psize.py utility included with APBS. Because of this increase in computational cost and the large number of structural frames in which we need to solve the LPBE, we chose to limit the resolution of the 30 \AA and 60 \AA box calculations.

To address our second outstanding question, determining methods that give the most accurate results for both absolute and difference measurements, we have studied the effect of the location of the second stage box to investigate whether decreasing the volume of the box occupied by implicit solvent would have a significant impact on the quality of the calculations. To solve the Poisson-Boltzmann equation to determine an electrostatic potential, APBS divides the system into distinct dielectric regions, based on the atom positions and the van der Waals radii of the atoms and solvent molecules. The high dielectric region is defined as the total region in which spheres with the radius of the solvent (H_2O) molecules exist without overlapping with the van der Waals radii of the

explicit (protein) molecules. All other space is considered part of the low dielectric system. This creates a discontinuity in the dielectric at the protein-solvent high dielectric-low dielectric interface.⁶² Setting aside that fact that dielectric is a macroscopic property that is a function of atomic polarizabilities, and thus fails to capture the local molecular environment within a region of the protein, we wanted to examine whether trying to minimize the surface area of this discontinuity in the calculation could be an easy and reproducible way to improve the accuracy of our results when compared to experiment. To do this we translated the second stage box away from the solvent to define three unique box locations: 1) centered on nitrile C₈; 2) translated toward the center of mass of the system; and 3) translated toward the center of mass of the RalGDS protein. In all cases, the volume of the box filled with explicit protein atoms was quantified and compared to the accuracy of the results, tested against our experimental data.

Additionally, we have compared the numeric result of the LPBE to the result obtained by taking the negative gradient of the numeric solvent reaction field potential (SRF), shown in equation (3-5) (where $\phi(\vec{r})$ is the potential, $\epsilon_{protein}$ is the protein dielectric and, and $\epsilon_{solvent}$ is the solvent dielectric), and adding the analytic Coulomb protein field, shown in equation (3-2) (where ϵ_0 is the permittivity of free space, $\epsilon_{protein}$ is the protein dielectric, q_i is the charge on atom i , \vec{r}_i is the vector from atom i to the location of interest, and \hat{r} is the unit vector of \vec{r}_i), projected along the bond vector at a dielectric of 2, hereafter referred to as the reaction field method.²⁷

In the reaction field method, the LPBE is solved twice for each frame. The first term in equation (3-5) is the numeric solution to the LPBE equation and the second term is the numeric solution of the LPBE in a reference dielectric. Taking the difference, the numeric, low-resolution protein field is removed, leaving the only low-resolution

electrostatic potential due to solvent. By using the exact analytic field due to protein atom partial charges with the low-resolution SRF, errors due to grid spacing and potential mapping to the dummy atoms should be reduced.

Many crystal structures of the GTPase-downstream effector docked complex have generated consensus on the structure of the WT Rap-WT RalGDS interface. However, the protein constructs employed in our experiments contain a number of small perturbations to these WT molecules (mutations to Rap and thiocyanate VSE probes on RalGDS) for which there is no structural data. Because of this, it is necessary for these differences in the molecular structure of the protein-protein interface to be modeled with molecular dynamics (MD) simulations to determine structural changes in the system due to the probe, mutations, and protein-protein docking. Furthermore, other studies looking at electrostatic effects have shown that allowing for structural reorientation improves the reliability of these sorts of calculations—not surprising for experimental data collected in a steady-state ensemble.^{95, 142, 143} In our previous simulations, a single degree of freedom, the χ_2 dihedral angle (shown in Figure 5-1), was biased in an enhanced MD sampling strategy to generate a Boltzmann-weighted statistical ensemble of structures. This was a logical choice for determining the orientation of the nitrile bond vector within the protein-protein complex in order to calculate the magnitude and direction of $\Delta\vec{F}$ through equation (3-14). However, close examination of the structures generated during these simulations revealed that the χ_2 probability distributions were functions of the χ_1 dihedral angle (Figure 5-1), and potentially sensitive to the χ_1 angle in the starting structure. Furthermore, examination of the structures revealed that the χ_1 dihedral was relatively fixed at a single local minimum over the course of a 3 ns simulation. This observation is not unreasonable; umbrella sampling of χ_2 was used to allow the probe to visit energetic states that have high transition barriers in that degree of freedom and thus have a low

probability of being observed over the course of an unenhanced MD simulation, but would not effectively sample other important degrees of freedom. In light of this, we decided to test a two-dimensional umbrella sampling technique to obtain probabilities as a function of χ_1 and χ_2 , and compare to previous results based on one-dimensional sampling. The goal of this work was to find an algorithm of MD sampling followed by Poisson-Boltzmann calculations that adequately reproduced our experimental data.

In the work reported here, electrostatics calculations using a continuum-solvent model were done for six nitrile-labeled RaIGDS proteins both in a monomeric state and when docked to each of four Rap constructs using APBS. We 1) investigated the effects of different box locations relative to the probe site and 2) compared numeric solutions to the LPBE to the reaction field method to optimize the accuracy of the calculations in APBS. To model structural fluctuations, one- and two-dimensional umbrella sampling was used to generate an ensemble of structures, appropriately weighted based on the potential of mean force landscape in the appropriate number of dimensions. We have determined that APBS is a viable strategy for calculating electrostatic fields in proteins using the reaction field method as well as for comparing changes in electrostatic fields to changes in vibrational absorption frequencies using the numeric solutions. Quantitative correlation between absolute values of the numeric LPBE calculations to experiments may be increased by careful consideration of second-stage box locations when using a two-stage focusing strategy, but in the reaction field method the second-stage box should be centered on the point of interest.

5.2 RESULTS AND DISCUSSION

5.2.1 Molecular Dynamics Sampling

One of the central challenges in any dynamic system, such as the protein-protein complexes investigated here, is determining the most important degrees of freedom relevant to the experimental observables and then sampling them appropriately and completely. Previous work in this laboratory has consistently observed that in the one-dimensional umbrella sampling of the cyanocysteine χ_2 dihedral angle, the χ_1 dihedral of the side chain very rarely moved more than a few degrees. There are two possible reasons for this observation: 1) the system had a significant preference for the starting χ_1 dihedral over all other possibilities; or 2) the system had insufficient time and energy to transition to another χ_1 dihedral with any significant probability. To test for the first possibility, the χ_1 dihedral angles of the six probes on the RalGDS monomers (as well as three additional probe sites not previously mentioned, I18C_{SCN}, R20C_{SCN}, and S33C_{SCN}) were rotated to different expected minima based on the alkane-like structure of the side chain, and sampled again. The results were similar to all previous observations; the new χ_1 dihedral remained fixed and did not explore alternative alkane-like values. This result suggested that the second possibility is correct. To overcome this, we turned to two-dimensional sampling of both χ_1 and χ_2 in our MD simulations. Figure 5-2 shows a representative log-scale probability distribution for RalGDS N27C_{SCN} and RalGDS N54C_{SCN} in the monomeric form (Figure 5-2A and B) and docked to Rap E30D/K31E (Figure 5-2C and D), and Figure 5-3 shows the log-scale probability distributions for all 30 structures sampled. The gauche-regions of an alkane-like molecule were found to have low probabilities of being populated in both degrees of freedom, while the staggered-regions of an alkane-like molecule, at 60°, 180°, and -60°, had a high probability of being sampled. Additionally, there was not a single, dominant χ_1 angle for

all probe sites; multiple χ_1 angles were found with similar probabilities. Finally, the two-dimensional distribution was the product of two one-dimensional alkane-like distributions. These observations strongly support the use of two-dimensional sampling over one-dimensional sampling to completely explore reasonable probe orientations by revealing that the barrier between minimum energy regions is sufficiently large that, in reasonable timescales, an insignificant number of transitions will occur to represent the nitrile probes' orientations about the amide backbone accurately with sampling only one degree of freedom.

The one-dimensional χ_2 dihedral probability distributions, shown in Figure 5-4, were also compared to the two-dimensional dihedral probability distributions integrated over χ_2 , shown in Figure 5-5. In general, while they both display alkane-like structure with high probability of being found at 180° , 60° , and -60° , the one-dimensional distributions were more prone to having regions of expected-high probability being under- or over-represented. Two examples of this are the 60° rotamer of Rap E30D/K31E docked to RalGDS Y31C_{SCN} and the -60° rotamer of WT Rap docked to RalGDS Y31C_{SCN}. It is not immediately clear whether those specific rotamers are actually improbable, or if they are just improbable for the chosen χ_1 dihedral angle. By examining the two-dimensional dihedral distributions, however, it becomes clear that the former was merely underrepresented in the chosen χ_1 , while the latter truly is improbable given adequate sampling. In summary, using a two-dimensional sampling strategy allows a greater degree of certainty that observed features are real and not artifacts of a relevant, unexplored degree of freedom.

Increasing the number of degrees of freedom in a simulation typically involves an exponential increase in simulation time. Since we are not looking for rare transition-state structures and instead want a representative ensemble where high-

probability conformations exceed low-probability conformations by at least six orders of magnitude, we have only performed a three-fold increase in the length of the simulation. This was sufficient to ensure that low probability regions only represented a small fraction of the overall statistical distribution, and thus did not need to be fully sampled to generate an accurate Boltzmann-weighted ensemble average.

An additional criterion of structural convergence was used based on our LPBE-based calculations of the electrostatic field at the nitrile midpoint. No matter how reliable the accuracy of these calculations are compared to experimental data (the subject of extensive discussion below), the magnitude of the calculated field at the midpoint of the nitrile bond should converge on a single value as the MD structural ensemble converges on the highest probability structures. To test this, an updated probability distribution was calculated for every $n\Delta t$, where $\Delta t = 0.72$ ns and n is an integer from 1 to 80 (the total number of frames for a given trajectory), to determine the probability distribution as a function of simulation time. This was then used with the calculated numeric PBE field values to determine the Boltzmann-weighted average electrostatic field as a function of simulation time. This is shown in Figure 5-6. In all simulations, the field stopped changing significantly relative to the standard deviation after the first half of the simulation, indicating that each additional time step is not significantly altering the average field, and an adequate simulation time has been achieved.

5.2.2 Calculation of absolute electrostatic fields

APBS solves the LPBE by mapping force field potentials to discrete grid points inside a sample box defined by the user by means of box dimensions, grid spacing, and location. These parameters therefore play a significant role in the values of calculated electrostatic fields. Here we have examined two 19^3 Å³ boxes with a GS of 0.119 Å/grid

point and 0.099 Å/grid point, two 10^3 Å³ boxes with a GS of 0.062 Å/grid point and 0.052 Å/grid point, a 30 Å x 45 Å x 40 Å box with a GS of (0.234, 0.234, 0.250) Å/grid point, and a 60 Å x 45 Å x 40 Å box with a GS of (0.234, 0.234, 0.250) Å/grid point. As a reminder, boxes will be referred to as the 10 Å box, 19 Å box, 30 Å box, and 60 Å box, respectively.

Box positions were adjusted in order to minimize the volume of the box filled with the high-dielectric continuum (solvent) and maximize the volume filled with protein atoms. Table 5-1 shows the Boltzmann-weighted average of the percent of the box volume filled by protein atoms, treated as spheres with radii equal to their Amber99 van der Waals radii, for the NC δ box strategy in the left column, and the change relative to the NC δ box for RalGDS center of mass and system center of mass in the right two columns. From Table 5-1, it is clear that shifting the box towards the center of mass of RalGDS (RalGDS center of mass) universally increased the percentage of the box filled with protein atoms. In some cases this change was by a factor of two or more, such as for probe sites G28C_{SCN}, Y31C_{SCN}, N54C_{SCN}, which showed an average increase in the volume of the box filled with protein atoms of 82.3% from NC δ .

Figure 5-7 and Figure 5-8 show the calculated fields for the six probes on the RalGDS monomer and the six probes on RalGDS docked to WT Rap, respectively, compared to the experimental frequencies measured by Ragain *et al.* Results for RalGDS-based probes docked with Rap E30D, K31E, and E30D/K31E are shown in Figure 5-9, Figure 5-10, and Figure 5-11. In each figure, the top row shows the 60 Å box, the middle row the 19 Å box, and the bottom row the 10 Å box. The grid spacing (GS) values are listed in the row titles. The left column shows the results obtained from the numeric solutions to the LPBE and the right column shows the results obtained from the reaction field method. Colors indicate which box center the data describes: red

($\text{NC}\delta$), green (system center of mass), blue (RalGDS center of mass), or black (system center of mass; 60 Å boxes only). In Figure 5-7, results for the system center of mass are excluded because they are identical to the RalGDS center of mass on the nitrile-containing RalGDS monomers. The correlation coefficients between the calculated absolute field projected along the bond vector, in $k_b T/e\text{\AA}$, and the experimental vibrational absorption energy, in cm^{-1} , are listed in the corresponding colors in the bottom-left corners. Numeric PBE absolute fields (left) and numeric PBE relative fields (right) for the 161 grid point calculations the 30 Å box are shown in Figure 5-12, Figure 5-13, Figure 5-14, and Figure 5-15. The 161 grid point calculations and the 30 Å box are either worse than or not appreciably different results from the 193 grid point calculations or the 60 Å box calculations, and therefore are not the topic of any further discussion. The error bars have been excluded for clarity, with the vibrational absorption standard deviations ranging from 0.0 to 1.04 cm^{-1} and the calculated field standard deviations ranging from 1.2 to 8.2 $k_b T/e\text{\AA}$.

Numeric solutions to the LPBE

The left columns of Figure 5-7, Figure 5-8, Figure 5-9, Figure 5-10, and Figure 5-11 show the calculated fields obtained by taking the numeric solutions to the LPBE. In general, the 60 Å box for the numeric PBE fields cannot reliably replicate experimental results. It is possible that if the large box had a grid spacing comparable to the 19 Å or 10 Å boxes, correlation could increase; however, that would require an increase in memory usage and number of processors by approximately two orders of magnitude, and thus was not tested. The 19 Å boxes with coarse and fine grid spacing were fairly insensitive to box location, so further discussion about box location will be directed at the 10 Å boxes (bottom left) only.

From Figure 5-7, Figure 5-8, Figure 5-9, Figure 5-10, and Figure 5-11, calculations conducted in the RalGDS center of mass box had the highest correlation to experimental data, while system center of mass, with the exception of the undocked monomer (since system center of mass and RalGDS center of mass are the same), is consistently either approximately the same as NC δ (E30/K31-Figure 5-8; E30/K31E-Figure 5-10) or significantly worse (E30D/K31-Figure 5-9; E30D/K31E-Figure 5-11). The most striking example of the effect of changing the position of the box was seen for the RalGDS monomer in Figure 5-7, which has a correlation coefficient absolute value less than 0.2 for the NC δ calculation, but a correlation coefficient absolute value greater than 0.6 in the RalGDS center of mass/system center of mass calculation.

Examining the nitrile-containing RalGDS mutants docked with Rap E30/K31 (Figure 5-8), the correlation with experiment was approximately the same for system center of mass as for NC δ , while there was a significant increase for the RalGDS center of mass box location. These results can be justified by the data in Table 5-1, which shows that in most cases, shifting the box towards the system center of mass did not substantially increase the volume of the box occupied by protein, with only G28C_{SCN} showing more than a 50% increase in occupied volume compared to NC δ . As a whole, system center of mass only increased the volume of the box occupied by protein atoms by 30.8%, while RalGDS center of mass more than doubled that with an average of 64.5% increase from NC δ .

The correlation between the absolute field calculation and the measured vibrational absorption energy on the nitrile-labeled RalGDS monomers and on the WT Rap-RalGDS docked complex clearly increased as the volume of the box occupied by protein atoms increased. When nitrile probes were placed throughout the Rap mutants-RalGDS interface, the results were less straightforward. For example, Rap E30D/K31

(Figure 5-9) showed a decrease in correlation for the system center of mass strategy, which only has an average increase in percent of the box volume occupied of 19.6%. Many of the probes showed very little increase in percent box volume occupied, and in fact some showed a small decrease by moving the box. In the RalGDS center of mass strategy, the volume increases by 45.0% relative to NC δ , yet there is only a small increase in correlation in the coarser 0.062 Å/grid point GS and a small decrease in correlation in the finer 0.052 Å/grid point GS strategy. In Rap E30/K31E (Figure 5-10) and E30D/K31E (Figure 5-11), the RalGDS center of mass strategy increased the percent volume occupied by protein atoms by 47% and 54% respectively, yet also showed a decrease in correlation, relative to NC δ , in the finest grid calculations.

To summarize, increasing the percent of the second-stage box explicitly filled with protein atoms by moving the focusing center away from the object of interest can be both beneficial and deleterious to the accuracy of the calculation. On one hand, it may increase the correlation to experiment by focusing on a location as remote as possible from the boundary between low and high dielectric media. However, occasionally moving the focusing box may also cause the loss of information that is vital to the calculation of the electrostatic field by shifting atoms previously treated explicitly in the second-stage calculation outside of the box, where they are treated implicitly as a contribution to the boundary condition. Ensign *et al.*⁴² previously showed that in a similar system, Ras bound to various thiocyanate-labeled RalGDS, different probe locations were most sensitive to different contributions to the electrostatic field—solvent, charges on other RalGDS amino acids, charges on Ras, etc. Here, no consideration was given to how translating the box affected which protein atoms were inside the box, only that the nitrile stayed within the confines. In the monomer, losing nearest-neighbor residues was unlikely; the protein can be adequately described as a sphere with the probe

on the surface, and translating a cubic box towards the center of mass of a sphere would not remove nearby residues from the second-stage calculation. In the docked complexes, however, moving the box towards the system center of mass would move it away from RalGDS and thus remove nearby residues on RalGDS, while moving towards the RalGDS center of mass would move it away from Rap and thus remove nearby residues on Rap. In these cases, the loss of important, nearby residues partially or entirely negates the benefit of removing part of the dielectric discontinuity. Increasing the amount of protein in the box does not automatically help the calculation if, in doing so, the most important parts of the system are removed from the calculation. The selection of a focusing strategy and location must therefore be considered carefully when using focusing in these contexts, and the most ideal focusing strategy will most likely be unique to the chemical identity of the system under investigation and the desired information.

Reaction field method solutions to the LPBE

The right column of Figure 5-7, Figure 5-8, Figure 5-9, Figure 5-10, and Figure 5-11 show the calculated fields obtained by using the reaction field method solutions to the LPBE. In general, there is no appreciable difference between the box sizes or GS used; all perform comparably well. This is not a particularly surprising result given the primary contribution to the electrostatic field (magnitudes $\geq 600 k_b T/e\text{\AA}$) should be the protein atoms and not the SRF (magnitudes $\leq 10 k_b T/e\text{\AA}$).

From Figure 5-7, Figure 5-8, Figure 5-9, Figure 5-10, and Figure 5-11, calculations in the NC δ box showed either the highest correlations (Monomer-Figure 5-7; E30/K31-Figure 5-8, E30/K31E-Figure 5-10) or comparable correlations (E30D/K31-Figure 5-9, E30D/K31E-Figure 5-11) to the system center of mass and the RalGDS center of mass. Because the exact analytic protein field was used in these calculations,

only the SRF is affected by changing the box location. In this regard, these calculations are less sensitive to moving atoms from inside to outside the second-stage box than in the numeric PBE fields. Moving the box, regardless of how it affects the percent volume of the box occupied by atoms, does not improve the correlation to experiment. The best results were obtained by centering the second-stage box on the location of interest *or* by using a box large enough to include the entire protein, such as the 60 Å box used here.

Comparing the numeric solutions of the LPBE to the reaction field method solutions of the LPBE

On the one hand, the 60 Å box performed significantly better in the reaction field method when using the numeric PBE solutions. Using the NC δ box, the reaction field also nearly always reproduced experimental results better than the numeric PBE solutions. On the other hand, intelligently changing the second-stage box location can cause the numeric solutions to outperform the reaction field (monomer-Figure 5-7; E30/K31-Figure 5-8, E30/K31E-Figure 5-10). Given the unreliability of predicting how changing the box location will alter the correlation with experiment previous discussed, we conclude that the most consistent, reliable method for calculating protein electrostatic fields is to use the reaction field method and a high grid point density near the location of interest.

5.2.3 Calculations of relative electrostatic field

The VSE experiment defined by equation (5-1) compares changes in electric fields around the probe, $\Delta\vec{F}$, to changes in the absorption energy of that probe, $\Delta\nu$. Because of this, the we can make a direct comparison between computational predictions and experimental results is obtained from the difference in results between the docked Rap-RalGDS complex and the monomeric RalGDS. Figure 5-16 shows the change in the

calculated electric field versus change in absorption frequency due to docking the SCN-labeled RalGDS mutant to WT Rap, formatted identically to the previously presented figures. Figure 5-17, Figure 5-18, and Figure 5-19 show the change in calculated fields versus the change in absorption frequencies for RalGDS docked to Rap E30D, Rap K31E, and Rap E30D/K31E respectively.

Numeric relative field solutions to the LPBE

There are three interesting features in numeric Δ fields (left) in Figure 5-16 that are also present for the other Rap constructs. The first and most pronounced is the increase in correlation between experiment and calculation upon subtracting the monomer field and frequencies values compared to any of the absolute field calculations. Almost universally, the correlation to experiment increased in the difference calculations compared to the results of the absolute calculation, even when including information from data sets with poor correlation to begin with, such as the NC δ monomer calculations (Figure 5-7) or the system center of mass Rap E30D/K31E calculations (Figure 5-11). This was even true for the 19 Å boxes, which showed no significant improvement on moving the center of the box. This suggests that errors introduced into the absolute calculations, either from non-physical effects included in the LPBE or important physical effects excluded from consideration, cancel out reliably well in the difference calculations. The absolute calculations manage to capture some degree of the physics of the system and can be improved by logical decisions about the position and size of the calculation box, but taking the difference calculation significantly improves the correlation to experimental results.

The second interesting feature is the significant improvement in correlation seen in the 19 Å boxes compared to the absolute calculations. In the absolute calculations

(Figure 5-7, Figure 5-8, Figure 5-9, Figure 5-10, and Figure 5-11), the 19 Å boxes had very poor correlations to experiment compared to the absolute calculations (typically $|r| \leq 0.4$), and could not be noticeably improved by changing the size or location of the calculation box. In the difference calculations, however, the calculated correlations ranged from $r = 0.628$ (NC δ Rap E30D-Figure 5-7) to 0.843 (RalGDS center of mass Rap E30D/K31E-Figure 5-19). When these results are compared to the smallest and largest magnitude correlation coefficients for the 10 Å box of 0.283 and 0.916 (RalGDS center of mass and NC δ respectively for Rap E30D-Figure 5-7), it is apparent that although the smaller boxes have the possibility for a higher correlation to experiment, the larger boxes are still quite good. The 19 Å boxes are also significantly less sensitive to box position than the 10 Å boxes, discussed previously and shown in Figure 5-7, Figure 5-8, Figure 5-9, Figure 5-10, and Figure 5-11, suggesting that the large box would be ideal to use when computational time is short or expensive, since refining the box position is fairly insignificant and the correlations in the difference calculation are still comparable to or occasionally better than the 10 Å boxes. In general, correlations between the changes in fields compared to the changes in frequencies are consistently higher than the correlations for the absolute calculations and less sensitive to the specific Rap mutant.

The 10 Å boxes, however, are still significantly more sensitive to the box position than the 19 Å boxes. There is no general “best” box location, however, and for different Rap constructs, different box positions yield the highest correlation. On average, however, NC δ > system center of mass > RalGDS center of mass, which is very unlike the absolute field calculation’s hierarchy of RalGDS center of mass > NC δ > system center of mass. This is further evidence that very careful consideration about the position of multiple-state boxes is necessary when designing LPBE strategies.

The third interesting feature comes from examining the 60 Å boxes, which showed a greater correlation with experiment than in the previous, absolute field calculations for RalGDS bound to Rap E30/K31 (Figure 5-7). In fact, the 60 Å boxes only show an increased correlation with experiment in the E30/K31 (Figure 5-16), E30D /K31(Figure 5-17), and the double Rap mutant E30D/K31E (Figure 5-19) upon subtraction of the monomer-field, which is inconsistent with the observation that correlations are better when examining the differences between systems. This is likely due to the coarseness of the calculation resulting in too few grid points in the proximity of the bond vector to interpolate a potential along. For example, the coarsest 19 Å box calculation had a grid GS of 0.119 Å, while the 60 Å boxes have a GS of approximately 0.25 Å. This means that, in the best-case-scenario where the bond lies exactly parallel to one of the box sides, the number of grid points to interpolate a potential from for each of the 10 dummy atoms is fewer than the number of dummy atoms by nearly a factor of four (CN bond length is approximately 1.14 Å). Since the field is related to the gradient of the potential, a coarser GS gives an average field over a larger area, and thus resulting in a coarser field.

Reaction field method relative fields

The right columns of Figure 5-16, Figure 5-17, Figure 5-18, and Figure 5-19 show the calculated change in field, computed using the reaction field method, compared to the experimental change in field of the nitrile-labeled RalGDS upon docking to the various Rap constructs. As in the absolute field calculations, the box size and GS were largely irrelevant and the NC δ box locations gave the highest correlation to results. However, with the exception of Rap E30D/K31E (Figure 5-19), all correlations for the

difference calculations were lower than the absolute field correlations. We did not observe the sort of cancellation of error observed using the numeric solutions.

Comparing relative fields calculated from the numeric method to the reaction field method

In all cases of the NC δ box locations, the numeric method relative correlations are better than the reaction field method relative correlations. Regardless of correlation in the absolute calculations, the numeric method gives changes in fields that are well correlated to experiment, indicating that the sources of error in the absolute calculations being subtracted are also being subtracted, i.e.: the cause of low correlation in the NC δ monomer (Figure 5-7) and the cause of low correlation in the NC δ Rap K31E (Figure 5-10) are due to the same source of systematic error in the calculation, which is removed upon subtracting the two values. This is contrary to the reaction field method, where the cause of low correlation in the NC δ monomer (Figure 5-7) is in no way related to a cause of a magnitude of correlation less than one in NC δ Rap K31E (Figure 5-10), and no such subtraction of error occurs.

A reasonable hypothesis is the source of error is the low-resolution of the numeric solutions, which is removed upon taking the difference in the numeric solutions. In the reaction field method, however, there is a LPBE numeric solution term, $F_{reference}^{(2)}$, added back to the final answer:

$$\begin{aligned}
 F_{numeric} &= F_{protein} \\
 F_{reaction\ field} &= F_{protein} - F_{reference} + F_{Coulomb} \\
 \Delta F_{numeric} &= F_{protein}^{(2)} - F_{protein}^{(1)} \\
 \Delta F_{reaction\ field} &= F_{protein}^{(2)} - F_{reference}^{(2)} + F_{Coulomb}^{(2)} - \left(F_{protein}^{(1)} - F_{reference}^{(1)} + F_{Coulomb}^{(1)} \right) \quad (5-2) \\
 \Delta F_{reaction\ field} &= +F_{protein}^{(2)} - F_{protein}^{(1)} - F_{reference}^{(2)} + F_{reference}^{(1)} + F_{Coulomb}^{(2)} - F_{Coulomb}^{(1)} \\
 \Delta F_{reaction\ field} &= \Delta F_{numeric} - F_{reference}^{(2)} + F_{reference}^{(1)} + F_{Coulomb}^{(2)} - F_{Coulomb}^{(1)}
 \end{aligned}$$

In equation (5-2), the superscripts indicate the index of the system, $F_{protein}$ is the field obtained from the numeric solution to the LPBE with $\epsilon_{interior} \neq \epsilon_{exterior}$, $F_{reference}$ is the field obtained from the numeric solution to the LPBE with $\epsilon_{interior} = \epsilon_{exterior}$, and $F_{Coulomb}$ is the analytic Coulomb field due to the force field charges on the protein atoms. As the final line of equation (5-2) clearly shows, the $\Delta F_{reaction\ field}$ includes the numeric field as well as additional terms that include two low-resolution LPBE solutions. It may be that error removed in the $\Delta F_{numeric}$ term is reintroduced by the two $F_{reference}$ terms. In short, the best results are obtained from a single subtraction between a single pair of LPBE solutions, as in the absolute fields from the reaction field method and in the relative fields in the numeric PBE method.

It should be noted that other works have demonstrated the importance of water in the nitrile stretching mode,¹⁰⁹ which we appear to have treated in an entirely implicit manner when calculating electrostatic fields. This is not entirely true, because we treated the water explicitly in the MD sampling procedure. Hydrogen bonding with the nitrile nitrogen can lead to carbon-nitrogen bond length changes as well as increased stability of hydrogen-bonding probe orientations, which is accounted for in the MD electrostatic force calculations during sampling. Orientation stabilizations are included in our WHAM PMF while bond-length changes are included in the structural information used in electrostatic calculations. So although we have implicit solvent in our APBS electrostatic calculations, solvent effects on the nitrile vibrational frequency are not ignored.

Table 5-1: Percent Volume of Second-Stage APBS Box Filled with Protein Atoms

Probe/Construct	Volume (% of box)		$\Delta(\text{Volume})$ (% of box) ^a			
	NC δ		system center of mass - NC δ		RaLGDS center of mass - NC δ	
	10 Å	19 Å	10 Å	19 Å	10 Å	19 Å
N27C _{SCN} /Monomer	42 ± 4	39 ± 3	30 ± 5	39 ± 4	-- ^b	-- ^b
G28C _{SCN} /Monomer	24 ± 3	22 ± 2	29 ± 4	39 ± 4	-- ^b	-- ^b
N29C _{SCN} /Monomer	63 ± 3	52 ± 2	22 ± 4	33 ± 3	-- ^b	-- ^b
Y31C _{SCN} /Monomer	36 ± 3	39 ± 3	31 ± 4	44 ± 4	-- ^b	-- ^b
K32C _{SCN} /Monomer	45 ± 3	47 ± 2	34 ± 3	34 ± 3	-- ^b	-- ^b
N54C _{SCN} /Monomer	28 ± 3	30 ± 2	30 ± 4	35 ± 3	-- ^b	-- ^b
N27C _{SCN} /WT	32 ± 3	32 ± 2	15 ± 5	30 ± 3	30 ± 4	36 ± 4
G28C _{SCN} /WT	27 ± 3	34 ± 3	20 ± 4	33 ± 4	28 ± 4	34 ± 4
N29C _{SCN} /WT	65 ± 3	70 ± 2	6.4 ± 3.7	9.1 ± 2.5	20 ± 4	17 ± 3
Y31C _{SCN} /WT	49 ± 2	60 ± 2	21 ± 3	23 ± 3	24 ± 4	22 ± 3
K32C _{SCN} /WT	63 ± 2	80 ± 1	4.6 ± 3.3	1.1 ± 1.8	14 ± 3	6.5 ± 1.9
N54C _{SCN} /WT	38 ± 3	48 ± 3	2.5 ± 4.2	24 ± 3	32 ± 4	31 ± 3
Y31C _{SCN} /E30D	80 ± 3	64 ± 2	-0.66 ± 3.75	13 ± 2	5.9 ± 3.6	26 ± 3
N27C _{SCN} /E30D	28 ± 3	37 ± 2	19 ± 4	34 ± 3	21 ± 4	28 ± 4
G28C _{SCN} /E30D	55 ± 3	59 ± 3	9.3 ± 4.1	19 ± 4	24 ± 4	25 ± 4
N29C _{SCN} /E30D	46 ± 3	56 ± 2	20 ± 4	22 ± 3	27 ± 4	27 ± 3
K32C _{SCN} /E30D	63 ± 2	80 ± 1	-0.9 ± 3.16	1.1 ± 1.7	16 ± 3	5.5 ± 1.7
N54C _{SCN} /E30D	44 ± 2	45 ± 2	-4.0 ± 3.6	27 ± 3	26 ± 4	33 ± 3
N27C _{SCN} /K31E	39 ± 3	42 ± 3	20 ± 5	30 ± 4	30 ± 5	39 ± 4
G28C _{SCN} /K31E	35 ± 3	42 ± 3	25 ± 5	34 ± 4	20 ± 5	28 ± 4
N29C _{SCN} /K31E	56 ± 3	68 ± 2	3.6 ± 4.5	10 ± 2	23 ± 4	19 ± 3
Y31C _{SCN} /K31E	51 ± 3	62 ± 2	25 ± 4	22 ± 2	15 ± 4	17 ± 3
K32C _{SCN} /K31E	72 ± 2	84 ± 1	3.5 ± 3	-0.51 ± 1.89	5.6 ± 3	3.3 ± 1.9
N54C _{SCN} /K31E	26 ± 2	32 ± 2	-7.0 ± 3.3	29 ± 3	18 ± 4	29 ± 3
N27C _{SCN} /E30D K31E	40 ± 4	41 ± 3	16 ± 6	25 ± 4	30 ± 5	35 ± 4
G28C _{SCN} /E30D K31E	32 ± 3	42 ± 3	26 ± 4	36 ± 4	18 ± 4	25 ± 3
N29C _{SCN} /E30D K31E	62 ± 3	70 ± 2	3.8 ± 3.7	13 ± 3	19 ± 4	19 ± 3
Y31C _{SCN} /E30D K31E	42 ± 3	54 ± 2	21 ± 5	22 ± 3	26 ± 5	26 ± 4
K32C _{SCN} /E30D K31E	74 ± 3	78 ± 1	-6.7 ± 3.3	0.21 ± 1.86	14 ± 3	11 ± 2
N54C _{SCN} /E30D K31E	36 ± 2	41 ± 2	10 ± 3	28 ± 3	28 ± 4	34 ± 3

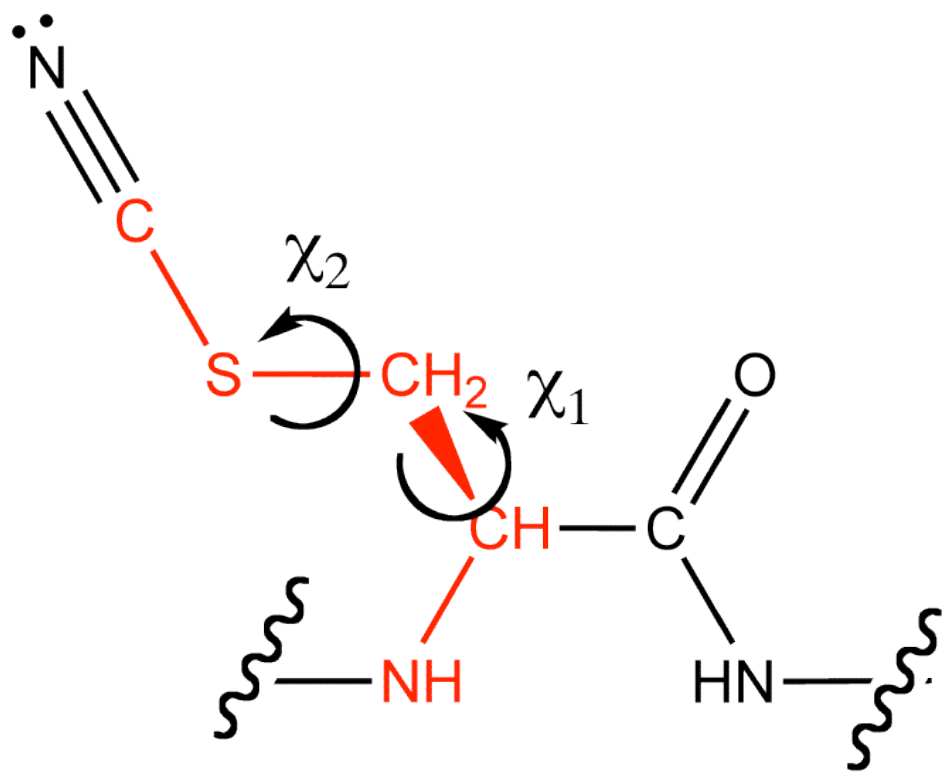


Figure 5-1: Cyanocysteine Sidechain Dihedral Definitions

The thiocyanate probe, with the χ_1 and χ_2 rotation axes highlighted and the atoms involved shown in red. The χ_1 dihedral angle is defined as the dihedral of the $\text{N-C}\alpha\text{-C}\beta\text{-S}\gamma$ atoms. The χ_2 dihedral angle is defined as the dihedral of the $\text{C}\alpha\text{-C}\beta\text{-S}\gamma\text{-C}\delta$ atoms.

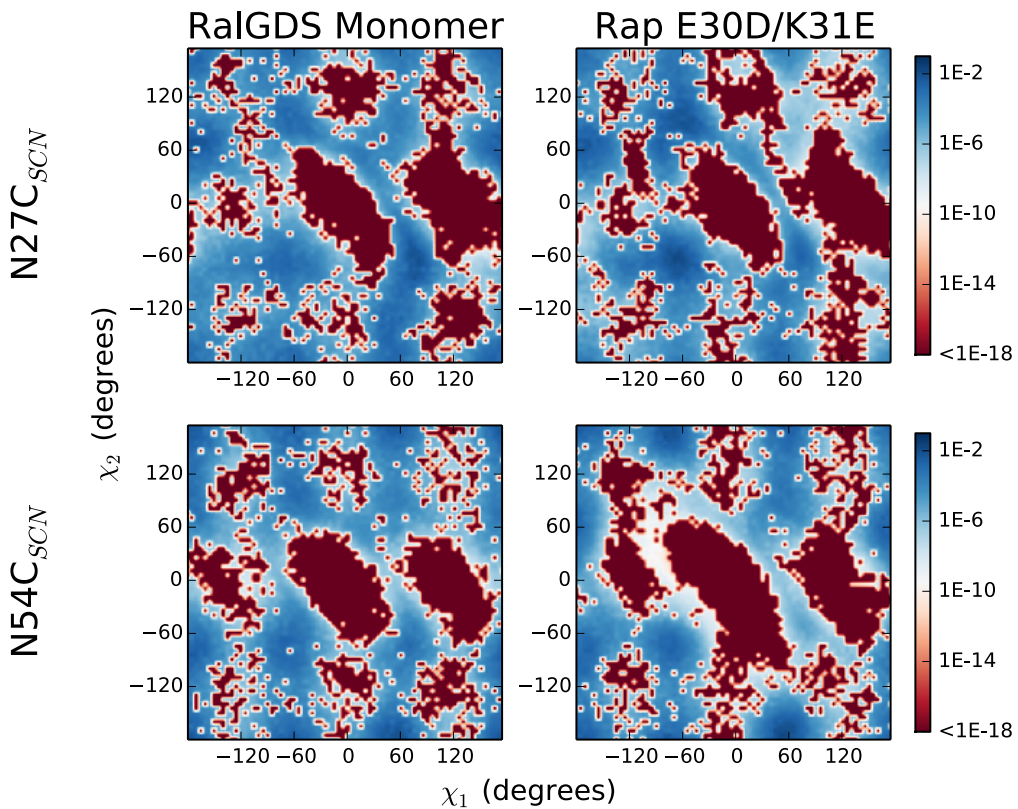


Figure 5-2: Representative 2D Dihedral Probability Distributions

A representative two-dimensional probability distribution for $\text{N}27\text{C}_{\text{SCN}}$ (top row) and $\text{N}54\text{C}_{\text{SCN}}$ (bottom row) in the monomeric state (left column) and bound to Rap E30D/K31E (right column). On the x-axis is the χ_1 dihedral angle and on the y-axis is the χ_2 dihedral angle. The log scale shown on the right allows easy visualization of lower-probability states.

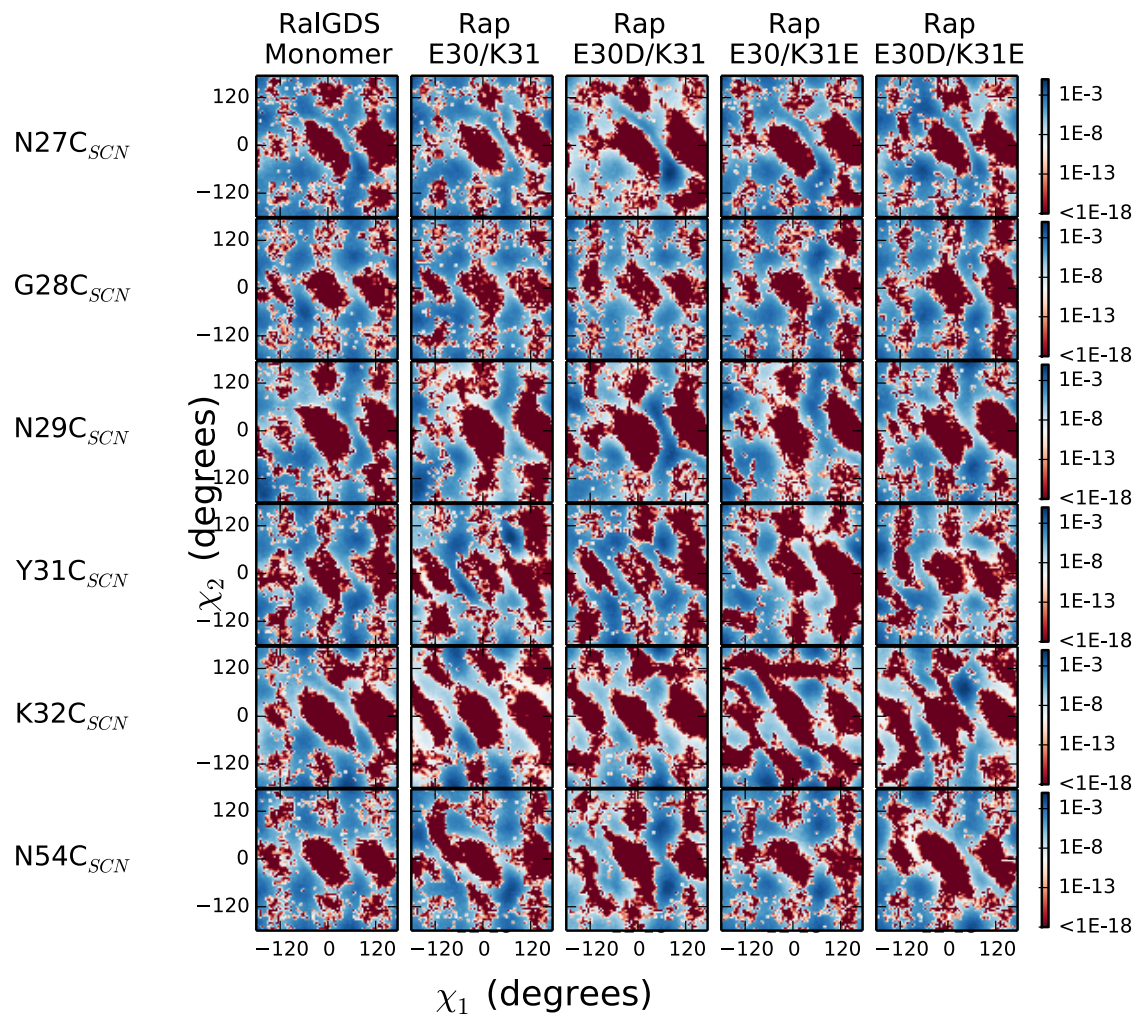


Figure 5-3: 2D Dihedral Probability Distributions

Two-dimensional probability distribution of the six probes on monomeric RalGDS and docked to the various Rap constructs. On the x -axis is the χ_1 dihedral angle and on the y -axis is the χ_2 dihedral angle. Each row represents an individual nitrile-labeled RalGDS mutant (identified to the left of the figure) either in a monomeric form or docked with a Rap construct (identified on the top of the figure). The log scale shown on the right allows easy visualization of lower-probability states.

χ_2 Probability Distributions from 1-Dimensional Umbrella Sampling

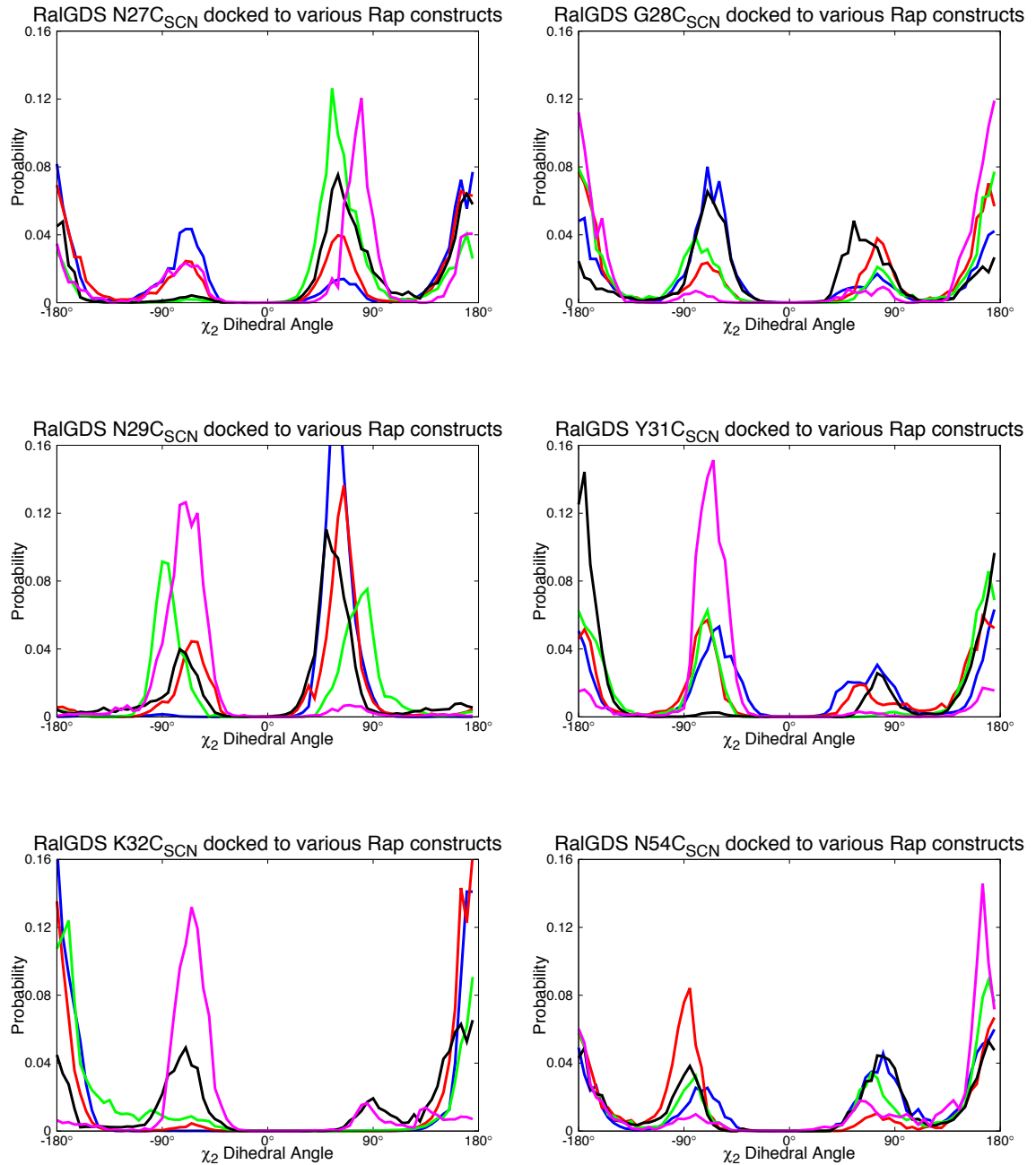


Figure 5-4: 1D Umbrella Sampling χ_2 Dihedral Distributions

The χ_2 probability distributions of nitrile-labeled RalGDS mutants in various states determined by one-dimensional umbrella sampling. Magenta: RalGDS monomer; black: WT Rap; red: Rap E30D; green: Rap K31E; blue: Rap E30D/K31E.

χ_2 Probability Distributions from 2-Dimensional Umbrella Sampling

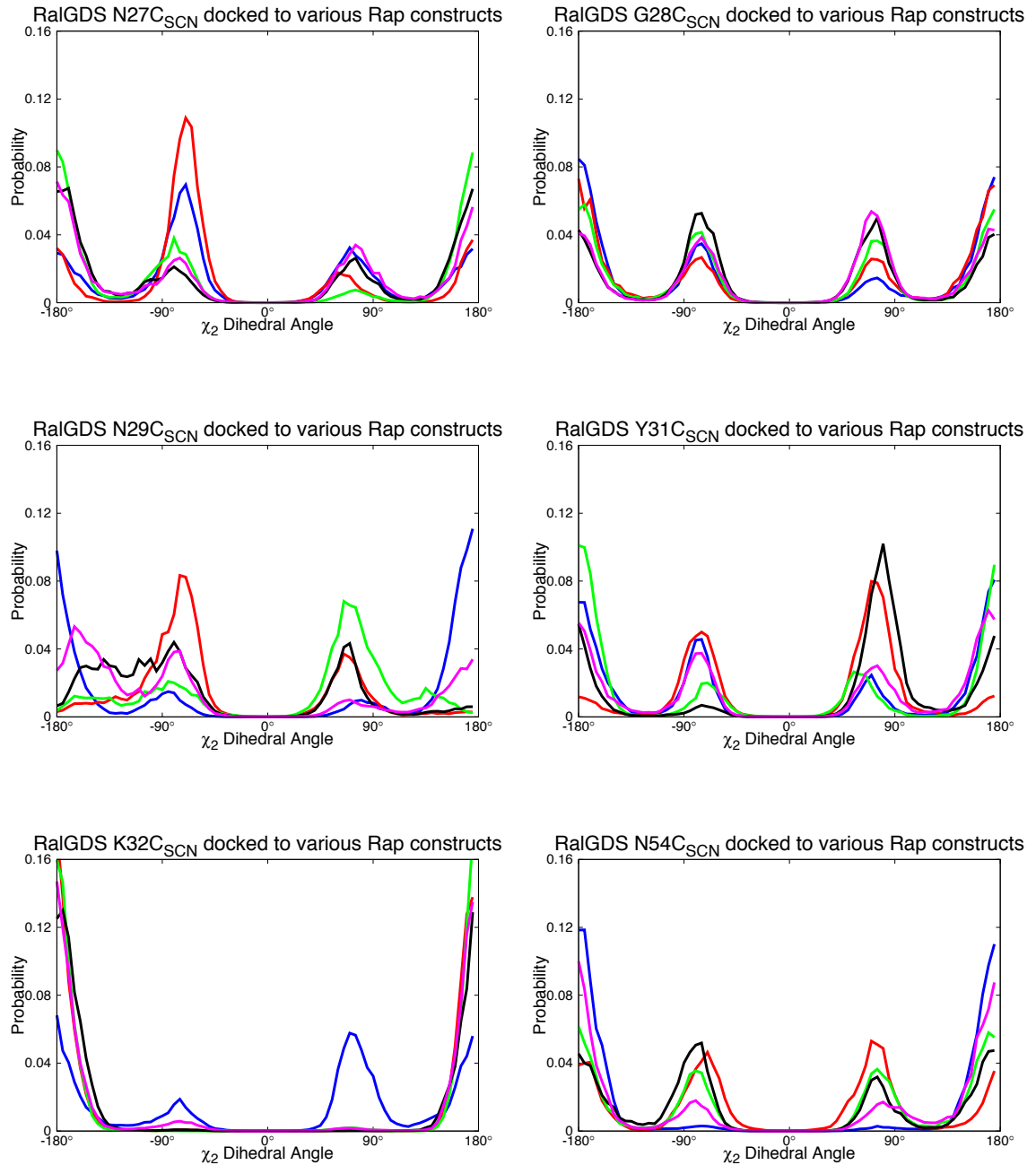


Figure 5-5: 2D Umbrella Sampling χ_2 Dihedral Distribution

The χ_2 probability distributions of nitrile-labeled RalGDS mutants in various states determined by two-dimensional umbrella sampling. Magenta: RalGDS monomer; black: WT Rap; red: Rap E30D; green: Rap K31E; blue: Rap E30D/K31E.

Boltzmann-weighted average electrostatic field as a function of sampling time

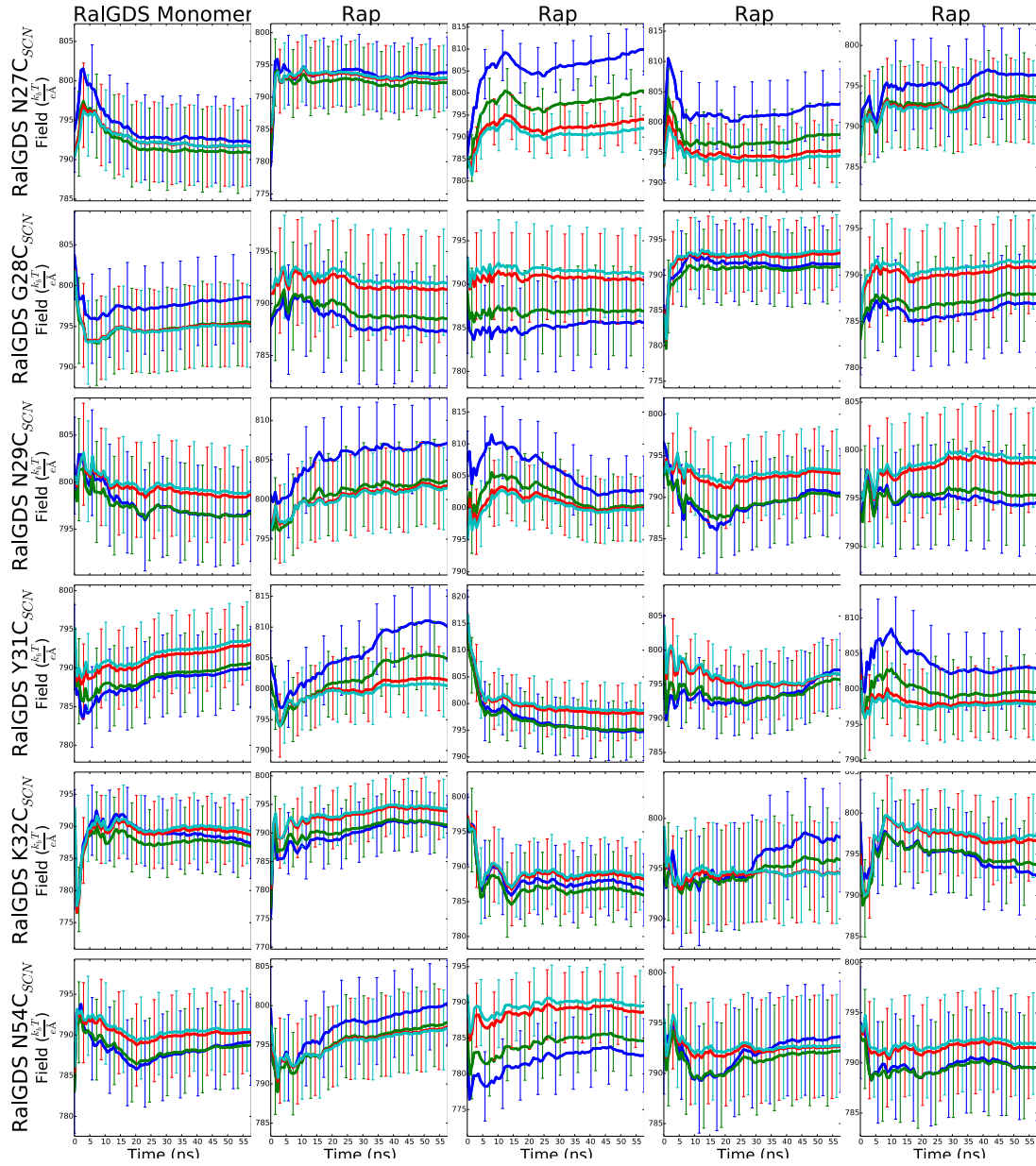


Figure 5-6: Field Convergence Test

The Boltzmann-weighted average field as a function of simulation time. Blue: GS = 0.119 Å/grid point; green: GS = 0.099 Å/grid point; red: GS = 0.062 Å/grid point; cyan: GS = 0.052 Å/grid point. Error bars show one standard deviation from calculations conducted on the Boltzmann-weighted ensemble of snapshots.

SCN-labeled RaIGDS monomers

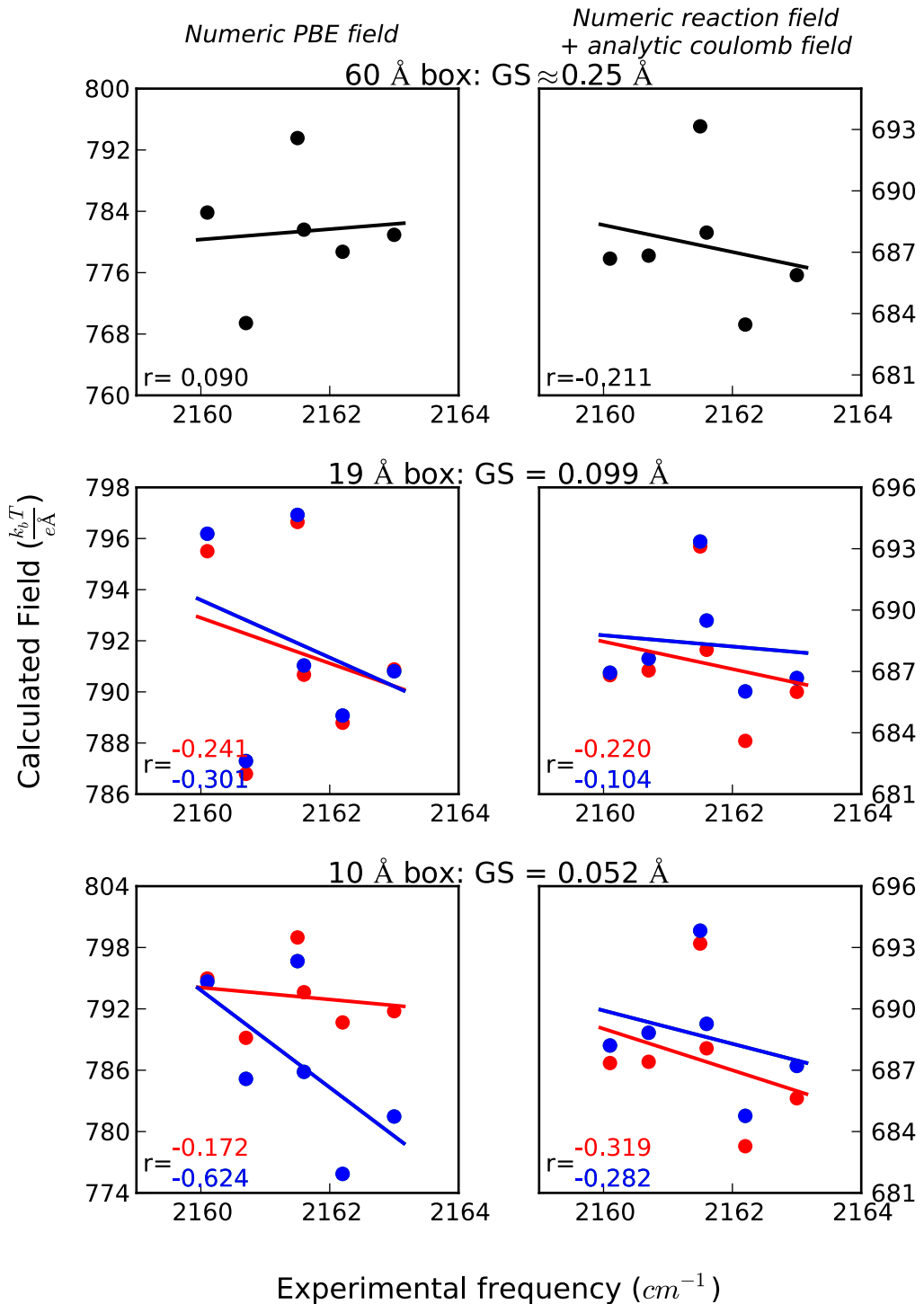


Figure 5-7: Absolute Field Plots for Various Box Locations - Ral Monomer

The absolute field calculations from solving numerically solving one LPBE (left) and from summing the numeric reaction field obtained from two LPBE calculations with the analytic Coulomb field (right) compared to the experimental frequencies for various nitrile probe locations on the RalGDS monomer. Black: system center of mass (60 \AA boxes); red: NC δ ; blue: system center of mass = RalGDS center of mass. Correlation coefficients are labeled in the corresponding color on each plot.

SCN-labeled RalGDS mutants docked with WT Ral

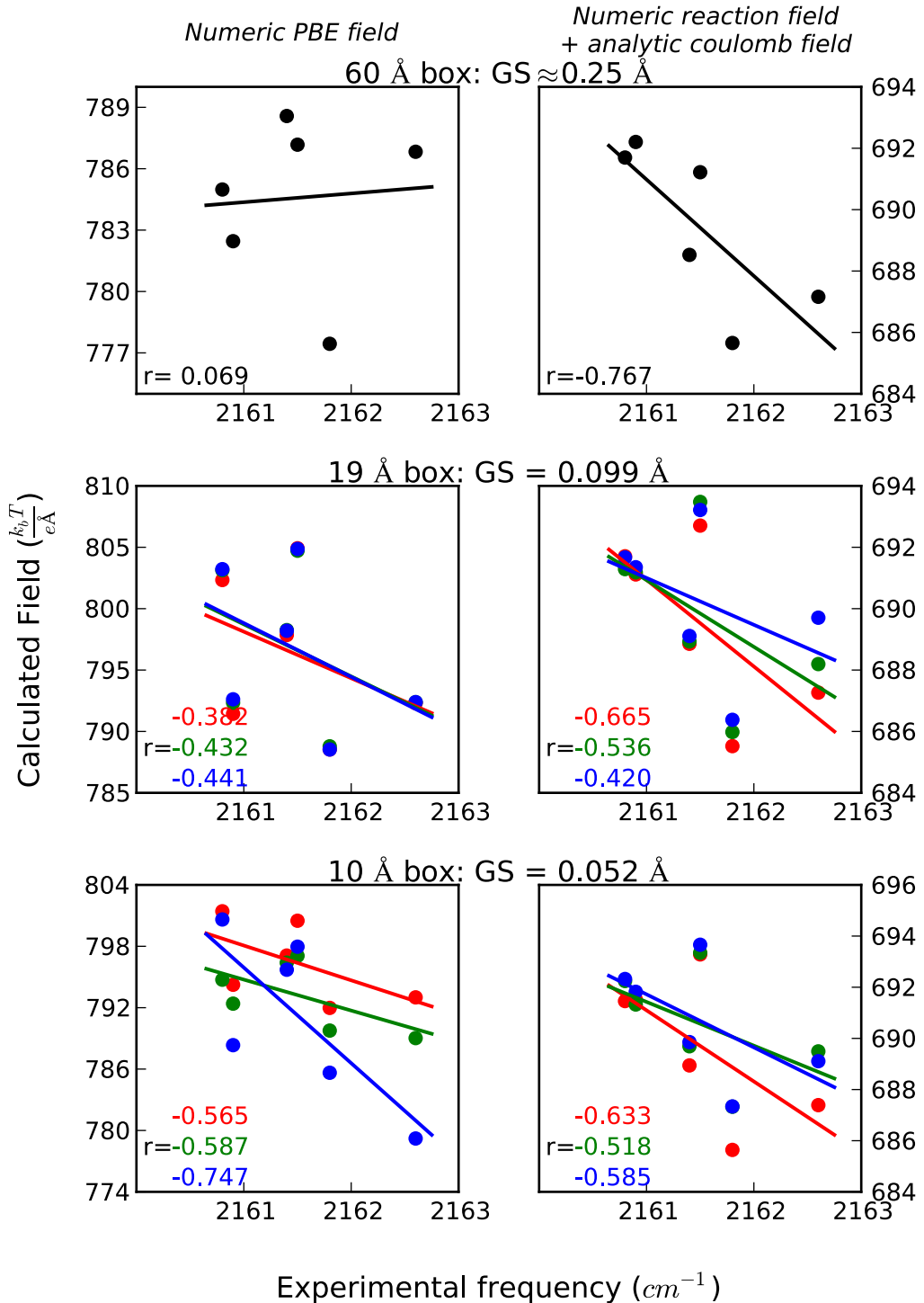


Figure 5-8: Absolute Field Plots for Various Box Locations – Rap E30/K31

The absolute field calculations from solving numerically solving one LPBE (left) and from summing the numeric reaction field obtained from two LPBE calculations with the analytic Coulomb field (right) compared to the experimental frequencies for various nitrile probe locations on RalGDS docked to WT Rap. Black: system center of mass (60 Å boxes); red: NC δ ; green: system center of mass; blue: RalGDS center of mass. Correlation coefficients are labeled in the corresponding color on each plot.

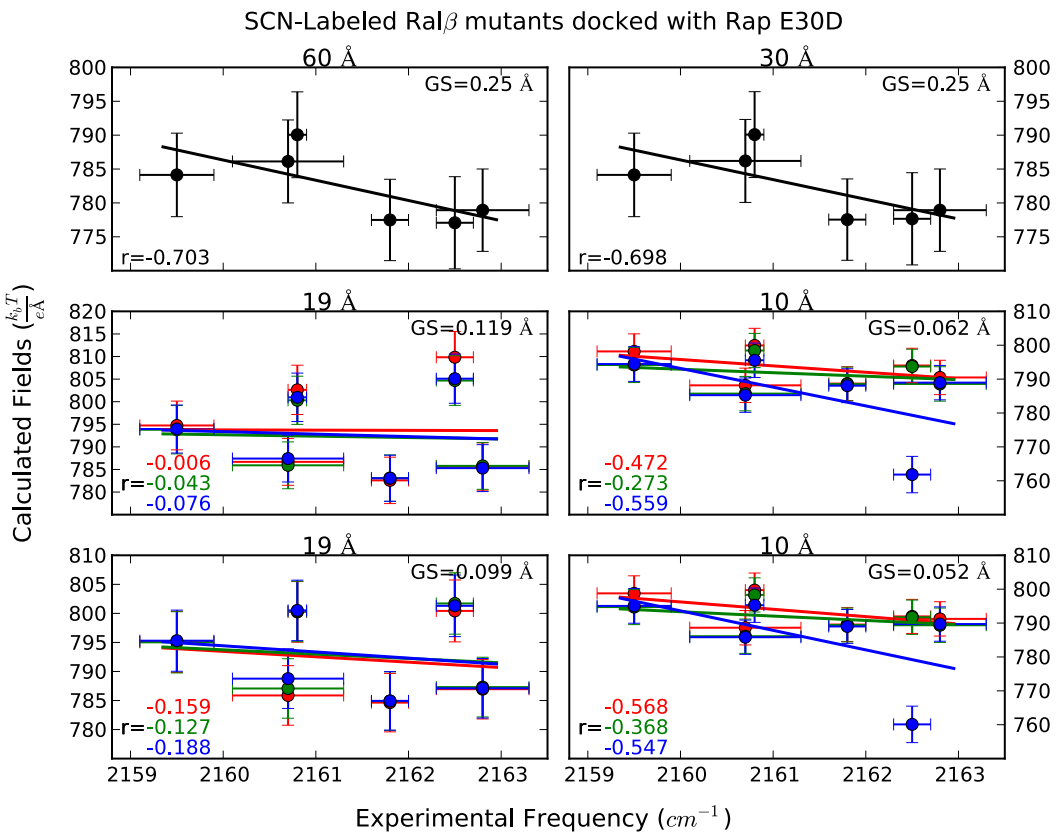


Figure 5-9: Absolute Field Plots for Various Box Locations – Rap E30D/K31

The absolute field calculations from solving numerically solving one LPBE (left) and from summing the numeric reaction field obtained from two LPBE calculations with the analytic Coulomb field (right) compared to the experimental frequencies for various nitrile probe locations on RalGDS docked to Rap E30D. Black: system center of mass (60 Å boxes); red: NC δ ; green: system center of mass; blue: RalGDS center of mass.

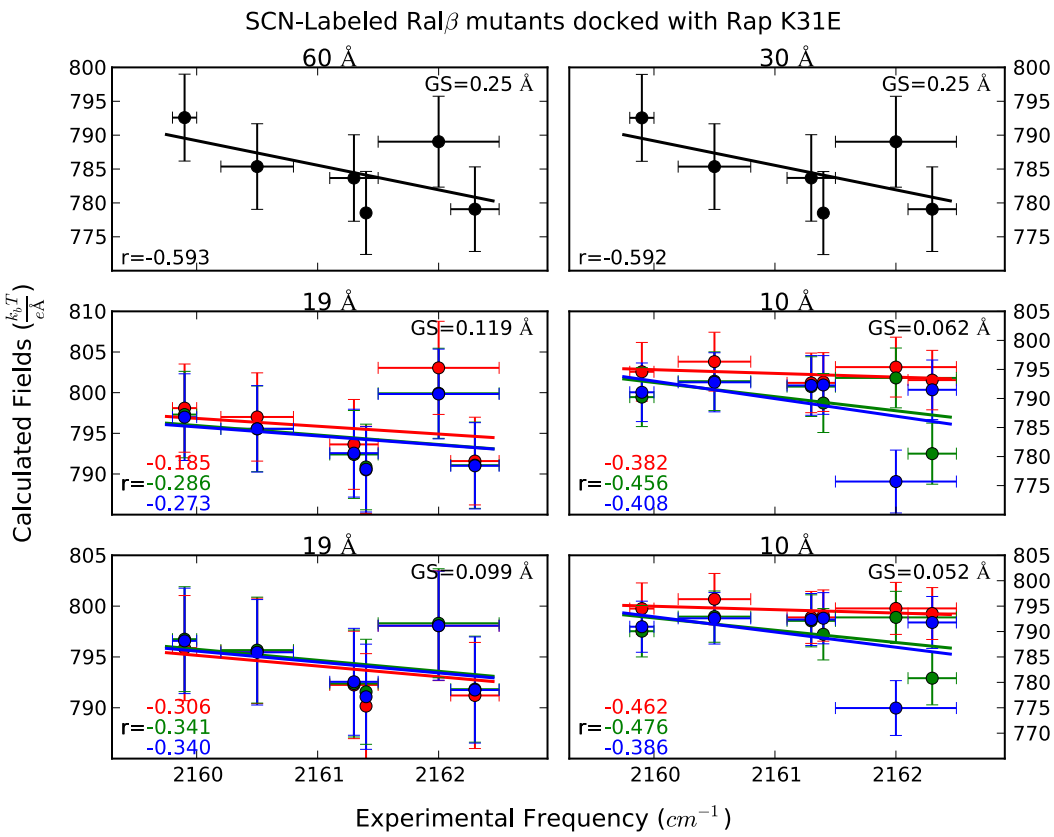


Figure 5-10: Absolute Field Plots for Various Box Locations – Rap E30/K31E

The absolute field from solving numerically solving one LPBE (left) and from summing the numeric reaction field obtained from two LPBE calculations with the analytic Coulomb field (right) calculations compared to the experimental frequencies for various nitrile probe locations on RalGDS docked to Rap K31E. Black: system center of mass (60 Å boxes); red: NC δ ; green: system center of mass; blue: RalGDS center of mass.

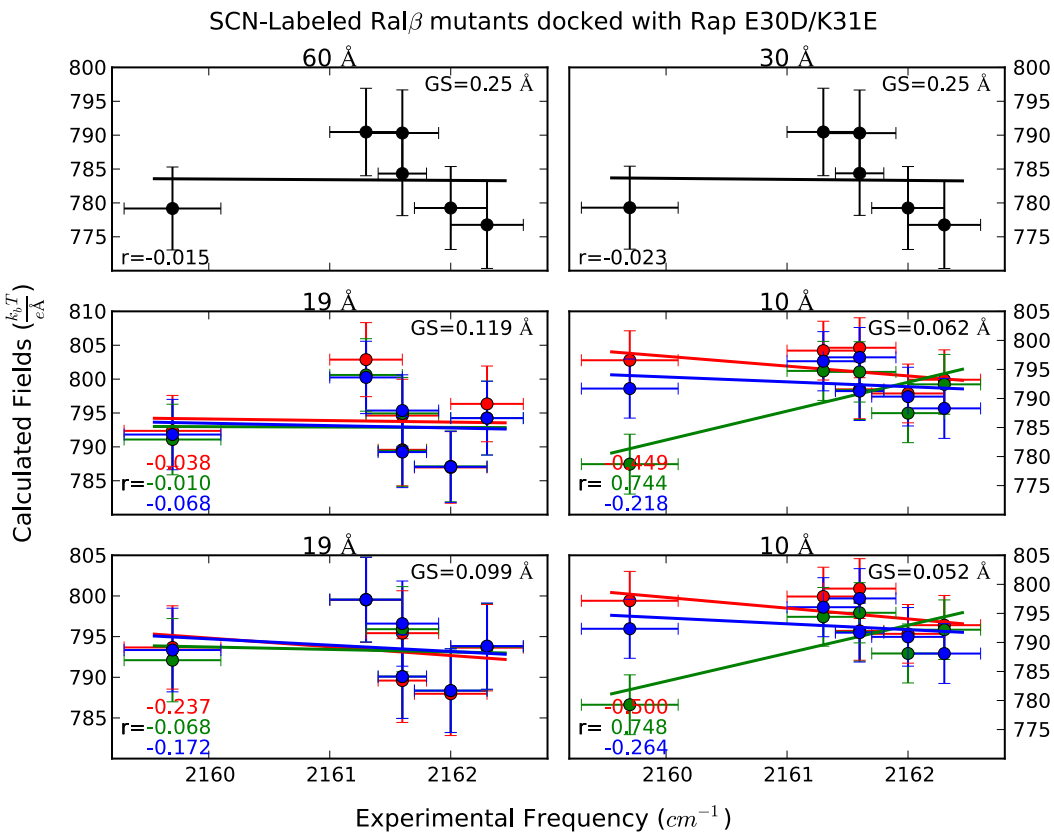


Figure 5-11: Absolute Field Plots for Various Box Locations – Rap E30D/K31E

The absolute field calculations from solving numerically solving one LPBE (left) and from summing the numeric reaction field obtained from two LPBE calculations with the analytic Coulomb field (right) compared to the experimental frequencies for various nitrile probe locations on RalGDS docked to Rap E30D/K31E. Black: system center of mass (60 Å boxes); red: NC δ ; green: system center of mass; blue: RalGDS center of mass.

SCN-labeled RaIGDS mutants docked with WT RaI

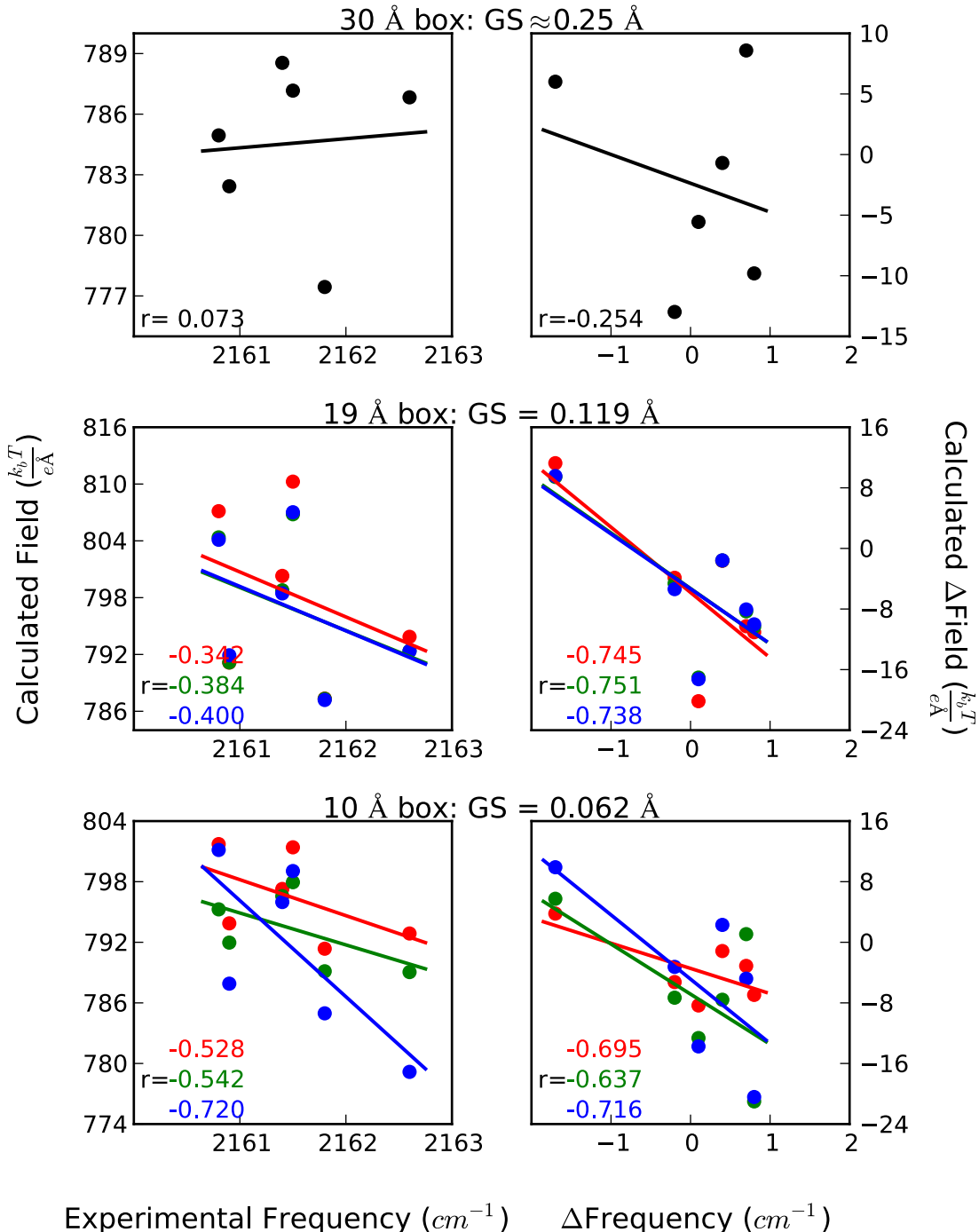


Figure 5-12: Comparing Absolute and Relative Fields - Rap E30/K31

The absolute field (left column) and relative field (right column) calculated using coarse grid spacing compared to the experimental frequencies for various nitrile probe locations on RalGDS docked to WT Rap. Black: system center of mass (30 Å boxes); red: NC δ ; green: system center of mass; blue: RalGDS center of mass.

SCN-labeled RaIGDS mutants docked with Rap E30D

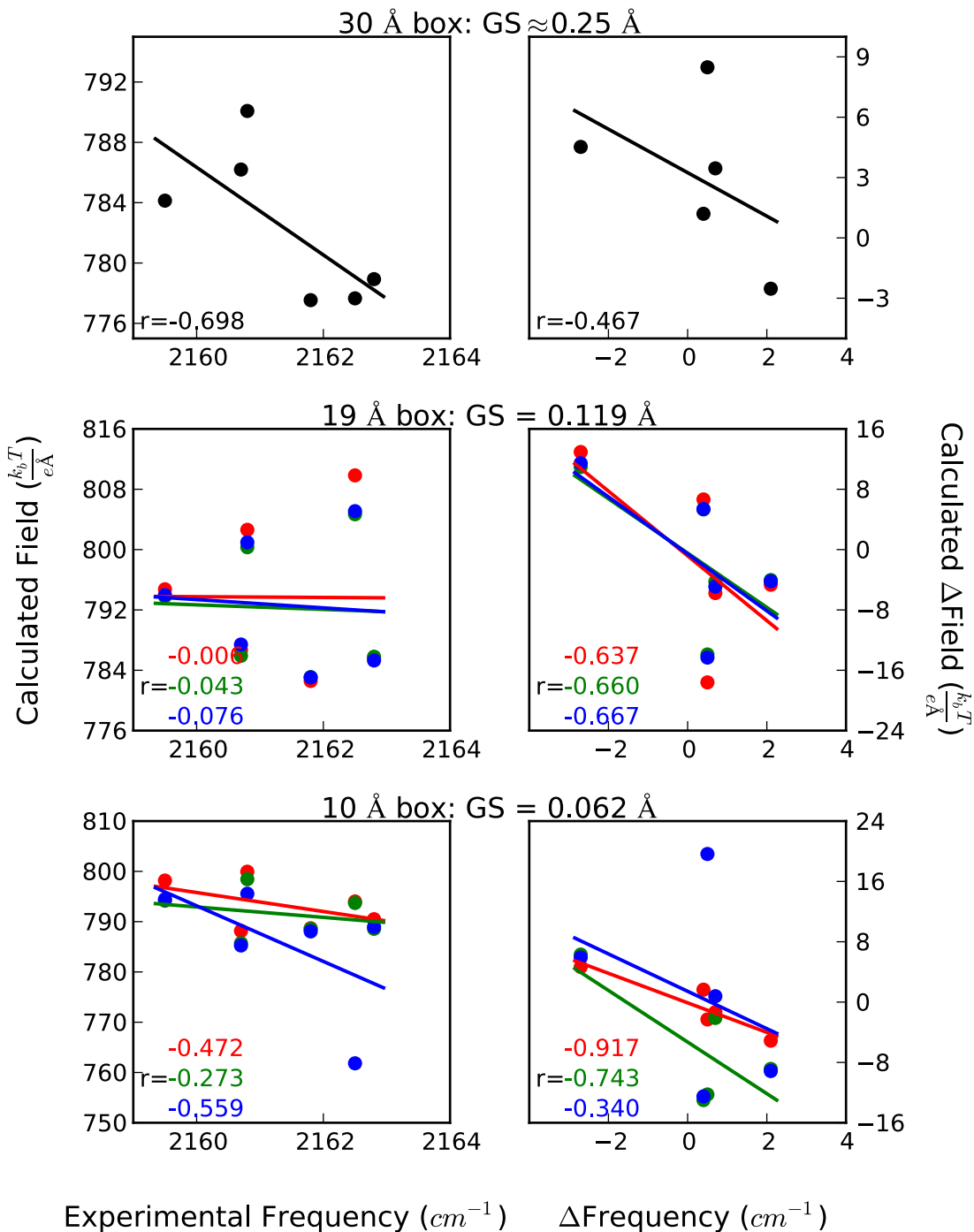


Figure 5-13: Comparing Absolute and Relative Fields - Rap E30D/K31

The absolute field (left column) and relative field (right column) calculated using coarse grid spacing compared to the experimental frequencies for various nitrile probe locations on RalGDS docked to Rap E30D. Black: system center of mass (30 Å boxes); red: NC δ ; green: system center of mass; blue: RalGDS center of mass.

SCN-labeled RaIGDS mutants docked with Rap K31E

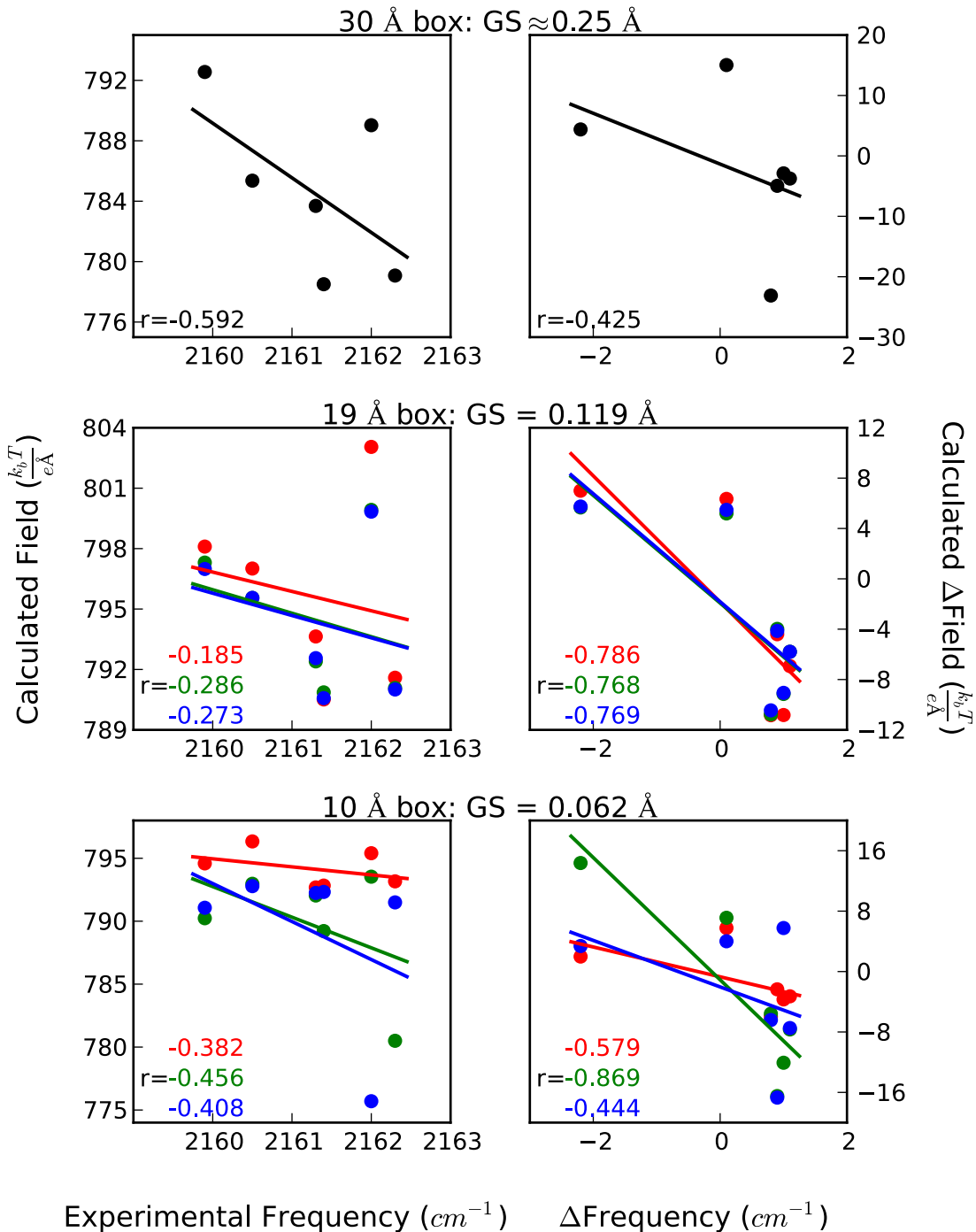


Figure 5-14: Comparing Absolute and Relative Fields - Rap E30/K31E

The absolute field (left column) and relative field (right column) calculated using coarse grid spacing compared to the experimental frequencies for various nitrile probe locations on RalGDS docked to Rap K31E. Black: system center of mass (30 Å boxes); red: NC δ ; green: system center of mass; blue: RalGDS center of mass.

SCN-labeled RaIGDS mutants docked with Rap E30D/K31E

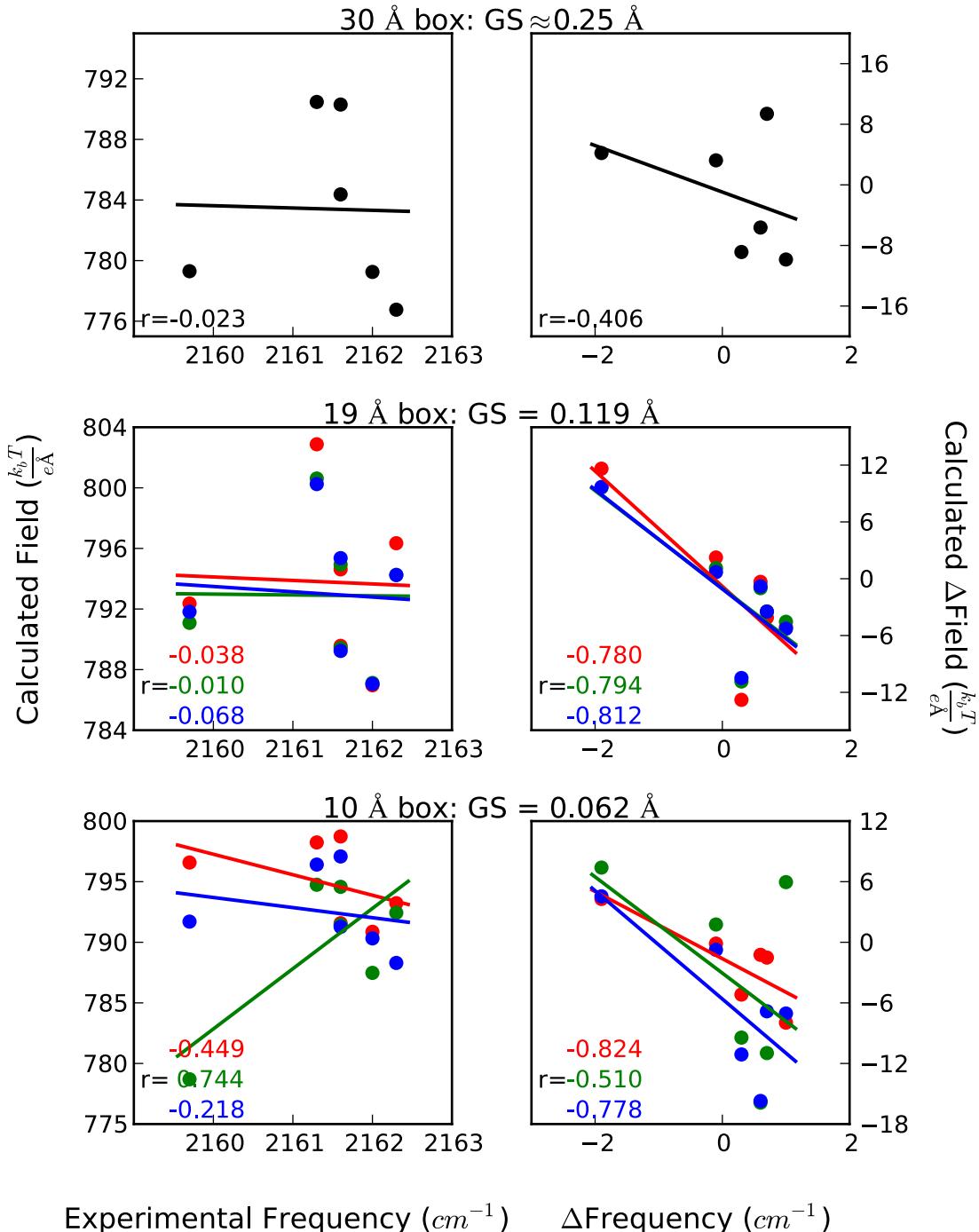


Figure 5-15: Comparing Absolute and Relative Fields - Rap E30D/K31E

The absolute field (left column) and relative field (right column) calculated using coarse grid spacing compared to the experimental frequencies for various nitrile probe locations on RalGDS docked to Rap E30D/K31E. Black: system center of mass (30 Å boxes); red: NC δ ; green: system center of mass; blue: RalGDS center of mass.

SCN-labeled RalGDS mutants docked with WT Ral

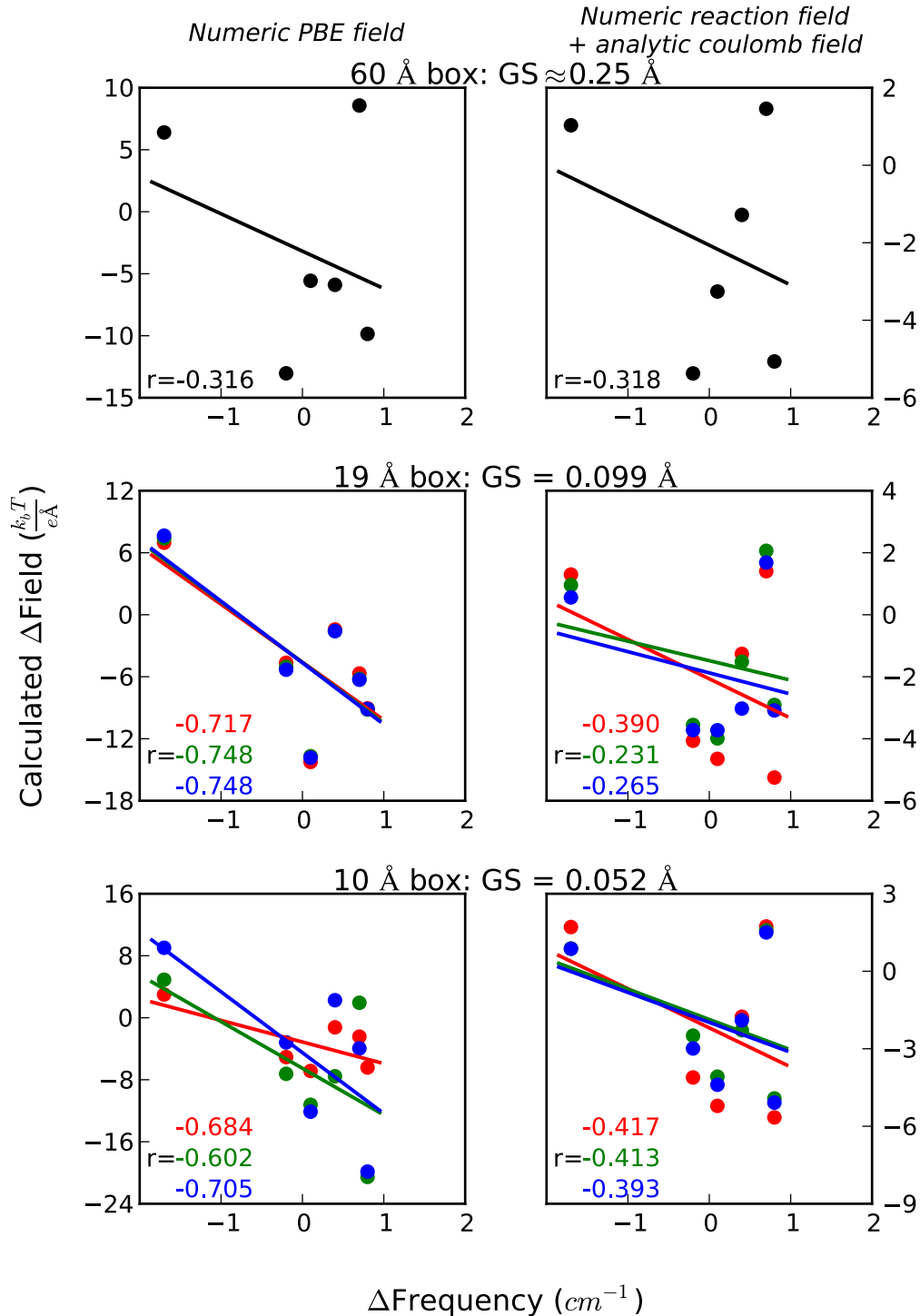


Figure 5-16: Comparing Numeric PBE and RFM Relative Fields - Rap E30/K31

The calculated change in field from subtracting two numerically solved LPBE (left) and from subtracting the numeric reaction fields obtained from four LPBE calculations with the analytic Coulomb fields (right) at various nitrile probe locations on RalGDS due to docking with WT Rap compared to the experimental change in frequency due to docking. Black: system center of mass (60 Å boxes); red: NC δ ; green: system center of mass; blue: RalGDS center of mass. Correlation coefficients are labeled in the corresponding color on each plot.

SCN-labeled RaIGDS mutants docked with Rap E30D

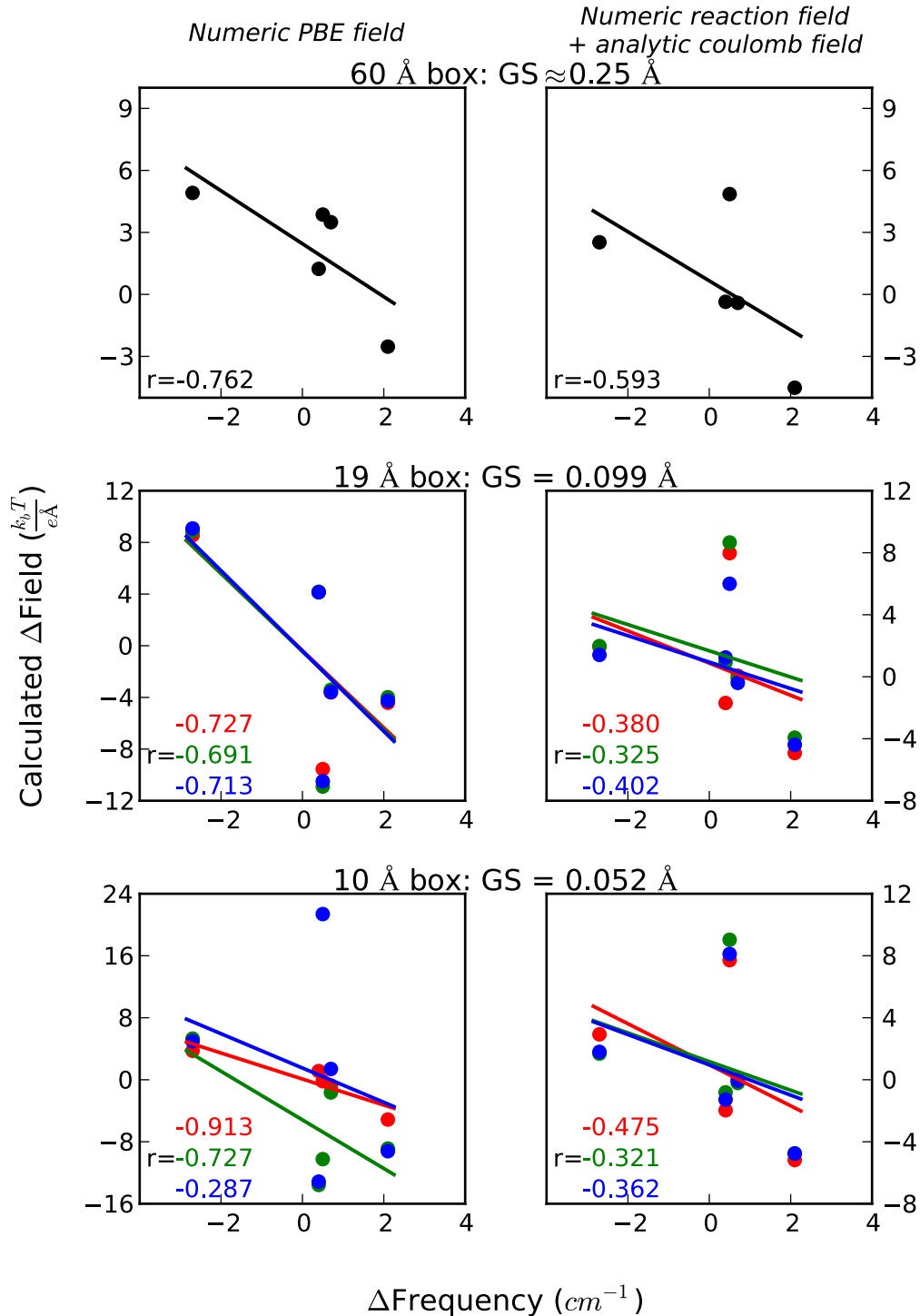


Figure 5-17: Comparing Numeric PBE and RFM Relative Fields - Rap E30D/K31

The calculated change in field from subtracting two numerically solved LPBE (left) and from subtracting the numeric reaction fields obtained from four LPBE calculations with the analytic Coulomb fields (right) at various nitrile probe locations on RalGDS due to docking with Rap E30D compared to the experimental change in absorption frequency due to docking. Black: system center of mass (60 Å boxes); red: NC δ ; green: system center of mass; blue: RalGDS center of mass.

SCN-labeled RalGDS mutants docked with Rap K31E

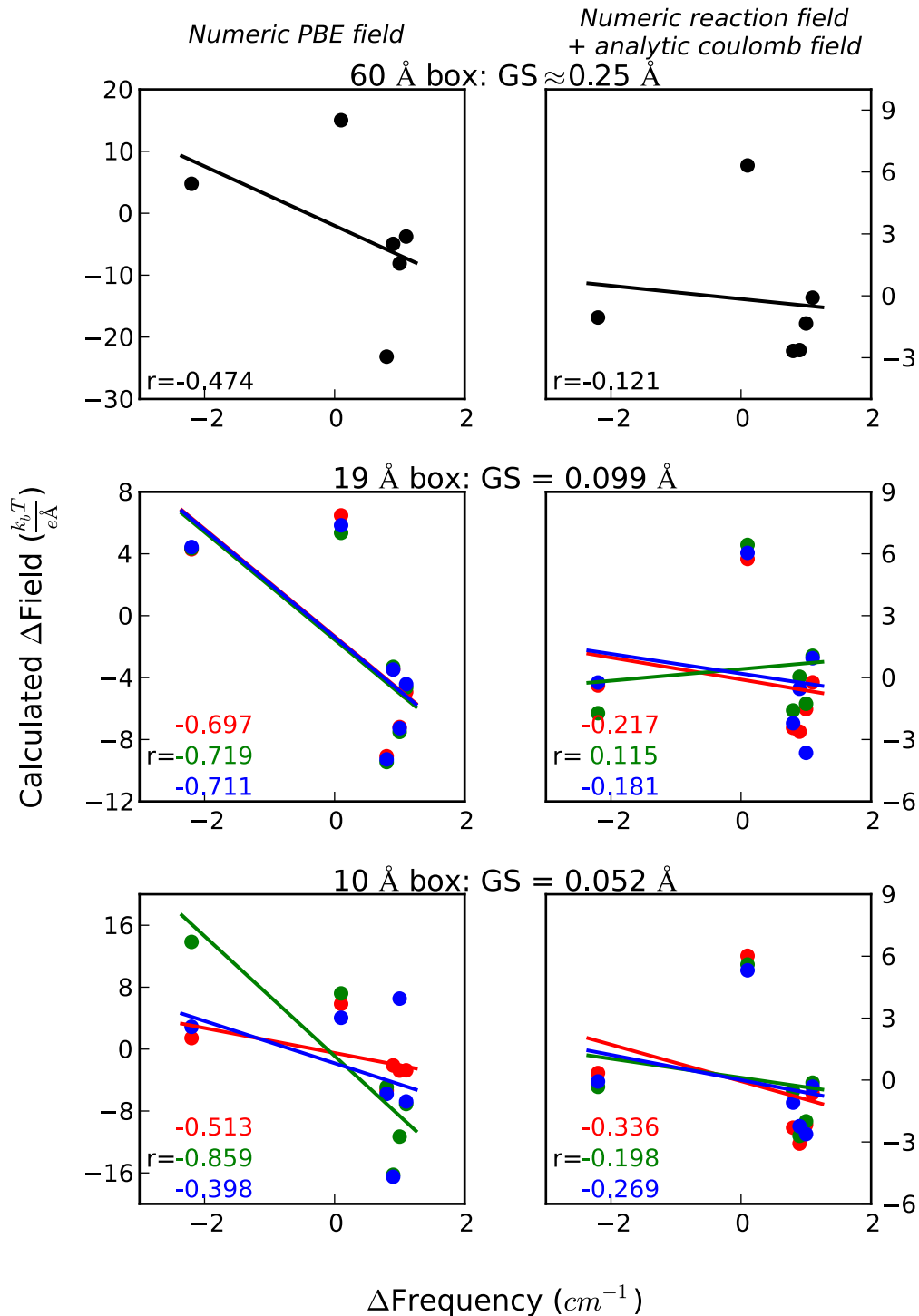


Figure 5-18: Comparing Numeric PBE and RFM Relative Fields - Rap E30/K31E

The calculated change in field from subtracting two numerically solved LPBE (left) and from subtracting the numeric reaction fields obtained from four LPBE calculations with the analytic Coulomb fields (right) at various nitrile probe locations on RalGDS due to docking with Rap K31E compared to the experimental change in absorption frequency due to docking. Black: system center of mass (60 Å boxes); red: NC δ ; green: system center of mass; blue: RalGDS center of mass.

SCN-labeled RaIGDS mutants docked with Rap E30D/K31E

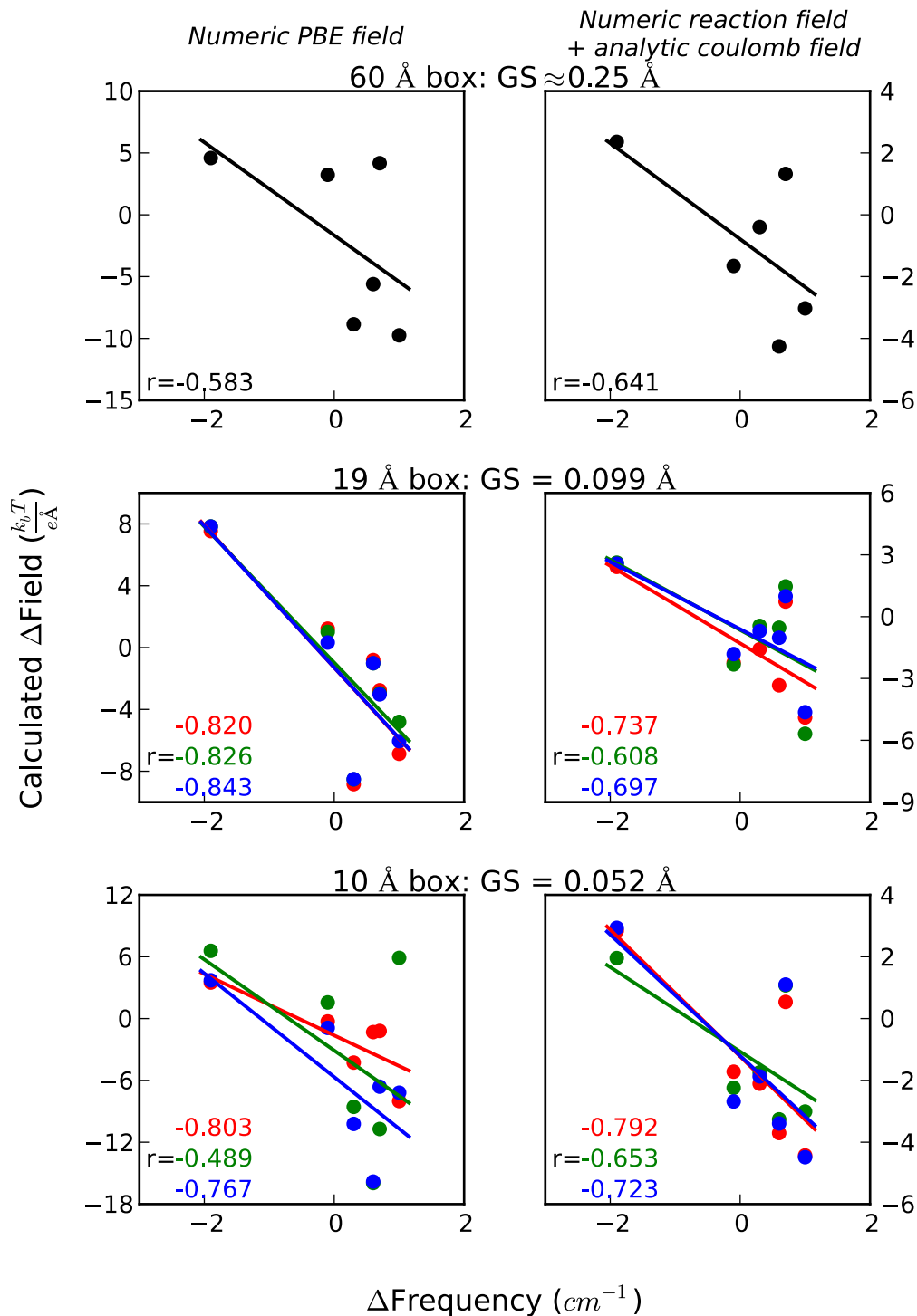


Figure 5-19: Comparing Numeric PBE and RFM Relative Fields - Rap E30D/K31E

The calculated change in field from subtracting two numerically solved LPBE (left) and from subtracting the numeric reaction fields obtained from four LPBE calculations with the analytic Coulomb fields (right) at various nitrile probe locations on RalGDS due to docking with Rap E30D/K31E compared to the experimental change in absorption frequency due to docking. Black: system center of mass (60 Å boxes); red: NC δ ; green: system center of mass; blue: RalGDS center of mass.

Chapter 6 Optimizing Electrostatic Field Calculations with the Adaptive Poisson-Boltzmann Solver to Predict Electric Fields at Protein-Protein Interfaces II: Explicit Near-Probe and Hydrogen Bonding Water Molecules

6.1 INTRODUCTION

Quantitative calculations of electrostatic fields in biological molecules are ubiquitous throughout the biophysical literature in aiding many types of investigations, but their accuracy has proven difficult to confirm from experimental measurements.^{2,4,6,7,11,17,18,29,42,67,69,86,95,109,110,112,115,117,128,131,134,144-153} We have previously reported the accuracy of calculated protein electrostatic fields determined by docking various functional mutants of the protein Rap1a to six different constructs of the downstream effector protein Ral guanosine dissociation inhibitor carrying a cyanocysteine vibrational probe (hereafter referred to as Rap and RalGDS, respectively) using the linear Poisson-Boltzmann equation (LPBE), equation (3-4).⁷⁹

For complex geometric shapes, such as a protein, the LPBE cannot be solved analytically. Instead the LPBE is solved numerically by discretizing atomic partial charges and the local dielectric to a grid and solving using finite element or multigrid methods to perform a series of single-point LPBE calculations to obtain the numeric potential at each grid point.^{65,66,102} A numerical electrostatic field is then obtained by taking the negative gradient of the calculated potential. This numerical solution to the LPBE is hereafter referred to as the numeric method.

We previously presented how changes in 1) the calculation method, 2) the box size and grid point density, and 3) the box location affected the experimental correlation observed. For example, the solvent reaction field potential (SRF), shown in equation

(3-5), can be computed from the difference between the electrostatic potential calculated with different values for the protein and solvent dielectrics, ϵ_{solute} and $\epsilon_{solvent}$, respectively. The SRF can be solved numerically using the LPBE to average out solvent effects to the total electrostatic field and take advantage of the less-rigorous solvent sampling requirement of an implicit solvent model. The numerical negative gradient of the SRF is then added to the analytic coulomb protein field, shown in equation (3-7).

In the previous study, we looked at different calculation methods by comparing the sum of the numeric solvent field and the analytic protein field, which we called the reaction field method, to the numeric method. We determined that the reaction field method yielded the highest correlation to experimentally observed vibrational frequencies for absolute field calculations with a box centered on the nitrile, regardless of box size and grid point density.²⁷ *Changes* in the experimentally observed vibrational absorption frequencies were best correlated to *changes* in the numeric total field calculations with a box centered on the nitrile, also regardless of box size and grid point density. Both trends were linearly correlated to vibrational absorption frequencies, as expected due to the vibrational Stark effect (VSE), shown in equation (3-14).^{35, 43, 73, 75-77, 154} For our thiocyanate vibrational probe, the Stark tuning rate is $0.77 \text{ cm}^{-1}/(\text{MV cm}^{-1}) = 1.99 \text{ cm}^{-1}/(k_b T/e\text{\AA})$.

The LPBE is an implicit solvent, continuum electrostatic model subject to approximations about the dielectric environment that have already been discussed at length.^{6, 7, 67, 69, 79, 155} A second approximation, however, is the difference between bulk water, modeled implicitly as a dielectric of 78, and water that is structurally or chemically important in the system. In our previous work, all solvent was treated as bulk solvent and all explicit references to solvent atoms were removed from structures prior to solving the LPBE. However, it is known that bulk water is distinct from water that is interacting

with the surface of the protein, and is identified as so-called hydration water.¹⁵⁶⁻¹⁵⁹

Hydration water is less mobile than bulk water, has a lower dielectric constant than bulk water,³² and can play a role in stabilizing protein-protein or protein-ligand interactions.^{160,}

¹⁶¹ Dismissing these persistent waters as part of the bulk solution may be detrimental to the quality of calculations of various properties that depend on molecular structure and charge such as electrostatic potentials and fields. To address this, Layfield *et al.*¹⁰⁹ recently demonstrated the importance of explicit inclusion of the water molecule nearest the nitrile probe in a quantum mechanical calculation of the vibrational frequency of nitrile probes. The included water molecule helped account for polarization effects of the solvent and improved the accuracy their calculated vibrational shifts. Additionally, Fennell *et al.*¹⁶² showed that employing an implicit solvent model that distinguishes between bulk water and hydration water can better account for solvation shell properties than a purely implicit solvent model and yields results consistent with purely explicit models.

Our previous work compared calculated electrostatic fields to experimentally measured vibrational absorption frequencies for six nitrile probes placed along the Rap/RalGDS interface, at positions N27C_{SCN}, G28C_{SCN}, N29C_{SCN}, Y31C_{SCN}, K32C_{SCN}, and N54C_{SCN}, for monomeric RalGDS³⁵ as well as RalGDS docked to WT Rap, Rap E30D, Rap K31E, and Rap E30D/K31E.⁴³ This constitutes a set of experiments in which the exact quantity we are trying to calculate, the electrostatic field at the vibrational chromophore, is being directly measured via the VSE. In the work reported here, we test whether including explicit water molecules improves computational correlation to experiment compared to the original, purely implicit solvent, calculations in a purely classical continuum electrostatics calculation.

6.2 RESULTS AND DISCUSSION

All structures examined had a total of 56.7 ns of simulation with frames saved every 5 ps, resulting in 11664 frames in which we solved the LPBE. Since the goal of our investigation is to find an easy, generalizable way to calculate electrostatic fields representative of the VSE, one of our criteria is to limit the number of arbitrary user-choices, such as frame picking. Therefore, we used all of the frames saved when calculating our Boltzmann-weighted distributions and averages.

6.2.1 Calculations of Absolute Fields

Figure 6-1, Figure 6-2, Figure 6-3, Figure 6-4, and Figure 6-5 compare the calculated electrostatic fields at the nitrile bond midpoint projected along the nitrile bond vector using the various partially-explicit solvent methods (blue) to the experimentally observed nitrile vibrational absorption frequencies for the RalGDS monomer, RalGDS docked to WT Rap, and RalGDS docked to E30D, K31E, and E30D/K31E, respectively, and compared to previous results obtained with no explicit water molecules (red). Results using both the numeric LBPE solutions (left column) as well as the reaction field method (right column) are presented. Error bars have been omitted for clarity, but we consistently observed standard deviations of the electrostatic field calculations ranging from about $\pm 6.5 k_b T/e\text{\AA}$ and for vibrational frequencies ranging from about $\pm 1 \text{ cm}^{-1}$. The reaction field method yielded higher correlation to experiment than the numeric solutions, consistent with our previously reported results. Further discussion of the results of the absolute calculations will be limited to the reaction field method.

5 Å Sphere

The top rows of Figure 6-1, Figure 6-2, Figure 6-3, Figure 6-4, and Figure 6-5 show the electrostatic fields calculated when all water molecules within 5 Å of the nitrile Ne atom

are explicitly included. In all cases the reaction field method yields better correlation than the numeric method. In Figure 6-1, the monomeric RalGDS field correlations are significantly improved by the inclusion of the solvent sphere and yet in every docked system, the solvent sphere detracts from the overall correlation to experiment.

To understand this observation, we looked at each water molecule within 5 Å of the nitrile Nε and determined the probability of a water molecule staying within 5 Å of the nitrile for n frames (n ranging from 1 to 81, the number of frames in each trajectory), shown for the RalGDS monomer in Figure 6-6, as well for RalGDS docked to the various Rap constructs (Figure 6-7, Figure 6-8, Figure 6-9, and Figure 6-10), with the probe location listed as subtitles to each histogram and the trajectory average number of frames (not a Boltzmann-weighted average) listed in the upper-right corner. The error bar on each bin is the standard deviation among the 144 trajectories for that bin. These averages are also tabulated in Table 6-1. We see that the RalGDS monomers have the lowest average number of frames that each water molecule is within the solvent sphere (15.6), while the docked complexes average approximately 18-20, indicating that we have more water moving in-and-out of the simulated system for the monomers than for the dimers.

The improvement in experimental correlation seen (Figure 6-1) using the 5 Å explicit solvent spheres (blue) compared to the entirely implicit solvent model (red) for *only* the RalGDS monomers and not the docked complex may be an artifact of insufficient water sampling in the docked simulations. Not only do the RalGDS monomers have fewer atoms, and thus fewer degrees of freedom to sample, but the docked complexes also have the Rap constructs in close proximity to the nitrile probes. One of the advantages of an implicit solvent model is the effects of the solvent are treated as an average, bulk property, and are not limited by poor sampling. When using explicit solvent, care must be taken to ensure the solvent is fully relaxed and sampled. The

significant translational and rotational mobility of each water molecule requires a significant amount of simulation time to fully sample. Explicitly including some water molecules, we are seeing more water molecules trapped in local minima created by interactions with Rap than in the monomer calculations. This can be seen in Figure 6-6, Figure 6-7, Figure 6-8, Figure 6-9, and Figure 6-10 as the spike in the probability of water molecules staying within the solvent sphere for all 81 snapshots of each 400 ps simulation, such as in the K32C_{SCN} RalGDS mutant docked to WT Rap (Figure 6-7, lower-left corner).

The primary criteria for convergence of our simulations were 1) good sampling of the thiocyanate χ_1 and χ_2 dihedral rotamers and 2) the numeric reaction field with entirely implicit solvent cease to significantly change with additional sampling time.⁷⁹ Neither of these criteria are significantly dependent on the water being well sampled. In a similar study by Fried *et al.*¹⁶³ comparing vibrational frequencies of a carbonyl oscillator to the solvent electrostatics, they performed 2 ns of simulation on solvated small molecule and 20 ns of simulation on a solvated ribonuclease S in order to obtain well-sampled solvent. In contrast, we performed 144 x 400 ps simulations using an enhanced molecular dynamics strategy targeted at the probe only. For the solvent, backbone, and all non-cyanocysteine side chains, a relatively small amount of time was allowed for exploring the free energy landscape; this is a known limitation of the enhanced sampling method used which we accepted based on the hypothesis that the most significant degree of freedom in our system is the nitrile orientation.

To test our system for convergence, we calculated the Boltzmann-weighted average field at each time step $n\Delta t$, where Δt is 0.72 ns and n ranged from 1 to 81 (the number of frames in each trajectory), for all 30 systems examined. Briefly, we used WHAM at each time step to calculate new weights after each additional time step of each

trajectory (0.005 ns per trajectory, 144 trajectories for a total of 0.72 ns per step). Using the new weights and the frames present in calculating them, a Boltzmann-weighted average field was calculated for the 5 Å solvent sphere using both the numeric field method as well as the reaction field method. The average field as a function of time, relative to the average field at time $n\Delta t = 0$, is shown in Figure 6-11. The field relative to the initial field was chosen to allow easy visualization using a single y-axis of the average field calculated using the numeric field method (blue) and the reaction field method (green). Relative to the magnitude of the standard deviation in field, the average field is not changing significantly after the first half of the simulation in nearly all systems. To further show this feature, we have plotted the derivative with respect to time of the average field at each time step in Figure 6-12. This was obtained from using the finite difference between steps. In the first one-third to one-half of the simulation, the field gradient is changing rapidly as t increases, but by the last half of the simulation, the field gradient shows only small fluctuations centered about zero, indicating that, on average, each additional time step is not changing the calculated average significantly. Given this information, it is reasonable to conclude that, even with explicit water near the probe, each additional time step is not significantly altering the average calculated field and the simulation has converged with respect to the electrostatic field experienced by the nitrile probe.

Using APBS and treating all water molecules implicitly yielded better correlations to experimental data than treating water molecules within 5 Å of the nitrile probe explicitly in all the docked simulations given identical sampling. The typical, entirely implicit solvent treatment outperforms this selectively explicit solvent treatment at similar computational costs. Allowing adequate simulation time for the explicit solvent to be fully sampled, the 5 Å solvent sphere calculations and the entirely implicit solvent

calculations should give identical results. If the entirely implicit solvent model returns better results with less computational overhead than trying to ensure the water is fully sampled then, within the framework of this study, the entirely implicit solvent model is better. For a system in which the solvent may not be fully sampled, the 5 Å solvent sphere is likely to be more detrimental than the traditional, entirely implicit solvent model, which is insensitive to solvent under-sampling.

Nearest Water

The second rows of Figure 6-1, Figure 6-2, Figure 6-3, Figure 6-4, and Figure 6-5 show the electrostatic fields calculated when the water molecule closest to the nitrile Nε is explicitly included. In all cases, the correlation with experiment is not significantly improved with respect to the entirely implicit calculations. It was hypothesized that because the nearest water molecule in the QM/MM calculations done by Layfield *et al.* helped account for polarization effects by including water reorientation due to protein electrostatic fields, the same may be true for a purely classical set of calculations. This hypothesis can be tested against a second experimental measurement, the value of the Stark tuning rate, $\Delta\bar{\mu}$. Using the VSE and the slope of our best-fit line, we can back-calculate the solute dielectric, or “ideal” protein dielectric (ϵ'), required for the best-fit line to reproduce the known experimental value of the Stark tuning rate, which are tabulated in Table 6-2 along with the virtual Stark tuning rates (VSTR), correlation coefficients r, and p-values. Errors on the VSTR and ϵ' were obtained using equation (6-1) (where m is the slope, r is the correlation coefficient, and n is the number of data points in the fit) as the error of the fitted slopes.

$$\sigma_m = \frac{m}{r} \frac{\sqrt{1-r^2}}{\sqrt{n-2}} \quad (6-1)$$

However, as seen in Table 6-2, the “ideal” protein dielectric,⁷⁹ is typically slightly larger for the nearest water calculations compared to the entirely implicit solvent calculations. Since dielectric is the macroscopic analog for the molecular property of polarizability, in a system that perfectly includes all polarizability effects, the appropriate solute dielectric is 1.0 and higher dielectric values imply worse modeling of polarizability effects. The strategy including waters resulted in higher values of the “ideal” protein dielectric, indicating that explicit inclusion of the nearest water molecules, in addition to neither typically nor significantly improving experimental correlation, have failed to capture previously excluded polarizability effects in the continuum calculation.

Hydrogen-bonding Water

The third rows of Figure 6-1, Figure 6-2, Figure 6-3, Figure 6-4, and Figure 6-5 show the electrostatic fields calculated when the water molecule hydrogen-bonding (N--H distance $\leq 2.25 \text{ \AA}$, N--H--O smallest bond angle $\geq 138^\circ$) to the nitrile $\text{N}\varepsilon$ is explicitly included. In all cases, the correlation with experiment is not significantly different from the entirely implicit calculations. This is due to the relatively few number of frames in which hydrogen bonding is actually observed. The RalGDS monomers had the highest occurrence, with 10.69% of all frames having a hydrogen-bonding water. The docked complexes showed fewer frames with hydrogen bonding atoms; WT Rap, Rap E30D/K31E, Rap K31E, and Rap E30D with 9.92%, 9.39%, 9.36%, and 8.63% respectively. The frequency of frames containing hydrogen-bonding water for each system/probe combination is shown in Table 6-3. Because such a small number of frames even have a hydrogen-bonding water, the field calculations are dominated by frames with zero explicit water molecules—identical to those in the original calculations—and therefore the Boltzmann-weighted average is nearly identical to the original calculations.

There are not enough frames containing a water molecule to significantly shift the electrostatic field experienced by the nitrile probe.

Although the 5 Å water sphere calculation significantly altered the calculated electrostatic field, a targeted, enhanced molecular dynamics strategy which may leave solvent under-sampled is detrimental to the overall quality of the calculations in a way not observed when using an entirely implicit solvent model. Additionally, including only the nearest water molecules or water molecules hydrogen-bonding to the nitrile Nε also does not appear to significantly improve experimental correlation, and for absolute field calculations using a LPBE model, no consideration for interfacial or near-site-of-interest water is necessary.

6.2.2 Calculations of Field Differences:

Figure 6-13, Figure 6-14, Figure 6-15, and Figure 6-16 compare the calculated relative electrostatic fields due to docking at the nitrile bond midpoint projected along the nitrile bond vector using the various explicit solvent methods (blue) to the experimentally observed nitrile vibrational absorption frequencies for RalGDS docked to WT Rap, and RalGDS docked to E30D, K31E, and E30D/K31E, respectively. As in the absolute calculations, error bars have been omitted for clarity and are approximately $\pm 1 \text{ cm}^{-1}$ in the x-axis and $\pm 6.5 k_b T/e\text{\AA}$ in the y-axis. Previously published results using entirely implicit solvent are also shown in red for comparison. Results using both the numeric LBPE solutions (left column) as well as the reaction field method (right column) are presented. Consistent with our previous study, the numeric method yields higher correlation to experiment than the reaction field method for the relative calculations and therefore further discussion of the relative field calculations is limited to those obtained by the numeric method.

5 Å Sphere

The top rows of Figure 6-13, Figure 6-14, Figure 6-15, and Figure 6-16 show the relative electrostatic fields due to RalGDS docking to the WT Rap, Rap E30D, Rap K31E, and Rap E30D/K31E respectively, calculated when all water molecules within 5 Å of the nitrile Ne atom are explicitly included. Although the explicit solvent sphere was largely a failure for the absolute field calculations, the relative field calculations show the same recovery of correlation we previously reported.⁷⁹ The numeric relative fields were significantly more correlated to the experimental vibrational energies of the nitrile probe than the reaction field method absolute fields for the WT Rap, Rap K31E, and Rap E30D/K31E. The numeric relative field for RalGDS docked to Rap E30D was approximately the same as the reaction field correlation. The increased correlations are unlikely to be purely an artifact of the better-correlated RalGDS monomer calculation because of the poor correlation of the absolute field calculations for all of the docked complexes. As before, when taking the *difference* in electrostatic fields obtained from the LPBE, cancellation of errors in the continuum calculations was observed. These observations further support the conclusion of our previous investigation; some non-physical characteristic or important, excluded physical characteristics not adequately addressed in the absolute calculations can be cancelled out by the subtraction of fields in a comparison of two similar but slightly different states. Additionally, we see slightly greater experimental correlation using the explicit solvent sphere for the relative field calculations than when using the entirely implicit model. However, if trying to efficiently maximizing both absolute and relative field correlations, the additional computational cost of performing both entirely implicit calculations and the 5 Å sphere calculations favors the use of entirely implicit solvent.

Nearest Water and Hydrogen-bonding Water

The second rows Figure 6-13, Figure 6-14, Figure 6-15, and Figure 6-16 show the relative electrostatic fields due to RalGDS docking to the WT Rap, Rap E30D, Rap K31E, and Rap E30D/K31E respectively, calculated with the water molecule nearest the nitrile Nε atom explicitly included while the third rows show the relative fields calculated explicitly including only hydrogen-bonding waters. In both methods, the relative fields and the “ideal” dielectric constants estimated from the calculation are nearly identical to the original calculations with no explicit water molecules included. Although the nearest water method is guaranteed to have an additional source of charge close to the nitrile, the values for the relative fields were approximately the same as in the implicit model. This suggests that any effect that the nearest water molecule may have on the electrostatic environment of the nitrile probe is just as well modeled explicitly as implicit bulk water. This in turn implies that treating bulk water explicitly as part of the solute dielectric does not detract from the overall quality of the calculation and there is some leeway in assigning bulk versus hydration water. For relative field calculations, no consideration for nearest or hydrogen-bonding water is necessary.

For quantifying *changes* in electrostatic fields with *changes* in vibrational absorption frequency due to docking to another protein, explicitly including a 5 Å solvent sphere near the location-of-interest was beneficial to the overall correlation, but because of the poor absolute correlation, comes at an additional cost that may not justify the small increase in correlation over using entirely implicit solvent.

In summary, When calculating the absolute electrostatic environment of a nitrile covalently bound to the surface of a protein using the LPBE, unlike the results reported for QM/MM vibrational spectra calculations,¹⁰⁹ explicit solvent near the vibrational chromophore should not be included in lieu of an implicit model when solvent sampling

may be an issue. We do not see any consistent, significant increase in correlation by explicitly including all water near the nitrile probe, the closest water molecule to the nitrile probe, or water hydrogen bonding to the probe. However, for comparing vibrational absorption energy shifts due to docking, the inclusion of explicit solvent yielded slightly improved results for the 5 Å solvent spheres and nearly identical results for the nearest water and hydrogen-bonding waters compared to the wholly implicit solvent calculation. In computing changes in protein electrostatics due to some perturbation using the LPBE model, there appears to be neither significant, consistent advantage nor disadvantage to explicitly modeling the hydration water when there is little to no persistent hydrogen bonding and the desired information is the difference between two calculations, not an absolute value of the electrostatic field. However, explicitly including water requires an additional preparation step, selecting the waters, and thus is slightly more computationally expensive for very little additional information and significantly more expensive if the absolute fields are also important. We find that, although QM/MM calculations of the nitrile absorption frequency are largely benefitted by the inclusion of water near the nitrile probe,¹⁰⁹ explicit definition of water molecules near the vibrational Stark probe typically yields neither significant improvement nor deterioration of the predictive capability of vibrational Stark shifts using the LPBE electric field difference calculations and is likely not necessary for future, similar calculations. Additionally, because the use of explicit water does not address the lack of atomic polarizability and the choice of the protein dielectric is arbitrary, additional studies will be aimed at investigating the use of the polarizable model AMOEBA.^{13, 15, 164} To address the possibly poor solvent sampling, our next study presented significantly increased the sampling time for each umbrella window.

Table 6-1: Average number of Frames Water Molecules Remained within 5 Å of the Thiocyanate Nε Atom

	Monomer	WT	E30D	K31E	E30D/K31E
N27C_{SCN}	14.8	16.2	13.2	16.8	15.1
G28C_{SCN}	14.6	17.0	16.9	16.9	18.2
N29C_{SCN}	16.5	21.5	20.6	23.5	23.4
Y31C_{SCN}	17.2	19.5	19.1	17.2	18.3
K32C_{SCN}	15.6	27.8	22.0	24.7	22.7
N54C_{SCN}	14.9	18.6	18.8	16.9	18.4
Average^a	15.6 ± 1.0	20.1 ± 4.2	18.4 ± 3.1	19.3 ± 3.7	19.3 ± 3.1

^aNot a Boltzmann-weighted average.

Table 6-2: Virtual Stark Tuning Rate (VSTR), "ideal" Dielectric Constants (ϵ'), Correlation Coefficients (r), and p-values for APBS Calculations of Electrostatic Fields

Method	Implicit Solvent ^b							
	Numeric LPBE Solutions				Reaction Field Method			
	VSTR ^a	ϵ'	r	p-value	VSTR ^a	ϵ'	r	p-value
Monomer	1.7 ± 4.9	2.3 ± 6.7	-0.172	0.74	0.99 ± 1.47	4.0 ± 5.9	-0.319	0.53
WT	0.29 ± 0.21	13 ± 10	-0.565	0.22	0.36 ± 0.22	11 ± 7	-0.633	0.15
WT Docked	0.36 ± 0.19	11 ± 6	-0.684	0.17	0.66 ± 0.72	6.0 ± 6.5	-0.417	0.46
E30D	0.46 ± 0.33	8.6 ± 6.2	-0.568	0.22	0.26 ± 0.09	15 ± 5	-0.83	0.02
E30D Docked	0.60 ± 0.13	6.6 ± 1.5	-0.913	0.01	0.76 ± 0.70	5.2 ± 4.8	-0.475	0.39
K31E	1.5 ± 1.4	2.6 ± 2.5	-0.462	0.34	0.95 ± 0.40	4.2 ± 1.7	-0.768	0.05
K31E Docked	0.62 ± 0.52	6.4 ± 5.3	-0.513	0.35	1.1 ± 1.5	3.5 ± 5.1	-0.336	0.56
E30D/K31E	0.54 ± 0.47	7.3 ± 6.4	-0.5	0.29	0.40 ± 0.30	9.9 ± 7.4	-0.556	0.23
E30D/K31E Docked	0.34 ± 0.13	12 ± 4	-0.803	0.07	0.49 ± 0.19	8.1 ± 3.1	-0.792	0.07
5 Å Explicit Solvent Sphere								
Method	Numeric LPBE Solutions				Reaction Field Method			
	VSTR ^a	ϵ'	r	p-value	VSTR ^a	ϵ'	r	p-value
	0.77 ± 0.79	5.1 ± 5.3	-0.438	0.37	0.55 ± 0.27	7.1 ± 3.5	-0.714	0.09
Monomer	0.80 ± 1.47	4.9 ± 9.1	-0.263	0.61	0.89 ± 1.16	4.4 ± 5.8	-0.359	0.47
WT	0.32 ± 0.12	12 ± 5	-0.805	0.07	0.57 ± 0.45	7.0 ± 5.5	-0.536	0.32
WT Docked	0.37 ± 0.21	11 ± 6	-0.656	0.13	0.23 ± 0.10	17 ± 7	-0.769	0.05
E30D	0.50 ± 0.21	8.0 ± 3.3	-0.772	0.09	0.63 ± 0.61	6.3 ± 6.1	-0.457	0.41
E30D Docked	-2.0 ± 3.6	-2.0 ± 3.6	0.266	0.60	11 ± 40	0.37 ± 1.32	-0.135	0.79
K31E	0.46 ± 0.16	8.6 ± 3.1	-0.816	0.06	0.77 ± 0.55	5.2 ± 3.7	-0.571	0.28
K31E Docked	4.7 ± 40.6	0.85 ± 7.25	-0.058	0.91	0.91 ± 1.74	4.3 ± 8.3	-0.253	0.62
E30D/K31E	0.30 ± 0.10	13 ± 4	-0.839	0.04	0.43 ± 0.23	9.2 ± 4.9	-0.685	0.16
Nearest Water Molecule								
Method	Numeric LPBE Solutions				Reaction Field Method			
	VSTR ^a	ϵ'	r	p-value	VSTR ^a	ϵ'	r	p-value
	1.6 ± 4.5	2.5 ± 6.9	-0.176	0.73	0.92 ± 1.38	4.3 ± 6.4	-0.317	0.53
Monomer	0.28 ± 0.20	14 ± 10	-0.572	0.21	0.33 ± 0.18	12 ± 7	-0.676	0.12
WT	0.35 ± 0.18	11 ± 6	-0.688	0.16	0.63 ± 0.67	6.3 ± 6.7	-0.426	0.45
WT Docked	0.42 ± 0.27	9.4 ± 6.0	-0.617	0.17	0.25 ± 0.08	16 ± 4.9	-0.852	0.02
E30D	0.55 ± 0.13	7.2 ± 1.7	-0.905	0.01	0.69 ± 0.58	5.8 ± 4.8	-0.511	0.35
E30D Docked	1.1 ± 0.8	3.8 ± 2.6	-0.573	0.21	0.72 ± 0.28	5.5 ± 2.1	-0.79	0.04
K31E	0.57 ± 0.48	6.9 ± 5.8	-0.511	0.35	1.0 ± 1.4	3.9 ± 5.5	-0.341	0.56
K31E Docked	0.59 ± 0.65	6.7 ± 7.4	-0.412	0.40	0.41 ± 0.37	9.6 ± 8.7	-0.487	0.31
E30D/K31E	0.33 ± 0.11	12 ± 4	-0.824	0.05	0.48 ± 0.19	8.2 ± 3.2	-0.789	0.08
Hydrogen-Bonding Water Molecule								
Method	Numeric LPBE Solutions				Reaction Field Method			
	VSTR ^a	ϵ'	r	p-value	VSTR ^a	ϵ'	r	p-value
	1.7 ± 4.9	2.3 ± 6.7	-0.171	0.74	0.97 ± 1.46	4.1 ± 6.2	-0.315	0.53
Monomer	0.29 ± 0.21	14 ± 10	-0.57	0.21	0.35 ± 0.20	11 ± 7	-0.652	0.14
WT	0.36 ± 0.19	11 ± 5.8	-0.689	0.16	0.65 ± 0.70	6.1 ± 6.5	-0.423	0.46
WT Docked	0.46 ± 0.33	8.6 ± 6.3	-0.567	0.22	0.26 ± 0.09	15 ± 5	-0.836	0.02
E30D	0.59 ± 0.13	6.7 ± 1.5	-0.912	0.01	0.74 ± 0.66	5.3 ± 4.8	-0.489	0.38
K31E	1.4 ± 1.3	2.8 ± 2.6	-0.481	0.31	0.90 ± 0.37	4.4 ± 1.8	-0.772	0.05

K31E Docked	0.61 ± 0.52	6.5 ± 5.5	-0.508	0.35	1.1 ± 1.6	3.6 ± 5.1	-0.334	0.57
E30D/K31E	0.51 ± 0.43	7.7 ± 6.5	-0.513	0.28	0.38 ± 0.28	10 ± 8	-0.565	0.22
E30D/K31E Docked	0.33 ± 0.12	12 ± 5	-0.801	0.07	0.47 ± 0.18	8.3 ± 3.2	-0.797	0.07

Table 6-3: Percentage of Total Frames with a Nitrile-Water Hydrogen Bond

	Monomer	WT	E30D	K31E	E30D/K31E
N27C_{SCN}	10.25 %	11.79 %	7.81 %	10.85 %	9.45 %
G28C_{SCN}	13.45 %	13.35 %	12.60 %	11.86 %	12.57 %
N29C_{SCN}	6.51 %	6.69 %	7.33 %	7.79 %	5.82 %
Y31C_{SCN}	11.31 %	9.98 %	9.08 %	8.95 %	11.40 %
K32C_{SCN}	9.52 %	6.00 %	5.42 %	2.50 %	4.47 %
N54C_{SCN}	13.13 %	11.71 %	9.57 %	14.20 %	12.62 %
Average	10.69 %	9.92 %	8.63 %	9.36 %	9.39 %

^aNot a Boltzmann-weighted average.

SCN-labeled RaGDS monomer absolute fields

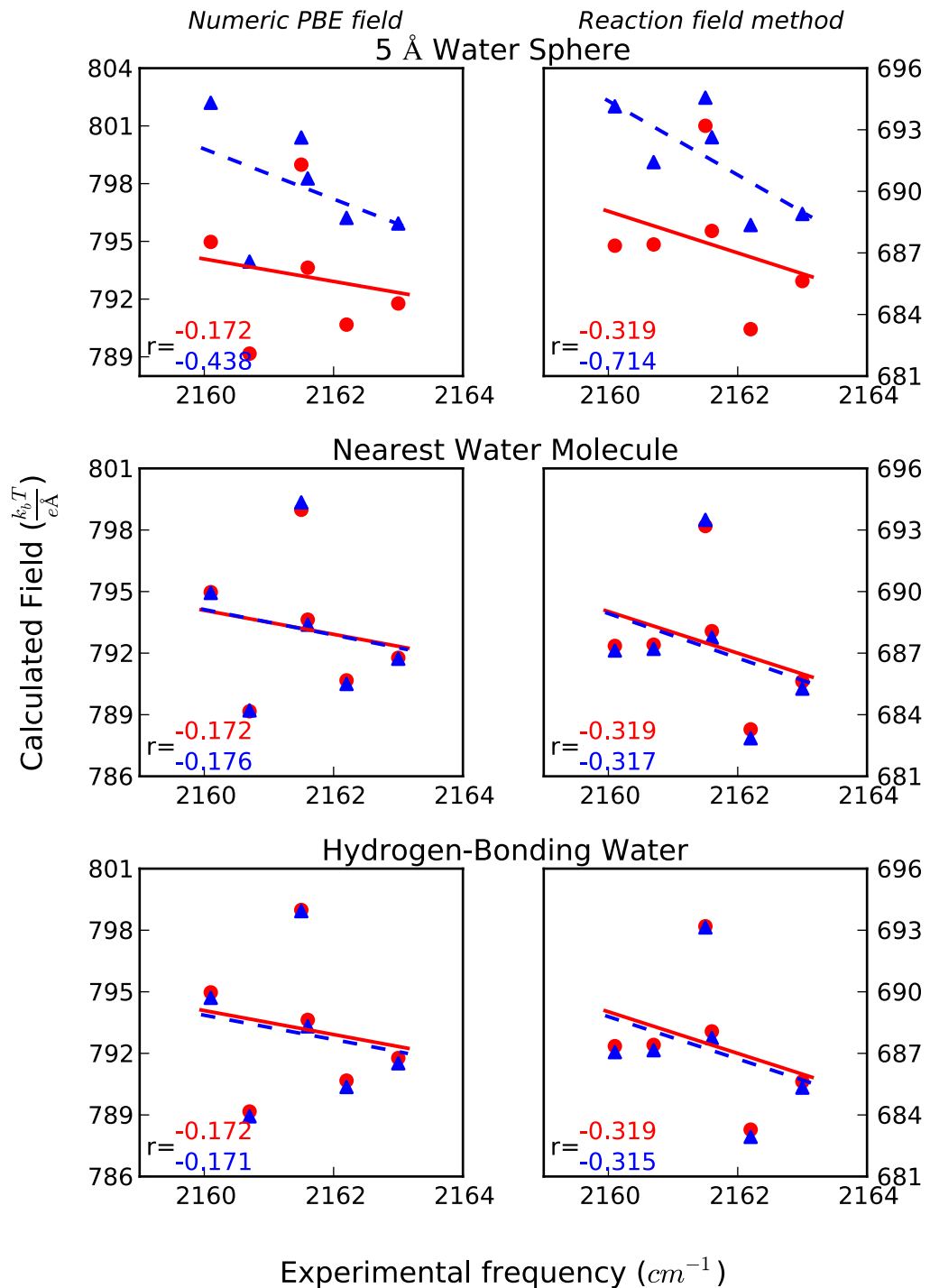


Figure 6-1: PB Absolute Field Plots - Monomer

The absolute field calculations using the numeric LPBE solutions (left column) and from the numeric reaction field method (right column) compared to the experimental frequencies for various nitrile probe locations on the RalGDS monomer. Red: originally reported, entirely implicit solvent fields; blue: fields using the solvent selection model described by the row subheading. Correlation coefficients are listed in the bottom left corner in the corresponding color. Standard deviations are approximately $\pm 1 \text{ cm}^{-1}$ and $\pm 6.5 \text{ k}_\text{b}\text{T/e}\text{\AA}$.

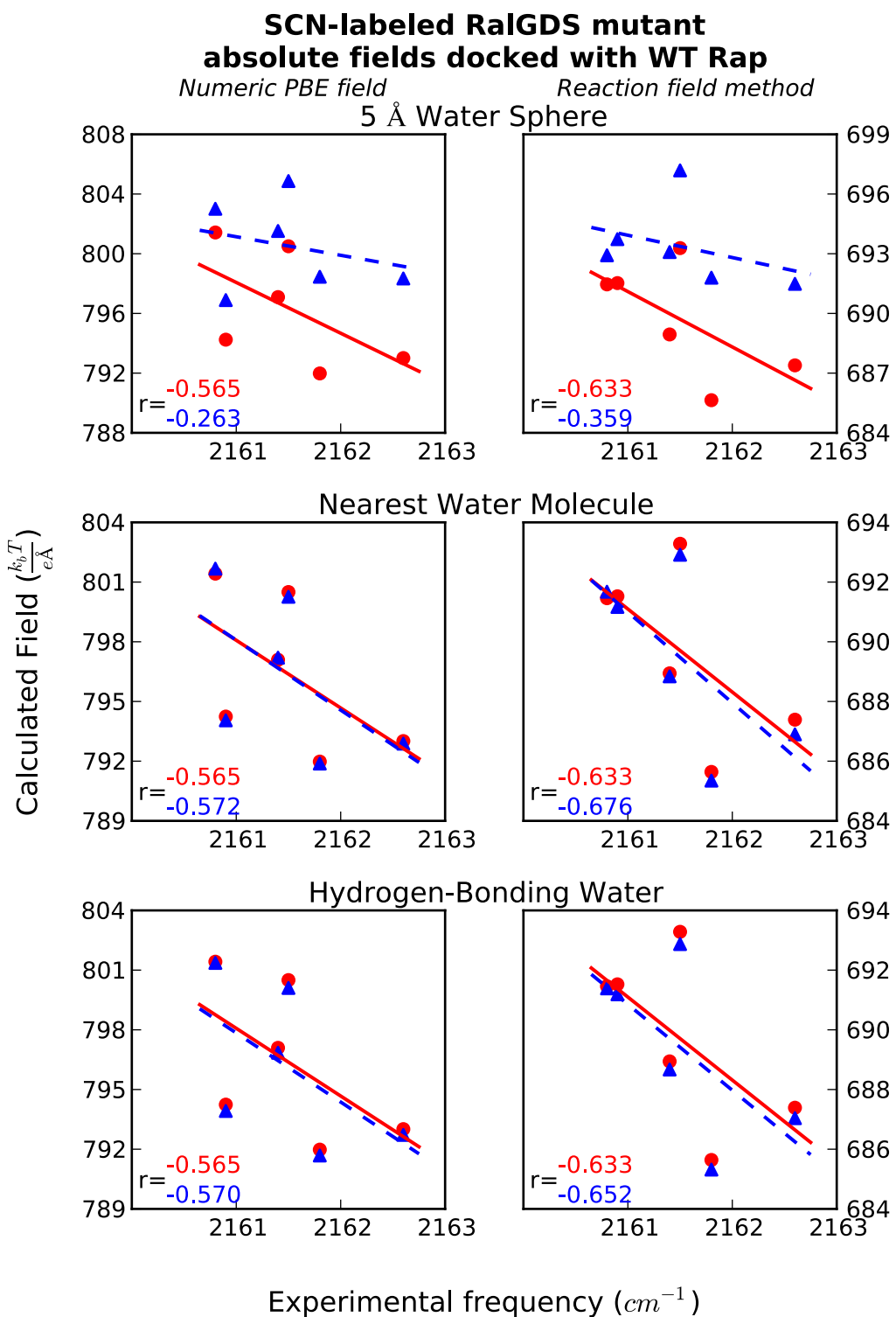


Figure 6-2: PB Absolute Field Plots – Rap E30/K31

The absolute field calculations using the numeric LPBE solutions (left column) and from the numeric reaction field method (right column) compared to the experimental frequencies for various nitrile probe locations on RalGDS docked to WT Rap. Red: originally reported, entirely implicit solvent fields; blue: fields using the solvent selection model described by the row subheading. Correlation coefficients are listed in the bottom left corner in the corresponding color. Standard deviations are approximately $\pm 1 \text{ cm}^{-1}$ and $\pm 6.5 \text{ k}_\text{b} \text{T/e}\text{\AA}$.

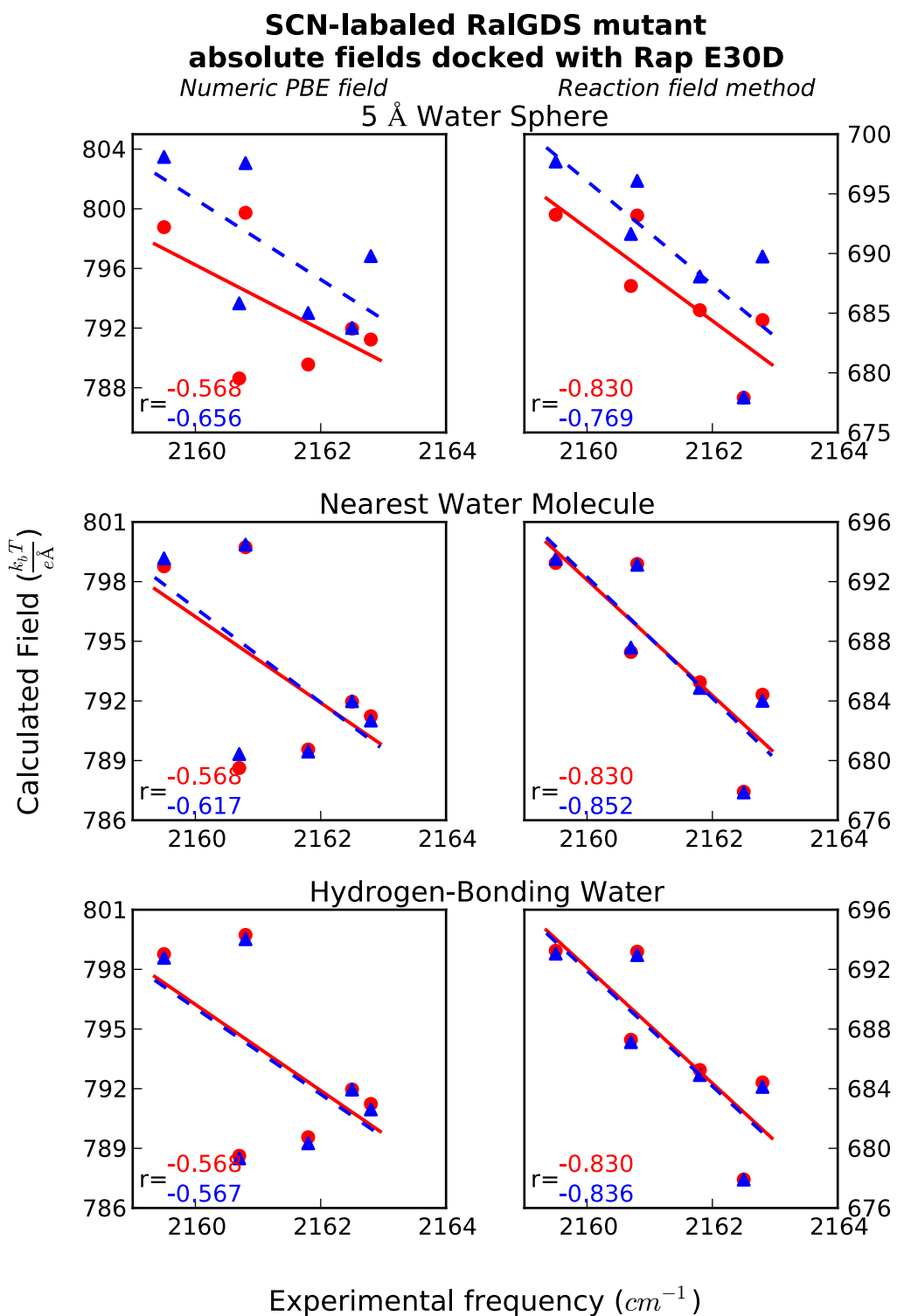


Figure 6-3: PB Absolute Field Plots – Rap E30D/K31

The absolute field calculations using the numeric LPBE solutions (left column) and from the numeric reaction field method (right column) compared to the experimental frequencies for various nitrile probe locations on RalGDS docked to Rap E30D. Red: originally reported, entirely implicit solvent fields; blue: fields using the solvent selection model described by the row subheading. Correlation coefficients are listed in the bottom left corner in the corresponding color. Standard deviations are approximately $\pm 1 \text{ cm}^{-1}$ and $\pm 6.5 \text{ k}_\text{b} \text{T/e}\text{\AA}$.

**SCN-labeled RaIGDS mutant
absolute fields docked with Rap K31E**

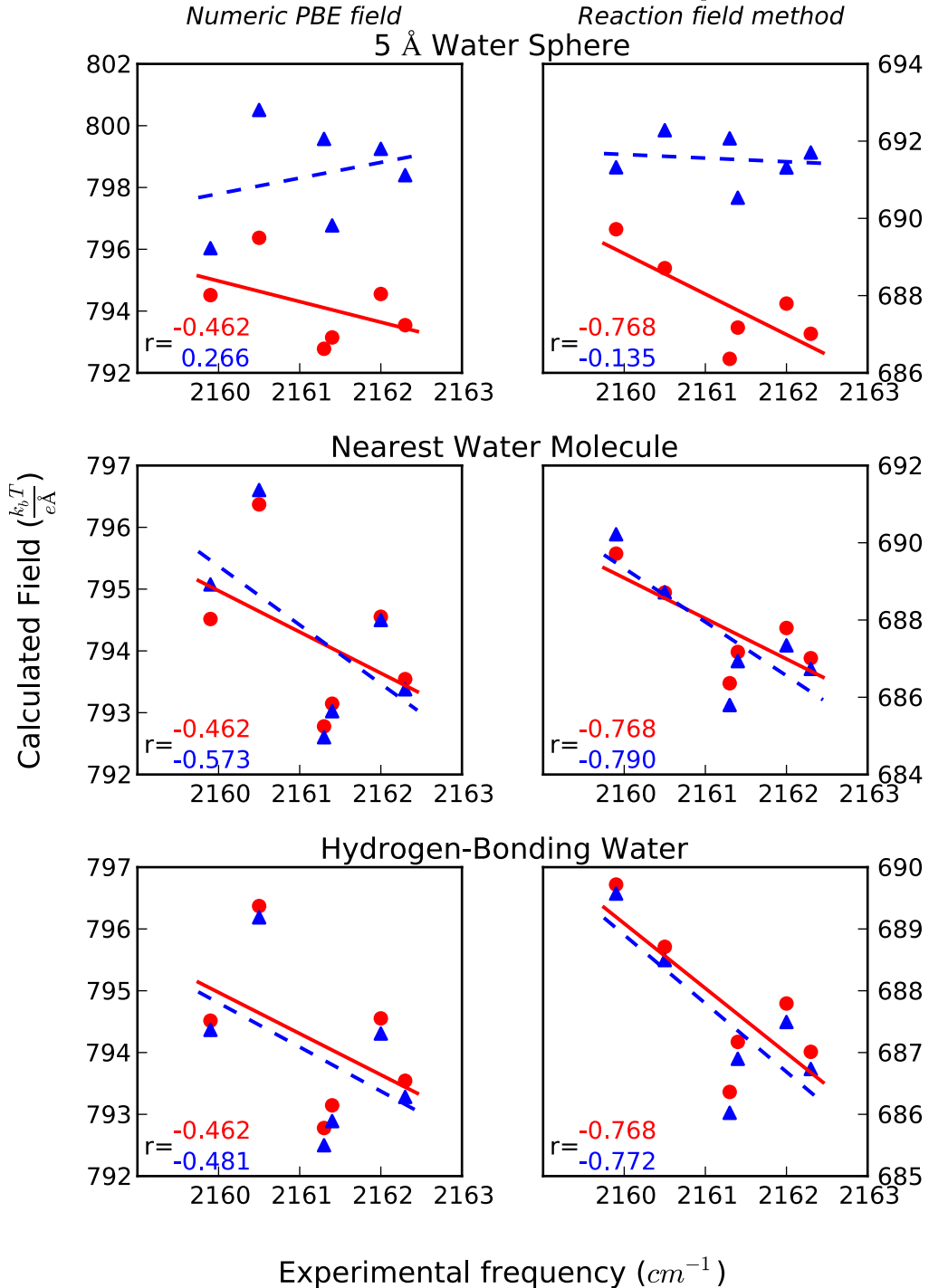


Figure 6-4: PB Absolute Field Plots – Rap E30/K31E

The absolute field calculations using the numeric LPBE solutions (left column) and from the numeric reaction field method (right column) compared to the experimental frequencies for various nitrile probe locations on RalGDS docked to Rap K31E. Red: originally reported, entirely implicit solvent fields; blue: fields using the solvent selection model described by the row subheading. Correlation coefficients are listed in the bottom left corner in the corresponding color. Standard deviations are approximately $\pm 1 \text{ cm}^{-1}$ and $\pm 6.5 \text{ k}_\text{b}T/\text{e}\text{\AA}$.

**SCN-labeled RaIGDS mutant
absolute fields docked with Rap E30D/K31E**

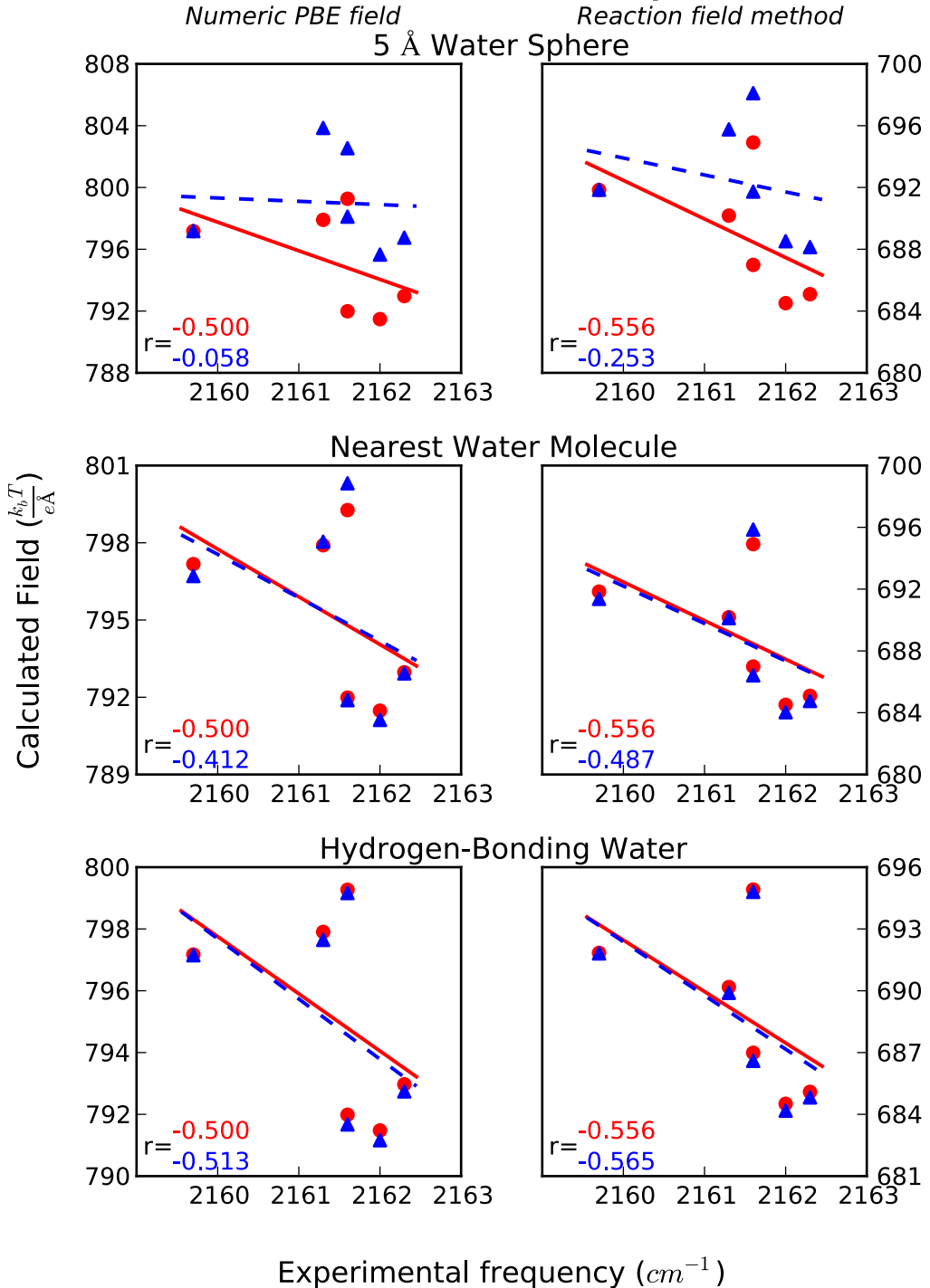


Figure 6-5: PB Absolute Field Plots – Rap E30D/K31E

The absolute field calculations using the numeric LPBE solutions (left column) and from the numeric reaction field method (right column) compared to the experimental frequencies for various nitrile probe locations on RalGDS docked to Rap E30D/K31E. Red: originally reported, entirely implicit solvent fields; blue: fields using the solvent selection model described by the row subheading. Correlation coefficients are listed in the bottom left corner in the corresponding color. Standard deviations are approximately $\pm 1\%$ in each dimension.

SCN-labeled RaIGDS Monomers

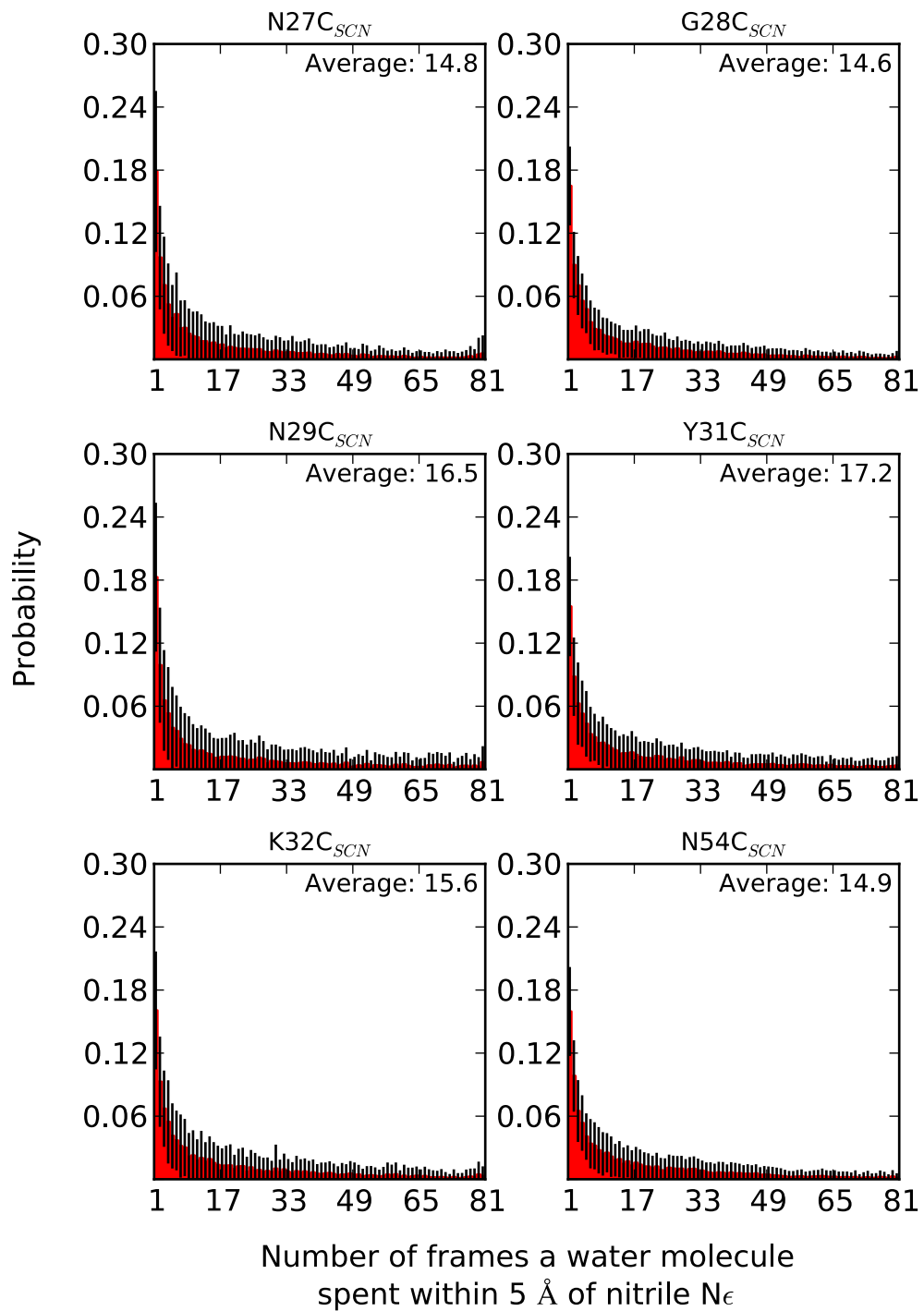


Figure 6-6: Probability of Water Lifetimes - Monomer

Observed probability of a water molecule being within 5 Å of the nitrile Nε for some number of frames in the simulation for various probe locations on the RalGDS monomer. The error bar on each bin is the standard deviation among the 144 trajectories for that bin.

SCN-labeled RalGDS mutants docked with Rap WT

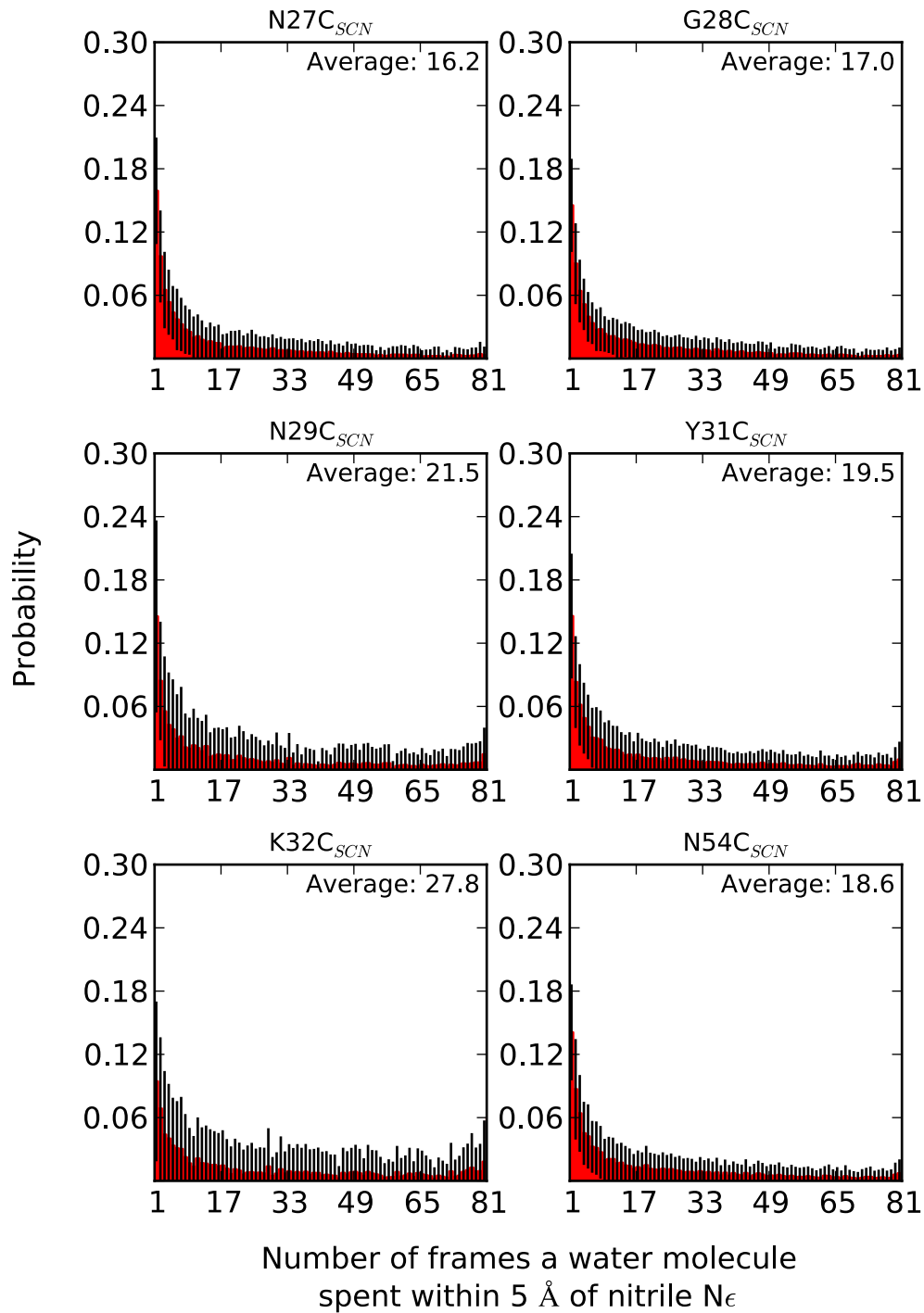


Figure 6-7: Probability of Water Lifetimes – Rap E30/K31

Observed probability of a water molecule being within 5 Å of the nitrile Nε for some number of frames in the simulation for various probe locations on the RalGDS monomer docked to WT Rap. Probabilities are not Boltzmann-weighted. The error bar on each bin is the standard deviation among the 144 trajectories for that bin.

SCN-labeled RalGDS mutants docked with Rap E30D

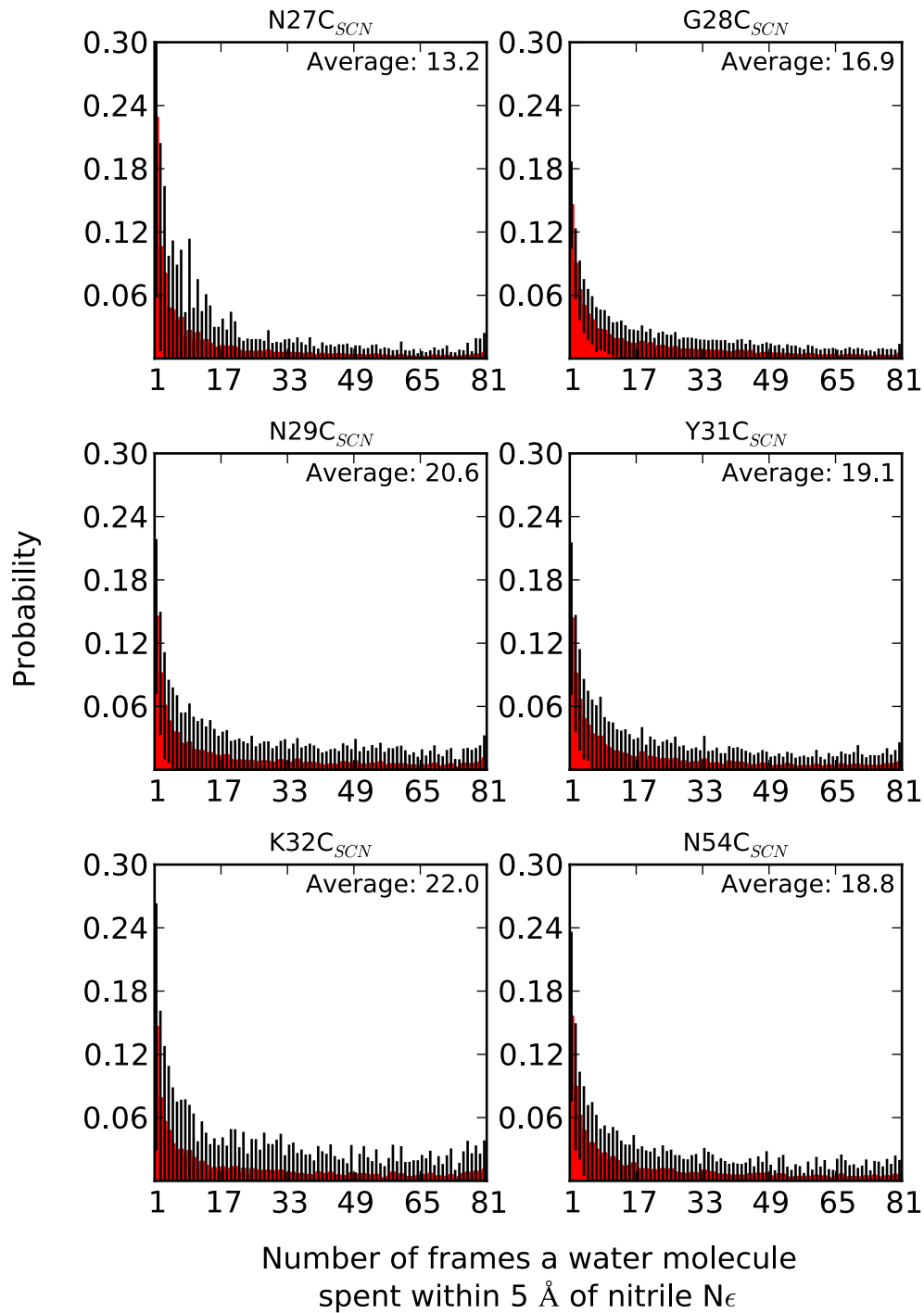


Figure 6-8: Probability of Water Lifetimes – Rap E30D/K31

Observed probability of a water molecule being within 5 Å of the nitrile Nε for some number of frames in the simulation for various probe locations on the RalGDS monomer docked to Rap E30D. The error bar on each bin is the standard deviation among the 144 trajectories for that bin.

SCN-labeled RaIGDS mutants docked with Rap K31E

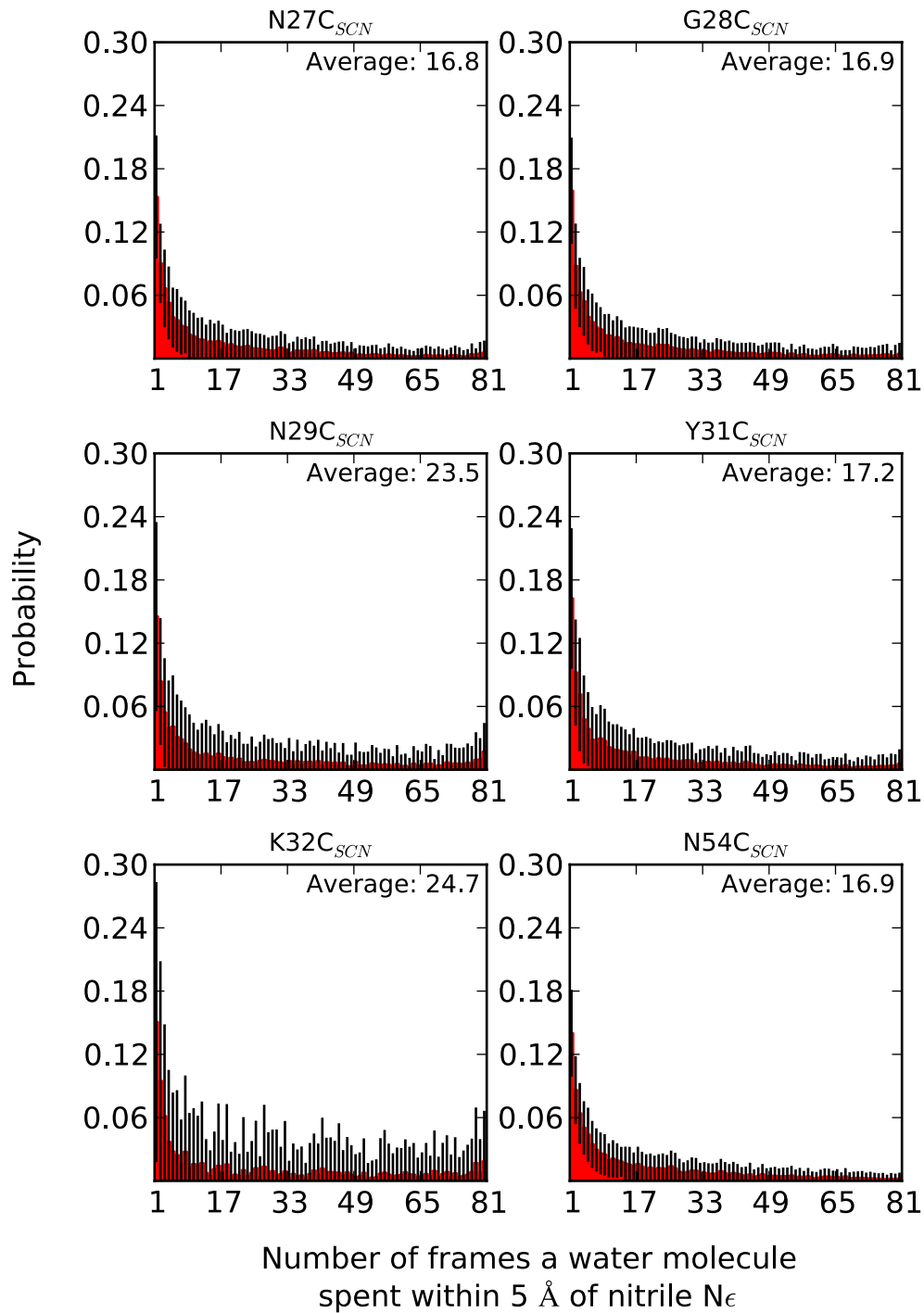


Figure 6-9: Probability of Water Lifetimes – Rap E30/K31E

Observed probability of a water molecule being within 5 Å of the nitrile Nε for some number of frames in the simulation for various probe locations on the RalGDS monomer docked to Rap K31E. The error bar on each bin is the standard deviation among the 144 trajectories for that bin.

SCN-labeled RalGDS mutants docked with Rap E30D/K31E

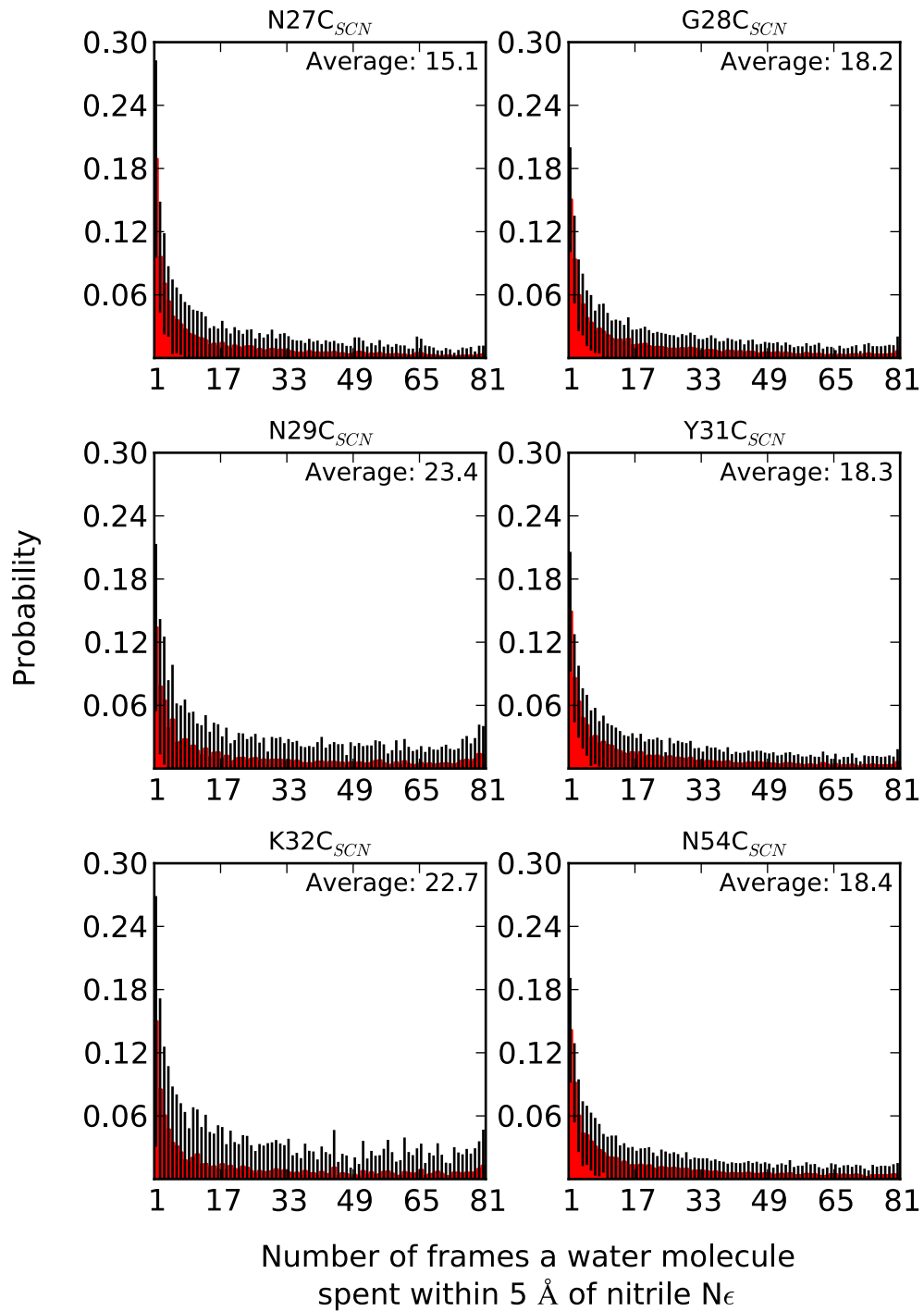


Figure 6-10: Probability of Water Lifetimes – Rap E30D/K31E

Observed probability of a water molecule being within 5 Å of the nitrile Nε for some number of frames in the simulation for various probe locations on the RalGDS monomer docked to Rap E30D/K31E. The error bar on each bin is the standard deviation among the 144 trajectories for that bin.

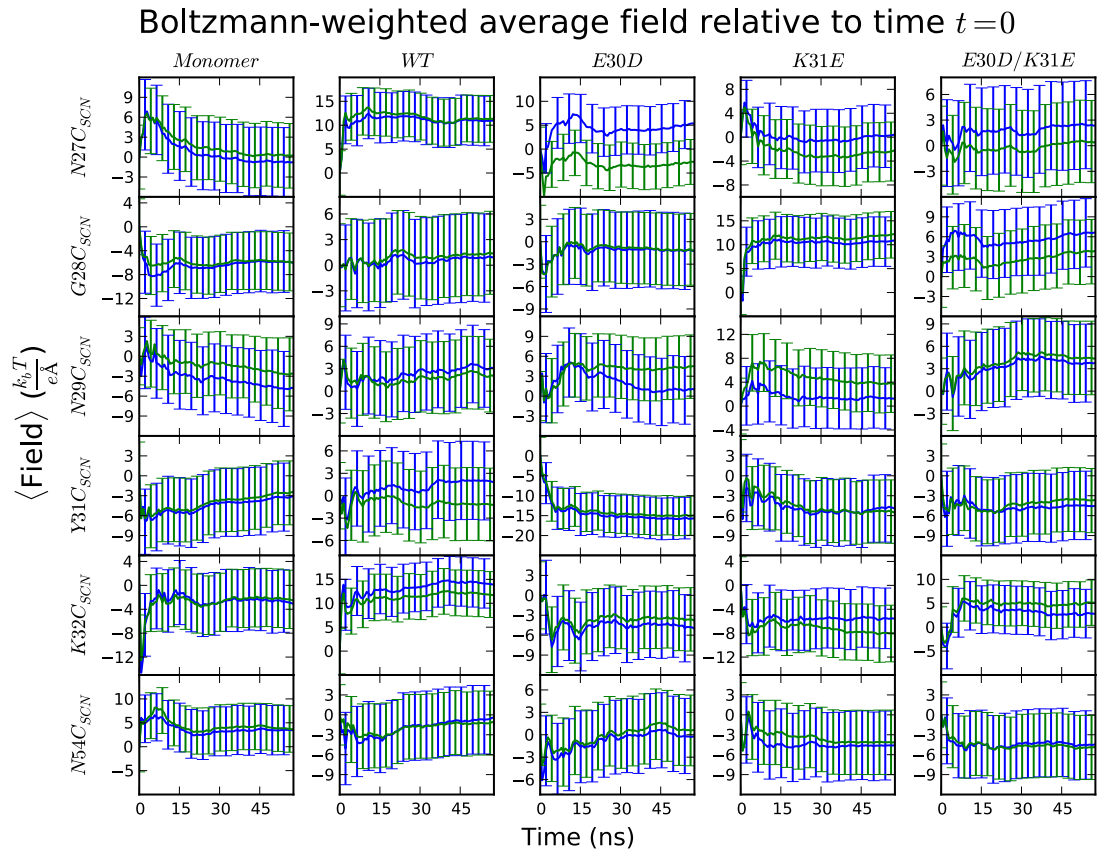


Figure 6-11: Average PB Field as a Function of Sampling Time

Boltzmann-weighted average field explicitly including water molecules within 5 Å of the nitrile Nε as a function of time relative to the field at time $t = 0$. Green: field calculated using the numeric field method; Blue: field calculated using the reaction field method. Error bars are standard deviations of the average field calculated from time $t = 0$ and $t = n\Delta t$.

Time gradient of the Boltzmann-weighted average field at time t

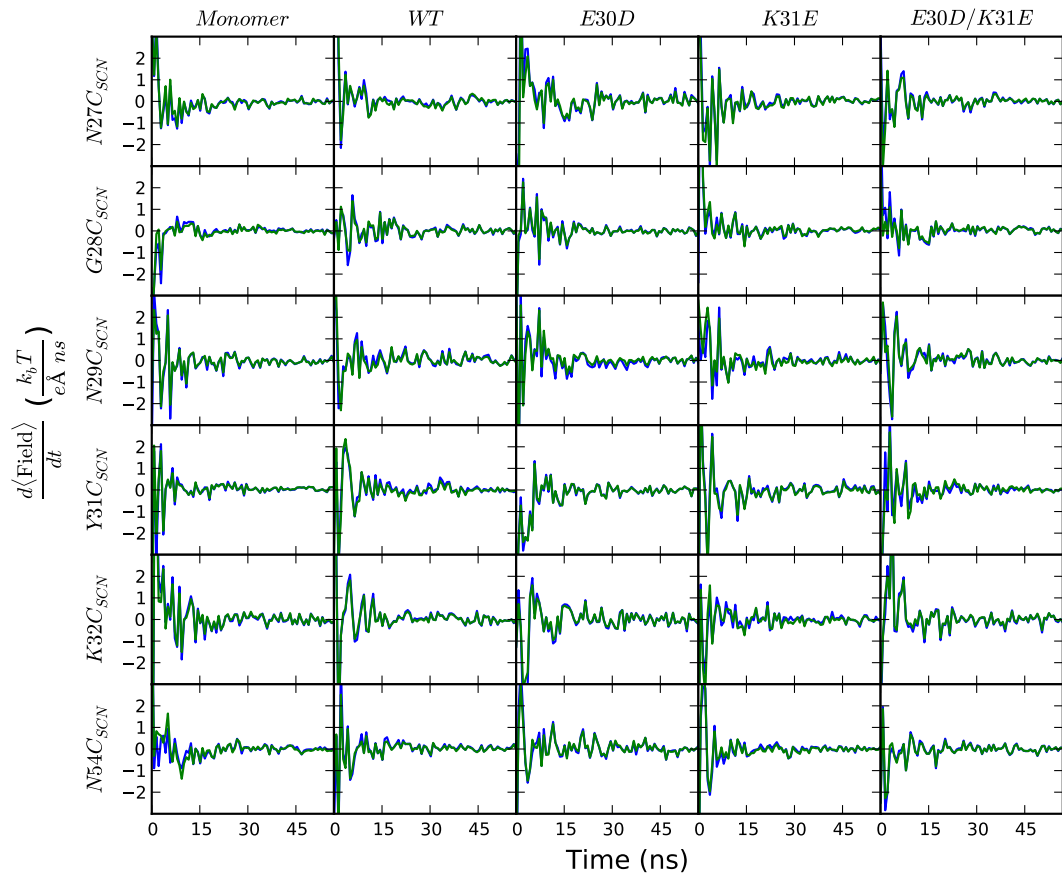


Figure 6-12: Average Field Gradient as a Function of Sampling Time

The first derivative with respect to time of the Boltzmann-weighted average field at each time step for the various Rap and RalGDS constructs. Green: numeric field method; Blue: reaction field method.

**SCN-labeled RaIGDS mutant
field differences docked with WT Rap**

Numeric PBE field

Reaction field method

5 Å Water Sphere

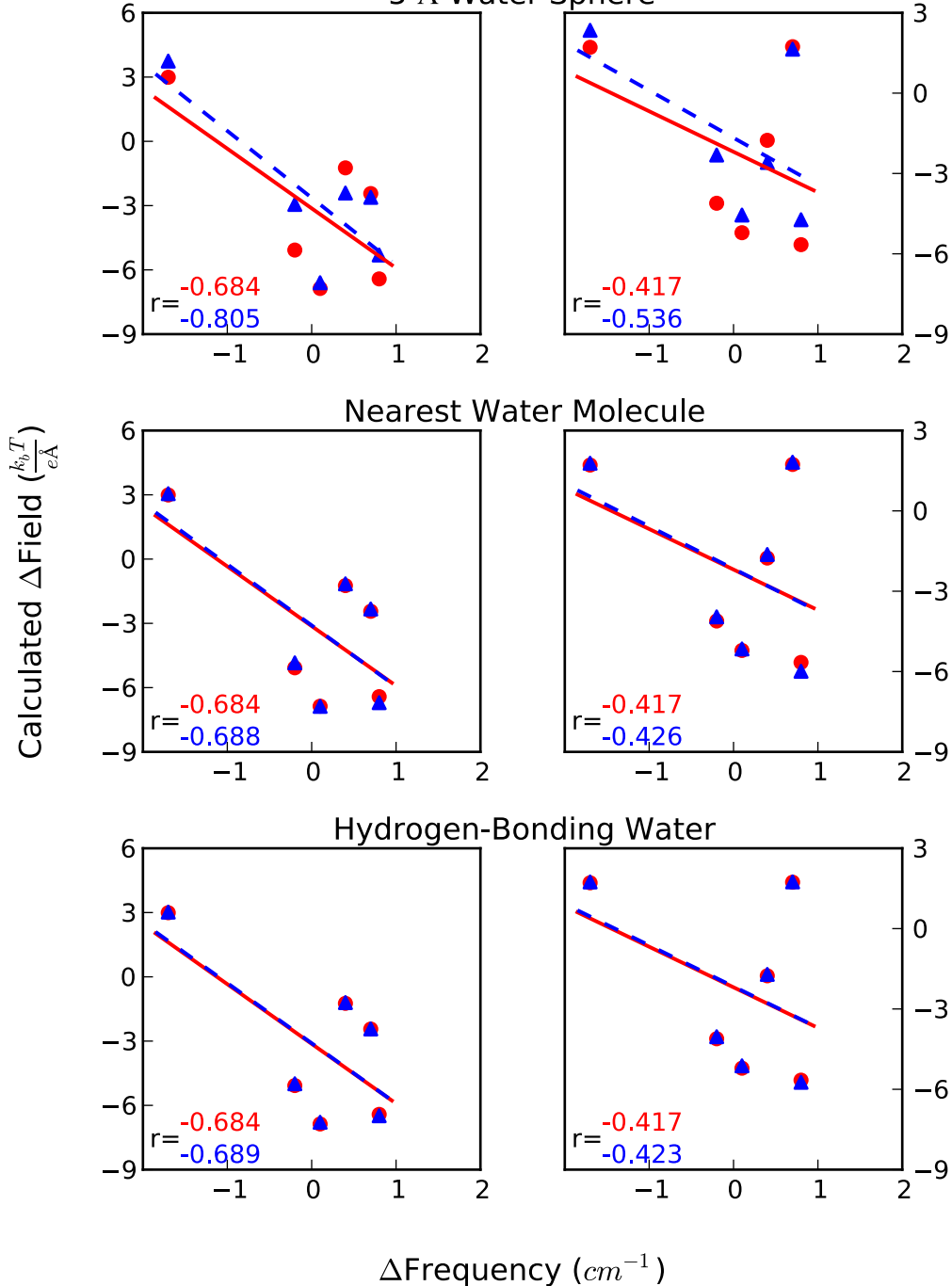


Figure 6-13: PB Relative Field Plots – Rap E30/K31

The relative field calculations using the numeric LPBE solutions (left column) and from the numeric reaction field method (right column) compared to the experimental changes in frequencies for various nitrile probe locations on RalGDS upon docking to WT Rap. Red: originally reported, entirely implicit solvent fields; blue: fields using the solvent selection model described by the row subheading. Correlation coefficients are listed in the bottom left corner in the corresponding color. Standard deviations are approximately $\pm 1 \text{ cm}^{-1}$ and $\pm 6.5 \text{ k}_\text{b}\text{T}/\text{e}\text{\AA}$.

**SCN-labeled RaIGDS mutant
field differences docked with Rap E30D**
 Numeric PBE field Reaction field method
 5 Å Water Sphere

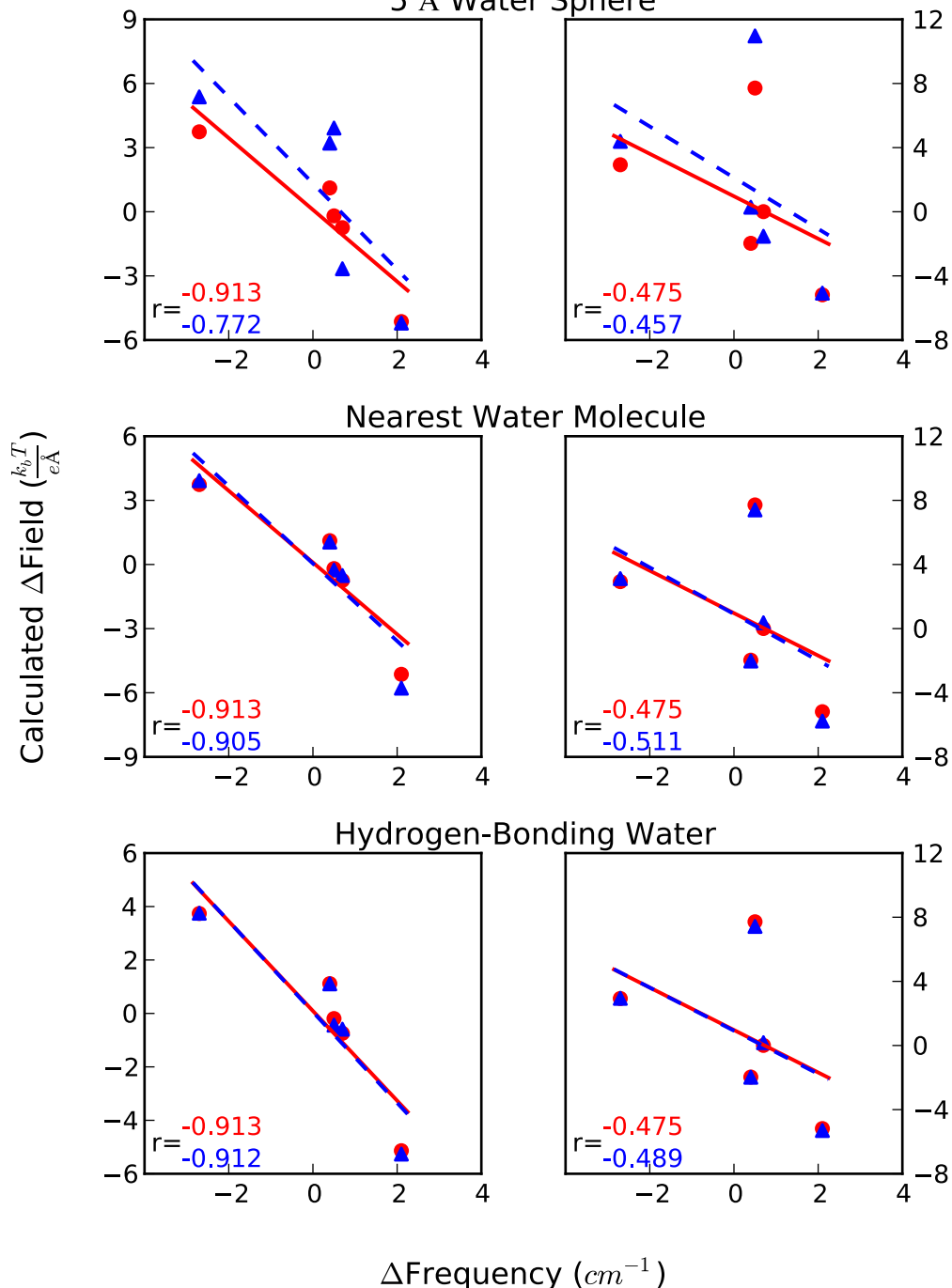


Figure 6-14: PB Relative Field Plots – Rap E30D/K31

The relative field calculations using the numeric LPBE solutions (left column) and from the numeric reaction field method (right column) compared to the experimental changes in frequencies for various nitrile probe locations on RalGDS upon docking to Rap E30D. Red: originally reported, entirely implicit solvent fields; blue: fields using the solvent selection model described by the row subheading. Correlation coefficients are listed in the bottom left corner in the corresponding color. Standard deviations are approximately $\pm 1 \text{ cm}^{-1}$ and $\pm 6.5 \text{ k}_\text{b}\text{T}/\text{e}\text{\AA}$.

**SCN-labeled RalGDS mutant
field differences docked with Rap K31E**
 Numeric PBE field Reaction field method

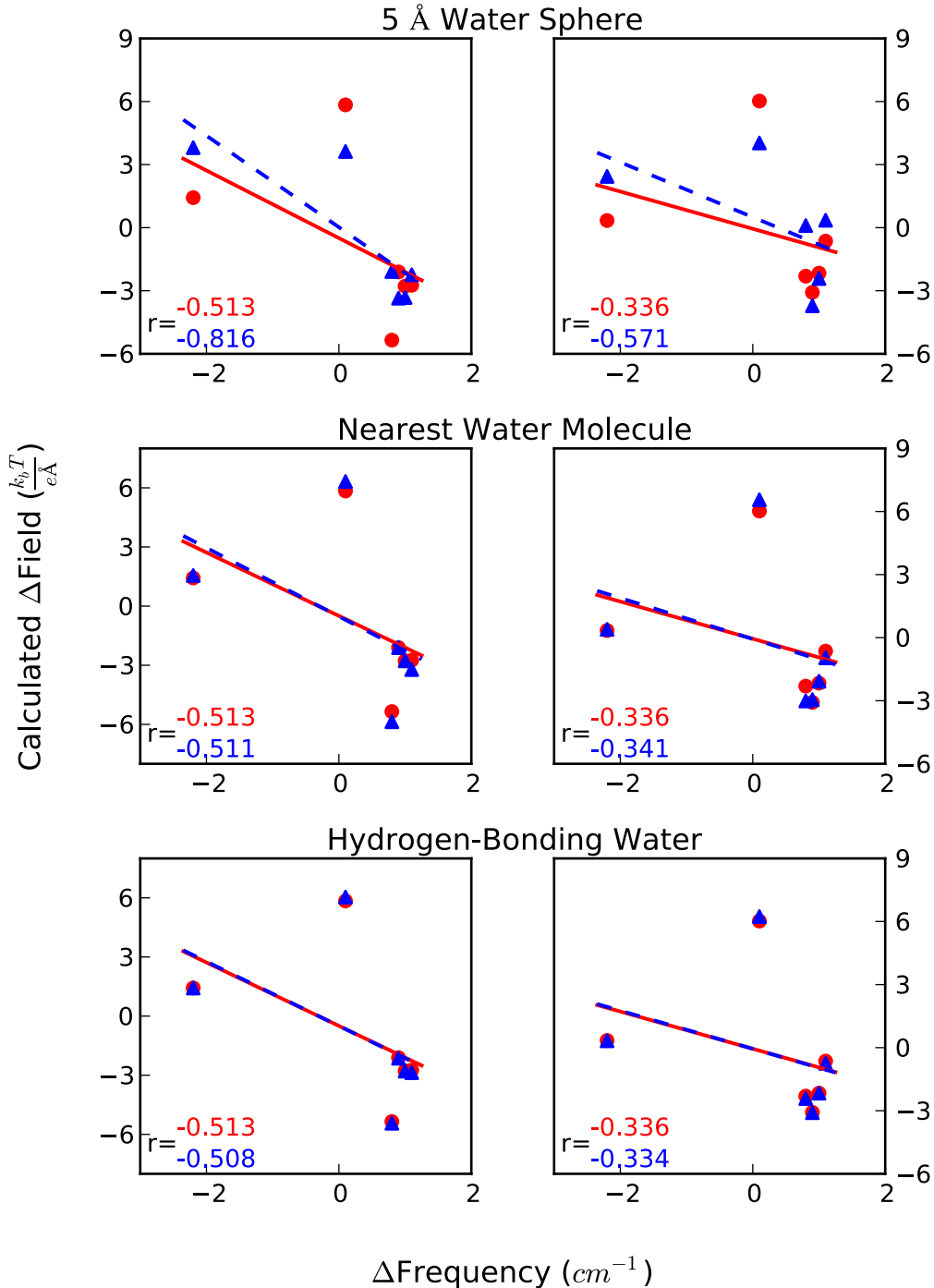


Figure 6-15: PB Relative Field Plots – Rap E30/K31E

The relative field calculations using the numeric LPBE solutions (left column) and from the numeric reaction field method (right column) compared to the experimental changes in frequencies for various nitrile probe locations on RalGDS upon docking to Rap K31E. Red: originally reported, entirely implicit solvent fields; blue: fields using the solvent selection model described by the row subheading. Correlation coefficients are listed in the bottom left corner in the corresponding color. Standard deviations are approximately $\pm 1 \text{ cm}^{-1}$ and $\pm 6.5 \text{ k}_\text{b}\text{T}/\text{e}\text{\AA}$.

**SCN-labeled RaIGDS mutant
field differences docked with Rap E30D/K31E**

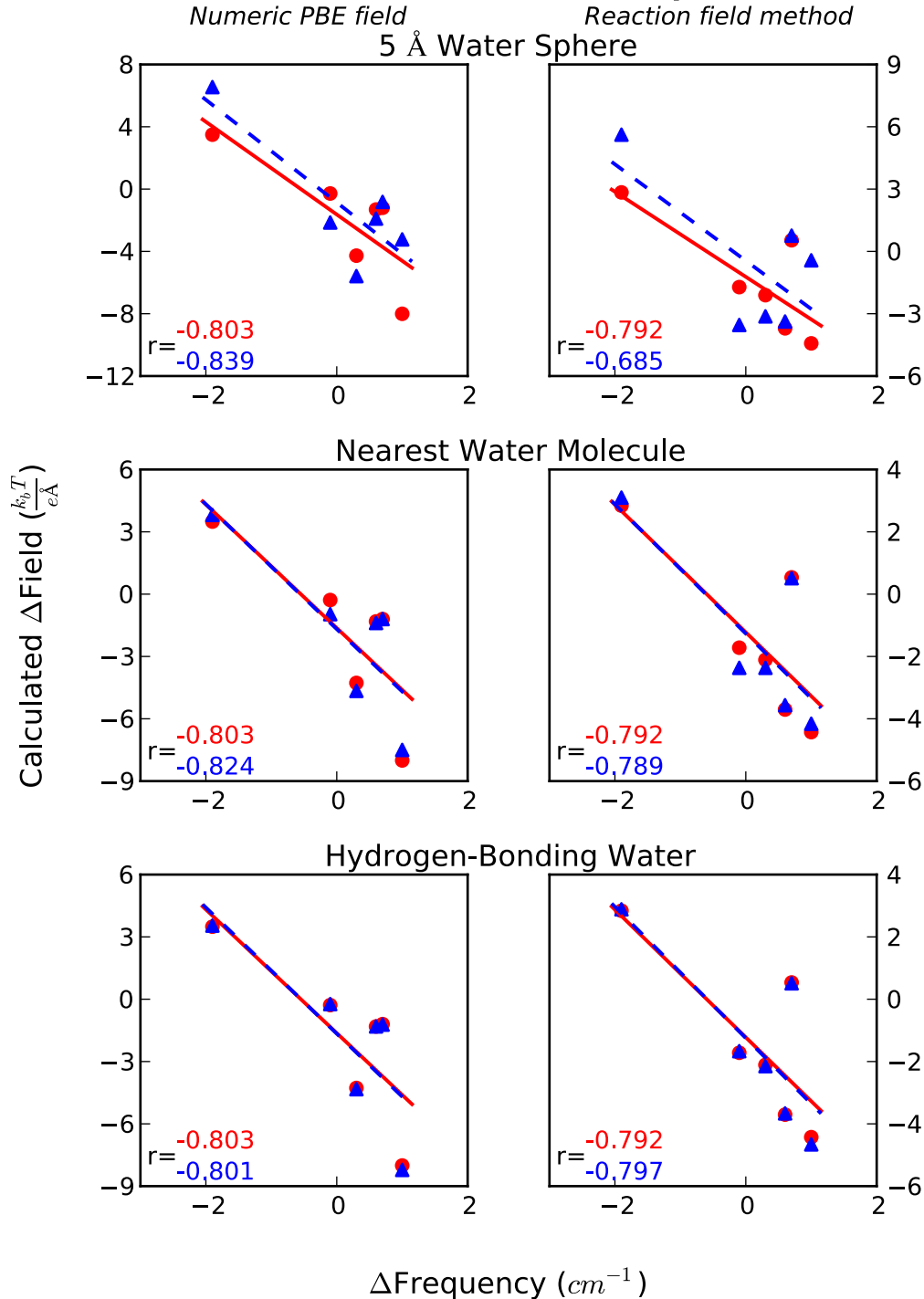


Figure 6-16: PB Relative Field Plots – Rap E30D/K31E

The relative field calculations using the numeric LPBE solutions (left column) and from the numeric reaction field method (right column) compared to the experimental changes in frequencies for various nitrile probe locations on RalGDS upon docking to Rap E30D/K31E. Red: originally reported, entirely implicit solvent fields; blue: fields using the solvent selection model described by the row subheading. Correlation coefficients are listed in the bottom left corner in the corresponding color. Standard deviations are approximately $\pm 1 \text{ cm}^{-1}$ and $\pm 6.5 \text{ k}_b\text{T/e}\text{\AA}$.

Chapter 7 Electrostatic Fields at Protein-Protein Interfaces: Increased Sampling Time and Various Electrostatic Methods: A Case for Simulating in Polarizable Force Fields

7.1 INTRODUCTION

<Body text to begin here.>

7.2 RESULTS

<Body text to begin here.>

7.3 DISCUSSION

<Body text to begin here.>

Chapter 8 Electrostatic Fields in Small Thiocyanate Molecules with Ensembles Generated using the AMOEBA Force Field

8.1 INTRODUCTION

<Body text to begin here.>

8.2 RESULTS

<Body text to begin here.>

8.3 DISCUSSION

<Body text to begin here.>

Appendix

Glossary

This page is optional—must be placed in this order if it is included in the dissertation. If you don't want to include a glossary, then delete the entire page and the following page break.

References

1. Weimann, A.; Zantop, T.; Rummler, M.; Hassenpflug, J.; Petersen, W., Primary stability of bone-patellar tendon-bone graft fixation with biodegradable pins. *Arthroscopy* **2003**, *19* (10), 1097-1102.
2. Gunner, M. R.; Nicholls, A.; Honig, B., Electrostatic Potentials in Rhodopseudomonas viridis Reaction Centers: Implications for the Driving Force and Directionality of Electron Transfer. *J. Phys. Chem.* **1996**, *100*, 4277-4291.
3. Honig, B.; Nicholls, A., Classical Electrostatics in Biology and Chemistry. *Science* **1995**, *268*, 1144-1149.
4. Nielsen, J. E.; Andersen, K. V.; Honig, B.; Hooft, R. W. W.; Klebe, G.; Vriend, G.; Wade, R. C., Improving Macromolecular Electrostatics Calculations. *Protein Eng.* **1999**, *12*, 657-662.
5. Warshel, A., What about protein polarity? *Nature* **1987**, *330*, 15-16.
6. Warshel, A.; Levitt, M., Theoretcial Studies of Enzymic Reactions: Dielectric, Electrostatic and Steric Stabilization of the Carbonium Ion in the Reaction of Lysozyme. *J. Mol. Biol.* **1976**, *103*, 227-249.
7. Warshel, A.; Papazyan, A., Electrostatic effects in macromolecules: fundamental concepts and practical modeling. *Curr. Opin. Struct. Biol.* **1998**, *8*, 211-217.
8. Ensign, D. L.; Webb, L. J., Statistical, Geometric, and Physical Factors Determining Electrostatic Fields at the Ras/Effecter Interface. **2010**, *in preparation*.
9. Jiao, D.; King, C.; Grossfield, A.; Darden, T. A.; Ren, P. Y., Simulation of Ca²⁺ and Mg²⁺ solvation using polarizable atomic multipole potential. *J Phys Chem B* **2006**, *110* (37), 18553-18559.
10. Petersen, A.; Aarestrup, F. M.; Hofshagen, M.; Sipila, H.; Franklin, A.; Gunnarsson, E., Harmonization of antimicrobial susceptibility testing among veterinary diagnostic laboratories in the five Nordic countries. *Microb Drug Resist* **2003**, *9* (4), 381-388.
11. Jiao, D.; Golubkov, P. A.; Darden, T. A.; Ren, P., Calculation of protein-ligand binding free energy by using a polarizable potential. *Proc. Natl. Acad. Sci.* **2008**, *105*, 6290-6295.
12. Burrell, K. H.; Allen, S. L.; Anderson, P. M.; Austin, M. E.; Baity, W. F.; Bakalarski, J. P.; Baker, D. R.; Baldwin, D. E.; Barber, D. E. G.; Bastasz, R., et al., Overview of recent experimental results from the DIII-D advanced tokamak program. *Nucl Fusion* **2003**, *43* (12), 1555-1569.
13. Ponder, J. W.; Wu, C.; Ren, P.; Pande, V. S.; Chodera, J. D.; Schnieders, M. J.; Haque, I.; Mobley, D. L.; Lambrecht, D. S.; DiStasio, R. A., et al., Current Status of the AMOEBA Polarizable Force Field. *J. Phys. Chem. B* **2010**, *114*, 2549-2564.
14. Petersen, R. K.; Jorgensen, C.; Rustan, A. C.; Froyland, L.; Muller-Decker, K.; Furstenberger, G.; Berge, R. K.; Kristiansen, K.; Madsen, L., Arachidonic acid-dependent inhibition of adipocyte differentiation requires PKA activity and is associated with sustained expression of cyclooxygenases. *J Lipid Res* **2003**, *44* (12), 2320-2330.

15. Schnieders, M. J.; Baker, N. A.; Ren, P.; Ponder, J. W., Polarizable Atomic Multipole Solutes in a Poisson-Boltzmann Continuum. *J. Chem. Phys.* **2007**, *126*, 124114-1-47.
16. Petersen, T. W.; van den Engh, G., Stability of the breakoff point in a high-speed cell sorter. *Cytom Part A* **2003**, *56A* (2), 63-70.
17. Lindquist, B. A.; Corcelli, S. A., Nitrile Groups as Vibrational Probes: Calculations of the CN Infrared Absorption Line Shape of Acetonitrile in Water and Tetrahydrofuran. *J. Phys. Chem. B* **2008**, *112*, 6301-6303.
18. Lindquist, B. A.; Haws, R. T.; Corcelli, S. A., Optimized Quantum Mechanics/Molecular Mechanics Strategies for Nitrile Vibrational Probes: Acetonitrile and para-Tolunitrile in Water and Tetrahydrofuran. *J. Phys. Chem. B* **2008**, *112*, 13991-14001.
19. Goforth, H. W.; Laurent, D.; Prusaczyk, W. K.; Schneider, K. E.; Petersen, K. F.; Shulman, G. I., Effects of depletion exercise and light training on muscle glycogen supercompensation in men. *Am J Physiol-Endoc M* **2003**, *285* (6), E1304-E1311.
20. Beghetto, E.; Buffolano, W.; Spadoni, A.; Del Pezzo, M.; Di Cristina, M.; Minenkova, O.; Petersen, E.; Felici, F.; Gargano, N., Use of an immunoglobulin G avidity assay based on recombinant antigens for diagnosis of primary Toxoplasma gondii infection during pregnancy. *J Clin Microbiol* **2003**, *41* (12), 5414-5418.
21. Wolkoff, P.; Skov, P.; Franck, C.; Petersen, L. N., Eye irritation and environmental factors in the office environment - hypotheses, causes and a physiological model. *Scand J Work Env Hea* **2003**, *29* (6), 411-430.
22. Allen, R.; Petersen, S.; Moore, P.; Allen, L.; Heller, Y.; Gurewitsch, E., Do antepartum and intrapartum risk factors differ between mild and severe shoulder dystocia? *Am J Obstet Gynecol* **2003**, *189* (6), S208-S208.
23. Mayo, A. L.; Morris, T. H.; Peltier, S.; Petersen, E. C.; Payne, K.; Holman, L. S.; Tingey, D.; Fogel, T.; Black, B. J.; Gibbs, T. D., Active and inactive groundwater flow systems: Evidence from a stratified, mountainous terrain. *Geol Soc Am Bull* **2003**, *115* (12), 1456-1472.
24. Petersen, J. E.; Kemp, W. M.; Bartleson, R.; Boynton, W. R.; Chen, C. C.; Cornwell, J. C.; Gardner, R. H.; Hinkle, D. C.; Houde, E. D.; Malone, T. C., et al., Multiscale experiments in coastal ecology: Improving realism and advancing theory. *Bioscience* **2003**, *53* (12), 1181-1197.
25. Perseghin, G.; Petersen, K.; Shulman, G. I., Cellular mechanism of insulin resistance: potential links with inflammation. *Int J Obesity* **2003**, *27*, S6-S11.
26. Petersen, K. K.; Hansen, C. W., Compact Campanula carpatica 'Uniform' without chemical growth regulators. *Eur J Hortic Sci* **2003**, *68* (6), 266-+.
27. Cerutti, D. S.; Baker, N. A.; McCammon, J. A., Solvent Reaction Field Potential inside an Uncharged Globular Protein: A Bridge between Implicit and Explicit Solvent Models. *J. Chem. Phys.* **2007**, *127*, 10.1063/1.2771171-1-28.
28. Petersen, G.; Martin, U.; Singhal, A.; Criner, G. J., Intralobar sequestration in the middle-aged and elderly adult: Recognition and radiographic evaluation. *J Thorac Cardiov Sur* **2003**, *126* (6), 2086-2090.

29. Choi, J. H.; Oh, K. I.; Lee, H.; Lee, C.; Cho, M., Nitrile and thiocyanate IR probes: Quantum chemistry calculation studies and multivariate least-square fitting analysis. *J. Chem. Phys.* **2008**, *128*, 134506.
30. Oh, K. I.; Choi, J. H.; Lee, J. H.; Han, J. B.; Lee, H.; Cho, M., Nitrile and thiocyanate IR probes: Molecular dynamics simulation studies. *J. Chem. Phys.* **2008**, *128*, 154504.
31. Eves, N. D.; Petersen, S. R.; Jones, R. L., Effects of helium and 40% O₂ on graded exercise with self-contained breathing apparatus. *Can J Appl Physiol* **2003**, *28* (6), 910-926.
32. Sheu, S. Y.; Yang, D. Y., Determination of Protein Surface Hydration Shell Free Energy of Water Motion: Theoretical Study and Molecular Dynamics Simulation. *J Phys Chem B* **2010**, *114* (49), 16558-16566.
33. Thorbjorn, L.; Petersen, G. H., The epifauna on the carbonate reefs in the Arctic Ikka Fjord, SW Greenland. *Ophelia* **2003**, *57* (3), 177-201.
34. Petersen, P. E., The World Oral Health Report 2003: continuous improvement of oral health in the 21st century - the approach of the WHO Global Oral Health Programme. *Community Dent Oral* **2003**, *31*, 3-23.
35. Stafford, A. J.; Ensign, D. L.; Webb, L. J., Vibrational Stark Effect Spectroscopy at the Interface of Ras and Rap1A Bound to the Ras Binding Domain of RaIGDS Reveals an Electrostatic Mechanism for Protein-Protein Interaction. *J. Phys. Chem. B* **2010**, *114*, 15331-15344.
36. Van der Spoel, D.; Lindahl, E.; Hess, B.; Groenhof, G.; Mark, A. E.; Berendsen, H. J. C., Gromacs: Fast, Flexible, and Free. *J Comput Chem* **2005**, *26* (16), 1701-1718.
37. Geyer, M.; Herrmann, C.; Wohlgemuth, S.; Wittinghofer, A.; Kalbitzer, H. R., Structure of the Ras-binding domain of RaIGEF and implications for Ras binding and signalling. *Nat. Struct. Biol.* **1997**, *4*, 694-699.
38. Huang, L.; Hofer, F.; Martin, G. S.; Kim, S. H., Structural basis for the interaction of Ras with RaIGDS. *Nat. Struct. Biol.* **1998**, *5*, 422-426.
39. Nassar, N.; Horn, G.; Herrmann, C.; Scherer, A.; McCormick, F.; Wittinghofer, A., The 2.2 Å crystal structure of the Ras-binding domain of the serine/threonine kinase c-Raf1 in complex with Rap1A and a GTP analogue. *Nature* **1995**, *375* (6532), 554-560.
40. Case, D. A.; Darden, T. A.; Cheatham, T. E.; Simmerling, C. L.; Wang, J.; Duke, R. E.; Luo, R.; Walker, R. C.; Zhang, W.; Merz, K. M., et al., *AMBER 11*. University of California, San Francisco: 2010.
41. Qamra, R.; Hubbard, S., - Structural basis for the interaction of the adaptor protein grb14 with activated. - *PLoS One*. 2013 Aug 13;8(8):e72473. doi: 10.1371/journal.pone.0072473. eCollection (- 1932-6203 (Electronic)).
42. Ensign, D. L.; Webb, L. J., Factors Determining Electrostatic Fields at the Ras/Effecter Interface. *Proteins* **2011**, *79*, 3511-3524.
43. Ragain, C. M.; Newberry, R. W.; Ritchie, A. W.; Webb, L. J., Role of Electrostatics in Differential Binding of RaIGDS to Rap Mutations E30D and K31E Investigated by Vibrational Spectroscopy of Thiocyanate Probes. *J Phys Chem B* **2012**, *116* (31), 9326-9336.

44. Jorgensen, W. L.; Chandrasekhar, J.; Madura, J. D.; Impey, R. W.; Klein, M. L., Comparison of Simple Potential Functions for Simulating Liquid Water. *J Chem Phys* **1983**, *79* (2), 926-935.
45. Dolinsky, T. J.; Czodrowski, P.; Li, H.; Nielsen, J. E.; Jensen, J. H.; Klebe, G.; Baker, N. A., PDB2PQR: expanding and upgrading automated preparation of biomolecular structures for molecular simulations. *Nucleic Acids Res* **2007**, *35*, W522-W525.
46. Dolinsky, T. J.; Nielsen, J. E.; McCammon, J. A.; Baker, N. A., PDB2PQR: an automated pipeline for the setup of Poisson-Boltzmann electrostatics calculations. *Nucleic Acids Res* **2004**, *32*, W665-W667.
47. McCleverty, C. J.; Columbus, L.; Kreusch, A.; Lesley, S. A., Structure and ligand binding of the soluble domain of a Thermotoga maritima membrane protein of unknown function TM1634. *Protein Sci* **2008**, *17*, 869.
48. Humphrey, W.; Dalke, A.; Schulten, K., VMD - Visual Molecular Dynamics. *J. Molec. Graphics* **1996**, *14*, 33-38.
49. van der Spoel, D.; Lindahl, E.; Hess, B.; Groenhof, G.; Mark, A. E.; Berendsen, H. J. C., GROMACS: Fast, Flexible, and Free. *J. Comput. Chem.* **2005**, *26*, 1701-1718.
50. Smith, T. F.; Waterman, M. S., Identification of Common Molecular Subsequences. *J Mol Biol* **1981**, *147* (1), 195-197.
51. Russell, R. B.; Barton, G. J., Multiple protein sequence alignment from tertiary structure comparison. *PROTEINS: Struct. Funct. Genet.* **1992**, *14*, 309-323.
52. Duan, Y.; Wu, C.; Chowdhury, S.; Lee, M. C.; Xiong, G.; Zhang, W.; Yang, R.; Cieplak, P.; Luo, R.; Lee, T., et al., A Point-Charge Force Field for Molecular Mechanics Simulations of Proteins Based on Condensed-Phase Quantum Mechanical Calculations. *J. Comput. Chem.* **2003**, *24*, 1999-2012.
53. Darden, T.; York, D.; Pedersen, L. G., Particle mesh Ewald: An $N \log(N)$ method for Ewald sums in large systems. *J. Chem. Phys.* **1993**, *98*, 10089-10092.
54. Essmann, U.; Perera, L.; Berkowitz, M. L.; Darden, T.; Lee, H.; Pedersen, L. G., A smooth particle mesh Ewald method. *J. Chem. Phys.* **1995**, *103*, 8577-8593.
55. Hess, B.; Bekker, H.; Berendsen, H. J. C.; Fraaije, J. G. E. M., - LINCS: A linear constraint solver for molecular simulations. **1997**, *- 18 (- 12)*, - 1472.
56. Roux, B., The calculation of the potential of mean force using computer simulations. *Comp. Phys. Commun.* **1995**, *91*, 275-282.
57. Gallicchio, E.; Andrec, M.; Felts, A. K.; Levy, R. M., Temperature Weighted Histogram Analysis Method, Replica Exchange, and Transition Paths. *J. Phys. Chem. B* **2005**, *109*, 6722-6731.
58. Mardia, K. V., Statistics of Directional Data. *J. Roy. Statist. Soc. Ser. B (Methodol.)* **1975**, *37* (3), 349-393.
59. Berendsen, H. J. C.; Spoel, D. v. d.; Drunen, R. v., GROMACS: A message-passing parallel molecular dynamics implementation. *Comp. Phys. Commun.* **1995**, *91*, 43-56.

60. Hess, B.; Kutzner, C.; van der Spoel, D.; Lindahl, E., GROMACS 4: Algorithms for highly efficient, load-balanced, and scalable molecular simulation. *J Chem Theory Comput* **2008**, *4* (3), 435-447.
61. Lindahl, E.; Hess, B.; Spoel, D. v. d., GROMACS 3.0: A package for molecular simulation and trajectory analysis. *J. Mol. Mod.* **2001**, *7*, 306-317.
62. Honig, B.; Nicholls, A., Classical Electrostatics in Biology and Chemistry. *Science* **1995**, *268* (5214), 1144-1149.
63. Fogolari, F.; Brigo, A.; Molinari, H., The Poisson-Boltzmann equation for biomolecular electrostatics: a tool for structural biology. *J Mol Recognit* **2002**, *15* (6), 377-392.
64. Fogolari, F.; Zuccato, P.; Esposito, G.; Viglino, P., Biomolecular electrostatics with the linearized Poisson-Boltzmann equation. *Biophys J* **1999**, *76* (1), 1-16.
65. Holst, M.; Saied, F., Multigrid Solution of the Poisson-Boltzmann Equation. *J Comput Chem* **1993**, *14* (1), 105-113.
66. Holst, M. J.; Saied, F., Numerical-Solution of the Nonlinear Poisson-Boltzmann Equation - Developing More Robust and Efficient Methods. *J Comput Chem* **1995**, *16* (3), 337-364.
67. Warshel, A.; Sharma, P. K.; Kato, M.; Parson, W. W., Modeling electrostatic effects in proteins. *Biochim. Biophys. Acta* **2006**, *1764*, 1647-1676.
68. Schnieders, M. J.; Baker, N. A.; Ren, P. Y.; Ponder, J. W., Polarizable atomic multipole solutes in a Poisson-Boltzmann continuum. *J Chem Phys* **2007**, *126* (12).
69. Schutz, C. N.; Warshel, A., What are Dielectric "Constants" of Proteins and How to Validate Electrostatic Models? *Proteins* **2001**, *44*, 400-417.
70. Ensign, D. L.; Webb, L. J., *Submitted 2013*.
71. Le Questel, J. Y.; Berthelot, M.; Laurence, C., Hydrogen-bond acceptor properties of nitriles: a combined crystallographic and ab initio theoretical investigation. *J Phys Org Chem* **2000**, *13* (6), 347-358.
72. Fafarman, A. T.; Webb, L. J.; Chuang, J. I.; Boxer, S. G., Site-Specific Conversion of Cysteine Thiols into Thiocyanate Creates an IR Probe for Electric Fields in Proteins. *J. Am. Chem. Soc.* **2006**, *128*, 13356-13357.
73. Webb, L. J.; Boxer, S. G., Electrostatic Fields Near the Active Site of Human Aldose Reductase: 1. New Inhibitors and Vibrational Stark Effect Measurements. *Biochemistry* **2008**, *47*, 1588-1598.
74. Suydam, I. T.; Snow, C. D.; Pande, V. S.; Boxer, S. G., Electric Fields at the Active Site of an Enzyme: Direct Comparison of Experiment with Theory. *Science* **2006**, *313*, 200-204.
75. Andrews, S. S.; Boxer, S. G., Vibrational Stark Effects of Nitriles I. Methods and Experimental Results. *J. Phys. Chem. A* **2000**, *104*, 11853-11863.
76. Andrews, S. S.; Boxer, S. G., Vibrational Stark Effects of Nitriles II. Physical Origins of Stark Effects from Experiment and Perturbation Models. *J. Phys. Chem. A* **2002**, *106*, 469-477.
77. Suydam, I. T.; Boxer, S. G., Vibrational Stark Effects Calibrate the Sensitivity of Vibrational Probes for Electric Fields in Proteins. *Biochemistry* **2003**, *42*, 12050-12055.

78. Fafarman, A. T.; Boxer, S. G., Nitrile Bonds as Infrared Probes of Electrostatics in Ribonuclease S. *J Phys Chem B* **2010**, *114* (42), 13536-13544.
79. Ritchie, A. W.; Webb, L. J., Optimizing Electrostatic Field Calculations with the Adaptive Poisson-Boltzmann Solver to Predict Electric Fields at Protein-Protein Interfaces I: Sampling and Focusing. *J Phys Chem B* **2013**, *117* (39), 11473-11489.
80. Krauss, G., *Biochemistry of Signal Transduction and Regulation*. 3 ed.; WILEY-VCH Verlag: Weinheim, Germany, 2003.
81. Cox, A. D.; Der, C. J., The dark side of Ras: regulation of apoptosis. *Oncogene* **2003**, *22*, 8999-9006.
82. Downward, J., Targeting Ras Signalling Pathways in Cancer Therapy. *Nature Canc. Rev.* **2002**, *3*, 11-22.
83. Repasky, G. A.; Chenette, E. J.; Der, C. J., Renewing the conspiracy theory debate: does Raf function alone to mediate Ras oncogenesis? *Trends Cell Biol.* **2004**, *14*, 639-647.
84. Thomas, C.; Fricke, I.; Scrima, A.; Berken, A.; Wittinghofer, A., Structural Evidence for a Common Intermediate in Small G Protein-GEF Reactions. *Molecular Cell* **2007**, *25* (1), 141-149.
85. Wu, C.; Lai, C.-F.; Mobley, W. C., Nerve Growth Factor Activates Persistent Rap1 Signaling in Endosomes. *The Journal of Neuroscience* **2001**, *21* (15), 5406-5416.
86. Alexov, E.; Mehler, E. L.; Baker, N.; Baptista, A. M.; Huang, Y.; Milletti, F.; Nielsen, J. E.; Farrell, D.; Carstensen, T.; Olsson, M. H. M., et al., Progress in the prediction of pK(a) values in proteins. *Proteins-Structure Function and Bioinformatics* **2011**, *79* (12), 3260-3275.
87. Herrmann, C., Ras-effector interactions: after one decade. *Curr. Opinion Struct. Biol.* **2003**, *13*, 122-129.
88. Rudolph, M. G.; Linnemann, T.; Grunewald, P.; Wittinghofer, A.; Vetter, I. R.; Herrmann, C., Thermodynamics of Ras/Effector and Cdc42/Effector Interactions Probed by Isothermal Titration Calorimetry. *J. Biol. Chem.* **2001**, *276*, 23914-23921.
89. Herrmann, C.; Horn, G.; Spaargaren, M.; Wittinghofer, A., Differential Interactions of the Ras Family of GTP-binding Proteins H-Ras, Rap1A, and R-Ras with the Putative Effector Molecules Raf Kinase and Ral-Guanine Nucleotide Exchange Factor. *J. Biol. Chem.* **1996**, *271*, 6794-6800.
90. Nassar, N.; Horn, G.; Herrmann, C.; Block, C.; Janknecht, R.; Wittinghofer, A., Ras/Rap effector specificity determined by charge reversal. *Nat. Struct. Biol.* **1996**, *3*, 723-729.
91. Davis-Searles, P. R.; Saunders, A. J.; Erie, D. A.; Winzor, D. J.; Pielak, G. J., INTERPRETING THE EFFECTS OF SMALL UNCHARGED SOLUTES ON PROTEIN-FOLDING EQUILIBRIA. *Annual Review of Biophysics and Biomolecular Structure* **2001**, *30* (1), 271-306.
92. Lee, L. P.; Tidor, B., Optimization of Binding Electrostatics: Charge Complementarity in the Barnase-Barstar Protein Complex. *Protein Science* **2001**, *10*, 362-377.

93. Simonson, T., Macromolecular electrostatics: continuum models and their growing pains. *Curr. Opin. Struct. Biol.* **2001**, *11*, 243-252.
94. Villa, J.; Warshel, A., Energetics and Dynamics of Enzymatic Reactions. *J. Phys. Chem. B* **2001**, *105*, 7887-7907.
95. Nielsen, J. E.; Gunner, M. R.; Garcia-Moreno, E. B., The pK(a) Cooperative: A collaborative effort to advance structure-based calculations of pK(a) values and electrostatic effects in proteins. *Proteins-Structure Function and Bioinformatics* **2011**, *79* (12), 3249-3259.
96. Jiao, D.; Zhang, J.; Duke, R. E.; Li, G.; Schnieders, M. J.; Ren, P., Trypsin-Ligand Binding Free Energies from Explicit and Implicit Solvent Simulations with Polarizable Potential. *J. Comput. Chem.* **2009**, *30*, 1701-1711.
97. Jiao, D. A.; Ren, P. Y., Calculation of protein-ligand binding free energy by a polarizable force field. *Abstr Pap Am Chem S* **2009**, 237.
98. Sigala, P. A.; Fafarman, A. T.; Bogard, P. E.; Boxer, S. G.; Herschlag, D., Do Ligand Binding and Solvent Exclusion Alter the Electrostatic Character within the Oxyanion Hole of an Enzymatic Active Site. *J. Am. Chem. Soc.* **2007**, *129*, 12104-12105.
99. Zhong, S.; MacKerell, A. D., Binding Response: A Descriptor for Selecting Ligand Binding Site on Protein Surfaces. *J. Chem. Inf. Model.* **2007**, *47*, 2303-2315.
100. Alakoskela, J. M. I.; Kinnunen, P. K. J., Control of a Redox Reaction on Lipid Bilayer Surfaces by Membrane Dipole Potential. *Biophys. J.* **2001**, *80*, 294-304.
101. Alakoskela, J. M. I.; Soderlund, T.; Holopainen, J. M.; Kinnunen, P. K. J., Dipole Potential and Head-Group Spacing are Determinants for the Membrane Partitioning of Pregnanolone. *Mol. Pharma.* **2004**, *66*, 161-168.
102. Baker, N. A.; Sept, D.; Joseph, S.; Holst, M. J.; McCammon, J. A., Electrostatics of nanosystems: Application to microtubules and the ribosome. *Proc. Natl. Acad. Sci.* **2001**, *98*, 10037-10041.
103. Baran, K. L.; Chimenti, M. S.; Schlessman, J. L.; Fitch, C. A.; Herbst, K. J.; Garcia-Moreno, B. E., Electrostatic Effects in a Network of Polar and Ionizable Groups in Staphylococcal Nuclease. *J. Mol. Biol.* **2008**, *379*, 1045-1062.
104. Bredenberg, J. H.; Russo, C.; Fenley, M. O., Salt-Mediated Electrostatics in the Association of TATA Binding Proteins to DNA: A Combined Molecular Mechanics/Poisson-Boltzman Study. *Biophys. J.* **2008**, *94*, 4634-4645.
105. Cui, Q.; Sulea, T.; Schrag, J. D.; Munger, C.; Hung, M. N.; Naim, M.; Cygler, M.; Purisima, E. O., Molecular-Dynamics-Solvated Interaction Energy Studies of Protein-Protein Interactions: The MP1-p14 Scaffolding Complex. *J. Mol. Biol.* **2008**, *379*, 787-802.
106. Gilson, M. K.; Honig, B. H., Calculation of Electrostatic Potentials in an Enzyme Active-Site. *Nature* **1987**, *330* (6143), 84-86.
107. Ji, C. G.; Zhang, J. Z. H., Electronic Polarization is Important in Stabilizing the Native Structures of Proteins. *J. Phys. Chem. B* **2009**, *113*, 16059-16064.
108. Kiel, C.; Selzer, T.; Shaul, Y.; Schreiber, G.; Herrmann, C., Electrostatically optimized Ras-binding Ral guanine dissociation stimulator mutants increase the rate of

- association by stabilizing the encounter complex. *Proc. Natl. Acad. Sci.* **2004**, *101*, 9223-9228.
109. Layfield, J. P.; Hammes-Schiffer, S., Calculation of Vibrational Shifts of Nitrile Probes in the Active Site of Ketosteroid Isomerase upon Ligand Binding. *J Am Chem Soc* **2013**, *135* (2), 717-725.
110. Lindquist, B. A.; Furse, K. E.; Corcelli, S. A., Nitrile groups as vibrational probes of biomolecular structure and dynamics: an overview. *Phys. Chem. Chem. Phys.* **2009**, *11*, 8119-8132.
111. Oh, K. I.; Choi, J. H.; Lee, J. H.; Han, J. B.; Lee, H.; Cho, M., Nitrile and thiocyanate IR probes: Molecular dynamics simulation studies. *J Chem Phys* **2008**, *128* (15).
112. Baker, N. A., Poisson-Boltzmann methods for biomolecular electrostatics. *Method Enzymol* **2004**, *383*, 94-+.
113. Rocchia, W.; Alexov, E.; Honig, B., Extending the Applicability of the Nonlinear Poisson-Boltzmann Equation: Multiple Dielectric Constants and Multivalent Ions. *J. Phys. Chem. B* **2001**, *105*, 6507-6514.
114. Simonson, T.; Archontis, G.; Karplus, M., A Poisson-Boltzmann Study of Charge Insertion in an Enzyme Active Site: The Effect of Dielectric Relaxation. *J. Phys. Chem. B* **1999**, *103*, 6142-6156.
115. Teixeira, V. H.; Cunha, C. A.; Machuqueiro, M.; Oliveira, A. S. F.; Victor, B. L.; Soares, C. M.; Baptista, A. M., On the use of different dielectric constants for computing individual and pairwise terms in Poisson-Boltzmann studies of protein ionization equilibrium. *J Phys Chem B* **2005**, *109* (30), 14691-14706.
116. Swanson, J. M. J.; Adcock, S. A.; McCammon, J. A., Optimized radii for Poisson-Boltzmann calculations with the AMBER force field. *J Chem Theory Comput* **2005**, *1* (3), 484-493.
117. Jiao, D.; Zhang, J. J.; Duke, R. E.; Li, G. H.; Schnieders, M. J.; Ren, P. Y., Trypsin-Ligand Binding Free Energies from Explicit and Implicit Solvent Simulations with Polarizable Potential. *J Comput Chem* **2009**, *30* (11), 1701-1711.
118. Muegge, I.; Qi, P. X.; Wand, A. J.; Chu, Z. T.; Warshel, A., The reorganization energy of cytochrome c revisited. *J Phys Chem B* **1997**, *101* (5), 825-836.
119. Rasmussen, T. D.; Ren, P. Y.; Ponder, J. W.; Jensen, F., Force field modeling of conformational energies: Importance of multipole moments and intramolecular polarization. *Int J Quantum Chem* **2007**, *107* (6), 1390-1395.
120. Ren, P. Y.; Chun, J. H.; Thomas, D. G.; Schnieders, M. J.; Marucho, M.; Zhang, J. J.; Baker, N. A., Biomolecular electrostatics and solvation: a computational perspective. *Q Rev Biophys* **2012**, *45* (4), 427-491.
121. Shi, Y.; Wu, C. J.; Ponder, J. W.; Ren, P. Y., Multipole Electrostatics in Hydration Free Energy Calculations. *J Comput Chem* **2011**, *32* (5), 967-977.
122. Carlsson, J.; Ander, M.; Nervall, M.; Aqvist, J., Continuum solvation models in the linear interaction energy method. *J Phys Chem B* **2006**, *110* (24), 12034-12041.

123. de Carvalho, S. J.; Fenley, M. O.; da Silva, F. L. B., Protein-Ion Binding Process on Finite Macromolecular Concentration. A Poisson-Boltzmann and Monte Carlo Study. *J Phys Chem B* **2008**, *112* (51), 16766-16776.
124. Freedman, H.; Huynh, L. P.; Le, L.; Cheatham, T. E.; Tuszyński, J. A.; Truong, T. N., Explicitly Solvated Ligand Contribution to Continuum Solvation Models for Binding Free Energies: Selectivity of Theophylline Binding to an RNA Aptamer. *J Phys Chem B* **2010**, *114* (6), 2227-2237.
125. Lei, B. L.; Hameed, M. D. M. A.; Hamza, A.; Wehenkel, M.; Muzyka, J. L.; Yao, X. J.; Kim, K. B.; Zhan, C. G., Molecular Basis of the Selectivity of the Immunoproteasome Catalytic Subunit LMP2-Specific Inhibitor Revealed by Molecular Modeling and Dynamics Simulations. *J Phys Chem B* **2010**, *114* (38), 12333-12339.
126. Suarez, D.; Diaz, N.; Merz, K. M., Molecular dynamics simulations of the dinuclear zinc-beta-lactamase from bacteroides fragilis complexed with imipenem. *J Comput Chem* **2002**, *23* (16), 1587-1600.
127. Zhou, Z. G.; Madura, J. D., Relative free energy of binding and binding mode calculations of HIV-1 RT inhibitors based on dock-MM-PB/GS. *Proteins-Structure Function and Bioinformatics* **2004**, *57* (3), 493-503.
128. Baran, K. L.; Chimenti, M. S.; Schlessman, J. L.; Fitch, C. A.; Herbst, K. J.; Garcia-Moreno, B. E., Electrostatic effects in a network of polar and ionizable groups in staphylococcal nuclease. *J Mol Biol* **2008**, *379* (5), 1045-1062.
129. Forsyth, W. R.; Antosiewicz, J. M.; Robertson, A. D., Empirical Relationships Between Protein Structure and Carboxyl pKa Values in Proteins. *Proteins* **2002**, *48*, 388-403.
130. Harms, M. J.; Castaneda, C. A.; Schlessman, J. L.; Sue, G. R.; Isom, D. G.; Cannon, B. R.; Garcia-Moreno, B. E., The pKa Values of Acidic and Basic Residues Buried at the Same Internal Location in a Protein Are Governed by Different Factors. *J. Mol. Biol.* **2009**, *389*, 34-47.
131. Matousek, W. M.; Ciani, B.; Fitch, C. A.; Garcia-Moreno, B.; Kammerer, R. A.; Alexandrescu, A. T., Electrostatic contributions to the stability of the GCN4 leucine zipper structure. *J Mol Biol* **2007**, *374* (1), 206-219.
132. Meng, Y. L.; Roitberg, A. E., Constant pH Replica Exchange Molecular Dynamics in Biomolecules Using a Discrete Protonation Model. *J Chem Theory Comput* **2010**, *6* (4), 1401-1412.
133. Thurlkill, R. L.; Grimsley, G. R.; Scholtz, J. M.; Pace, C. N., Hydrogen Bonding Markedly Reduces the pKa of Buried Carboxyl Groups in Proteins. *J. Mol. Biol.* **2006**, *362*, 594-604.
134. Mobley, D. L.; Graves, A. P.; Chodera, J. D.; McReynolds, A. C.; Shoichet, B. K.; Dill, K. A., Predicting absolute ligand binding free energies to a simple model site. *J Mol Biol* **2007**, *371* (4), 1118-1134.
135. Nicholls, A.; Mobley, D. L.; Guthrie, J. P.; Chodera, J. D.; Bayly, C. I.; Cooper, M. D.; Pande, V. S., Predicting small-molecule solvation free energies: An informal blind test for computational chemistry. *J Med Chem* **2008**, *51* (4), 769-779.

136. Nicholls, A.; Wlodek, S.; Grant, J. A., SAMPL2 and continuum modeling. *J Comput Aid Mol Des* **2010**, 24 (4), 293-306.
137. Falconer, R. J.; Penkova, A.; Jelesarov, I.; Collins, B. M., Survey of the year 2008: applications of isothermal titration calorimetry. *J Mol Recognit* **2010**, 23 (5), 395-413.
138. Wennerberg, K.; Rossman, K. L.; Der, C. J., The Ras superfamily at a glance. *J Cell Sci* **2005**, 118 (5), 843-846.
139. Holst, M., Adaptive numerical treatment of elliptic systems on manifolds. *Adv Comput Math* **2001**, 15 (1-4), 139-191.
140. Bank, R. E.; Holst, M., A new paradigm for parallel adaptive meshing algorithms. *Siam J Sci Comput* **2000**, 22 (4), 1411-1443.
141. Baker, N. *Adaptive Poisson-Boltzmann Solver*, 1.3; 2010.
142. Gunner, M. R.; Zhu, X. Y.; Klein, M. C., MCCE analysis of the pK(a)s of introduced buried acids and bases in staphylococcal nuclease. *Proteins-Structure Function and Bioinformatics* **2011**, 79 (12), 3306-3319.
143. Wallace, J. A.; Wang, Y. H.; Shi, C. Y.; Pastoor, K. J.; Nguyen, B. L.; Xia, K.; Shen, J. K., Toward accurate prediction of pK(a) values for internal protein residues: The importance of conformational relaxation and desolvation energy. *Proteins-Structure Function and Bioinformatics* **2011**, 79 (12), 3364-3373.
144. Pearson, J. G.; Oldfield, E.; Lee, F. S.; Warshel, A., Chemical-Shifts in Proteins - a Shielding Trajectory Analysis of the Fluorine Nuclear-Magnetic-Resonance Spectrum of the Escherichia-Coli Galactose Binding-Protein Using a Multipole Shielding Polarizability Local Reaction Field Molecular-Dynamics Approach. *J Am Chem Soc* **1993**, 115 (15), 6851-6862.
145. Danielson, M. A.; Falke, J. J., Use of 19F NMR To Probe Protein Structure and Conformational Changes. *Annu. Rev. Biophys. Biomol. Struct.* **1996**, 25, 163-195.
146. Forsyth, W. R.; Antosiewicz, J. M.; Robertson, A. D., Empirical relationships between protein structure and carboxyl pK(a) values in proteins. *Proteins-Structure Function and Bioinformatics* **2002**, 48 (2), 388-403.
147. Castaneda, C. A.; Fitch, C. A.; Majumdar, A.; Khangulov, V.; Schlessman, J. L.; Garcia-Moreno, B. E., Molecular determinants of the pK(a) values of Asp and Glu residues in staphylococcal nuclease. *Proteins-Structure Function and Bioinformatics* **2009**, 77 (3), 570-588.
148. Harms, M. J.; Castaneda, C. A.; Schlessman, J. L.; Sue, G. R.; Isom, D. G.; Cannon, B. R.; Garcia-Moreno, B., The pK(a) Values of Acidic and Basic Residues Buried at the Same Internal Location in a Protein Are Governed by Different Factors. *J Mol Biol* **2009**, 389 (1), 34-47.
149. Nielsen, J. P.; Petersen, H. H., Objective measurement of health pigs - Application of acute phase proteins. *Acta Vet Scand* **2003**, 125-125.
150. Urbanek, D. C.; Vorobyev, D. Y.; Serrano, A. L.; Gai, F., The two-dimensional vibrational echo of a nitrile probe of the villin HP35 protein. *J. Phys. Chem. Lett.* **2010**, 1, 3311-3315.

151. Waegele, M. M.; Gai, F., Computational modeling of the nitrile stretching vibration of 5-cyanoindole in water. *J. Phys. Chem. Lett.* **2010**, *1*, 781-786.
152. Waegele, M. M.; Gai, F.; Culik, R. M., Site-Specific Spectroscopic Reporters of the Local Electric Field, Hydration, Structure, and Dynamics of Biomolecules. *J. Phys. Chem. Lett.* **2011**, *2*, 2598-2609.
153. Waegele, M. M.; Tucker, M. J.; Gai, F., 5-Cyanotryptophan as an infrared probe of local hydration status of proteins. *Chem. Phys. Lett.* **2009**, *478*, 249-253.
154. Park, E. S.; Andrews, S. S.; Hu, R. B.; Boxer, S. G., Vibrational Stark Spectroscopy in Proteins: A Probe and Calibration for Electrostatic Fields. *J. Phys. Chem. B* **1999**, *103*, 9813-9817.
155. Neves-Petersen, M. T.; Petersen, S. B., **2003**, - Volume 9, - 395.
156. Chen, X. F.; Weber, I.; Harrison, R. W., Hydration water and bulk water in proteins have distinct properties in radial distributions calculated from 105 atomic resolution crystal structures. *J Phys Chem B* **2008**, *112* (38), 12073-12080.
157. Higo, J.; Nakasako, M., Hydration structure of human lysozyme investigated by molecular dynamics simulation and cryogenic X-ray crystal structure analyses: On the correlation between crystal water sites, solvent density, and solvent dipole. *J Comput Chem* **2002**, *23* (14), 1323-1336.
158. Nakasako, M., Large-scale networks of hydration water molecules around bovine beta-trypsin revealed by cryogenic X-ray crystal structure analysis. *J Mol Biol* **1999**, *289* (3), 547-564.
159. Yokomizo, T.; Higo, J.; Nakasako, M., Patterns and networks of hydrogen-bonds in the hydration structure of human lysozyme. *Chem Phys Lett* **2005**, *410* (1-3), 31-35.
160. Chung, E.; Henriques, D.; Renzoni, D.; Zvelebil, M.; Bradshaw, J. M.; Waksman, G.; Robinson, C. V.; Ladbury, J. E., Mass spectrometric and thermodynamic studies reveal the role of water molecules in complexes formed between SH2 domains and tyrosyl phosphopeptides. *Struct Fold Des* **1998**, *6* (9), 1141-1151.
161. Funahashi, J.; Takano, K.; Yamagata, Y.; Yutani, K., Positive contribution of hydration structure on the surface of human lysozyme to the conformational stability. *J Biol Chem* **2002**, *277* (24), 21792-21800.
162. Fennell, C. J.; Kehoe, C. W.; Dill, K. A., Modeling aqueous solvation with semi-explicit assembly. *Proceedings of the National Academy of Sciences of the United States of America* **2011**, *108* (8), 3234-3239.
163. Fried, S. D.; Bagchi, S.; Boxer, S. G., Measuring Electrostatic Fields in Both Hydrogen-Bonding and Non-Hydrogen-Bonding Environments Using Carbonyl Vibrational Probes. *J Am Chem Soc* **2013**, *135* (30), 11181-11192.
164. Ren, P. Y.; Ponder, J. W., Polarizable atomic multipole water model for molecular mechanics simulation. *J Phys Chem B* **2003**, *107* (24), 5933-5947.

